# Understanding how anti–proliferative drug modulates arterial healing following stent deployment

Alistair K. McQueen

Submitted in fulfilment of the requirements for the
Degree of Doctor of Philosophy

School of Engineering
College of Science and Engineering
University of Glasgow


September 2022

# Abstract

The treatment of coronary artery disease (CAD) was revolutionized following the advent of drug–eluting stents (DES). Since their adoption, patient outcome has significantly improved over earlier systems devoid of drug, where notable indices such as in–stent restenosis (ISR) and repeat revascularisations were reduced. However, such indices remain stubbornly high despite this technological innovation, with patients often returning after one–year for a follow–up procedure.

In an attempt to better understand the physical mechanisms that give rise to ISR, many computational models have emerged in recent years. Chapter 1 discusses these in more depth, where the literature is neatly separable into three distinct categories: (i) structural mechanics and computational fluid dynamics, (ii) drug transport models and (iii) mechano–biological models of restenosis. Although the first category is important, it is limitations in (ii) and (iii) that are more pressing. Firstly, drug transport models assume static arteries, where the effect of drug on cell function is ignored, and the artery does not change in response to the growing population of cells. As such, Chapter 2 explores this simplification in depth through a variety of different models describing the effectiveness of drug. Results allude to possible issues with current state–of–the–art drug transport models, such that when coupled to cell function, they are unable to capture the dose–dependent effect of drug on cell growth *in vitro*. In an attempt to better understand these issues, Chapter 3 explores the efficacy of these drugs when their cell cycle specificity is accounted for, discussing the possible implications of this, particularly *in vivo*.

Moreover, mechano–biological models of restenosis often neglect the delivery of drug, with the devices considered emulating earlier bare metal stents (BMS). Those which do account for the anti–proliferative nature of drug do so through inadequate means, where key findings from (ii) are ignored. Thus, building on the efforts of Chapter 2, Chapters 4–6 explore the spatiotmeporal effect of drug on restenosis, emulating drug delivery *in vivo*. Key conclusions from Chapter 5 reveals an intricate interplay between stent drug dose and release rate; simultaneously illustrating the impact of stent design on performance. The model is then built upon in Chapter 6, with the implications of delayed arterial healing analysed, a recurring issues associated with DES. The model is the first of its kind to explore the explicit role of anti–proliferative drug on multiple cell types (endothelial and smooth muscle cells), further highlighting the need for optimal drug release strategies to ensure the drug is both efficacious and safe.

# Contents

# Acknowledgements

It has been a long four years since my research project commenced back in October 2018. Firstly, I would like to thank my primary supervisor, Dr. Sean McGinty, for his invaluable support throughout my research. There is no doubt that the thesis would not be in its current form without your continuous support, patience and expertise. I appreciate all the time you have given me, and I wish yourself, Michelle, and Correy all the best for the future. Secondly, my gratitude extends to the guidance provided from my other supervisors: Dr. Ankush Aggarwal, Prof. Simon Kennedy, Dr. Christopher McCormick, and Prof. Keith Oldroyd. I have appreciated your input immensely over the last four years.

I would also like to thank the many members of the research group, past and present: David, Lauren, André, Marcia, Parna, and Sathish. Thank you for all your meaningful input throughout my studies. For those still studying, all the best in the remainder of your studies, and those that have since graduated, good luck on your careers! I would also like to extend this thanks to Javier for his continuous support and guidance through the wonderful world that is COMSOL Multiphysics.

Next, I would to thank my friends, and in particular, Scott. A good friend and flat mate, thanks for all the memories during our undergraduate and postgraduate studies. To my other friends, you know who you are and thank you.

Finally, I would like to express my deepest gratitude to my family. Mum, Dad, Chris, Joe, and Natalie, thank you all for your continuous support. To my mum and dad especially, thank you for pushing me to become the best version of myself. To Chris, Joe, and Natalie, thank you, it will be Dr. McQueen from now on. Lastly, a special thank you to Monica. You have been with me every step of the way over the last four years and for that I cannot thank you enough. I hope I have made you all proud.

# Declaration

With the exception of the introductory material present in each chapter, all work in this thesis was carried out by the author unless otherwise explicitly stated.

# Presentations and publications

***Poster presentation***
“Modelling the healing response of a stented artery"
Centre of mathematics applied to life sciences (CMALS) 2018, Glasgow, UK

***Poster presentation***
“Modelling the pharmacological inhibition of arterial smooth muscle cell proliferation by drug"
Lord Kelvin Adam Smith (LKAS) 2019, Glasgow, UK

***Video presentation***
“The evolution of coronary artery stents"
Centre of mathematics applied to life sciences (CMALS) 2019, Glasgow, UK

***Oral presentation***
“Modelling of arterial healing subject to drug delivery"
SofTMech 2020, Glasgow, UK

***Poster and oral presentation***
“Modelling arterial healing post stent deployment"
Biomedical Engineering (BME) away day 2020, Glasgow, UK

***Conference proceedings and poster presentation***
**McQueen A**, Kennedy S, McCormick C, et al. “P17: Mathematical modelling of the effect of drug on smooth muscle cell proliferation", *Heart*, 2020;106:A12.
Scottish cardiovascular forum (SCF) 2020, Glasgow, UK

***Oral presentation***

“Preliminary approaches to understand how anti–proliferative drugs modulate in–stent restenosis"

Mathematical modelling and control for healthcare and biomedical systems (MCHBS) 2021, Rome (Online), Italy

***Journal article***

**McQueen A**, Escuer J, Aggarwal A, Kennedy S, McCormick C, Oldroyd K, McGinty S. “Do we really understand how drug eluted from stents modulates arterial healing?" *International Journal of Pharmaceutics*, 2021;601:120575. doi: 10.1016/j.ijpharm.2021.120575.

***Oral presentation***

“Computational modelling of stent–induced drug delivery: A short overview"

CMALS 2021, Glasgow (Online), UK

***Poster presentation***

“Computational modelling reveals an intricate interplay between drug release rate and dose on restenosis"

CMALS 2022, Glasgow, UK

***Conference proceedings and oral presentation***

**McQueen A**, Escuer, J, Schmidt, A, Aggarwal, A, Kennedy, S, McCormick, C, Oldroyd, K and McGinty, S, “In silico modelling of in-stent restenosis subject to spatiotemporal delivery of drug", ISSN 2227–3085.

Computational & Mathematical Biomedical Engineering (CMBE) 2022, Milan, Italy

***Journal article***

**McQueen A**, Escuer J, Schmidt, A, Aggarwal A, Kennedy S, McCormick C, Oldroyd K, McGinty S. “An intricate interplay between stent drug dose and release rate dictates arterial restenosis" *Journal of Controlled Release*, 2022;349:992–1008. doi: 10.1016/j.jconrel.2022.07.037.

# Chapter 1

# Introduction & Motivation

## 1.1 Background

Cardiovascular disease (CVD) is present in approximately 7.6 million individuals in the UK at any given time, equivalent to 11.5% of the population [1]. Specifically, coronary heart disease (CHD) is the most common type of CVD and is the primary cause of premature death in the UK as of 2019 [1]. So detrimental is CHD, that every 8 minutes a life is lost in the UK, killing 1 in 8 men, and 1 in 15 women. Although the current death rate associated with CHD is alarming, vast improvement in both lifestyle and treatment has seen CHD–associated deaths fall by approximately 65% over the last 40 years [2].

CHD blocks blood flow to parts of the heart, occluding nearby vessels through the build–up of fatty deposits in the arterial wall. This accumulation of fatty deposits is a progressive disease called atherosclerosis, where over time the occlusion can become more severe, starving the heart muscle of oxygenated blood, resulting in myocardial infarction (*heart attack*) and possibly death.

Although more common in men than woman, developing twice as fast before the age of 60 [3], the general population is exposed to a list of environmental and genetic factors that increase the risk of disease progression [3, 4] (Fig. 1.1). Moreover, recent studies have begun to highlight in more detail the impact sex can have on CHD progression, particularly in women post–menopause [5].

### 1.1.1 Structure of the arterial wall

CHD is a disease which impacts the morphology and structure of the arterial vasculature by altering the state of the vessel wall. Coronary arteries are a compliant structure that function to deliver blood to heart tissue, and are thus critical in supplying nutrients, thereby sustaining life. The general structure of an artery can be divided into three layers: the intima, media, and adventitia as illustrated by Fig. 1.2.

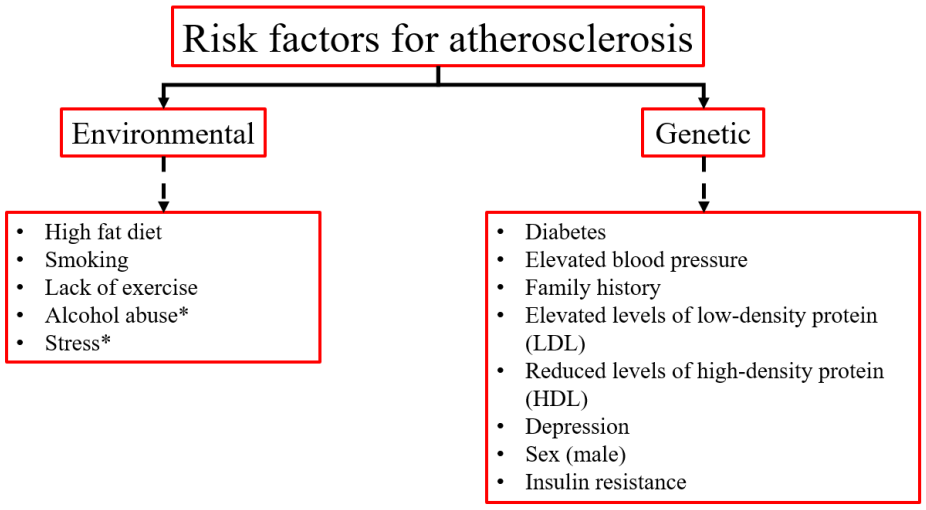


Figure 1.1: A list of environmental and genetic risk factors that can progress atherosclerosis. * Emerging risk factors under further scientific investigation as noted by [4].

The innermost layer of the artery is the intima, comprised primarily of a thin layer of endothelial cells (ECs), called the endothelium. The primary function of this layer is to act as barrier between circulating blood and the artery, regulating the movement of molecules across the wall. These cells have additional responsibilities,. Firstly, ECs are responsible for control of vascular tone, permitting either vasoconstriction or dilation through the release of numerous chemical mediators [6]. Secondly, these chemical mediators also regulate SMC phenotype. Lastly, these cells are particularly important in the prevention of thrombosis. Failure in this layer, termed endothelial dysfunction, is the starting point for disease progression [6, 7].

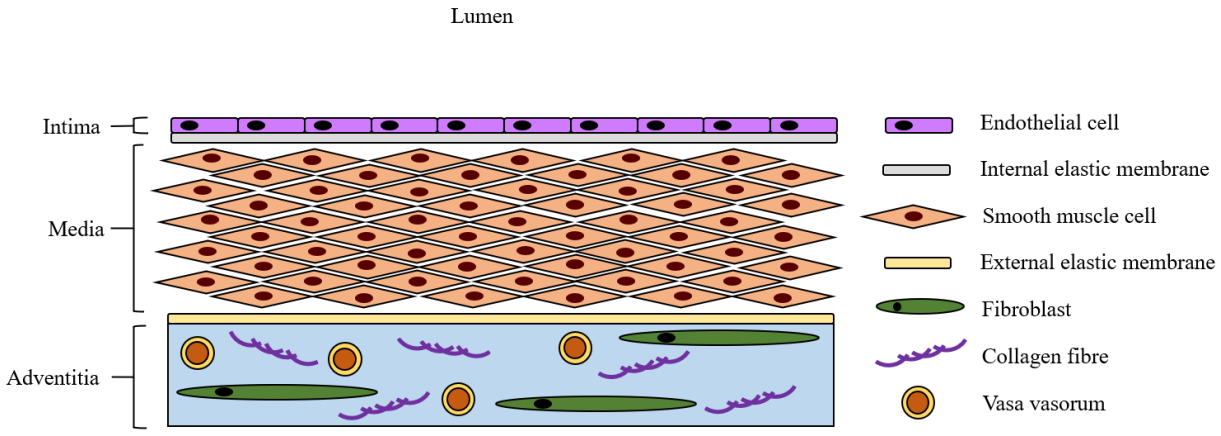


Figure 1.2: A schematic diagram detailing the structure of the artery wall.

Adjacent to the intima is the media, separated by an internal elastic lamina (IEL). It hosts several, organized layers of smooth muscle cells (SMCs), embedded within a collagen rich extracellular matrix (ECM) [8, 9]. When the artery exists in a healthy state, the SMCs are of a contractile phenotype, differentiating into their synthetic phenotype only in response to disease

and/or injury, where proliferation and migration occurs, promoting tissue growth and remodelling.

The adventitia is the outermost layer of the arterial wall. This is separated from the media by the external elastic lamina (EEL) and is composed primarily of collagenous fibres and fibroblast cells. This sheath of connective tissue functions primarily to protect the vessel, supporting it from rupture at high pressures and to ensure wall rigidity [10]. Moreover, the adventitia hosts the vasa vasorum which supplies nutrients to the other layers of the artery, as well as immune cells which function to survey the environment for foreign antigens [11].

### 1.1.2 Progression of Atherosclerosis

The onset of atherosclerosis is a highly complex process that is triggered following chronic inflammation to the endothelium. It involves the accumulation of lipids, inflammatory cells, and fibrous elements; often occurring at predilection sites (such as branches in the artery) where disturbed flow is present [3, 12, 13]. At the early stages of disease, lipoproteins congregate within the intima, where monocytes adhere to the endothelium before entering the wall. Upon transmigration, monocytes proliferate and subsequently differentiate into macrophages taking up nearby low–density lipoproteins (LDLs) to become foam cells (Fig. 1.3b). This process is enabled through endothelial dysfunction, where the confluent nature of the cell layer is disturbed, a consequence of disturbed blood flow or elevated cholesterol and blood pressure [3, 4, 14]. Eventually, foam cells die, which results in debris accumulation within the plaque, forming a necrotic core. This site of 'death' releases chemicals that recruit further monocytes and LDLs to the site such that the process becomes iterative, and the plaque grows. Additionally, plaque size may increase through SMCs that undergo a phenotype switch in response to the disease [15].

In time, the increasing burden of disease may result in stenosis: a narrowing of the vessel so severe that blood flow is disturbed, and possibly occluded. It is the evolution of this plaque that results in a patient being diagnosed with CHD. With the function of the coronary vessels being to supply the heart muscle with oxygen, when impeded, vessel performance is inhibited and the possibility of myocardial infarction arises. Moreover, as the disease progresses, the plaque may become more vulnerable, notable by its large lipid pool and thin fibrous cap (Fig. 1.3a) [16]. Following rupture, a cardiac event is likely, where a blockage occurs as a result of a blood clot (*thrombus*). Therefore, interventional treatments, the focus of Section 1.2, were devised in an attempt to address the issues associated with atherosclerosis.

## 1.2 The evolution of treatment for CHD

Traditionally, open heart surgery was performed to treat obstructive CHD. This required a bypass, involving the removal of a blood vessel from elsewhere in the body, to provide blood flow

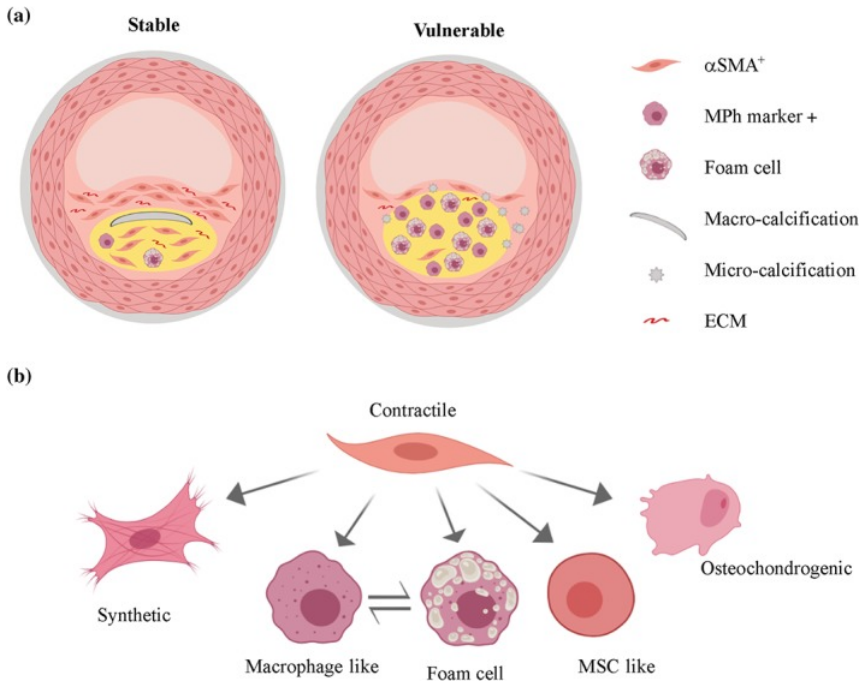


Figure 1.3: A schematic diagram highlighting: (a) stable versus vulnerable plaque. (b) cell differentiation. Acquired with permission from [16].

with an alternative pathway away from the diseased occlusion. In time, technological innovations ensued which allowed for a more minimally invasive procedure to be carried out called percutaneous coronary intervention (PCI), which has since evolved as depicted in Fig. 1.4. Typically, a small incision is made in the groin (or wrist), permitting the delivery of the medical device (stent or balloon) by a catheter to the site of disease. The device is deployed by means of expansion which aims to relieve restricted blood flow by compressing the plaque.

Initially, this treatment utilised balloons (plain old balloon angioplasty, POBA) as the primary medical device, but drawbacks were apparent, with elastic recoil common and vessel re–occlusion high by means of restenosis. For example, elastic recoil occurred in 5–10% of patients immediately after the procedure, where severe adverse events were observed, requiring an emergency bypass surgery [17]. Even when successful, the severity of injury as a consequence of the procedure resulted in severe restenosis (re–narrowing) rates of around 40% [20]. If severe enough, where vessel re–narrowing is $>$50%, then the regrowth is termed in–stent restenosis (ISR), where a follow–up procedure is often necessary.

Challenges associated with POBA led to the advent of the bare metal stent (BMS). The presence of a permanent device within the vessel ensured abrupt closure following expansion was unlikely. Although charting superior results to POBA, it was not without its own limitations. The high metallic density and low biocompatibility of these stents meant that the risk of stent thrombosis (ST) and ISR remained [21]. To combat the former, patients were often prescribed an oral course of dual–antiplatelet therapy (DAPT), of which the optimal course of treatment is still under investigation [22].

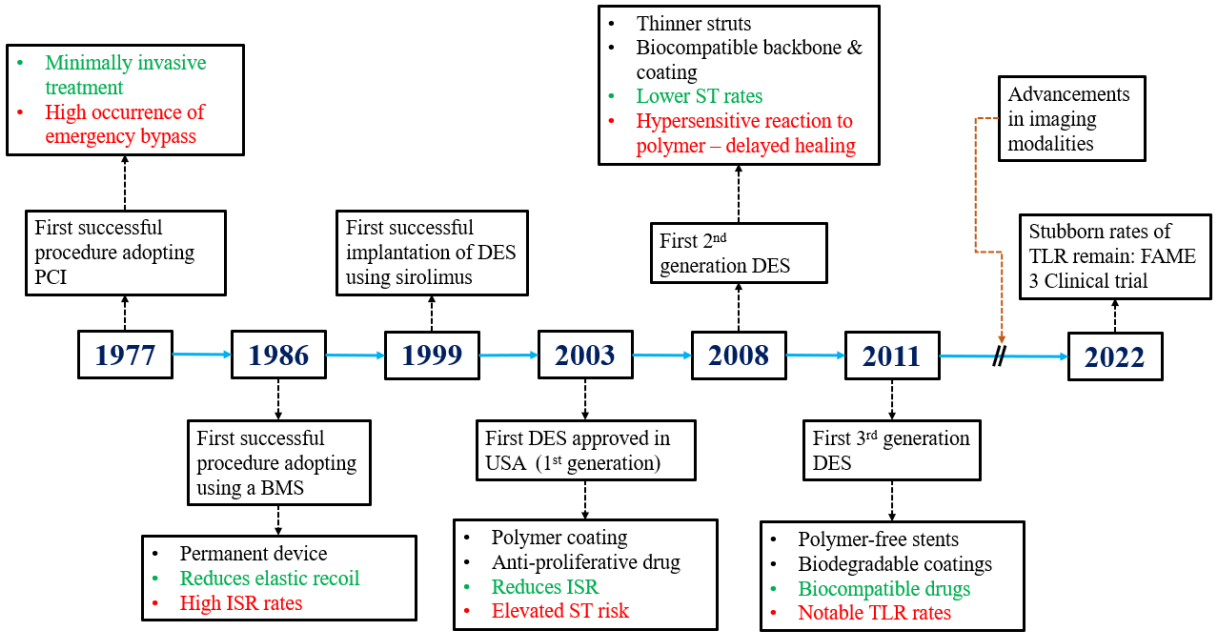


Figure 1.4: A schematic diagram highlighting the evolution of percutaneous coronary intervention (PCI). Inspired from [17–19]. Green and red text refer to advantages and disadvantages of each milestone, respectively. For extensive information on the evolution of CHD treatment, the reader is referred to the following review articles [17–19]. BMS = bare metal stent, DES = drug–eluting stents, TLR = target lesion revascularisation, ISR = in–stent restenosis, ST = stent thrombosis.

At the turn of the century, drug–eluting stents (DES) were deployed into diseased vessels in an attempt to address limitations associated with BMS, particularly ISR. Their novelty introduced anti–proliferative drug, embedded within a polymer coating on the surface of the stent to combat excessive restenosis rates present in treatments adopting BMS. DES significantly improved patient outcome where the incidence of target–lesion revascularisation (TLR) compared to BMS was significantly lowered (6% *c.f.* 18%) at one year after implantation [22]. Within the same time window, ST rates were comparable (1.1% *c.f.* 1.3%) [22]. However, at a long–term follow–up, these first–generation DES were associated with late–stage thrombosis (LST) with respect to BMS, demonstrating an increased risk of death through a major adverse cardiac event (MACE) (7% *c.f.* 3.2%) [23].

Albeit still the subject of intense research, both the polymer coating and drug have been attributed to the likelihood of LST as a result of delayed healing; where recovery of the endothelial layer interfacing the wall and lumen is impeded [24–28]. Poor biocompatibility associated with the polymer coating induces a hypersensitive response, where the inflammation stage of the healing process was notably prolonged [24]. Moreover, delayed (or dysfunctional) re–endothelization, may also be attributed to the non–specific nature of the anti–proliferative drug, inhibiting both endothelial and smooth muscle cell proliferation [29–31]. With these issues in mind, technological innovation led to a new ($2^{nd}$) generation of DES which markedly improved

patient outcome. These devices adopted more biocompatible backbone materials which were also thinner, reducing the likelihood of ISR [22, 32]. Additionally, the bicompatibility of the polymer coating also improved, and the hypersensitive reaction of durable stents reduced as a result [33–36]. Moreover, the drugs coated on stents changed, shifting away from paclitaxel, where newer devices predominantly included sirolimus or one of its analogues [36]. This was supported by a large meta–analysis of over 18,000 patients, reporting reduced rates of myocardial infarction, TLR, and ST in favour of sirolimus over paclitaxel [37]. Further changes in design brought about the 3$^{\text{rd}}$ generation. Initially, two alternatives to traditional polymer–coated DES were considered: (i) a biodegradable polymer coating on a metallic stent backbone [35] or (ii) a polymer–free approach [38, 39]. However, these novel devices were unable to establish superiority to durable 2$^{\text{nd}}$–generation devices. For example, meta–analysis studies have demonstrated a comparable efficacy between DES employing a durable coating and those which are absent of the coating entirely [39], supported by further evidence which took blood samples for inflammatory markers [40]. Additionally, no significant difference was charted in MACEs and TLR rates between stents which employ a durable or biodegradable coating [33–35]. In time, efforts explored a fully degradable structure, aiming to remove the negative impact associated with the long–term presence of the device [41]. The Absorb$^{\text{TM}}$ (Abbott Vascular, Santa Clara, USA) biodegradable scaffold was the first of its kind, presenting efficacy that was comparable with durable second–generation DES at a 1–year follow–up [42]. However, beyond this, an increasing risk of myocardial infarction and TLR were apparent, most likely because of the heightened risk of ST compared to durable second–generation DES (2.4% *c.f.* 0.6%) [22, 43].

Innovation continues as the next generation of DES is approached, with devices now hosting smaller struts still (ultra–thin $< 80\ \mu$m), where alternative coating strategies which are abluminal are considered over the traditional circumferential style [35, 44]. Moreover, although significant changes in the design of DES have been absent over the last decade, imaging modalities have markedly improved, which in turn benefit patient outcome following PCI by enhancing the visualisation of both the disease and the procedure [45]. Notably, virtual histology–intravascular ultrasound (VH–IVUS) was able to highlight the burden of disease by separating the plaque into distinct categories: calcified, fibro–fatty, fibrous cap, and necrotic core [46]. Optical coherence tomography (OCT) was also introduced, which permitted greater resolution over IVUS at a lower penetration depth, enabling the evaluation of strut apposition, commonly associated with ST risk [24, 27]. Both modalities present with their own advantages and disadvantages but both IVUS–guided and OCT–guided PCI demonstrated improved patient outcome over standard angiography–guided PCI with respect to the incidence of MACEs after 1–year [45, 47].

However, as highlighted by a recent clinical trial [48], the rates of TLR remained high at 6% following the deployment of a 3$^{\text{rd}}$–generation stent at a 1–year follow–up with an expected annual increase of 3–5%. This places immense pressure on the healthcare system, where in 2018, close to 4.5 million PCI procedures were performed worldwide, an increase of 13% on the

previous year [49]. Thus, based upon the values above, an estimated quarter of a million patients will return for a repeat procedure after 1–year, increasing significantly year–on–year thereafter. Although many factors attribute to TLR rates and stent failure, ISR has been found to be the primary culprit [50]. Thus, in an attempt to better understand the dynamics of restenosis, and the performance of DES, recent research has probed measures that permit real–time monitoring of constituents involved in vessel remodelling [22, 41, 51, 52]. However, there still exists no means to monitor restenosis *in vivo*, without the re–appearance of angina or worse; a myocardial infarction [22]. Thus, *in silico* models serve as a powerful tool, where computational efforts which emulate various aspects of the stenting procedure can be devised. This is discussed in more depth in Section 1.4. First, an understanding of the restenosis process is necessary to better appreciate how DES work to combat excessive tissue growth.

## 1.3 Biological response of the artery following stent implantation

Focusing on the biology, one needs to understand how the stent impacts vascular dynamics to grasp how the process of restenosis may be modelled mathematically. Stent deployment is a procedure that carries with it much force and destruction. The expansion of the stent from the balloon catheter system is intended to restore natural blood flow by compressing plaque, which in some cases may be severely calcified. In doing so, vascular injury is often significant, which induces a complex biological cascade involving inflammation, growth and remodelling to promote arterial healing. This section briefly details key biological processes that occur as a consequence of stenting, where vessel re–narrowing is the result. The section will follow the structure of Fig. 1.5, which neatly summarises how stent deployment induces injury to the arterial wall, triggering a healing response where constituents primarily congregate within the intima to promote vessel re–narrowing, forming what is termed the *neointima*, until healing is complete.

The trigger to neointimal growth is the denudation of the endothelial layer that lines the inside of the vessel [61]. When unperturbed, the ECs within the intima synthesize a plethora of chemicals (e.g. NO) that are instrumental in regulating vascular tone. However, vascular injury as a consequence of stenting significantly damages the protective endothelial barrier, triggering a healing response.

Vascular injury has been strongly linked with restenosis severity, where more intrusive stent deployment correlates to higher rates of ISR [56, 62]. To establish the severity of stent–induced damage, various ‘scores’ were devised, most notably the ‘Gunn Injury Score’ [63] which has been utilised within pre–clinical animal models [64] as well as computational ISR models [65, 66]. Summarised in Table 1.1, there exists 3 categories of the Gunn Injury score across 5 levels ($0 \rightarrow 4$), ranging from no injury (0), to arterial stretch (1 and 2), and finally to deep injury (3 and

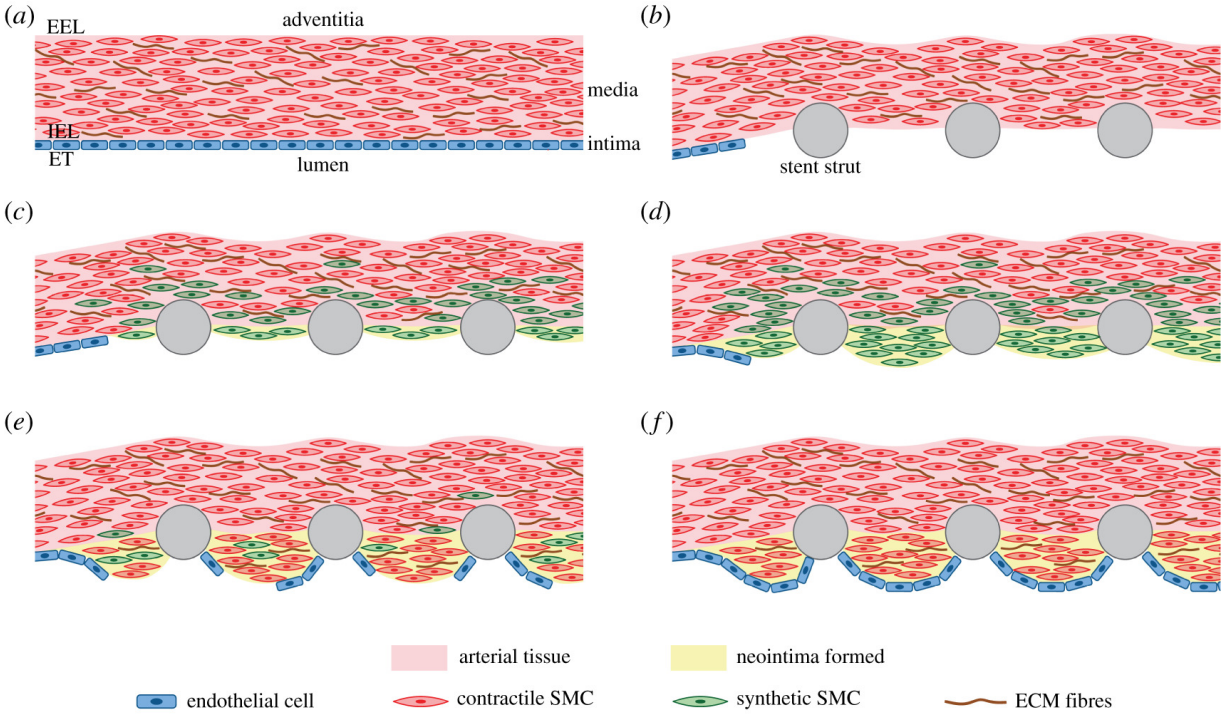


Figure 1.5: A schematic diagram illustrating the process of restenosis. (a) Depicts a healthy artery, dominated by contractile, quiescent smooth muscle cells (SMCs). (b) Illustrates stent deployment, where the endothelial layer is denuded [53]. (c) Vascular injury exposes the arterial wall to circulating growth factors which promote differentiation of cells to their active, synthetic phenotype [54, 55]. (d) In time, the excessive growth intensifies, and vessel re–narrowing occurs as SMCs proliferate and migrate into the neointima [56, 57]. (e) As the endothelial layer regenerates, normality begins to resume, and SMCs begin differentiating back to their dormant phenotype [58, 59]. (f) Ideal state depicting a fully healed vessel with a complete and functional endothelial layer. Predominantly, the majority of growth occurs within the first three months [56, 60]. Taken with permission from [55]. ET = endothelium, IEL = internal elastic lamina, EEL = external elastic lamina.

4). The definition of vascular injury is significant, as stretching of the IEL introduces a number of fenestrations that increase the area of the arterial wall exposed to stimulants circulating in the blood [56, 65, 67]. Moreover, deeper tears beyond the EEL trigger constituents in the adventitia, exacerbating restenosis further [11, 68, 69].

| Injury Score | Description |
|---|---|
| 0 | No injury |
| 1 | Stretch: IEL deformed by $< 45^\circ$ |
| 2 | Stretch: IEL deformed by $> 45^\circ$ |
| 3 | Deep injury: IEL ruptured |
| 4 | Deep injury: EEL ruptured |

Table 1.1: The Gunn Injury Score. Inspired from [63].

Following vascular injury, restenosis begins through the migration and proliferation of smooth muscle cells (SMCs) from the media to the intima (Fig. 1.5c–d). Briefly, SMCs respond to cues following arterial injury, where partial or complete damage to the endothelial barrier exposes underlying tissue to a plethora of constituents that may induce growth, whilst reducing inhibitory mediators that maintain vessel quiescence [70]. As such, a SMC phenotype switch occurs where the once dormant, contractile SMCs (cSMCs) become active, synthetic SMCs (sSMCs) [71]. This transition is thought to occur through growth factors (GFs) produced as a result of the following stimuli: injured endothelium and media [62]; ECM degradation [54, 55]; platelets and inflammatory cells at the wound site [56] and; compressive forces within arterial wall from the deployed stent [54, 56, 71]. Fig. 1.6 presents these two SMC phenotypes, where differences are present not only in gene and protein expression, but also in cell morphology.

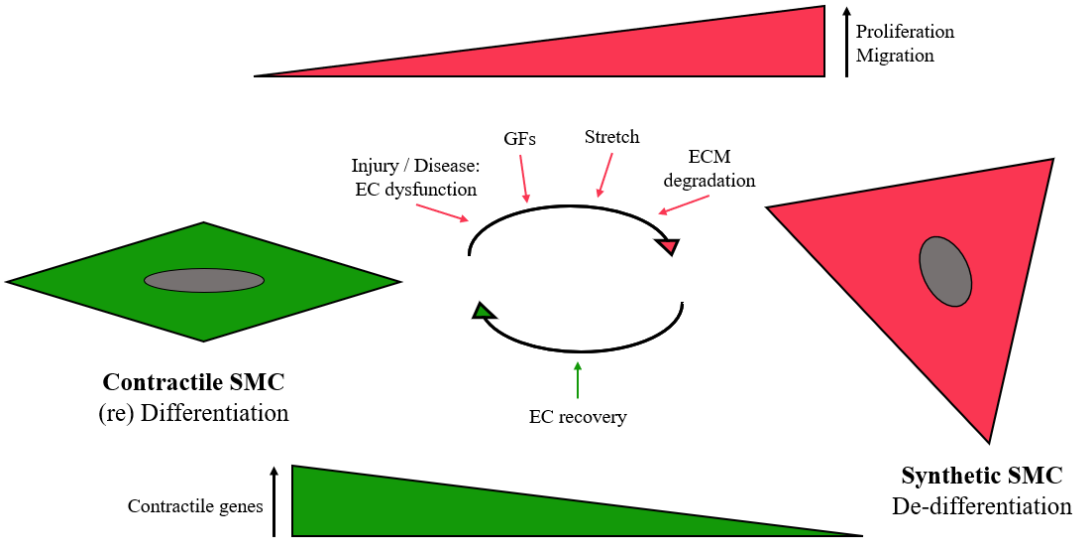


Figure 1.6: Schematic of the differing morphology of each SMC phenotype. The contractile SMCs exist in healthy arteries, with injured and diseased arteries hosting synthetic SMCs which proliferate and migrate to form atherosclerotic plaques and neo–intimal growth as a result of disease or vascular injury, respectively.

Upon differentiation, prolonged exposure to platelet derived growth factor (PDGF) and fibroblast growth factor (FGF) from numerous sources permit the migration of sSMCs into the intima, where proliferation ensues [56]. Subsequently, to promote positive remodelling, these cells deposit ECM which results in further neointimal growth through the adhesion of cells and pooling of GFs [55, 56]. The ECM deposited by sSMCs, and other species, is said to contribute significantly to neointimal growth, more so than cellular species at later times [72, 73].

Excessive tissue growth is eventually halted through the recovery of the once–damaged endothelial layer; the marker of a fully healed vessel, and thus the cornerstone of arterial healing [56]. Re–endothelization predominantly occurs from surviving patches of ECs post–stent implantation, stimulated to proliferate by growth factors [62, 65, 74]. As one can expect, delayed re–endothelization following stenting has a significant impact on restenosis, a prevalent issue

following the implantation of DES [25, 62, 75]. This is particularly problematic when vascular injury is severe, as re–endothelialization is delayed as a result [62]. Thus, a timely recovery of the endothelium is desired in minimising excessive tissue growth such that, once confluent and fully functional, the vessel should revert back to its once, healthy state as presented schematically in Fig. 1.5f [53].

Summarising, the healing process, dominated by the migro–proliferative properties of SMCs, can be divided generally into three distinct phases: (i) inflammation; (ii) tissue growth as a consequence of SMC migration, proliferation, and ECM deposition and; (iii) remodelling. Inflammation occurs immediately following stent deployment and comprises of numerous cells, where the number of adherent monocytes and macrophages to the wound site are related to the level of vascular injury [56, 76]. Subsequently, SMCs are recruited to the site of injury and play a crucial role in vascular healing [70]. Vascular injury triggers their proliferative capacity by inducing de–differentiation into an active phenotype [54, 56, 60]. As cells proliferate, additional matrix is deposited to provide vascular structure and ensure vessel rigidity as part of the remodelling process [56, 60]. In time, the neointima becomes hypo–cellular, and matrix synthesis dominates, comprising approximately 70–80% of the restenotic tissue over the course of several months [60, 73]. The general time–scale of restenosis is summarised in Fig. 1.7, where various studies report minimal growth beyond 6 months [55, 60, 77].

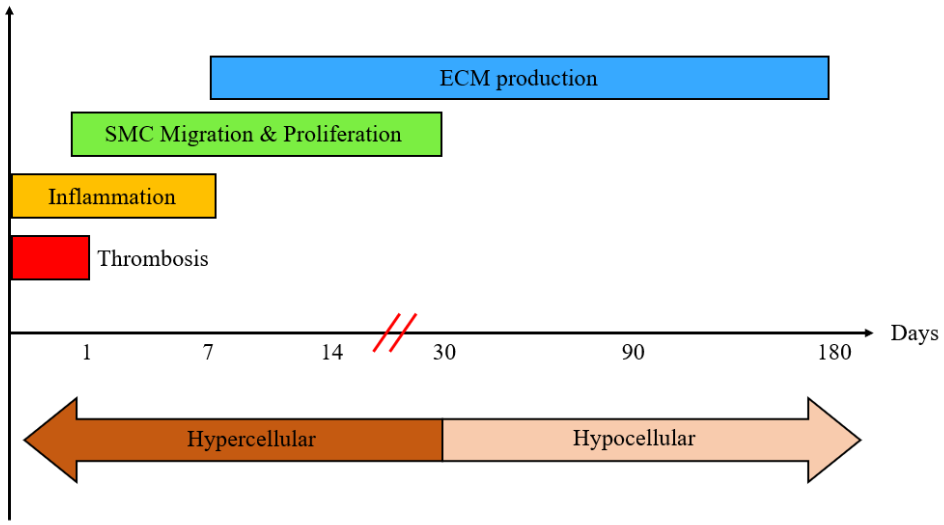


Figure 1.7: Time-frame of restenosis, denoting that in time, the neointima stabilises and is thus dominated by ECM. Inspired from [60, 77].

### 1.3.1 The action of anti–proliferative drugs

With ISR rates notably high following the deployment of BMS, technology explored the use of drugs with anti–proliferative properties to combat excessive tissue growth. Required at the site of injury, these drugs were embedded within a polymer matrix, released from the stent in a

controlled manner during the active stage of vessel remodelling [78, 79]. Discussed in depth in the subsequent chapter, the role and purpose of these drugs is briefly summarised below.

First–generation DES considered sirolimus and paclitaxel which impede cell function by different means. The former ceases proliferation by blocking the mammalian target of rapamycin (mTOR) pathway, whilst the latter does so by binding to microtubules [80, 81]; both present within the cell. Although profoundly improving patient outcome, notable issues arose with DES treatment, where MACEs became more common as a result of ST (Fig. 1.4). Further innovation improved stent design which employed more biocompatible coatings and drugs (analogues of sirolimus), reducing ST rates below that present in BMS [22]. However, delayed arterial healing persisted, where the drug impeded the functionality of both endothelial cells and SMCs [24, 25]. With recent studies suggesting non–inferiority between durable and biodegradable coatings [34, 35], and TLR rates still stubborn [48], then further investigation into the drug delivery protocol seems worth pursuing. The significance of anti–proliferative drugs is unquestionable, and their benefit evidenced. However, further investigation into the role of drug on restenosis may aid in the optimization of DES design.

## 1.4 The role of computational models in understanding stent performance

Computational modelling is a powerful tool, used in an abundance of applications to gain insight into various processes. Such models can be employed to improve the understanding of complex scenarios, which may be difficult to grasp through experimental approaches alone [82]. Of interest here is advancements in mathematical models of biology, where often a complex cascade of events occur in response to some trigger. This may be the growth of a tumour [83]; the response of skin when healing a wound [84]; the flow of blood through vessel architecture [85] or; the monitoring of electrical stimuli in the treatment of muscle rehabilitation. The point is that through sufficient research, these models can be built up in complexity such that patient outcome can be predicted to advise clinicians of the optimal treatment strategy. Preliminary models provide useful insights into complex behaviours but are often simplistic and not fully representative of the *in vivo* environment. In time, model complexity grows in an attempt to more closely emulate *in vivo* behaviours, where experimental data is often necessary to fully validate efforts such that predictions are reliable and experimental turnover may be reduced.

With this in mind, the extensive literature encompassing an array of computational models of stents is briefly summarised below. Work can often be separated into three distinct categories, with some overlap (Fig. 1.8). These include models of: (i) structural mechanics and computational fluid dynamics (CFD); (ii) drug delivery, transport and subsequent drug retention in tissue and; (iii) mechno–biological models of restenosis. Each aspect of the literature has the same fundamental aim which is to pursue optimal stent design.

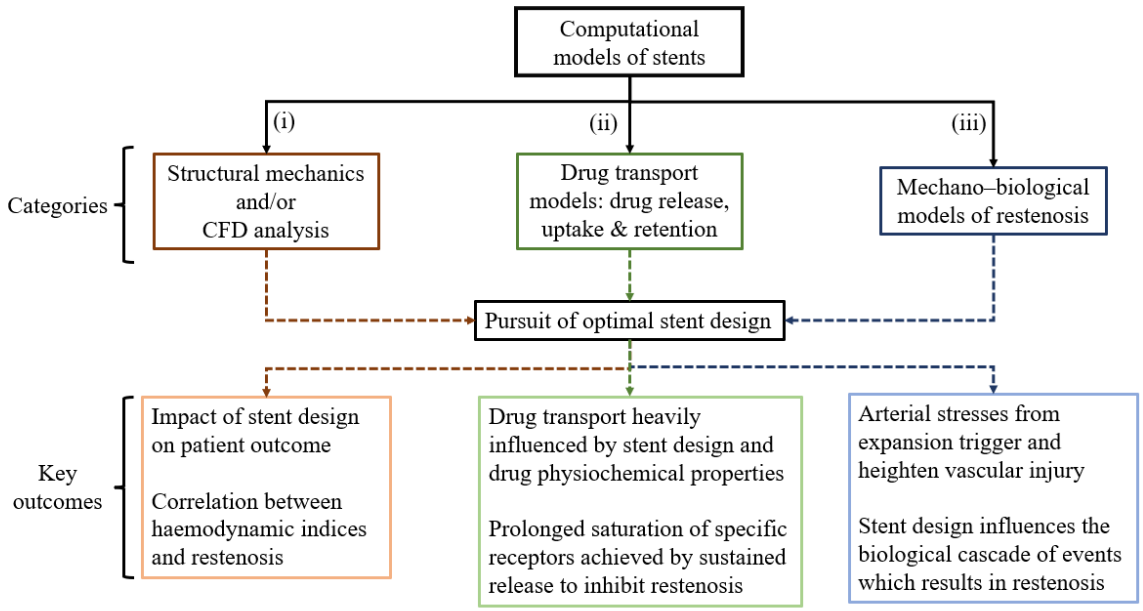


Figure 1.8: Flow chart dividing the literature into three distinct categories, highlighting key outcomes from each. CFD = computational fluid dynamics.

### 1.4.1 The impact of stent deployment: Structural mechanics and fluid dynamics

Finite element analysis (FEA) is a numerical simulation technique which has been widely adopted to evaluate stent performance, particularly investigating the contact between the stent and the arterial wall, inclusive of plaque if simulating diseased vessels. Pioneering works considered free–expansion models that investigated various stent designs [86], evaluating conformability and resistance to compression [87], and the impact of metal–to–artery ratio on stent performance [88]. In time, methods became more sophisticated, where stents were expanded following balloon dilation [89–91]. Subsequent efforts then investigated the impact of both stent and balloon geometrical properties on performance; aiming to depict a possible link to the likelihood of ISR [92–95].

Simulating disease, preliminary work considered an idealised vessel, where the stenosis was parabolic and the artery cylindrical [96]. Both the plaque and artery were highly simplified, where material properties were isotropic and homogeneous whilst the stent was expanded through a boundary condition. Within a similar geometry, stent expansion was improved, now simulated by the aid of a balloon catheter, highlighting areas of the wall that incurred large stresses during deployment [97]. Methods became more sophisticated, and various efforts demonstrated the predictive capacity of their models, correlating higher areas of arterial stress with ISR [98, 99]. In time, models probed methods that informed optimal stent design, emphasising the importance of increased strut spacing and reduced strut thickness in limiting high stresses and minimizing strut–induced flow disturbance following stent deployment that

improved patient outcome (Fig. 1.9) [100–107].

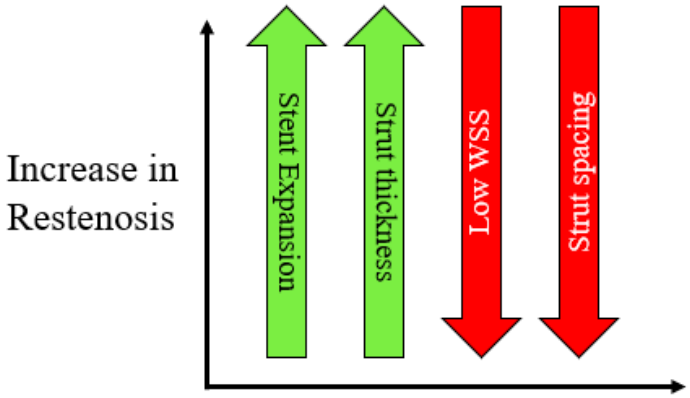


Figure 1.9: Features associated with stenting that correlate with increased restenosis, inclusive of stent design (strut thickness and strut spacing), procedure (stent expansion), and fluid dynamics (WSS = wall shear stress).

These preliminary studies demonstrated the significance of FEA as a tool to optimise stent design. This became clear as the complexity of models increased, where expansion within patient–specific arteries was considered, permitting the use of these models as preclinical tools [108, 109]. Subsequent research considered comparative studies, highlighting the performance of different stents and how plaque composition may influence expansion protocol through increasingly sophisticated constitutive models [100, 110, 111]. Moreover, complex scenarios have since been modelled, where efforts have investigated the significance of bifurcations and/or stent overlap on device performance [112–115].

As rates of ISR and ST remained unsatisfactory, technological innovation led to the development of new stents (3$^{rd}$–generation) hosting different materials. As such, many studies have recently emerged that investigated the mechanical performance of these newer degradable stents, where the backbone is composed of a naturally weaker material compared to traditional metallic options [116–124]. Preliminary results suggested that plaques which are highly calcified may be troublesome for polymeric stents over metallic ones, where the former was found to have a lower rate of expansion [118, 122]. This highlights the need for extensive research into further stent designs which incorporate new materials, with a recent resorbable stent Absorb$^{TM}$ (Abbott Vascular, Santa Clara, USA) pulled from the market due to poor patient outcome [22, 43].

Following the deployment of the stent, CFD presents itself as a valuable tool, permitting the assessment of local haemodynamics; particularly wall–shear stress (WSS) and the oscillatory shear index (OSI). Various clinical studies at the turn of the century have since demonstrated a correlation between these indices and subsequent neointimal growth [125, 126]. Preliminary studies, in agreement with purely expansion studies above, demonstrated that reduction of both strut number and strut thickness were less likely to subject the vessel to WSS distributions that

have correlations with high rates of restenosis [127, 128]. This was met with improvements in other aspects of design, where increased inter–strut spacing was perceived advantageous in addition to a streamlined strut profile to reduce the severity of recirculation zones adjacent to the struts (Fig. 1.10) [85, 129–140]. Moreover, with disease predominantly originating at bifurcations, as opposed to along straight geometries [141], significant research where geometries were either idealised [85, 139, 140, 142, 143] or patient–specific [85, 144–149] has probed alternative treatment protocols in an attempt to address the difficulty of the current procedures for lesions of this type.

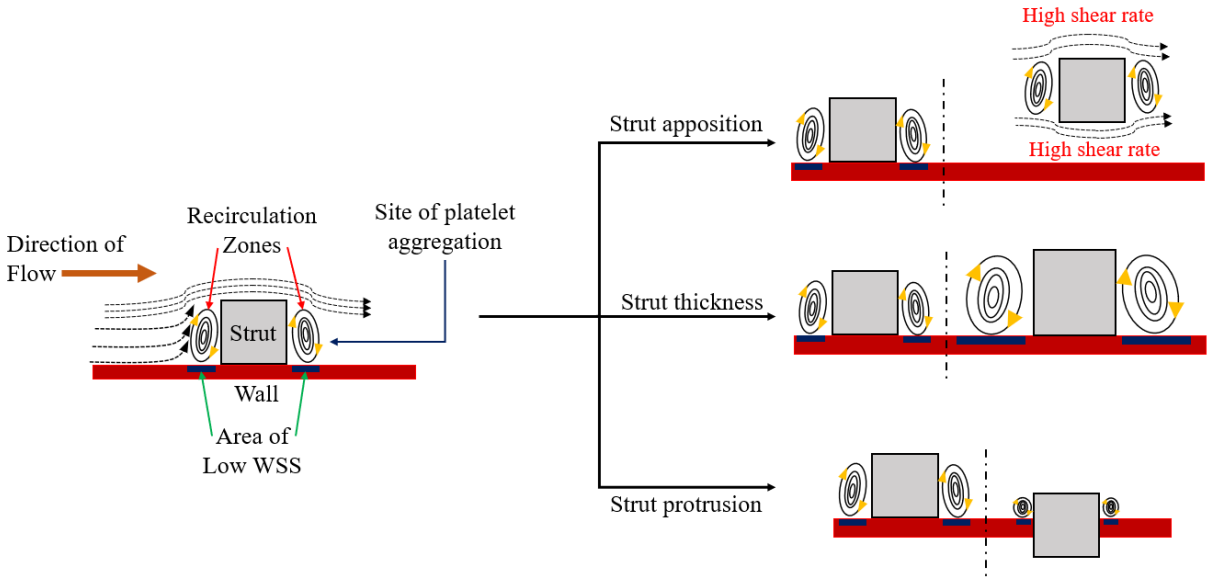


Figure 1.10: How strut profile may influence WSS values through the presence of recirculation zones. Image on the left illustrates a default case, demonstrating direction of flow, possible recirculation zones (sites of platelet aggregation), and sites of possible areas of low WSS, denoted by the blue rectangles. Three cases on the right show possible impact of malapposition, strut thickness and strut protrusion. The dashed black lines separate two cases. All images are presented to illustrate possible effects from literature (e.g. [150, 151]), and are not too scale. WSS = wall shear stress.

With the importance of endothelial cells already highlighted, CFD modelling has emerged as a powerful tool to explore the impact of low shear stress on cell function, and thus arterial healing [152–154]. For example, CFD analysis has been utilised in conjunction with various clinical studies, illustrating that low WSS ($< 1$ Pa) profiles are indicative of severe endothelial dysfunction [155] and/or plaque progression [156], suggesting the need for continuous innovation in stent design where optimal strut apposition and size should be at the forefront [150, 157, 158]. These areas of low WSS are a consequence of recirculation zones, particularly evident when the strut profile is larger, less streamlined, or as a result of poor apposition following expansion (Fig. 1.10) [150, 151, 159].

Within the last decade, both fluid dynamics and structural mechanics have been considered

in harmony. To the best of the author's knowledge, Morlacchi *et al.* [160] were the first to assess the impact of flow within stented coronary bifurcations, which has since evolved to probe optimal treatment strategies [85]. Additional efforts alluded to the importance of deformed arterial geometries on haemodynamics, noting a significant difference to the non–deformed cases across a range of stent models [161, 162]. Following these findings, research focused on emulating *in vivo* conditions, where studies were aimed to demonstrate the use of their models as pre–clinical tools. In particular, a 'John Doe' programme was considered, where computational models were compared directly to clinical intervention. To emulate the patients' vessel architecture, a computational geometry was reconstructed using computerized tomography (CT) and IVUS, where a XIENCE Primus stent was deployed in a similar fashion to that the patient received *in vivo* [149]. Positive findings then suggested that such computational methods could be used in the future to aid clinicians on the optimal course of treatment, particularly for highly complex lesions [163]. In light of this, as new stents emerge, structural and fluid dynamics studies should be considered together to investigate device performance [164].

### 1.4.2 Drug elution kinetics: Role of drug release, uptake & retention

Drug elution kinetics are critical in device performance, and have thus been the focus of intense research in an attempt to inform manufacturers of the optimal drug dose and release rate to combat ISR. DES are often tested *in vitro*, where the process of drug release is controllable, ensuring that the desired release profile is repeatable. As such, the validation of mathematical models is less challenging where variability in the data is smaller compared to *in vivo*.

For example, preliminary work using one–dimensional (1D) models illustrated that the release of drug was typically dominated by diffusion in first–generation stents hosting a durable coating (Eqn. 1.1) [78, 165–167]. Therefore, to date, the release of drug into the arterial wall from the stent surface is predominantly modelled through a purely diffusive process [168–170]:

$$\frac{\partial c_p}{\partial t} = D_p \nabla^2 c_p, \qquad c_p(0) = c_p^0 \tag{1.1}$$

where $c_p$ is the concentration of drug within the polymer coating, initially taking the constant and uniform value $c_p^0$, and $D_p$ is the diffusion coefficient of drug within the coating, typically assumed to be constant and isotropic. Extensions of this model considered bi–modal diffusion, where drug has two routes out of the polymer. This can be either through drug–filled pores or via stored diffusion from the polymer matrix. Release from the former is typically very fast, slowing down as this empties and the remainder of drug is released from the polymer matrix [79, 165, 167, 171, 172].

In recognition that drug may exist in two forms on the polymer coating (dissolved and undissolved) dissolution–diffusion models appeared [173]. Although [173] presented how one mode of diffusion detailed the release of drug from the CYPHER$^{\text{TM}}$ stent, such models could be used

in the analysis of different stents that present alternative release profiles. Such a methodology (or similar) has been widely adopted since when modelling drug release [172, 174–179]. This is inclusive of polymer–free devices [176, 177], biodegradable coatings [180–182] and even fully biodegradable stents [183]. As such, depending on the situation being modelled, the boundary conditions imposed may vary from case–to–case. For full details on the modelling of different devices, the reader is referred to [78].

Following the release of drug, one must understand the mechanisms that occur as the drug enters the arterial wall, to ensure that the drug is both efficacious and safe. The transport of free drug within the wall is more complex than in the polymer coating, where the process is described by an advection–diffusion–reaction equation:

$$\frac{\partial c}{\partial t} + \boldsymbol{v} \cdot \nabla c = \nabla \cdot (\boldsymbol{D_c} \nabla c) - R_c \tag{1.2}$$

where $c$ is the free drug concentration, $\boldsymbol{v}$ is the transmural velocity as a result of the pressure difference across the wall, $\boldsymbol{D_c}$ is the diffusivity tensor of drug which accounts for the different rates of diffusion in the arterial wall (particularly the media) as a consequence of its layered structure, and $R_c$ describes the reactions associated with free drug. In simpler models, the transport properties are assumed constant throughout the arterial wall. However, as the wall contains three layers, each with their own constitutive properties (permeability, porosity, etc.), then recent work has detailed how each layer should employ its own transport properties, where the separation between layers is described through the elastic membranes using Kedem–Katchalsky equations [78, 169, 170, 184].

Different drugs incorporate different binding mechanisms, and thus the transport properties of drug within the wall may vary. Thus, the release from the coating should be tailored accordingly, where various clinical studies have demonstrated that a sirolimus–eluting stent presented more favourable retention when released over a 60–day period, rather than over a 7–day period [185]. However, for paclitaxel, the optimum result was achieved following either a very slow or very fast release [186–189]. As such, the diffusivity tensor ($\boldsymbol{D}_c$) and reaction term ($R_c$) are likely to vary from drug–to–drug.

Zunino *et al.* [166] introduced the concept of drug binding through $R_c$, found in subsequent work to be a key mediator in drug efficacy [79]. Initially, the binding process was emulated via linear kinetics, where free drug was lost at some rate, $\kappa_L$ (Eqn. 1.3) [166, 184, 190]. More complex approaches were later considered, where drug was proposed to exist in two phases (free and bound), where it could bind via a forward reaction rate, $k_{on}$, or unbind through a dissociation rate, $k_{off}$ (Eqn. 1.4); a process which has since been deemed essential [78, 165, 191, 192]:

$$R_c = \kappa_L c, \tag{1.3}$$

$$R_c = \frac{\partial c_b}{\partial t} = k_{on}\, c - k_{off}\, c_b, \tag{1.4}$$

where $c_b$ is the bound drug concentration. However, as the understanding of the binding process enhanced, models of drug binding increased in sophistication to mimic the receptor/ligand complex. This was first adopted by Sakharov et al. [193], where they modelled the concentration of free drug, $c$, and unoccupied binding sites, $c_u$ (Eqn. 1.5). Alternatively, Tzafriri *et al.* [194] detailed free drug, $c$, and the number of occupied binding sites, $c_b$ (bound drug), which has since been widely adopted (Eqn. 1.6) [79, 169, 170, 177, 178, 188, 195, 196]:

$$R_c = \frac{\partial c_u}{\partial t} = k_{on}\, c_u\, c + k_{off}(B_{max} - c_u), \tag{1.5}$$

$$R_c = \frac{\partial c_b}{\partial t} = k_{on}\, c(B_{max} - c_b) - k_{off}\, c_b, \tag{1.6}$$

where all parameters are previously detailed, except $B_{max}$ which refers to the maximum density of binding sites. Following the derivation of these binding kinetics, subsequent work eluded to the necessity of two binding phases, where bound drug can exist either specifically bound to target receptors (i.e. SMCs) or to non–specific sites (i.e. ECM) [79]. As such, $R_c$ is now separated by phase as so:

$$R_c^i = \frac{\partial c_b^i}{\partial t} = k_{on}^i\, c(B_{max}^i - c_b^i) - k_{off}^i\, c_b^i, \qquad i = s, ns, \tag{1.7}$$

where the superscript, $i = s$, $ns$, states whether the binding phase is specific ($s$) or non-specific ($ns$), which themselves are subject to different binding kinetic parameters [78, 178, 179, 197]. The importance of these two binding phases has been alluded to when emulating an *in vivo* environment, where drug efficacy is directly related to the percentage of specifically saturated receptors [79, 178].

With these kinetics established, studies have since explored the optimal design of DES. For example, Tzafriri *et al.* [79] modelled the impact of drug release from different sirolimus–eluting stents, charting specific receptor saturation; an efficacy indicator associated with the number of occupied specific binding sites ($c_b^s/B_{max}^s$). They noted that a sustained release of drug over the course of 30 days results in almost complete saturation during that time, where inhibition of restenosis is more profound compared with faster release strategies. Similarly, McKittrick *et al.* [172] illustrated the difference between two stents that differ in their initial drug coating dose. In agreement with the general consensus present in the literature, they showed that a higher drug dose demonstrated a prolonged saturation of specific receptors which in turn reduced neointimal thickness at the cost of elevated tissue drug content levels, associated with device safety (Fig. 1.11). Further description into the various stent performance indicators discussed (e.g. receptor saturation) are provided in Chapter 5, where the focus is to simulate the performance of DES.

Summarising efforts which extend the dimensionality of the problem, Bozsak *et al.* [188] considered a 2D–axisymmetric model that emulated the release of paclitaxel and sirolimus from

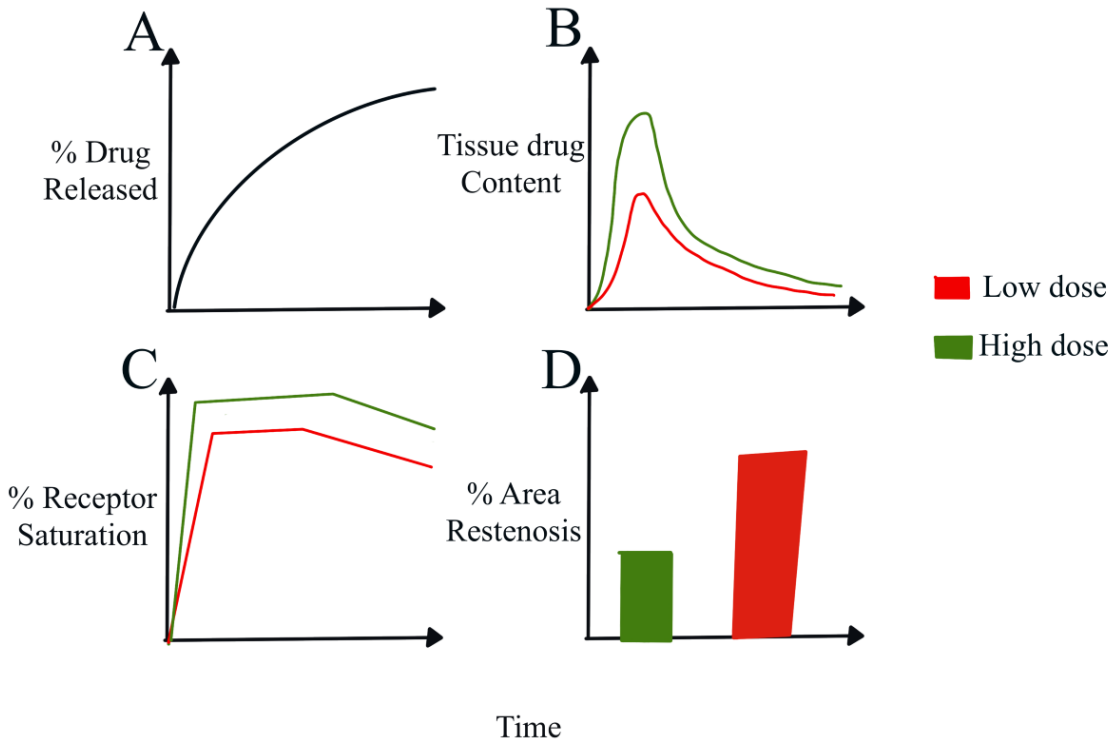


Figure 1.11: Depiction of stents coated in different dosages of the same drug may influence patient outcome. A: Generic release profile. B: Safety indicator, tissue drug content. C: Efficacy indicator, % of specific saturated receptors. D: Patient outcome, measured by severity of re–narrowing. Responses are not too scale, and represent typical outcome as discussed in [172].

stent struts. Albeit limited in including only one phase of binding, their work clearly highlighted how drug transport was mediated by different transport properties, where paclitaxel was dominated by convection and sirolimus by binding. As such, subsequent efforts explored the optimization of DES, highlighting how drug release and the initial coating dose for sirolimus and paclitaxel–coated stents should differ to ensure optimal patient outcome [189]. Further work built upon this model, investigating how the expansion of the stent influenced drug transport [169] as well as the impact of plaque composition and vessel curvature [196]. More recently, the same authors adapted their 2D model framework to compare the performance of DES and drug–coated balloons (DCB) [170]. The authors compared the efficacy and safety of a series of devices, detailing how DCB can be designed to achieve similar levels of safety and efficacy as DES. Moreover, several studies adopting a 2D environment have arisen that simulate the influence of CFD on drug deposition within the arterial wall. Initial work conducted a 2D analysis of drug transport within biological tissue [198], extended in subsequent work to include thrombus formation [199] and the release of drug from a polymeric coating, focusing on how stent design influences drug distribution [169, 188, 200–202].

Moreover, 3D studies also exist where Kolachalma *et al.* [138] investigated drug deposition in both bifurcated and non–bifurcated vessels, where stent position was noted to be significant in the former. Further, Zunino *et al.* [203] presented a highly coupled model considering stent expansion, CFD, and drug release into the wall. Due to the computational demands, only information on drug release one hour after implantation was available, and thus cannot fully categorise drug efficacy or safety adequately. More recently, Colombo *et al.* [204] implemented an idealised geometry to investigate drug retention following the deployment of DCB hosting paclitaxel; where design characteristics, procedural aspects and arterial geometry influence transport kinetics of the drug. The authors also considered a more sophisticated drug transport model by simulating both free and bound drug (one–phase), absent from [138, 203].

Regardless of the drug considered, it is clear that the elution kinetics have a strong impact on patient outcome. A series of articles have alluded to the significance of specific receptor saturation as an indicator of drug efficacy in sirolimus–eluting stents, with correlations to restenosis inhibition established [79, 172, 179]. However, these articles all fail to model how the drug actually impedes cell function and are ultimately incapable of demonstrating how drug release mediates restenosis. Further investigation illustrated that very few articles exist that examine the effect of drug on cell function [183, 205–208]. These articles are highly simplified where neither elution nor retention kinetics are modelled, in line with the current state–of–the–art models above. Therefore, a clear gap exists, where further analysis could provide insight that may improve treatment through current PCI strategies. It is essential that the release is optimised in line with the general healing response, where sSMC proliferation dominates early after stent implantation [55, 56, 209]. Models which emulate restenosis are thus discussed below, before summarising the key limitations of the field which aim to be addressed in this thesis.

### 1.4.3 Modelling restenosis: Arterial response to stenting

There exists a growing array of literature that details the healing response of the artery following stent deployment. Such models are mechano–biological, adopting one of two frameworks, where most commonly, models tend to employ a rule–based approach (Agent–based models, ABM) to simulate restenosis [53, 54, 57, 65–67, 206, 208, 210–221]. On the other hand, continuum based models have recently emerged that utilise coupled partial differential equations (PDE's) to describe an array of arterial wall constituents and their significance to excessive tissue growth [55, 115, 208, 222–224]. These two frameworks are summarised in Fig. 1.12, depicting the overall aim of any mechano–biological model. Briefly, each approach (ABM or continuum) simulates stent deployment which facilitates the accumulation of inflammatory cells as a measure of vascular injury. These cells then trigger the activation of various chemicals, notably growth factors and cytokines, which in turn stimulate a healing response through cell proliferation and ECM synthesis. It is then the excess production of these constituents in particular that comprise the restenotic tissue. In a range of articles, CFD analysis is also included, which acts as

input to the biological cascade of events, as highlighted by the dashed box (Fig. 1.12) [225–227]. Moreover, emphasised by the purple arrow, in more complex models, time–dependent growth is also simulated. Here the artery remodels sequentially, at pre–defined time intervals where the new geometry then influences the subsequent variables within the model [226]. This is a quasi–time–dependent approach, where growth is modelled as a series of stationary steps, as opposed to a single step considered in [55, 228].

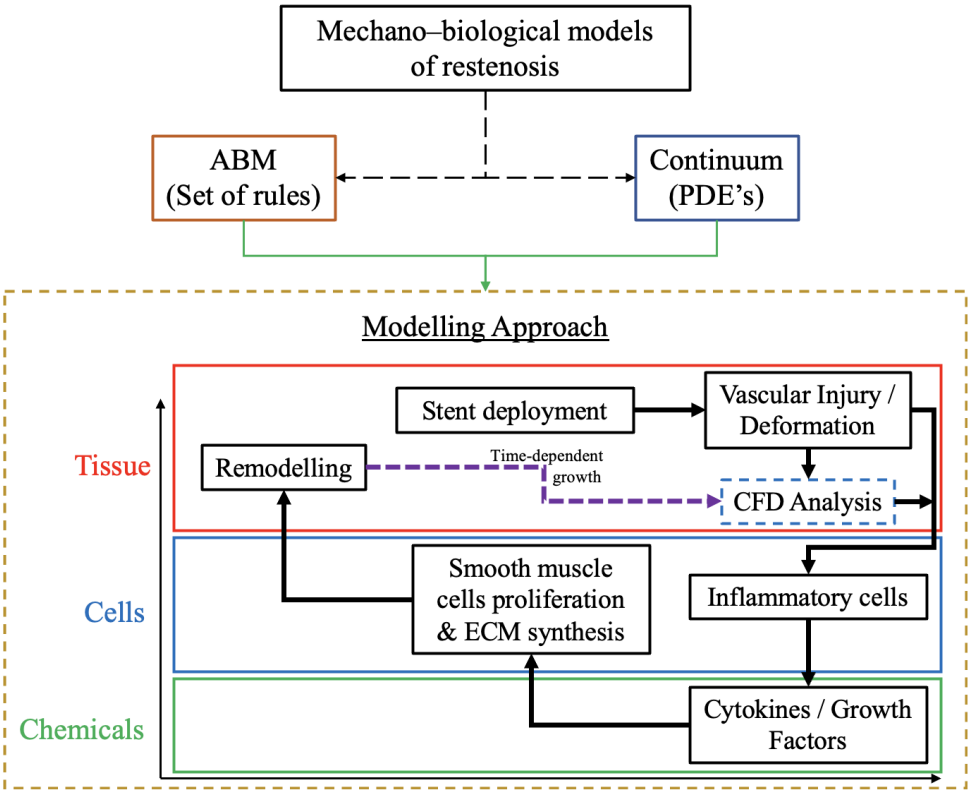


Figure 1.12: Standard framework for mechano–biological models of restenosis. Dashed entities (line / box) within the modelling approach box depict optional steps present in current state–of–the–art models which introduce additional complexities within their framework of arterial healing.

Briefly, preliminary work by Evans *et al.* [210] introduced complex autonoma (CxA) models that then permitted the description of the main physical and biological elements associated with restenosis through an ABM framework. Since, a series of models by Boyle *et al.* [54, 57, 211, 212, 215] grew in complexity to highlight the significance of stent design on restenosis. Models by other authors have also demonstrated the importance of stent design, expansion and re–endothelialization in 2D before extending efforts to 3D [53, 65–67, 206, 217, 229]. Corti *et al.* [225, 226] built upon a model of atherosclerosis to detail the growth of restenosis in response to haemodynamic indices (i.e. WSS). Their analysis showed that areas exposed to lower WSS ($< 0.5$ Pa) presented with an increased risk of lumen re–narrowing at a 1–month and 1–year follow–up [219, 226, 227]. However, with the focus of their models on femoral arteries, Chen *et al.* [220] adopted a similar protocol within a coronary artery environment, establishing a similar

conclusion.

Recently, continuum models have been proposed as an alternative to ABMs, where a highly coupled, nonlinear set of PDE's are implemented to describe ISR following stent deployment. The current state–of–the–art model considers a 2D–axisymmetric healthy arterial geometry, where various constituents (SMCs, ECM, GFs etc.) all respond to vascular injury. Moreover, an alternative continuum framework exists, where the growth model for restenosis is implemented within the finite element framework describing arterial kinematics [115, 208, 223, 224, 230]. Efforts tend to explore sophisticated models of stent expansion, advising clinicians on the optimal course of treatment, with a particular emphasis on overlapping stents.

In summary, models of arterial healing have advanced significantly in recent years, and provide insightful information into the physical mechanisms that occur in response to stent deployment. Either in a rule–based or continuum framework, these models have established a correlation between stent characteristics (deployment depth, strut thickness etc.) and restenosis. However, very few models consider the influence of drug on healing, and when doing so neglect the sophisticated drug transport models that dictate drug behaviour within both the polymer coating and the wall. Current models which do so, with severe limitations, are discussed within the following section, highlighting key areas which aim to be addressed in this thesis.

#### 1.4.3.1 Cell inhibition: Modelling how drug inhibits restenosis

To the best of the author's knowledge, very few models exist that consider the influence of drug on the arterial healing response, and those which do employ simple drug transport kinetics. For example, in preliminary ABMs, [205, 206] the action of drug was modelled. The binding process was neglected, where free drug was coupled to cell function by mapping between the two modelling frameworks: ABM of restenosis and continuum model of drug transport. Subsequently, Rossi *et al.* [183] simulated drug release and degradation from a bioresorbable stent whilst considering the influence on SMC growth. Their model assumed an overly simplistic approach, with drug stimulating cell death through a linear dependence. Moreover, Peddle *et al.* [207] considered a theoretical approach to study the impact of drug on SMC proliferation using a series of PDE models that depict the two SMC phenotypes, contractile and synthetic. They employed simplified elution kinetics, where binding is again neglected, and an exponential decay is used to define the diminishing effect of drug on cell function. Finally, more recent research [208] has probed the effect of DCB on restenosis. Owing to the lack of development in this field, the effect of drug was simulated by a simple perturbation in the SMC proliferative parameter, where the simulation of drug transport was absent.

## 1.5 Thesis Aims & Outline

Despite all the significant advancements in stent design, where computational efforts have informed manufacturing protocol following analysis of arterial stresses and fluid dynamics, little–to–no effort has investigated the explicit role of drug on the restenosis process. Instead, an abundance of literature adopting static arteries [79], where cells and binding sites are constant, have informed the optimal course of drug release that permits sustained efficacy, without examining the subsequent impact on cellular function. Investigation into models which couple drug efficacy and cell function is essential since various clinical studies have demonstrated non–inferiority between DES employing durable and degradable coatings [34, 35]. This is further evidenced by a recent clinical trial, [48], which charted stubbornly high TLR rates following PCI with a modern stent design. Taken together, this suggests that the drug delivery protocol is under–explored, where further modelling efforts may aid in understanding the current downfalls of DES, and where possible improvements in design may lie.

With this in mind, the fundamental aim of this thesis is to devise mathematical and computational models that enable the assessment of drug mediation on cellular processes that drive restenosis. In line with many computational efforts, the following chapter presents a model which is dimensionally simplified to vary only in time (Ordinary differential equation (ODE) model). With the aid of *in vitro* data, the applicability of several models which probe the effect of drug on cell proliferation are assessed. These efforts are extended in Chapter 3, where the cyclic behaviour of cell proliferation is accounted for, and the affinity of drug to cell cycle check points analysed. Chapter 4 then presents a continuum–based restenosis model to simulate how SMC proliferation drives restenosis through the behaviour of many other constituents involved in arterial healing. Chapter 5 then incorporates stent–based drug delivery into the restenosis model. Through sophisticated coupling, the design of DES can be explored and the subsequent impact on patient outcome analysed in depth. Chapter 6 then addresses key limitations present in the restenosis model, isolating a key issue of DES: delayed arterial healing. The thesis will then conclude its findings whilst stating further work to be considered that could enrich modelling efforts to help better address the fundamental aim of this work.

# Chapter 2

# Modelling the effect of anti–proliferative drug on *in vitro* smooth muscle cell proliferation

Although drug–eluting stents (DES) proved revolutionary, reducing rates of in–stent restenosis (ISR) significantly when compared directly with bare metal stents (BMS) [32], clinical evidence continues to show that there is room for improvement. For example, the recent FAME 3 clinical trial [48] demonstrated non–inferiority between modern 3$^{rd}$–generation DES and a coronary artery bypass graft (CABG) in the treatment of coronary artery disease (CAD); with the latter known to be significantly more invasive. The outcome of this trial highlighted that approximately 6% of patients treated with DES required a follow–up procedure (target lesion revascularisation, TLR) after 1–year; with ISR the primary reason for TLRs [50]. Moreover, with rates of TLR likely to increase at a rate of 3–5% year–on–year [48, 231], and further heightened in patients with complex lesions [232], deeper exploration into the performance of these devices is necessary.

In particular, over the last 15 years, delayed arterial healing has been a recurring feature with DES, known to significantly increase the risk of poor patient outcome [24, 25, 27, 75]. With this initially observed in first and second–generation devices, the durable polymer coating was perceived as the primary culprit [24]. However, various clinical trials have since demonstrated non–inferiority between durable and degradable coatings that host sufficient biocompatible properties [33–35]. Further attempts looked to remove the coating entirely (polymer–free) or proposed a fully bio–resorbable structure. Similar to the degradable coatings, non–inferiority was present between permanent–polymer and polymer–free devices [39, 40]. However, the polymer–free BioFreedom (Biosensors, Europe) stent, accompanied by dual–antiplatelet therapy (DAPT) established superiority in a particular subset of patients who had a high risk of bleeding. As for the fully resorbable structures, patient outcome was severely comprised beyond 1–year and devices were subsequently pulled from the market with further research required [22, 43, 118, 223].

Taken together, it is clear that the role of drug on restenosis is under–explored, with much of the focus in recent years associated with the physical design of DES. This was emphasised in the introductory chapter, where there was a clear lack of models that detail the effect of anti–proliferative drugs on smooth muscle cell (SMC) proliferation. Such models are necessary because the purpose of the drug is to halt SMC proliferation which ultimately has an impact on restenosis. For example, although current drug transport models have demonstrated the importance of drug elution kinetics, tissue uptake and retention on key indicators of safety and efficacy, they completely ignore the explicit role of drug on cellular function [78,79,165,169,170,172,173,177–179,188,189,194,196,203,233]. As such, these models consider a static artery (where growth is neglected), with the binding sites that drug occupy assumed constant, and the subsequent effect on cell function neglected. Further motivation exists, where current mechanical models which emulate the deployment of stents in patient–specific arteries do so with BMS, devoid of drug [85,115,147,219,223,225–227,234,235]. In response to stent deployment, several mechano–biological models have recently emerged that depict the process of restenosis. Although these have improved the understanding of the physical mechanisms that drive restenosis, the role of drug in inhibiting this process is often neglected or employed by inadequate means; where a sophisticated model of drug release and transport in tissue is not considered.

Thus, the aim of this chapter is to better understand how anti–proliferative drug impedes SMC growth through the use of mathematical models. Prior to simulating drug delivery following stent deployment, models adopting ordinary differential equations (ODEs) are considered to focus solely on the anti–proliferative effects of drug on cell growth. The models are then built upon in Chapter 5, where the emphasis is on the performance of DES. In this chapter, experimental data from *in vitro* proliferation assays are obtained to calibrate and validate a series of models that attempt to capture the dose–dependent effect of drug on cell proliferation. In the first instance drug is continuously exposed to the cells throughout the experiment. A further objective is to then test whether each model can capture drug retention and thus the diminishing effect of drug as the populations of cells re–proliferate. Throughout, the predictive capabilities of the models are tested in an attempt to obtain the best–fitting parameters for each model whilst allowing for predictions to be made where possible.

The chapter begins by providing a brief review of the literature, discussing mathematical models emulating tumour regression and ISR. The role of the anti–proliferative drugs used in the treatment of ISR is then discussed, with experimental studies illustrating their actions detailed. A series of mathematical models are then proposed, immediately followed by the numerical fitting approach implemented to obtain the best–fitting parameters to each model. With two experimental data sets considered for model calibration, the results are divided into two distinct categories. The results of the model are then discussed alongside any limitations, highlighting the possible implications they may have on future research.

## 2.1 Review of literature

There are many mathematical models in the literature that emulate the role of anti–proliferative drug in the treatment of cancer [83, 236–238]. As alluded to briefly in Section 2.1.1, these models facilitate cell death through the action of drug by means of a cytotoxic effect. Such models have considered an array of drugs in an attempt to identify optimal treatment therapies for a plethora of different cancers [237, 238].

Despite the abundance of tumour regression models following drug exposure, very few models demonstrate the role of anti–proliferative drug on SMC function [183, 205–208]. In fact, those models which do exist are often borrowed from the cancer literature. This is particularly problematic given that the fundamental action of drug is different between the two applications. For example, when treating cancer the drug is cytotoxic, with the primary aim of killing hostile cells. However, in the treatment of CAD, drugs which were once employed as chemotherapeutic agents (sirolimus and paclitaxel) had their dosage finely tuned to ensure a cytostatic response, such that SMC proliferation was halted or delayed without initiating apoptosis [239–241]. Moreover, the administration protocols of drug differ between the treatment of cancer and CAD. In the former, medication is often routine and administered intravenously or orally to target and rid the patient of all hostile cells. Whereas, for CAD treatment, drug is delivered by means of a stent or balloon locally to the site of disease in a one–off application.

With this in mind, the primary purpose of this section is to provide a brief discussion of mathematical models of *in vitro* experiments of tumour growth subject to drug exposure. Such research has inspired model derivation that aims to simulate the anti–proliferative effect of drug on SMC proliferation. An overview of how such models have been applied to the inhibition of SMC proliferation is explored in detail. The limitations of these are models are highlighted, emphasising where improvements can be made.

### 2.1.1 Brief review of mathematical models of tumour growth

Generally, models that depict the action of drug on the proliferation of tumour cells are of the following form:

$$\frac{\mathrm{d}c}{\mathrm{d}t} = \phi_c(c) - \lambda(c)\, c, \tag{2.1}$$

where $c$ is the number of cells, $\phi_c$ resembles the growth model of interest (e.g. exponential or logistic), and $\lambda$ can is often a constant which mimics the effect of drug, a function of the current cell number.

Models of the simplest form adopt Eqn. 2.1, where $\lambda$ is constant, corresponding to the dose or effect of drug applied. Subsequent models have since amended this approach, where $\lambda$ is extended to simulate the impact of drug exposure with or without resistance [237, 242–244]. Further still, models have explored the cell–cycle nature of these drugs such that the

cell population is divided into *phases* [242, 245–248]. Such models are easily divided into two categories. The first assumes *phases* to mean the different stages of the cell cycle [242, 246], which is discussed in more depth in the following chapter, where the focus shifts to the cyclic behaviour of cells, with an emphasis placed on drug specificity. Or, they assume *phases* to mean different cell phenotypes, where drug has a specific role in promoting cell quiescence, impeding the proliferative capacity of the active cell type, or promoting cell death [245, 247, 248]. A further interesting point was brought to light recently by Jarrett et al. [83], where drugs with alternative modes of action, intracellular versus extracellular binding, may require different models to describe their effect on cell function.

It is clear there exists a vast literature of tumour regression models which account for the effect of anti–proliferative drug [236–238]. Such models have made a profound impact, investigating the role of drug specificity and resistance with an aim of influencing chemotherapeutic treatment protocol [245]. Although the underlying mechanisms of the drugs in tumour regression and the inhibition of restenosis are similar, the administration and goal of these drug compounds differ and thus the models have to be tailored accordingly between the two applications. For a more thorough discussion on mathematical modelling of tumour growth subject to drug exposure, the reader is referred to the following reviews [236–238].

### 2.1.2 Existing models of the effect of drug on smooth muscle cell proliferation

To the best of the author's knowledge, Caiazzo *et al.* [205] were the first to consider the effect of anti–proliferative drug on SMC function, within a model of restenosis. Their restenosis model was agent–based, where SMCs and other constituents followed a set of rules in response to some stimuli. However, the drug transport kinetics were described using a continuum model through a separate kernel which was mapped to be coincident with the SMCs, where the free drug concentration on each cell was approximated. The transport of drug was described through an anisotropic diffusion equation, where binding kinetics were entirely neglected and drug, therefore, existed in only one phase (free). Efforts were subsequently replicated within a model inclusive of flow [206]. Such models pre–dated key findings in the literature, which highlighted the benefits of specific SMC receptor saturation, particularly for sirolimus–eluting stents [78, 79]. However, this groups' subsequent models of restenosis [53, 65–67] failed to revisit the performance of drug as in inhibitor to this process; possibly owing to the lack of understanding of its role in modulating arterial healing [25, 208, 249].

In the years following, Rossi *et al.* [183] published a model study of a bioresorbable polymer–coated stent. To accompany their models of polymer degradation and drug transport, a population balanced corpuscular approach was also implemented to describe neointimal thickening, with the effect of drug considered. Specific details of the coupling of drug to the restenosis

model and how it subsequently inhibits cell proliferation is not explicitly detailed, with the authors referring the reader to [250] instead. Assuming the same approach is implemented, drug reduces the proliferative capacity of cells by promoting cellular death through a linear apoptotic term. Here, cell death is proportional to the concentration of drug via some rate constant (e.g. Eqn. 2.2). Thus, instead of the desired cytostatic response of anti–proliferative drugs employed to treat ISR, their model assumes that drug elicits a cytotoxic response. Elaborating further on the implications of this approach, the following general model of exponential cell proliferation subject to drug exposure is presented:

$$\frac{\mathrm{d}c}{\mathrm{d}t} = g\,c - k^{drug}\,c, \tag{2.2}$$

where $c$ is the number of cells, $g$ is the cell growth rate, and $k^{drug}$ is some rate constant which defines the effectiveness of drug through apoptosis. Exponential growth occurs in natural circumstances ($k^{drug} = 0$). This is still true when $k^{drug} < g$, but invalid when $k^{drug} > g$, where $dc/dt < 0$ and cell death ensues, reiterated graphically in Fig. 2.1. Moreover, by extending Eqn. 2.2, it is possible to incorporate the time–dependent effect of drug on cell proliferation through a general expression, $k^{drug}\,e^{-\phi_d\,t}c$, where $\phi_d$ is some arbitrary decay constant. With this, a cytotoxic response is present initially before cell recovery dominates as the effectiveness of drug diminishes. Regardless of the sophistication of the 'sink' term, the fact that $dc/dt < 0$ is attainable is not warranted in the present application. For example, various experimental–focused articles have since established that the fine–tuning of the dose of once cytotoxic drugs (e.g. chemotherapeutic agents, paclitaxel) can enable a cytostatic response [240, 251]. The cytostatic outcome is desirable in the treatment of ISR because cell death, through cytotoxic drugs, may trigger a prolonged inflammatory response where macrophages are needed to clear residing debris, a process that could further delay the remodelling process [56, 252]. Thus, unlike [183], future *in silico* models of drug effectiveness should employ a reduction in growth rate (cytostatic) as opposed to promoting death (cytotoxic).

Limitations aside, by means of a fitting protocol which the authors do not detail, the model proposed was able to adequately capture the dose–dependent effect of drug on cell proliferation *in vitro*. This model was then utilised to emulate *in vivo* conditions, charting neointimal thickness and making predictions on patient outcome.

Subsequently, Peddle *et al.* [207] proposed a generic partial differential equation (PDE) model of SMC proliferation subject to the effects of drug. In a theoretical attempt to emulate restenosis, their model of cell behaviour comprised of two phases, mimicking the active and dormant phenotypes of SMCs. The authors considered two drug–effectiveness models, where drug was assumed to mediate cell function by either preventing phenotype switching or halting growth. One limitation is that the first approach assumed that drug blocks the differentiation from quiescent to proliferative cells, whilst literature often details that drugs commonly coated on stents (e.g. sirolimus) induce differentiation back to the quiescent phenotype as opposed to a

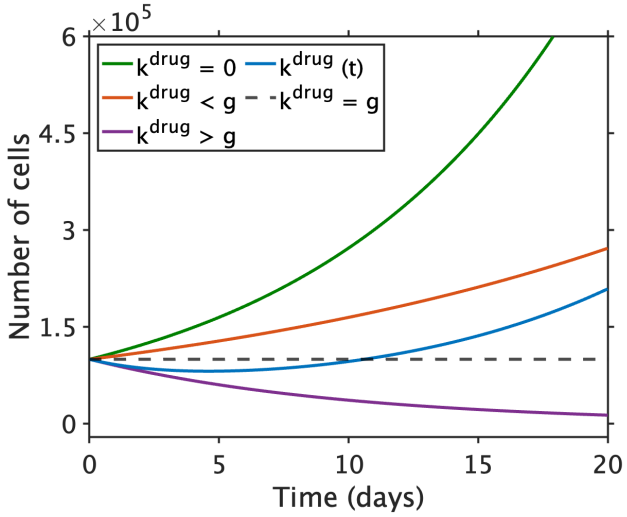


Figure 2.1: Exploring the behaviour of Eqn. 2.2. In all simulations $g = 0.1$. (i) $k^{drug} = 0$: Growth in the absence of drug. (ii) $k^{drug} < g$: Curtailed growth due to the presence of drug. $k^{drug} = 0.05$. (iii) $k^{drug} > g$: Cell death as a result of drug effectiveness dominating over growth. $k^{drug} = 0.2$. (iv) $k^{drug}(t) = k^{drug}\, e^{-\phi_d t}$: Time–dependent effect of drug. $\phi_d = 0.15$, $k^{drug} = 0.2$. (v) $k^{drug} = g$: Drug is as effective as cell growth.

complete block to their proliferative state [253–255].

Drug–effectiveness aside, the model proposed is further limited by its drug transport model, where an exponential decay expression (Eqn. 2.3) that describes the diminishing effect of drug concentration is implemented as an alternative to more sophisticated transport kinetics that account for drug binding and retention within tissue:

$$\mu_D = C \exp\left(\frac{-1-\alpha_t}{\tau}\right), \tag{2.3}$$

where $\mu_D$ details drug effectiveness, which decays exponentially given that $C$ and $\tau$ are constants of proportionality, and $\alpha_t$ defines the total drug concentration. However, to enable emulation of patient outcome *in vivo*, a consideration into more sophisticated transport kinetics of free and/or bound drug should be considered; as highlighted ubiquitously throughout drug transport models isolated from cellular function [78, 79, 178, 188, 194].

Very recently, Maes *et al.* [208] published a constrained mixture model of restenosis following balloon expansion. As a tangent from their primary study, the authors explored the effect of drug, assuming it mediated the SMC population via the following expression:

$$\frac{\mathrm{d}\phi}{\mathrm{d}t} = -k_d\phi - k_d^{DEB}(1-e), \tag{2.4}$$

where $\phi$ is fraction of active SMCs, $k_d$ is a rate constant that controls phenotype switching, $e$ is the extracellular matrix concentration, and $k_d^{DEB}$ is another rate constant associated with the effect of drug, where $k_d^{DEB} \leq k_d$ such that the change to a more synthetic phenotype is

reduced as a consequence of drug, an approach similar to that in [207]. However, drug transport kinetics are ignored in their entirety. Instead the authors proposed a local sensitivity analysis, concluding that perturbations in $k_d^{DEB}$ presented sensible results, where smaller values presented with a further decrease in SMC proliferation. The authors attribute this simplification to the lack of development in the field, such that further model improvements should consider a more sophisticated approach that encapsulates the drug transport process.

Taken together, all of the aforementioned models fail to adequately incorporate drug delivery and retention. In particular, none of these models incorporate the state–of–the-art, nonlinear saturable binding model. This is somewhat surprising given that static drug transport models, reviewed in depth in [78], have demonstrated the importance of the drug release rate and retention on characteristics associated with drug efficacy and safety. Summarising, the state–of–the–art literature suggests that the saturation of specific receptors (e.g. those present within SMCs) is essential, achieved through a sustained release of drug, at least for sirolimus [79]. Although static models have demonstrated good agreement with experimental data (e.g. [79, 172]), neglecting the effect of drug on cell growth is limiting, especially with the aim of adopting such models as pre–clinical tools which simulate a remodelling, dynamic artery following stent deployment. Moreover, mathematical models discussing how drug impedes restenosis through the inhibition of SMC proliferation do not account for these complex binding kinetics. In fact, in [207] and [208], drug transport kinetics are completely neglected. Therefore, a clear disconnect exists, where the role of saturable binding on SMC proliferation has not previously been simulated in a dynamic environment, where the number of cells is increasing, or the tissue is regrowing (restenosis). With the proliferation of SMCs known to be the driving force behind restenotic tissue growth, a better understanding of how drug hinders its functionality is necessary.

## 2.2 The role of anti-proliferative drugs on SMC growth as demonstrated from *in vitro* data

### 2.2.1 Overview

An understanding of how drugs elicit their effect on cell function is beneficial prior to model development. Of particular interest is the action of anti–proliferative drugs paclitaxel (PTX) and sirolimus (SIR), present on polymeric coatings of preliminary DES. The inhibition of cell function, particularly proliferation, has been well established through *in vitro* studies, where the effect is dose–dependent [31, 80, 81, 240, 251, 256–260]. Note, the modes of action of both PTX and SIR are different, exerting their effect with greater affinity at different checkpoints along the cell cycle (Fig. 2.2).

Upon entering the cell via passive diffusion [80, 261], the drug of interest will elicit its action by binding to a particular molecule within the cell. PTX will bind to the $\beta$ subunit of tubulin,

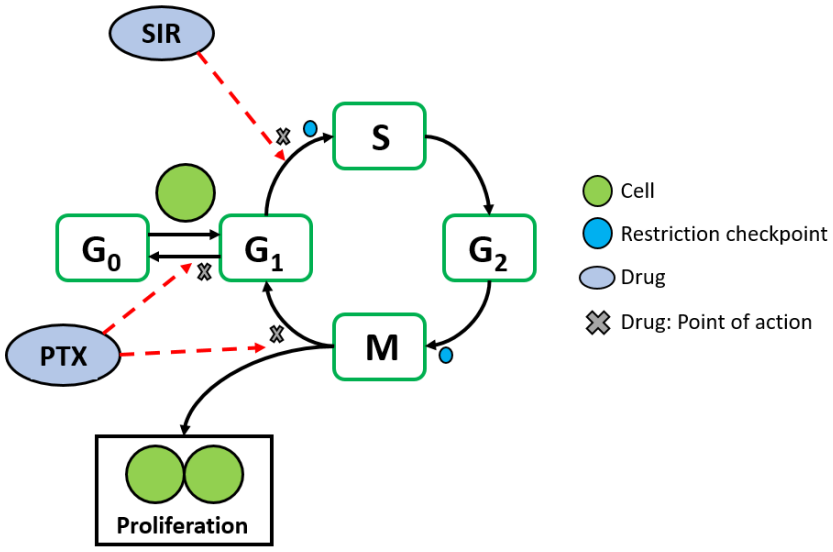


Figure 2.2: Schematic illustrating the cell cycle as well as the mode of action for SIR (as well as its analogues) and PTX. Acquired with permission from [249].

present on microtubules, where it will predominantly halt cell cycle progression at $G_2$/M, inducing cell cycle arrest during chromosome separation [80,81,251]. On the other hand, studies have highlighted an arrest at $G_0/G_1$, associated with exposure to a lower dose [251]. SIR molecules bind to FKBP12 protein which inhibits the functionality of FKBP–rapamycin associated protein (FRAP), interfering with biological events that may occur as a result of growth factor stimulation. SIR predominantly exerts its effect prior to the first checkpoint, at $G_1$/S, where the cell cycle is delayed, and cells remain quiescent, unable to proliferate for a prolonged period of time [80, 258]. A plethora of articles have demonstrated an inhibition of SMC proliferation (*in vitro*) following exposure to PTX [81, 240, 251, 257, 259] and/or SIR [31, 256, 262–265].

However, as delayed arterial healing continues to be a prevalent issue with DES, alternative compounds were considered with the aim of finding a drug which specifically targets SMCs over endothelial cells (ECs). To name a few, Matter *et al.* [31] compared sirolimus and tacrolimus, observing that the latter was more favourable in not adversely inhibiting EC regeneration. Additionally, analogues of SIR (zotarolimus, everolimus, and biolimus) all demonstrated favourable inhibition of SMC proliferation and migration [266–268]. Moreover, anti–inflammatory options were also considered that suppress cyclooxygenase–1,2 (COX–1,2) where Marra *et al.* [269] investigated the dose–dependent response of sodium salicylate (SAL) on cell proliferation. Lastly, alternative drugs that showed promise in the inhibition of tumour cells were considered, where Sun *et al.* [270] analysed the dose–dependent behaviour of elemene, illustrating a positive inhibition of SMCs and the stimulation of EC recovery.

Although it is clear that a large array of data exists detailing the anti–proliferative nature of various drugs on SMC proliferation, the experimental methodologies chosen to depict this are often not suitable for model calibration and validation. Summarising, various efforts depict

the dose–dependent response of drug, but as a percentage of the control value, which is not quoted [31,257,266,267,271]. Other studies may present the data in a desired format, yet do not account for the effect of multiple doses and/or drug retention [268, 270, 271], a key component associated with the performance of DES [79, 172, 188, 194].

As a result, the following selection criterion was utilised to identify studies that could provide suitable data for model calibration and validation: (i) data is presented as cell number/density; (ii) multiple drug doses are considered to establish a dose–dependent response; and (iii) the retention capabilities of the drug are examined. Studies that satisfy these are highlighted subsequently in Sec. 2.2.2 where the experimental data is presented. Fig. 2.3 schematically details a generic experimental set–up which follows the proposed selection criteria, assessing the impact of drug on cell proliferation with a particular emphasis on retention as represented by step three.

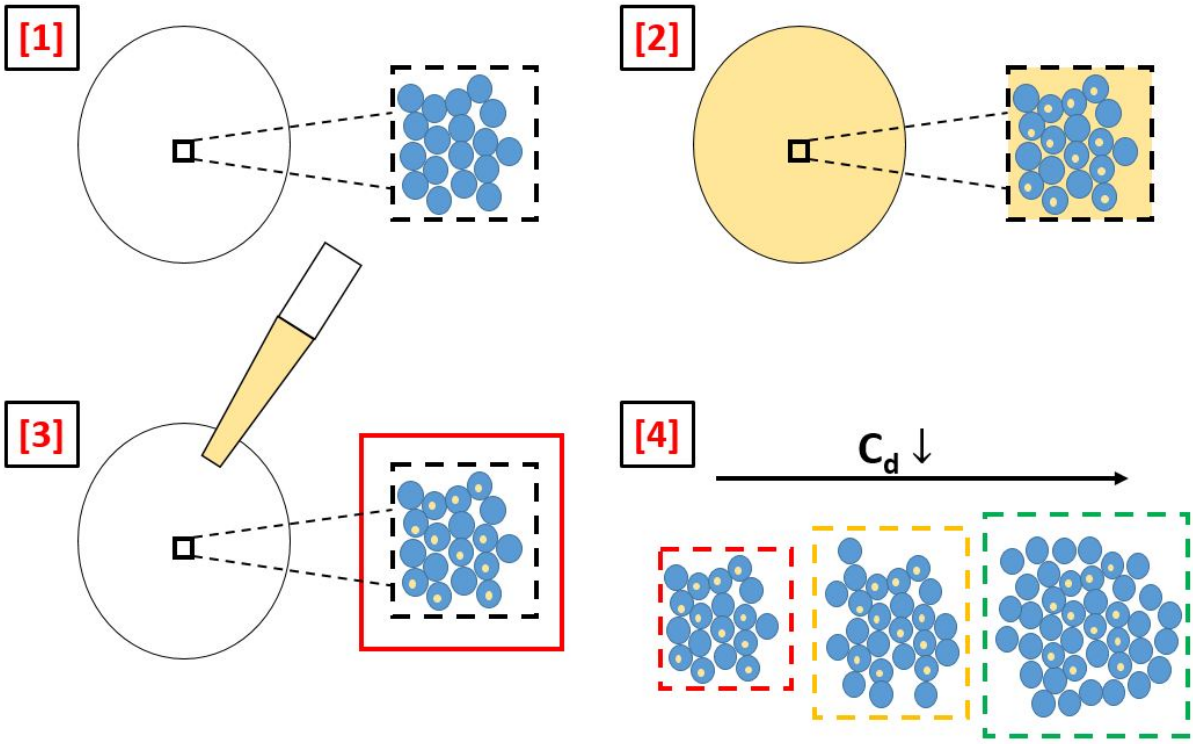


Figure 2.3: **[1]:** Cells are seeded at some number onto a well plate. **[2]:** Drug is added to the media (*yellow*) to inhibit the proliferation of cells. **[3]:** Drug is removed from the media after some time to observe the effect of drug retention. **[4]:** Repeat 1–3 for a range of drug doses, $c_d$.

### 2.2.2 Studies considered for model calibration

Scheller *et al.* [81], as part of a larger study on alternate drug administration strategies, analysed the influence of PTX at various doses and exposure times on SMC proliferation (Fig. 2.4). Cells exposed to a lower dose (1.46 $\mu$M) demonstrated a re–proliferative potential following a short, 60–minute exposure. A higher dose (14.6 $\mu$M) was then applied for three different

exposure times: 3, 10, and 60 minutes, where no significant difference was observed in SMC proliferation between the three cases. Upon the removal of the supernatant, cell behaviour was studied over a 12–day period, in intervals of 3 days. The data were initially presented as a density (cells/cm$^2$), although for consistency with [269], this has been converted to number of cells assuming experiments were performed in 48–well plates.

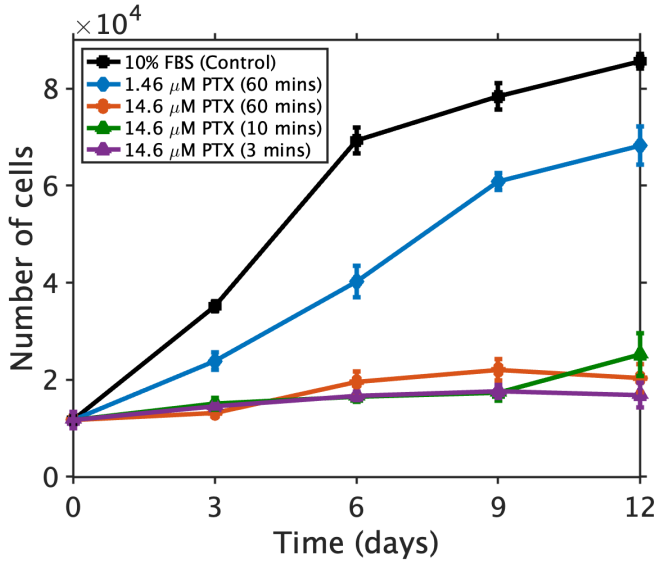


Figure 2.4: PTX at 14.6$\mu$M exposed to bovine SMCs for 3, 10, and 60 minutes, and for 60 minutes at 1.46$\mu$M. FBS = Fetal bovine serum. Reproduced from [81].

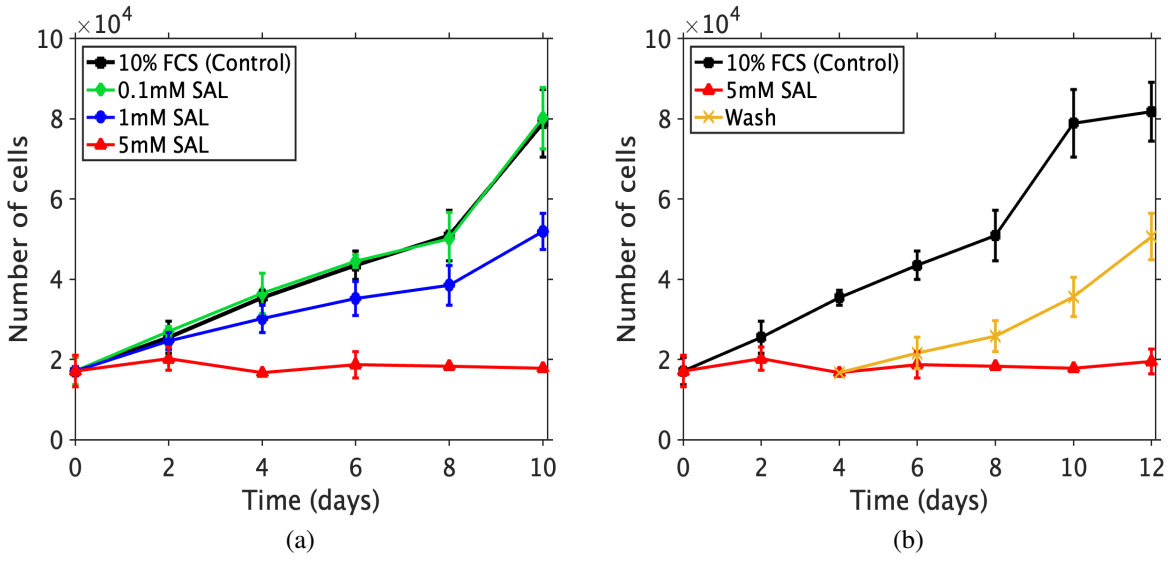


Figure 2.5: (a) Human saphenous SMCs exposed to 3 doses (0.1mM, 1mM, and 5mM) of SAL for 10 days. (b) 5mM of SAL removed at day 4, illustrated by change in line style, depicting cell recovery upon the removal of drug. FCS = Fetal calf serum. Reproduced from [269].

Marra *et al.* [269] considered an alternative drug with anti–inflammatory properties, SAL, in the search for alternatives to PTX and SIR, implemented in previous stenting applications for an array of purposes (Fig. 2.5) [272–274]. Two separate studies were carried out to investigate: (a) the dose–dependent response of SMCs to a continuous exposure of SAL for 10 days, in two–day intervals and (b) the retention properties of SAL following a brief 4–day exposure to a high dose of drug for a further 8 days, again in 2 day intervals.

The consideration of two separate studies is both advantageous and limiting. It allows for the model(s) to be tested against different drugs that have distinct retention capabilities, i.e. PTX is more lipophillic than SAL. On the other hand, the studies are conducted with different methodologies, where, for example, different cell lines are considered which may have different proliferative trends [275].

## 2.3 Methodology

### 2.3.1 Governing equations

#### 2.3.1.1 Control model: absence of drug

In the absence of drug, a logistic growth model (Eqn. 2.5) is proposed to describe the growth of cells *in vitro*; an approach considered ubiquitously within mathematical biology [276]:

$$\frac{\mathrm{d}c(t)}{\mathrm{d}t} = g\,c(t)\left(1-\frac{c(t)}{K}\right), \quad t>0, \quad c(0)=c^0, \tag{2.5}$$

where $c(t)$ describes the number of cells as a function of time, initially at $c^0$, $g$ is the intrinsic growth rate, and $K$ is the carrying capacity, the maximum number of cells permitted within the culture plate. Note, it is assumed that the growth serum is present in a high concentration such that the intrinsic growth rate, $g$, can be assumed constant. In all models that follow, Eqn. 2.5 can be returned by assuming that the drug concentration ($c_d$) equals zero.

#### 2.3.1.2 Drug models: presence of drug

To assess the impact of drug on cell proliferation, three (D1, D2, D3) mathematical models of varying complexity are presented. Each model permits the assessment of either a brief or continuous exposure of drug, investigating the re–proliferative potential of pre–inhibited cells. Where binding kinetics are present, the appropriate rate constants (e.g. $k_{on}$) are assumed to be dose independent. Alternatives to the aforementioned state–of–the–art non–linear, saturable binding model are presented, assuming that the internal concentration of drug mediates the inhibition of SMCs, or that the action of drug is instantaneous.

**Model D1**

The most complex model accounts for the state–of–the–art non–linear, saturable binding kinetics [78,79] with a subtle amendment to the upper limit to describe bound drug. The justification for a time–dependent limit over a constant (*steady–state* [79]) one is rather trivial. With proliferation the focus, then an increase in cell number should convey an increased number of receptors from the initial state, particularly in an environment comprising primarily of a growing cell population. Moreover, in agreement with [79], Eqn. 2.5 is extended to ensure drug effectiveness influences the outcome (Eqn. 2.7), where outcome is perceived as the inhibition of SMC proliferation, such that:

$$\frac{\mathrm{d}b(t)}{\mathrm{d}t} = k_{on}\, c_d \left(B_{max}\,(t) - b(t)\right) - k_{off}\, b(t), \quad t > 0, \quad b(0) = 0, \tag{2.6}$$

$$\frac{\mathrm{d}c(t)}{\mathrm{d}t} = g\, c(t) \left(1 - \frac{c(t)}{K}\right) \left(1 - \frac{b(t)}{B_{max}\,(t)}\right), \quad t > 0, \quad c(0) = c^0, \tag{2.7}$$

where $b(t)$ is the bound drug concentration as a function of time and $k_{on}$ and $k_{off}$ are the binding on and off rates, respectively. The concentration of drug in the media is denoted $c_d$ and is assumed time–independent as a consequence of homogeneous distribution. The receptor density, $B_{max}(t)$, is equivalent to:

$$B_{max}(t) = B\, c(t), \tag{2.8}$$

where $B$ is the receptor density per cell. In previous nonlinear, saturable binding models, $B_{max}$ is assumed constant [78,79], unperturbed by local changes in the environment as drug transport is studied in isolation of remodelling processes (i.e. restenosis). Consequently, the expression proposed allows for the binding site density to vary in time. The principle behind the binding site density term is unchanged, such that a complete halt in cell proliferation exists when $B_{max}(t) = B\, c(t)$ as all binding sites are occupied. If this condition is met then a further increase in binding sites is impossible, hence the rationale for the effect of drug on cell growth in Eqn. 2.7; such that increased receptor saturation correlates to increased drug effectiveness [78,79].

**Model D2**

Model D2 adopts a simpler approach and instead assumes that the internalised bound drug mediates SMC proliferation. The effectiveness of the drug is defined by a Michaelis–Menten like term; an approach implemented extensively to describe the dose–dependent response of drug in various applications (e.g. tumour regression) [237,277–281]. Adjusting model D1 accordingly, internalised bound drug and cell growth are described by:

$$\frac{\mathrm{d}b^I(t)}{\mathrm{d}t} = \alpha\left(c_d - \frac{b^I(t)}{K^P}\right), \quad t>0, \quad b^I(0)=0, \tag{2.9}$$

$$\frac{\mathrm{d}c(t)}{\mathrm{d}t} = g\,c(t)\left(1-\frac{c(t)}{K}\right)\left(1-\frac{k_{max}\,b^I(t)}{b^I(t)+k_{50}}\right), \quad t>0, \quad c(0)=c^0, \tag{2.10}$$

where $b^I(t)$ represents the internalised bound drug concentration; $\alpha$ is the internalisation rate and; $K^P$ is the non–dimensional partition coefficient such that, in equilibrium, $b^I = K^P c_d$. To describe the effect of drug on cell growth, Michaelis–Menten kinetics are considered, where $k_{max}$ is the maximum effect the drug has on cell growth and $k_{50}$ is the drug concentration at which the effect is half–maximal.

**Model D3**

Finally, a model which neglects the binding kinetics entirely is considered. Internalised drug, $b^I(t)$, is replaced with $c_d$, the applied dose, which remains constant, assuming a uniform distribution. Model D3 is a special case of D2, where it is assumed that $\alpha \to \infty$ and $K^P = 1$. The model is divided into two parts such that:

$$\frac{\mathrm{d}c(t)}{\mathrm{d}t} = \begin{cases} g\,c(t)\left(1-\dfrac{c(t)}{K}\right)\left(1-\dfrac{k_{max}\,c_d}{c_d+k_{50}}\right), & 0<t\leq\tau, \quad c(0)=c^0, \qquad (2.11a) \\ g\,c(t)\left(1-\dfrac{c(t)}{K}\right)\left(1-\dfrac{k_{max}\,c_d\,e^{-k_d(t-\tau)}}{c_d\,e^{-k_d(t-\tau)}+k_{50}}\right), & t>\tau, \qquad (2.11b) \end{cases}$$

where Eqn. 2.11a simulates cell growth in the presence of drug. However, removing drug ($c_d = 0$) would reduce Eqn. 2.11a to the logistic growth model. Thus, in scenarios where the influence of drug retention on cell growth needs to be established, an extension to Eqn. 2.11a needs to be considered. To account for drug retention, it is assumed that upon the removal of drug, its diminishing effect on cell growth ($c_e$) follows linear decay:

$$\frac{\mathrm{d}c_e(t)}{\mathrm{d}t} = -k_d c_e(t), \quad c_e(t=\tau) = c_d \tag{2.12}$$

where $k_d$ is the relevant rate constant. An analytical solution to Eqn. 2.12 exists. Substituting this in replace of $c_d$ in Eqn. 2.11a gives rise to Eqn. 2.11b, which is only valid when $t > \tau$, indicating the removal of the supernatant from the petri dish.

### 2.3.2 Model parameters

Across the four models (Eqn. 2.5–2.12), there exists an array of different variables and parameters to detail cell growth and the effect of drug, summarised in Table 2.1.

| Parameter | Description | Unit |
|---|---|---|
| *Cell Related Parameters* | | |
| $c^0$ | Initial number of cells | no. of cells |
| $g$ | Intrinsic growth rate | $s^{-1}$ |
| $K$ | Maximum cell number (carrying capacity) | no. of cells |
| *Drug Related Parameters* | | |
| $c_d$ | Drug concentration in the media | M |
| $k_{on}$ | Binding–on rate | $s^{-1}\,M^{-1}$ |
| $k_{off}$ | Binding–off rate | $s^{-1}$ |
| $B$ | Average receptor density per cell | $\frac{\text{M}}{\text{no. of cells}}$ |
| $\alpha$ | Internalisation rate | $s^{-1}$ |
| $K^P$ | Non–dimensional partition coefficient | – |
| $k_{max}$ | Maximum effect drug has on cell growth | – |
| $k_{50}$ | Drug concentration at $k_{max}/2$ | M |
| $k_d$ | The decay of the drug's effect on cell growth | $s^{-1}$ |

Table 2.1: Description of the parameters and variables of the mathematical models.

### 2.3.3 Numerical approach: solution method and inverse estimation of model parameters

For numerical convenience, and to reduce the number of unknown parameters, all drug models (D1–D3) were non–dimensionalised. Details on the non–dimensional protocol are provided in the Appendix (Section A.1). MATLAB (MATLAB 2020a, The MathWorks, Inc., Natwick, MA, USA) was the software considered to solve the model equations, specifically the *ode15s* routine, numerically integrating the equations over a time span defined by the experimental data.

Since two experimental studies are considered, these are used independently of one another, with the experimental methods differing significantly between [81] and [269]. Firstly, Marra *et al.* [269] considered a continuous exposure of twelve days, for three different drug doses: low ($L^m_{12}$), medium ($M^m_{12}$), and high ($H^m_{12}$), charting a dose–dependent effect on cell proliferation. Additionally, a baseline study is considered, where cells are permitted to grow free of any drug, allowing for comparisons to be drawn against simulations which curtail growth ($C^m_{12}$). Moreover, the re–proliferative potential of drug is assessed following a brief four–day exposure to a high dose of drug ($H^m_4$).

The second study, published by Scheller *et al.* [81], presents itself as slightly more challenging. Similarly, a baseline scenario is presented, assessing cell growth in the absence of any inhibitors ($C^s_{12}$). However, the effect of prolonged drug exposure on cell proliferation is not assessed, where only brief periods of exposure are shown. Considering just two doses, cells are exposed to the lower dose of drug for 60 minutes ($L^s_{12}$), whilst to the higher dose for 3 ($H^s_3$), 10

($H^s_{10}$), and 60 ($H^s_{60}$) minutes. Upon removal of the supernatant, cell recovery is investigated over a twelve–day period.

In each aforementioned label, the following format is considered $X^{\Psi}_{\Upsilon}$. $X$ dictates the experimental conditions, which range from the control (C) to a variety of drug doses (Low, Medium, or High: L, M, or H). The superscript, $\Psi$, details the study from which the data originates, either Scheller ($s$) or Marra ($m$). Finally, the number on the subscript, $\Upsilon$, defines the duration of drug exposure (if present). For clarity, the various data sets and their syntax have been reiterated in Table 2.2.

| Syntax Label | Drug dose (Value) | Drug exposure duration |
|---|---|---|
| *Marra [269]* | | |
| $H^m_{12}$ | High dose (5 mM) | Continuous: 12 days |
| $M^m_{12}$ | Medium dose (1 mM) | Continuous: 12 days |
| $L^m_{12}$ | Low dose (0.1 mM) | Continuous: 12 days |
| $H^m_4$ | High dose (5 mM) | Brief: 4 days |
| $C^m_{12}$ | No drug (N/A) | Absent: 0 days |
| *Scheller [81]* | | |
| $H^s_{60}$ | High dose (14.6 $\mu$M) | Brief: 60 minutes |
| $H^s_{10}$ | High dose (14.6 $\mu$M) | Brief: 10 minutes |
| $H^s_3$ | High dose (14.6 $\mu$M) | Brief: 3 minutes |
| $L^s_{60}$ | Low dose (1.46 $\mu$M) | Brief: 60 minutes |
| $C^s_{12}$ | No drug (N/A) | Absent: 0 days |

Table 2.2: Summary of all experimental data sets used in the inverse estimation of model parameters. The syntax labels are used in all subsequent plots.

The approach proposed has a number of limitations, primarily associated with the experimental data being obtained from studies using different methodologies. For example, a particular limitation which presented as a challenge was the lack of measurements in [81] during the periods of drug exposure, or just after, where there exists no measurement of cell number or drug concentration. Although it is likely the former is indifferent to the initial condition, the latter is essential to illustrate the levels of saturation/effect present within each window of exposure. Consequently, the approach considered during the estimation of model parameters was to simulate drug exposure in a forward simulation. Following its end, the cell number, $c(t)$, and drug concentrations, $b(t)$ or $b^I(t)$, were exported and implemented as initial conditions in the second phase, where model equations are updated to assess drug retention as $c_d = 0$. Inverse estimation of appropriate model parameters used the remaining data points (day 3–12) as well as this *new* initial condition. Estimation of parameters using [269] are less challenging, where sufficient data points are present during and after drug exposure.

To estimate model parameters, MATLAB's '*fminsearch*' routine was adopted, where a least–

squares method was implemented to minimise the error ($\varepsilon$) between the experimental ($c_j^e$) and simulated ($c_j$) data points, normalized with the experimental data:

$$\varepsilon = \sum_{j=1}^{N} \sum_{i=1}^{T} \left( \frac{c_j(t_i) - c_j^e(t_i)}{c_j^e(t_i)} \right)^2, \tag{2.13}$$

where $t_i, \quad i = 1,2,...,T$, are the measurement time points. Parameter estimation involves either one ($j = 1$) or multiple ($j > 1$) data sets as part of the fitting process such that $j$, $j = 1,2,...,N$, where $N$ is the total number. In subsequent analysis, the former will be deemed an 'individual fit' whilst the latter a 'multi–fit'. Note that 'data sets' refer to the different curves present within a given experimental study, produced by either Marra *et al.* [269] or Scheller *et al.* [81].

The '*fminsearch*' routine minimises error using the Nelder–Mead optimization protocol through a simplex method. The simplex hosts $n+1$ points, one greater than the dimension ($n$) of the problem. The parameter space can be visualised as a contour plot, where the simplex aims to identify the series of parameters that constitute to the smallest error ($\varepsilon$) through a range of transformations (contraction, expansion, reflection, etc.) presented visually in an example parameter case ($x$, $y$) in Fig. 2.6. The protocol comes to an end either upon approaching some tolerance limit or following the execution of a pre–defined number of iterations. The former was set to $10^{-4}$ and the latter to 100,000 to ensure the appropriate minimal error was obtained.

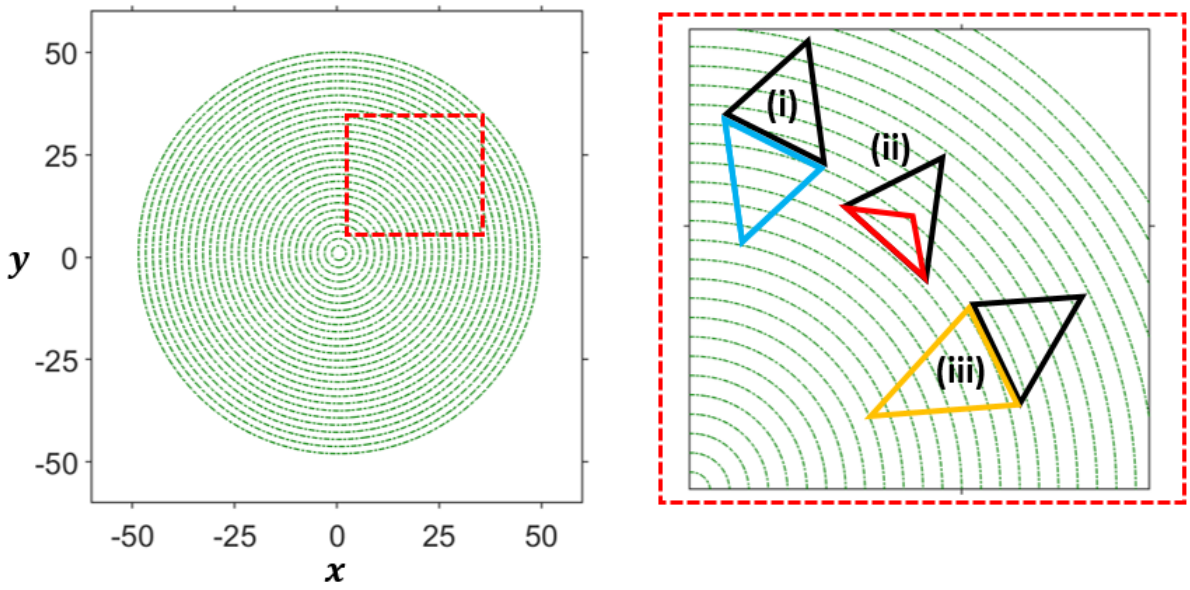


Figure 2.6: The image of the left presents a generic contour ($(x-0.5)^2 + (y-1)^2 - r^2 = 0$) of varius radii ($0 \rightarrow 50$) representing a random parameter space, $x$, $y$. The image on the right focuses in on a segment of this contour, illustrating various simplex transformations following an initial parameter guess (black triangle), such that a: (i) reflection, (ii) contraction, or (iii) expansion are considered following a computation of the centroid of the best two points, as the simplex aims to converge towards to the minimum (circle centre here).

A limitation of '*fminsearch*' is that the algorithm is unconstrained. In the absence of reliable parameter estimates, it is believed that this approach is adequate at the benefit of computational cost. However, a manual constraint is put in place such that only absolute values of parameters are considered, as none of the model parameters should return negative. Moreover, a further limitation of this approach is the possibility of being trapped in a local minimum, where the contour of the parameter space may present with multiple minima. To prevent this, a multi–search algorithm (*Global Search*) was also implemented, assessing the reliability of the parameter estimates for a range of different initial conditions to ensure the global minimum was reached.

The inverse estimation protocol is summarised in Fig. 2.7. Of the parameters listed in Table 2.1, only the initial number of cells ($c^0$) is known prior to model simulation. Information on cell culture plates is absent, and therefore, in addition to the growth rate, $g$, the carrying capacity, $K$, is also estimated as part of step 1. Moreover, Marra *et al.* [269] argued a plateau in Fig. 2.5b. However, with only two data points, and large error bars, that conclusion is difficult to rationalise, and as a result, $K$, has not been fixed. In simulation tests, fixing this value would adjust the growth rate parameter accordingly.

For model simulations that include the effect of drug, control parameters ($g$ and $K$) are fixed. The next step in the protocol then attempts to acquire the best–fitting parameters for each drug model (D1–D3) prior to predicting the other responses; testing model robustness. The final step involves multiple data sets (Eqn. 2.13, $j > 1$) as part of the fitting process, artificially constraining model parameters. Note, the associated error for each fitting procedure documented in Fig. 2.7 is found within its respective table in the Appendix (Section A.2).

## 2.4 Results

### 2.4.1 Marra *et al.* data set: comparisons between the model results and experimental data

As per step one of the fitting protocol (Fig. 2.7), the best–fitting parameters to the logistic growth model (Eqn. 2.5) were obtained, demonstrating an adequate agreement with the experimental data in [269] (Fig. 2.8a). The approach returned $g = 0.204$ s$^{-1}$ and $K = 130,777$ for the intrinsic growth rate and carrying capacity, respectively, with an error of $\varepsilon = 0.0301$. Further efforts which modelled the effect of drug on cell growth kept these control parameters ($g$ and $K$) consistent throughout.

Moving onto step 2 of the fitting protocol (Fig. 2.7), the capability of each model (D1–D3) to capture the Marra *et al.* [269] data when drug was exposed to the cells for the duration of the experiment was tested. To do so, the best–fitting parameters for each model were obtained from fitting to each data set (dose) separately ($H^m_{12}$, $M^m_{12}$ and $L^m_{12}$). For clarity, the parameters to be fitted for each model are: (i) Model D1 – $k_{on}$ and $k_{off}$, (ii) Model D2 – $k_{max}$, $\alpha/k_{50}$ and $\alpha/K_P$,

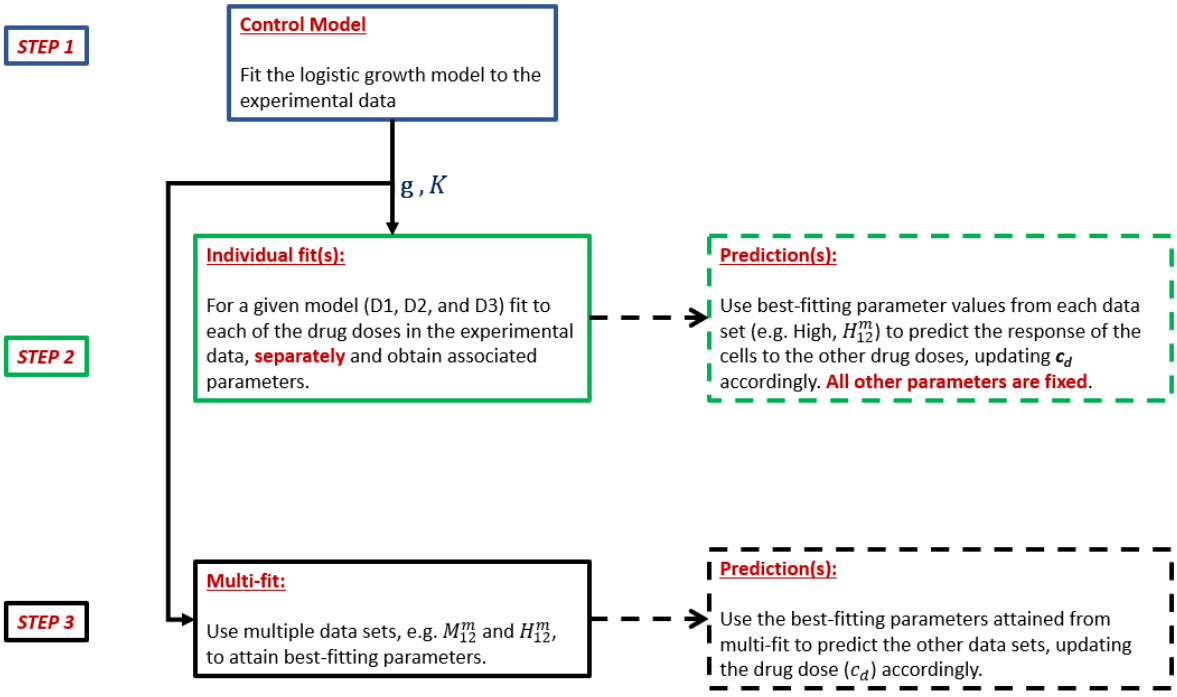


Figure 2.7: Flowchart detailing the parameter fitting process. **Step 1:** The logistic growth model (Eqn. 2.5) hosts two unknowns: $g$ and $K$, which are then fixed for subsequent drug simulations. **Step 2:** For each drug dose considered, an individual fit is performed (Eqn. 2.13, $j = 1$) to permit predictions of the other responses present in the data set. **Step 3:** An alternate fitting strategy is adopted (Eqn. 2.13, $j > 1$) where multiple data sets are used simultaneously to acquire the best-fitting parameters, to then make predictions of the remaining data set(s). Experimental set–ups differ between [269] and [81] and therefore, the three step fitting process is performed on each study individually.

and (iii) $k_{max}$ and $k_{50}$, which were obtained following the non–dimensional analysis (Appendix: Section A.1). Although the results demonstrate good agreement with data qualitatively (Fig. 2.8b–2.8d), and the errors between models are similar (Appendix: Table A.3), there is a notable difference in best–fitting parameters across the three data sets for any given model, and between models where the same parameter (e.g. $k_{max}$: Model D2, D3) applies (Appendix: Table A.1).

Rationalising the results, the discrepancy in parameter values could be a consequence of the fitting protocol, where the parameters may not be uniquely identifiable or the models themselves inadequate, requiring further sophistication. The first point made here is emphasised with particular reference to the two extremes ($H_{12}^m$ and $L_{12}^m$) of model D1, where a threshold exists such that further reduction in an already small binding off rate or increase in a rather large binding on rate, respectively, would have negligible impact on the results. It is in these scenarios where reliable estimates of such parameters, obtained from experimental data, may aid in the fitting protocol by constraining parameters of the model to lie within a pre–defined range; hopefully improving the overall fit as a result. Another explanation is that the parameters may not be

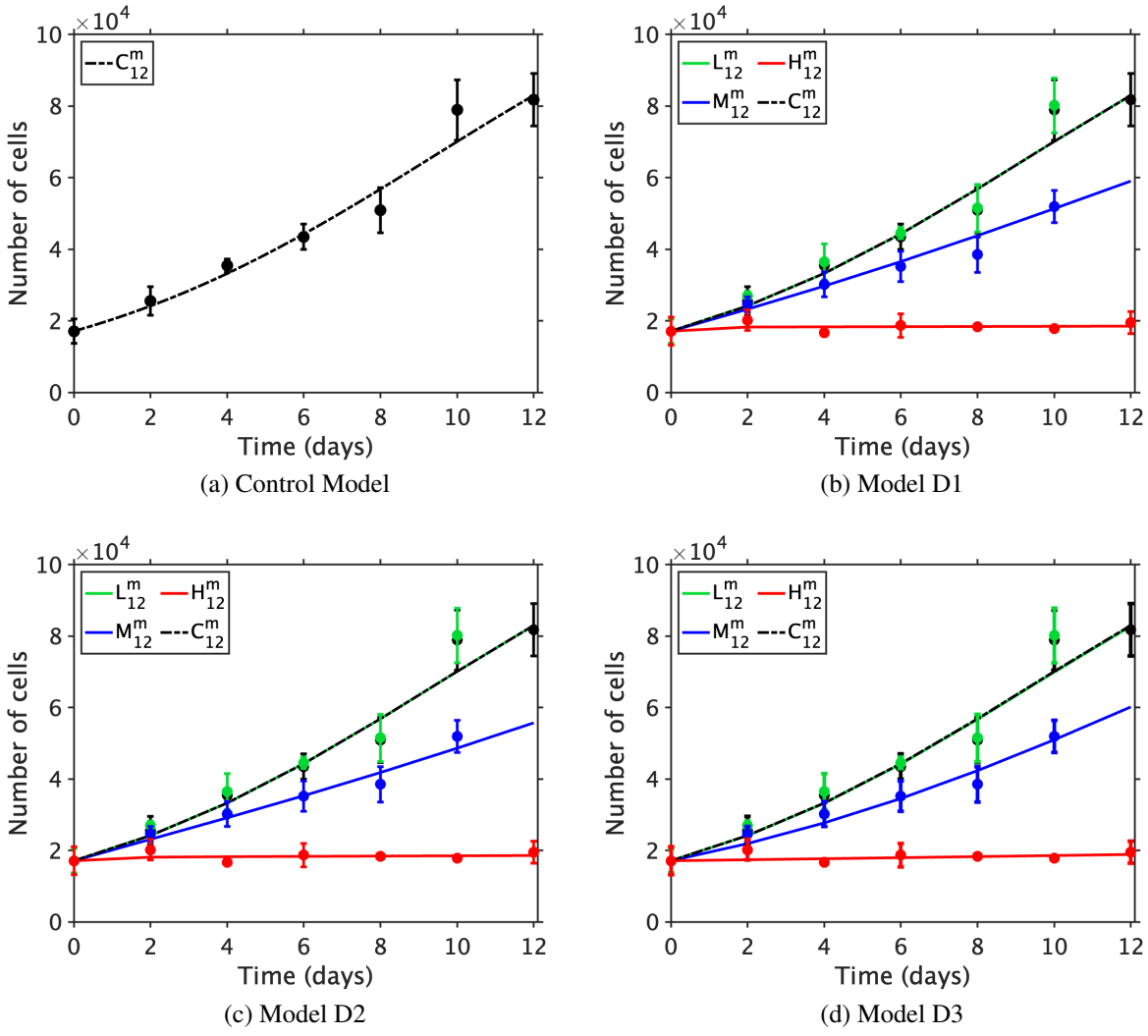


(a) Control Model (b) Model D1

(c) Model D2 (d) Model D3

Figure 2.8: Comparison between mathematical models (curves) of cell growth and the data (markers) provided by Marra *et al.* [269], where $c^0 = 17,100$. (a) Cell growth in the absence of drug, present in all further figures as a dashed line. (b)–(d): Results of model D1–D3 (b–d, respectively) following an individual fit to each data set ($H^m_{12}$, $M^m_{12}$, $L^m_{12}$). The best–fitting parameters obtained from each fit are reported in Table A.1 with the associated errors present in Table A.3, denoted by the coloured cells.

uniquely identifiable because they may be, for example, dose and drug dependent.

To explore this further, the predictive capabilities of each model (D1 & D2) by assessing whether they could capture cell recovery following a short, four–day exposure to drug ($H^m_4$) were tested. The best–fitting parameters obtained following a fit to $H^m_{12}$ were used, where $c_d = 0$ in the respective models after four days to emulate the removal of drug from the media. Fig. 2.9a and 2.9c chart the predicted model response against the experimental data using the best–fitting parameters from $H^m_{12}$, where Model D1 is clearly a poor predictor ($\varepsilon = 0.6174$), whilst model D2 illustrates reasonable agreement with the experimental data ($\varepsilon = 0.0603$). The poor predictive capacity of model D1 could be attributed to an underestimation of $k_{off}$, where previ-

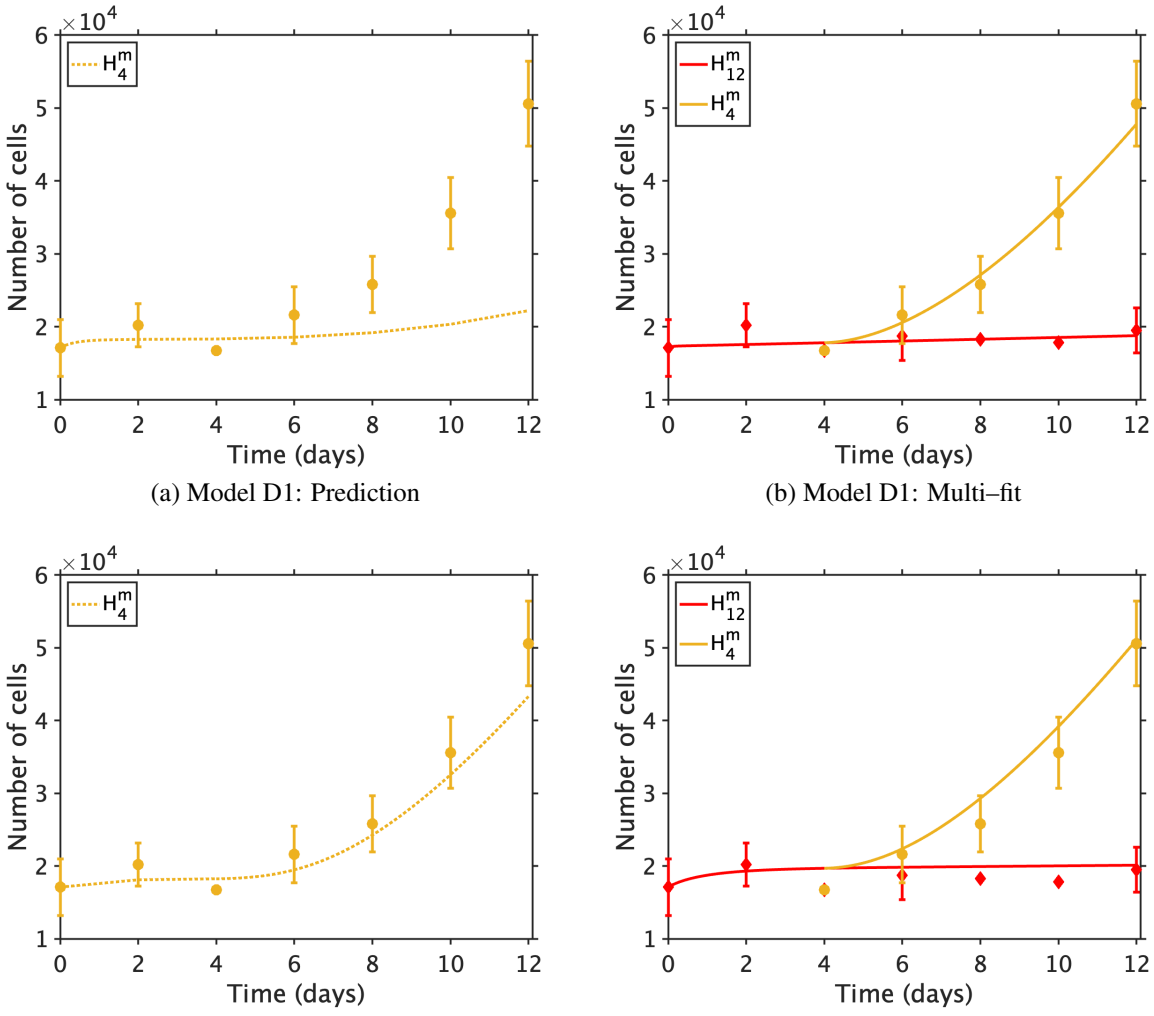


(a) Model D1: Prediction

(b) Model D1: Multi–fit

(c) Model D2: Prediction

(d) Model D2: Multi–fit

Figure 2.9: Comparison between mathematical models (curves) of cell growth and the data (markers) provided by Marra *et al.* [269] when drug was applied for a finite time (four days), where $c^0 = 17,100$. (a, c) Predictions of $H_4^m$ for models D1 and D2, using best–fitting parameters from $H_{12}^m$, respectively. (b, d) Multi–fit for model D1 and D2, using both $H_{12}^m$ and $H_4^m$ simultaneously to acquire best–fitting parameters, respectively. The associated errors between the model and experimental data are present in Table A.2.

ously, under constant exposure, the binding on rate, $k_{on}$, may dominate. As a result of this, the parameter estimation approach was amended (Step 3: Fig. 2.7) such that best–fitting parameters for model D1 and model D2 were obtained following a multi–fit of $H_4^m$ and $H_{12}^m$ ($j = 2$, Eqn. 2.13) in an attempt to bypass the lack of reliable estimates. As shown in Fig. 2.9b and 2.9d, model D1 benefits from a significant improvement in agreement with $H_4^m$ ($\varepsilon = 0.0126$) without impacting the fit to $H_{12}^m$ ($\varepsilon = 0.0257$). This was repeated for consistency with model D2, where no significant difference was apparent in ($\varepsilon$) values for both data sets ($H_4^m$ and $H_{12}^m$) from the previous scenario where the best–fitting parameters obtained from fitting the model to $H_{12}^m$ were used to predict $H_4^m$ (Step 2: Fig. 2.7). Predictions of $H_4^m$ using the best–fitting parameters of $H_{12}^m$

with model D3 are not possible without the estimation of a further parameter ($k_d$). Performing a further parameter estimation of $k_d$, the model was able to capture the experimental data ($H_4^m$) well (Fig. 2.10). However, since there is no further experimental data charting the effect of a brief drug exposure on cell proliferation, the estimation of $k_d$ cannot be fully validated.

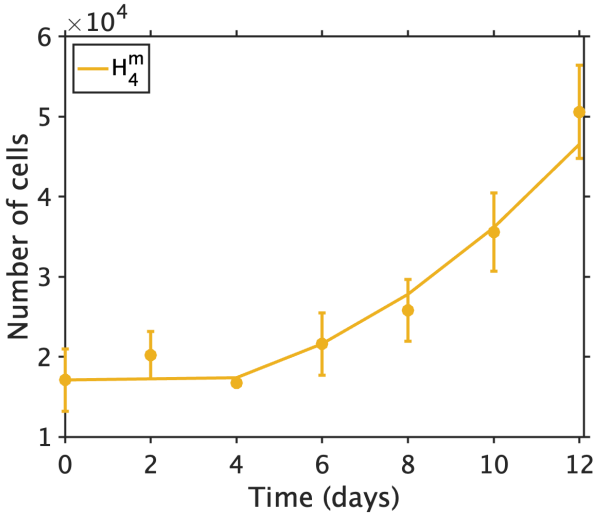


Figure 2.10: Model D3 captures experimental data well, albeit requiring a further parameter estimation ($k_d$). Best–fitting parameters and associated errors reported in Table A.3.

Having investigated the capability of each model to capture drug retention, the next step was to assess the ability of each model (D1–D3) to predict cell growth when exposed to drug indefinitely. As such, the best–fitting parameters from one case (e.g. $L_{12}^m$) are considered, then, by amending the drug dose ($c_d$) accordingly, the other two responses (e.g. $M_{12}^m$ and $H_{12}^m$) are predicted. This was repeated twice such that best–fitting parameters from each data set were used to predict those remaining. As anticipated, the quality of predictions were poor for all three models (Appendix: Table A.3). This may be attributed to the large variance in best–fitting parameters between cases, which could be a consequence of the unconstrained fitting method proposed.

Therefore, in light of the efforts above which explored the effect of drug retention, the parameter estimation approach (Step 3: Fig. 2.7) is amended to include multiple data sets ($j > 1$, Eqn. 2.13). For model D1 and D2, a multi–fit of $M_{12}^m$, $H_{12}^m$ and $H_4^m$ ($j = 3$, Eqn. 2.13) produced the overall best fit to each data set, whilst sufficiently predicting the remaining data set ($L_{12}^m$). On the other hand, the best prediction using model D3 was obtained when best–fitting parameters were acquired using $M_{12}^m$ and $H_{12}^m$ ($j = 2$, Eqn. 2.13) and $L_{12}^m$ predicted. As before, an additional fitting procedure is necessary to capture the $H_4^m$ data set emulating drug retention. Summarising the results, Fig. 2.11 illustrates that model D1 is the poorest performer. Both model D2 and D3 present good agreement with the experimental data, with both displaying sufficient agreement to the fitted (solid) and predicted (dotted) data sets. Information on the best–fitting parameters and error values for each model can be found in the Appendix (Table A.4).

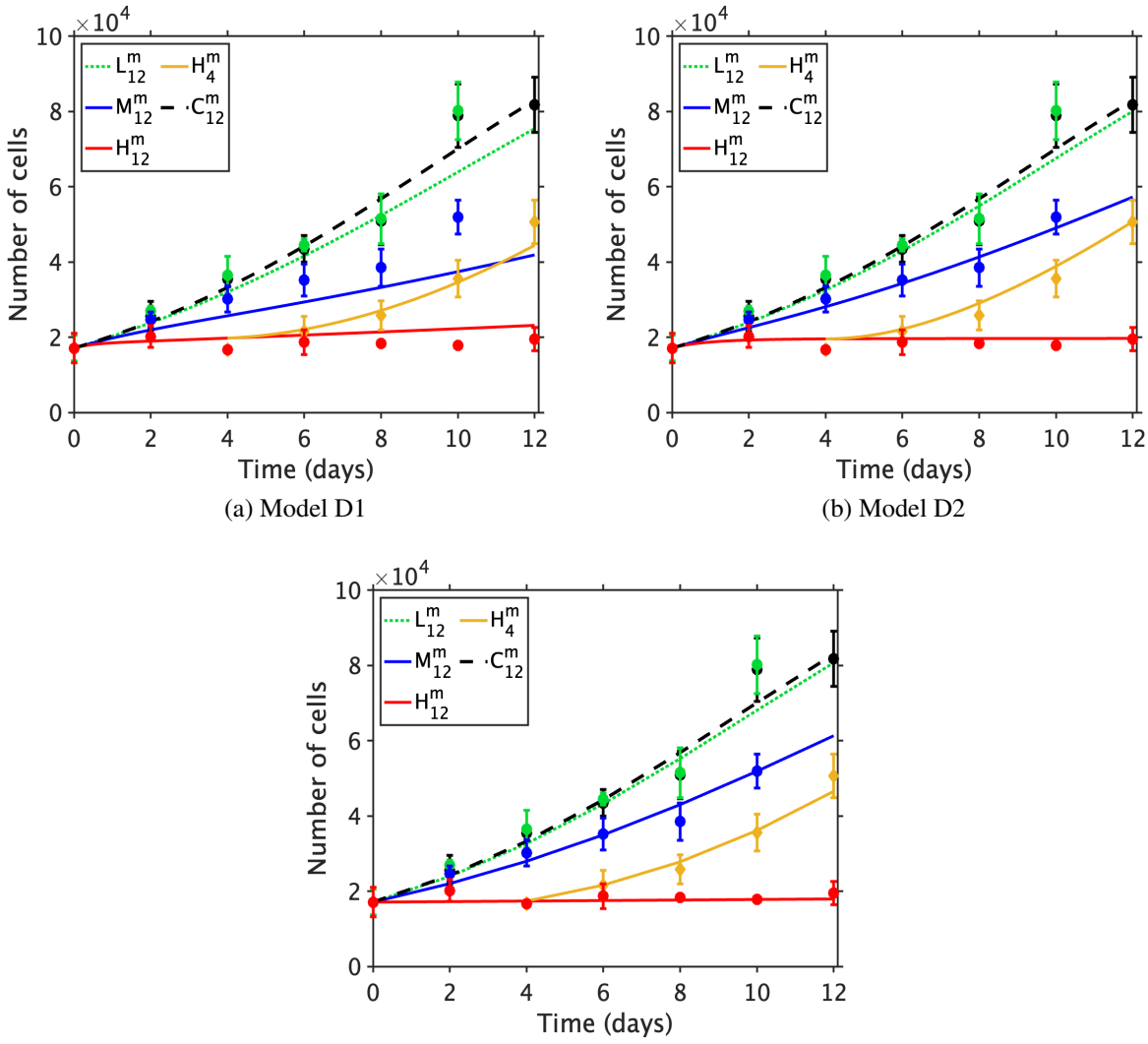


(a) Model D1

(b) Model D2

(c) Model D3

Figure 2.11: Comparison between data (markers) provided by Marra *et al.* [269] and mathematical models (curves) of cell growth and recovery when a multi–fit (Model D1 & D2: $H^m_{12}$, $M^m_{12}$, and $H^m_4$), Model D3: $H^m_{12}$, $M^m_{12}$) is used to obtain the best–fitting model parameters before the effect of the low drug dose ($L^m_{12}$) is predicted (illustrated by the dotted line). In all cases, the control model ($C^m_{12}$) is represented by a black dashed line, distinguishing it from response where drug is considered. Best–fitting parameters and associated errors reported in Table A.4.

### 2.4.2 Scheller *et al.* data set: comparisons between model results and experimental data

A similar approach is implemented for the Scheller data [81]. First and foremost, Eqn. 2.5 charts a good agreement with experimental data for cell proliferation in the absence of drug. The best–fitting parameters for the intrinsic growth rate ($g$) and carrying capacity ($K$) were 0.204 $s^{-1}$ and 130,777 respectively, where the associated error was $\varepsilon = 0.00382$.

Again, individual fitting ($j = 1$, Eqn. 2.13) to each data set demonstrated adequate agree-

ment to the experimental data for models D1–D3 (Fig. 2.12). This is emphasised in Table A.5 (Appendix), where the quality of fits, defined by the $\varepsilon$ values, are documented, for which model D1 performs poorest. The best–fitting parameter values are reported for each case, where, similar to earlier work for [269], a difference is not only observed between models emulating the effect of drug that host the same parameters, but also between data sets. Subsequent efforts assessed the predictive capacity of each model, where the best–fitting parameters from a single data set (e.g. $H^s_{60}$) were used to determine whether the other responses can be captured by only adjusting the applied dose ($c_d$). With there being a total of four data sets ($H^s_{60}$, $H^s_{10}$, $H^s_3$, $L^s_{60}$), the model (D1–D3) when fitted against one data set is a poor predictor of the remaining data sets, with associated error values reported in Appendix: Table A.6.

As per Fig. 2.7, step 3 was implemented with the aim of trying to improve agreement between the model results and experimental data. A series of multi–fits were tested ($j > 1$ Eqn. 2.13), with the aim of artificially constraining the parameters to depict various model responses. To ensure the best multi–fit approach was utilised, a variety of multi–fit combinations were considered: (i) $H^s_{60}$ and $L^s_{60}$, (ii) $H^s_{60}$ and $H^s_3$, and (iii) $H^s_{60}$, $H^s_{10}$, and $L^s_{60}$.

The best predictions were obtained from case (i) and model D3, where the 60–minute low ($L^s_{60}$) and high ($H^s_{60}$) data sets were used to predict model behaviour at shorter exposure times. On the other hand, model D1 (Fig. 2.13a) and D2 (Fig. 2.13b) failed to capture the response of cells to high doses of drug for shorter exposure times ($H^s_{10}$ and $H^s_3$), illustrating a notable difference between the model responses for each of these data sets; disagreeing with the experimental results. However, in model D3, where binding is neglected and the effects of drug are *instantaneous*, a negligible difference is present between the three exposure times (3, 10, and 60 minutes) for a high dose of drug (Fig. 2.13c), where curves are superimposed onto one another. The reasoning for this, and possible significance behind these results are discussed more in Sec. 2.5. Other tested cases failed to demonstrate reasonable agreement across all models (D1–D3). For example, in case (ii), although a reasonable prediction for $H^s_{10}$ was attainable, the effect of the lower dose ($L^s_{60}$) was severely overestimated and as a result, proliferation was significantly inhibited. Moreover, in case (iii), which accounted for 3/4 data sets ($H^s_{60}$, $H^s_{10}$, and $L^s_{60}$), the fitting protocol failed to find best–fitting parameters that could portray an adequate model response to these data, particularly $H^s_{10}$ and $L^s_{60}$, where the prediction of $H^s_3$ suffered as a result. Thus, there is some confidence in case (i), which still allows for the prediction of at least one data set.

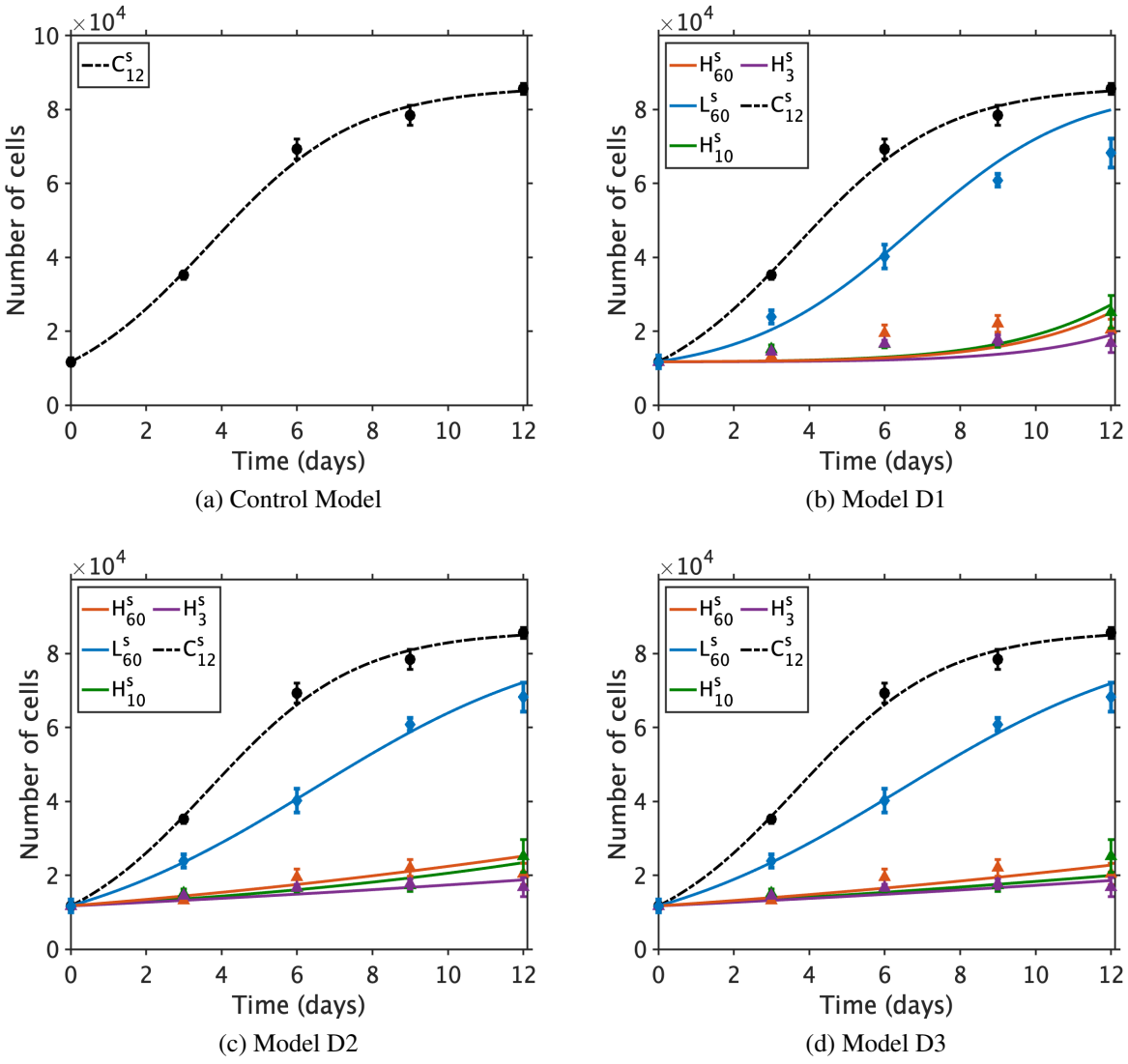


(a) Control Model (b) Model D1

(c) Model D2 (d) Model D3

Figure 2.12: Comparison between mathematical models (curves) of cell growth and the data (markers) provided by Scheller *et al.* [81], where $c^0 = 11,704$. (a) Cell growth in the absence of drug, present in all subsequent figures as a dashed line, distinguishing it from data which represents the effect of drug. (b)–(d): Results of model D1–D3 (b–d, respectively) following an individual fit to each data set ($H^s_{60}$, $H^s_{10}$, $H^s_3$, and $L^s_{60}$). The best–fitting parameters from each fit are reported in Table A.5 with the associated errors reported in Table A.6, denoted by the coloured cells.

## 2.5 Discussion & Limitations

### Logistic growth model captures cell proliferation in the absence of drug

The logistic growth model has been ubiquitously used to describe the growth of cells in culture [276]. For each experimental study considered, Eqn. 2.5 simulates a model response that agrees well with the data presented. Although neither [81] or [269] discuss their methodolo-

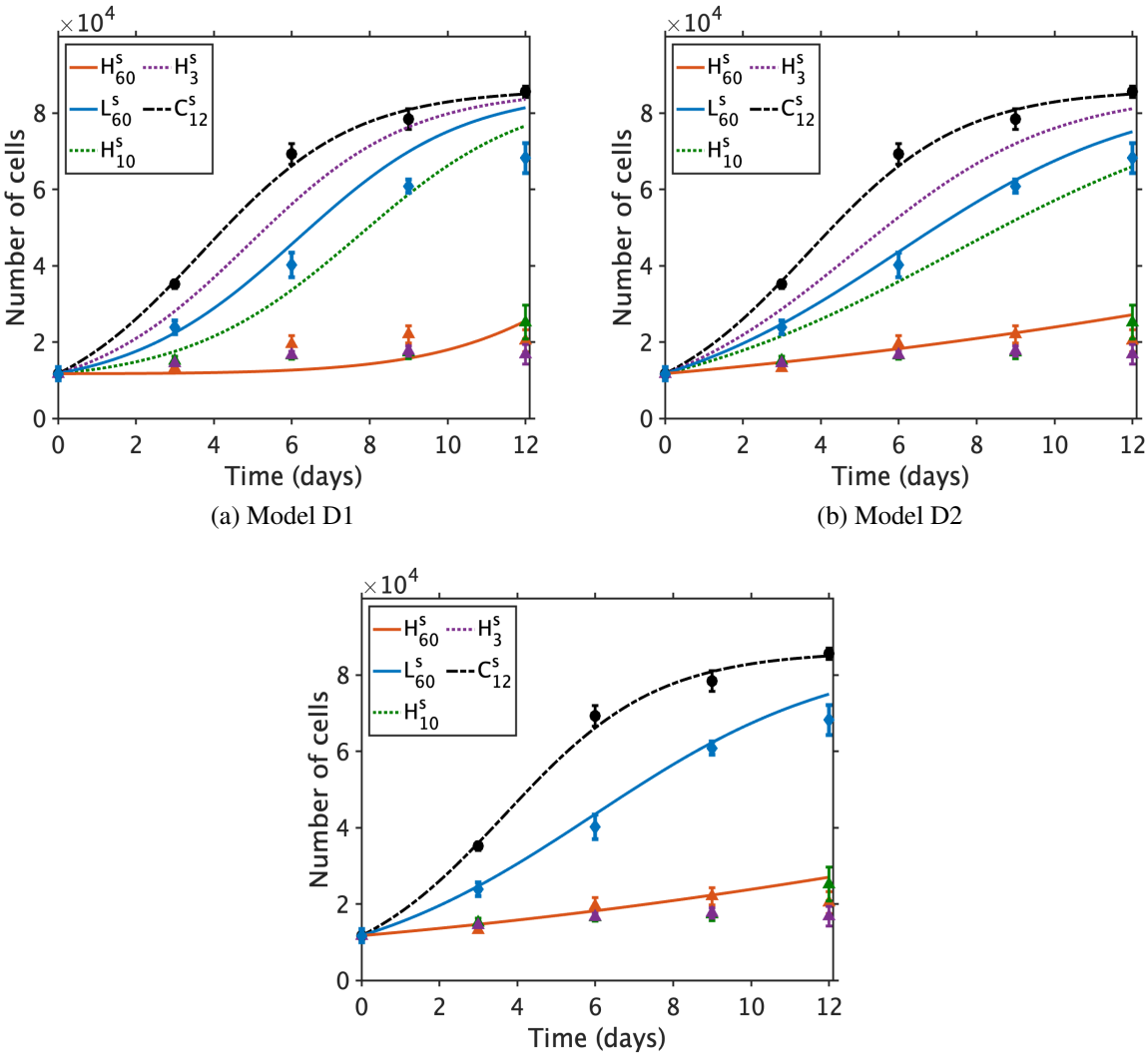


(a) Model D1

(b) Model D2

(c) Model D3

Figure 2.13: Comparison between data (markers) provided by Scheller *et al.* [81] and mathematical models (curves) of cell growth and recovery when a multi–fit, case (i), is used to obtain the best–fitting model parameters before $H^s_{10}$ and $H^s_3$ are predicted (illustrated by the dotted lines). In all cases, the control model ($C^m_{12}$) is represented by a black dashed line, distinguishing it from response where drug is considered. The best–fitting parameters and errors associated with each mutli–fit can be found in Table A.7.

gies in detail, the inferred carrying capacities from the fitting protocol return values broadly in agreement with those commercially available cell culture plates [282].

Fig. 2.12a presents a clear plateau in the model response, highlighting that cells have indeed reached their maximal cell number. On the other hand, Fig. 2.8a illustrates that cell growth is still present. An additional data point would provide more insight, indicating whether the value for $K$ is an over–estimate or not. If true, subsequent inverse estimation would return a larger value for $g$ as a result, where cell proliferation is quicker.

Moreover, note the that $g$ and $K$ differ substantially between the two data sets. As for the

former, [275, 283] demonstrate that the behaviour between different cell species varies, which can be translated into the *in vitro* scenario emulated here, where [81] and [269] consider SMCs of different origins. As for the latter, $K$, this is likely a consequence of different experimental set–ups and/or cell size between the two (Scheller *et al.* [81] and Marra *et al.* [269]) experimental studies.

## Each experimental data set can be captured, but predictions are poor

Attaining the best–fitting parameters to each model individually presented a good agreement to the experimental data for both studies (Fig. 2.8b–2.8d and Fig. 2.12b–2.12d); although the values obtained for the best–fitting parameters varied significantly between the different data sets. Moreover, when considering these best–fitting parameters to capture the response of the other data sets (e.g. parameters from $H^s_{60}$ are used to predict $H^s_{10}$, $H^s_3$, and $L^s_{60}$), the quality of all predictions were generally poor (Appendix: Table A.3 & A.6). Probing further, the poor predicative capacity of each model could be explained by the large variance in best–fitting parameters between successive data sets (Appendix: Table A.1 & A.5). The lack of reliable estimates of each parameter value may be attributed to this, where no constraints were placed on the bounds for each parameter. Acknowledging this, a multi–fit protocol was devised, where numerous data sets were used to acquire best–fitting parameters, artificially fitting them to the various extremes observed in the data. Although promising, a key disadvantage of this approach is that the number of data sets available to predict are reduced. Therefore, additional data sets are required, or more thorough studies of drug behaviour that allow for reliable estimates of model parameters to be obtained more readily. Moreover, the identifiablity of the parameters has been questioned. The fitting protocol could be the culprit, however, another possible explanation is that the associated parameters are both drug and or dose dependent. This has not been considered in the present work, but further research should design experimental studies to investigate this possibility in more depth.

## The *simplest* drug model performs the best

Two studies were considered for model calibration and validation (Scheller *et al.* [81], Marra *et al.* [269]), of which model D3 was able to best capture all data following a series of individual fits (Fig. 2.8d & 2.12d). Moreover, as the fitting strategy was updated, model D3 also presented most favourable here, agreeing with experimental data for model responses that were both fitted and also those that were predicted, a pitfall of the other two models, particularly for [81] (Fig. 2.11c & 2.13c). This may be somewhat counter intuitive given that the binding kinetics present in D1 are widely adopted in the literature. A possible explanation as to why is discussed in more depth below.

It is clear that the experimental data in Scheller *et al.* [81] presents no significant difference

between the three exposure times (3, 10, and 60 minutes) for the high dose of PTX. Thus, even an extremely brief exposure of cells to PTX elicits an inhibitory response that is long–lasting (at least 12 days). In particular, it is model D1 and D2 that fail to agree with this trend. Investigating further, Fig. 2.14 presents how the bound drug concentration for each model varies across the first 60 minutes, where the drug is present in culture. Looking at the high dose curves, it is clear that in both models, the bound drug concentration at 3 minutes is much lower than that at 60 minutes, rationalising the poor performance present earlier (Fig. 2.13a & 2.13b). Note, the level of bound drug concentration after 60 minutes following low dose exposure presents adequate when capturing the experimental data. As a result, the comparable levels of concentration between $H^s_{10}$, $H^s_3$, and $L^s_{60}$ in both models rationalises why the models may not give good agreement to the experimental data. Therefore, it is clear that for all doses to be captured with model D1 and D2, the parameters associated with binding kinetics need to be dose–dependent.

Moreover, a superior performance of model D3 is noted when emulating the experimental data in Scheller *et al.* [81]. In this model, drug binding is neglected entirely, where the effect of drug on cell proliferation is described via the applied dose ($c_d$) directly. In other words, this simplified approach assumes that the drug is bound instantaneously. Since the applied drug dose is constant, for 3, 10, and 60 minutes, the level of drug influencing cell growth is the same, where only the time of exposure differs. As a consequence, the effect on cell proliferation was indifferent between the three as present in the experimental data.

The other data set, Marra *et al.* [269], hosts three different drug doses, two of which present as extremes; where the low dose illustrates a response indistinguishable from the control case and the high dose is an almost complete inhibitor of cell growth. As a consequence, the fitting procedure considered the high and medium doses, whilst the response to a lower dose was predicted. However, model D1 was unable to capture the response to both the high and medium dose, whilst simultaneously predicting the the remaining data set ($L^m_{12}$: Fig. 2.11a). Reconsidering Fig. 2.5b, the experimental data shows that SAL is poorly retained in cells, where the re–proliferative potential is high following the removal of the supernatant. The improved performance of model D2 and D3, which considers simpler or no binding kinetics, captures this process as well the as the effect of prolonged exposure. The simpler kinetics have no *ramp up* period, and thus the effect of drug on cell proliferation is quick in comparison to model D1 which may explain why model D2 and D3 better capture the experimental data.

Although the simpler models present themselves as the favourable option, the description of cell growth here is applied within the *in vitro* environment only. A further model analysis should be considered in a setting that depicts a more realistic environment before drafting final conclusions. Rationale for the better performance of the simpler models is present in this work, but further analysis is necessary.

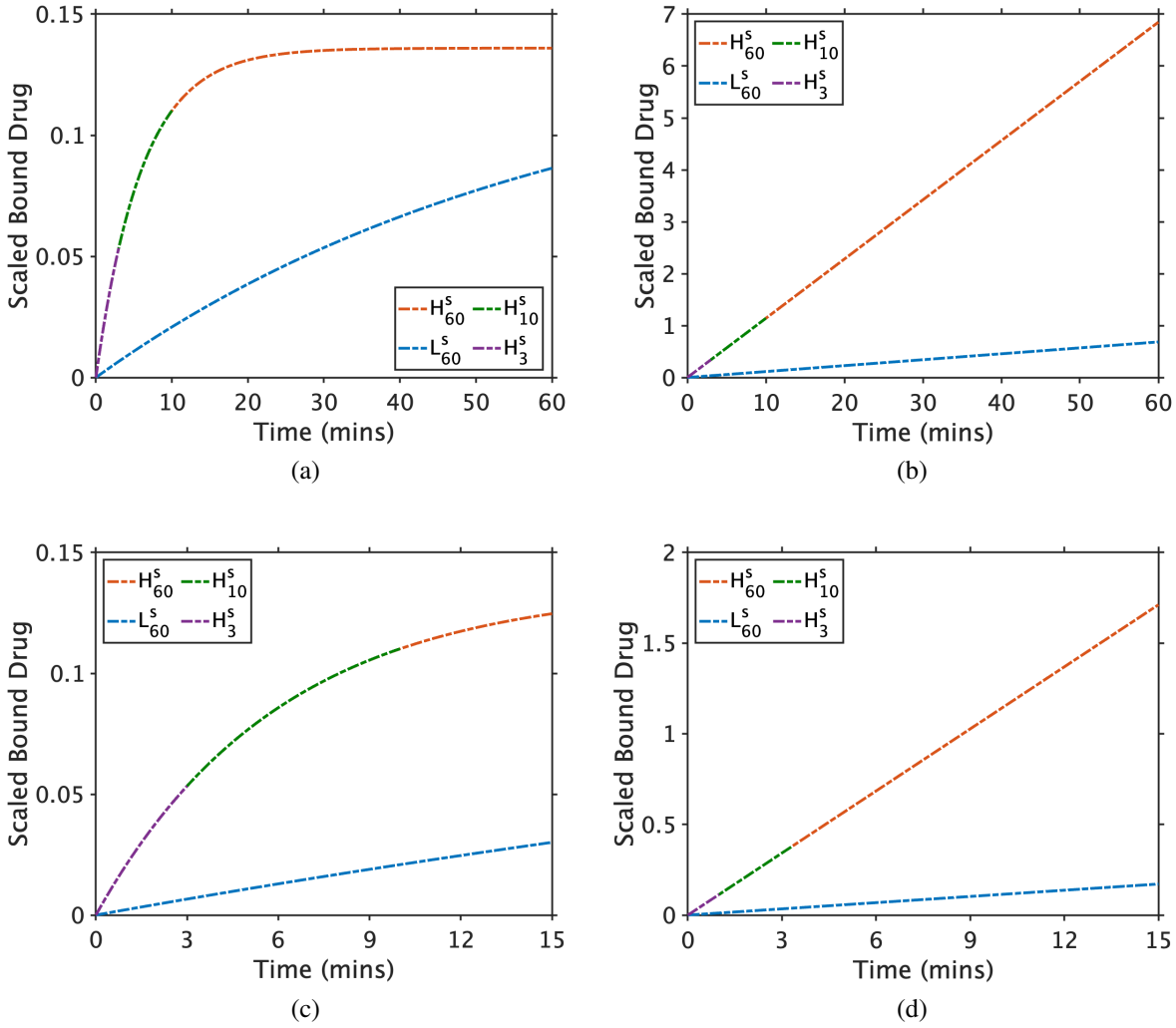


Figure 2.14: Following a multi-fit to $H^s_{60}$ and $L^s_{60}$, the bound drug concentration behaviour is presented within the short exposure window, where drug is present. (a) Model D1. (b) Model D2. (c) First 15 minutes of D1. (d) First 15 minutes of D2.

## Possible implications for further research

The results presented question the applicability of the state–of–the–art binding model to infer cell proliferation subject to drug exposure *in vitro*, assuming that drug effectiveness is defined by receptor saturation. Such a model often details drug transport kinetics in isolation of cell behaviour. The approaches presented here are the first of their kind to couple the processes together, where bound drug is assumed to influence cell proliferation directly (model D1). Simpler kinetics are also presented, which outperform those deemed to be more sophisticated.

Results demonstrated that neither the response of cells to SAL or PTX following *in vitro* exposure are adequately captured by model D1 across a range of drug doses and exposure times. This implies that the natural delay present in Eqn. 2.6 as drug binds is inadequate, or, that each parameter associated with (un–) binding should indeed be drug and or dose–dependent. To fully

explore the validity of these models, experimental efforts should investigate the performance of additional drugs (e.g. analogues to SIR).

It should be noted that the models presented here describe the behaviour of cells *in vitro* where factors such as drug specificity are neglected. Following release *in vivo*, drug binds to a plethora of sites, deemed either specific (e.g. SMCs) or non-specific (e.g. ECM) [79, 178, 178, 188]. Therefore, the effectiveness of drug could be detailed through an alternate mechanism which has not been considered in this work.

## 2.6 Conclusion

In conclusion, a series of mathematical models have been presented that explore the effect of drug on cell proliferation within an *in vitro* environment. The models of drug effect on cell proliferation range in complexity, inclusive of either: sophisticated, non–linear saturable binding kinetics; simpler, linear binding kinetics; or no binding of drug, where the applied dose ($c_d$) influences cell growth directly. Results demonstrate, that overall, simpler models outperform the more sophisticated ones when compared with the available data. However, these discussions are only valid within the environment emulated for the drugs considered. For example, models of drug uptake and binding are often parametrised using *in vitro* or *ex vivo* data, where they are extended into more complex, multiphysics models which try to capture the *in vivo* environment. Efforts here demonstrate the importance of attaining reliable parameter values, where model calibration and validation should be inclusive of numerous data sets, incorporating multiple drug doses and exposure times. It is anticipated that binding parameters alike will vary on a drug–to–drug basis, so this should be repeated for every subsequent drug considered. More sophisticated experimental set–ups should also be devised to ensure that model descriptions of drug effectiveness are accurate. For example, the *in vitro* data here is assumed uniform in space, although there is expected to be a spatiotemporal gradient of specific (and possibly non–specific) receptors *in vivo* which could have a knock–on effect on drug performance.

Moreover, the efforts of this chapter should be extended to address the various limitations present. Such work should consider the cyclic behaviour of cells in a similar way to those proposed when modelling cancer. This phenomenon should be explored more within a cardiovascular setting, where it is known that cells are inhibited by cell–cycle specific drugs. As a result, more sophisticated models depicting the effect of drug may be developed, such that comparisons between the simpler iterations can be made. Furthermore, efforts should also extend models to a higher dimension, where behaviours present *in vivo* can be studied in more confidence such that results can be translated into the context of DES, where spatiotemporal patterns of drug release exist. Such models can infer the effectiveness of various stent designs on the inhibition of restenosis, where drug impacts the behaviour of other species implicitly. Finally, with delayed arterial healing a profound issue in DES, co–cultures of EC/SMC proliferation

should be examined further, emulated through mathematical models. Here, the specificity of drugs to each of these cell types can be explored in more detail, providing possible insights into why a delay in re–endothelialization occurs and the possible implications on patient outcome. All of these concerns, within some capacity, are addressed in subsequent chapters within this thesis, building upon the work presented here.

# Chapter 3

# Mathematical model of cell cycle specific drug inhibition of smooth muscle cell proliferation

In Chapter 2, mathematical models were proposed to describe the effect of various concentrations of drug on smooth muscle cell (SMC) proliferation. The results of the models were compared with experimental data, where some models performed notably worse than others. For example, it was somewhat surprising that the state–of–the–art nonlinear saturable binding model failed to capture the dose–dependent effect of drug on SMC proliferation *in vitro*. Although a good fit to the experimental data was achieved across the models on a dose–by–dose basis, their predictive capabilities were poor when using the best–fitting parameters acquired from one dose to predict another.

With this in mind, a major limitation of the models proposed in Chapter 2 are that they assume that the drug elicits its effect on cell growth without regard for its current phase within the cell cycle. However, it is known drugs on stents (e.g. sirolimus and paclitaxel) tend to elicit their action at particular checkpoints along the cell cycle: they are cell cycle specific. Therefore, with the models in Chapter 2 not accounting for this behaviour, they could be under or over–estimating the anti–proliferative effect of drug, which could be contributing to the poor predictive capabilities of these models.

Although proliferation assays have been an essential tool to investigate the impact of drug exposure on cell growth, a common limitation is that cell cycle behaviour is ignored. Typically, cells are grown in culture using a growth serum, supplemented with a particular drug at various concentrations, assessing the dose–dependent effect on cell proliferation. These techniques have been essential in understanding the pharmacodynamic effects of drug, where data drives therapeutic dose ranges *in vivo*. Generally, these experimental techniques involve some sort of standardisation, where all cells are arrested in $G_1$ through a serum starvation protocol, ready to progress through the cell cycle in a synchronous fashion thereafter. However, when

implementing this standard serum starvation approach, Vittadello *et al.* [284], in the context of cancer, observed an inherent synchronization with the cell population across several independent experiments. In other words, the body of cells appeared to exist in several sub–populations, completing their cycle of growth at different times. As such, the authors questioned the reproducibility of proliferation assays and any mathematical models calibrated from them. Therefore, Vittadello *et al.* [284–286] employed an experimental technique that utilised cell cycle indicators (e.g. fluorescent universal cell cycle indicator, FUCCI) for mathematical model calibration and validation [284, 287, 288]. This allowed for real–time visualisation of cell behaviour as the population proliferated towards its carrying capacity. Although not considered within their modelling framework, it is likely that the issues of reproducibility will be compounded in assays which include anti–proliferative drugs. With these drugs (e.g. sirolimus) being cell cycle specific, it is likely that the initial distribution of cells could influence the perceived efficacy of the drug. Especially if the distribution of cells among the cell cycle is different from one experiment to the next.

With the efforts [284–288] focused on carcinogenic cell lines, no known literature exists which explores such a phenomenon on SMCs, particularly within the context of stenting. Given that SMCs are the driving force behind restenosis, exploration into the specific nature of how drugs inhibit their proliferative capacity may help in deriving more finely tuned models, capable of making better predictions.

A further limitation of experimental techniques is that the spatiotemporal aspect of drug delivery is commonly ignored, with cells exposed to a constant, uniform dose of drug. Such a feature may not be as important in carcinogenic applications, but is of the utmost importance in the success of drug–eluting stents (DES) [79]. With the initial distribution of cells likely to impact the efficacy of drug when exposed to cells from the start of the experiment, it is expected that any differences in drug performance will be further exacerbated in situations where the drug is released over a finite period of time. Therefore, to translate drug effectiveness adequately to the *in vivo* scenario, it is essential to simulate the release of drug into the environment where cells reside, assessing the role of cell cycle specific drugs when the cyclic behaviour of cells is accounted for.

As such, the first goal of this chapter is to understand if any discrepancies exist between a model which accounts for cell cycle dynamics versus one that does not, when modelling *in vitro* SMC proliferation. With the emphasis of this chapter being to better understand the role of anti–proliferative drugs on SMC proliferation, the mathematical models from Chapter 2 (where cell cycle behaviour was ignored) are built upon to account for this. The second goal of this chapter is to then assess whether any discrepancies between models which simulate cell cycle behaviour versus those which do not are exacerbated when a cell cycle specific, anti–proliferative drug is considered. With the importance of drug delivery in stenting applications noted, the final goal is to then assess whether spatiotemporal drug delivery exacerbates any differences further.

The chapter begins by providing an overview of the stages of the cell cycle. A review of relevant literature is then presented, highlighting recent work which has alluded to the importance of modelling the cell cycle process in the presence and absence of drug; providing rationale for the aforementioned goals of this chapter. The chapter is then separated into two distinct parts: one detailing a 0D model and the other a 1D model. The sections comprising of the 0D model will make direct comparisons between models neglecting or including cell cycle dynamics in the absence and presence of two drugs which are cell cycle specific. These are termed drug 1, a $G_1$/S transition blocker (e.g. sirolimus) and drug 2, a mitosis (M) blocker (e.g. paclitaxel). Here, it assumed that the drug is uniformly exposed to the cells. The second section will then extend the dimensionality of the model (1D), assessing the impact of spatiotemporal drug delivery on cell proliferation in the presence of the aforementioned anti–proliferative drugs. Here, possible implications are extrapolated to the *in vivo* environment, where the drug release strategy is known to be an important mediator for the success of DES.

## 3.1 Incorporating the cell cycle into mathematical models of cell proliferation

### 3.1.1 The cell cycle

With the primary goal of this chapter being to assess the benefit of models accounting for cell cycle dynamics following exposure to anti–proliferative, cell cycle specific drugs, an overview of the cell cycle itself is necessary. The cell cycle is a fundamental process which details the step–by–step progression of cell growth as it undergoes division. Within the cycle, there exists 4 stages: $G_1$, S, $G_2$, and M, as summarised in Fig. 3.1. There is an additional fifth stage, $G_0$, where cells are quiescent, awaiting activation for growth via a stimulus (e.g growth factor binding). Summarising, the $G_1$ phase is where the cell prepares for division prior to in–house checks at the first restriction checkpoint, immediately before entering the second phase. In the S–phase, DNA synthesis occurs, where the genetic material is copied. In the third phase, $G_2$, the material is condensed and organised in preparation for division, where the second checkpoint occurs. The final stage, M, is known as mitosis, where cells undergo a series of steps that ensure the equal division of chromosomes between the two daughter cells. This is concluded with cytokinesis, the process directly involved in the division of the parent cell into two daughter cells, where the cycle can begin again.

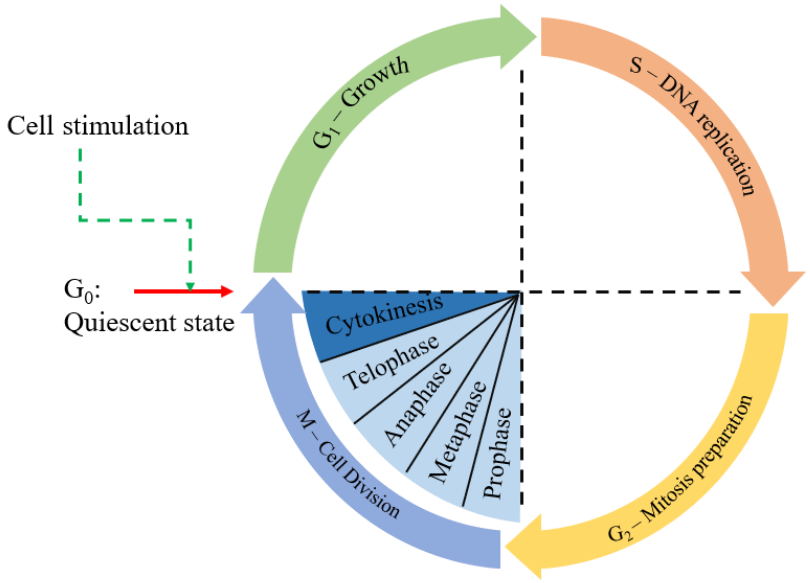


Figure 3.1: Schematic of the cell cycle. Separated into 4 growth phases ($G_1$, S, $G_2$, and M) and one quiescent phase, $G_0$. The M phase, has various steps associated with mitosis followed by cytokinesis, the ultimate splitting of the cell into two daughter cells.

### 3.1.2 Mathematical models of cell proliferation where cell cycle behaviour is considered

To highlight the importance of simulating cell proliferation as a cyclic process, various mathematical models have been devised. Although the majority of these place a particular emphasis on gene expression, as detailed extensively in various review articles [289–292], other models have recently emerged which allude to the importance of accounting for cell cycle behaviour when modelling cell proliferation [284–286]. Through the aid of experimental data, these authors noted an oscillatory proliferative response, a consequence of emerging sub–populations within the general population of cells. As such, the authors questioned the consistency and reproducibility of standard proliferation assays, and mathematical models calibrated from them.

The mathematical models focused on emulating cell proliferation reduced the cell cycle to two phases. Phase 1 describes the $G_0/G_1$ stages, where the cell grows in size and phase 2, capturing S, $G_2$, and M, details the phases following DNA synthesis, where the genetic material has since doubled from phase 1. Supporting this mathematical modelling approach is an experimental technique called FUCCI. This enables the real time visualisation of cell cycle dynamics through a staining protocol of particular proteins present in each phase: CDT1 for phase 1 (green), and geminin for phase 2 (red) [293]. More sophisticated protocols exist that can visualise 3 or 4 phases separately, but efforts in [285] discuss the ambiguity of such approaches, where, for example, an intermediate phase (eS), between $G_1$ and S, can be visualised in yellow: a combination of red and green.

Summarising, these new cyclic proliferation models by Vitadello *et al.* [284–286] have demonstrated the importance of accounting for cell cycle behaviour. The model presented in [284] simulated the exponential growth of cells over a short time frame (48 hours). When calibrated against experimental data, an oscillatory proliferation of cells was observed. This was a result of an inherent synchronization present within a pre–manipulated culture of cells, where even after cell cycle arrest was induced, a heterogeneous distribution of cells throughout the cell cycle was noted. The authors then alluded to the possible significance of this finding, where such a result may question the reproducibility of standard proliferation assays, particularly if the distribution of cells throughout the cell cycle were to differ from one experiment to the next.

The spatiotemporal behaviour of the cell population was also assessed in a scratch wound assay by Vittadello *et al.* [285]. As such, exponential models were extended to account for cell migration via a diffusive term, and the inhibition of proliferation as a consequence of spatial restrictions through the logistic growth model. Simple, two–phase models were able to well–capture the valley response present as cells migrated and proliferated over a wound following a scratch assay. Particularly with scratch assays, the idea of proliferation and/or migration can be ambiguous. Investigating further, Vittadello *et al.* [286] challenged the 'go–or–grow' hypothesis, stating that the motility of cells, across varies cell lines, is independent of their phase within the cell cycle. Moreover, cell cycle inhibiting drugs which induced $G_1$ arrest were considered in their experiments. Although the effect of drug itself was not explicitly modelled, left to future work by the authors, experimental results demonstrated that these cells had only minor variation in motility with respect to a cell population not treated by drug.

Vittadello *et al.* [284–286] demonstrated the possible importance of modelling cell proliferation as a cyclic process. Although not considered within their efforts, it is clear that the applicability of cell cycle specific drugs within this context may be significant. For example, the effect of such drugs in the context of cancer has been studied experimentally using FUCCI, where results have highlighted the importance of such experimental protocols when planning chemotherapeutic treatment strategies [287, 288]. However, to the best of the author's knowledge, an extension to other application areas remains under–explored, particularly within the context of SMCs and the progression of in–stent restenosis (ISR). For example, with drugs like sirolimus eliciting their effect at a particular checkpoint in the cell cycle (Chapter 2: Section 2.2), then the distribution of cells throughout the cell cycle may have an impact on the perceived efficacy of the drug; especially if the distribution of cells varied from one experiment to the next. As such, mathematical models that emulate the specific action of drug may permit fine–tuning of best–fitting parameters associated with drug efficacy, improving the predictive capacity of associated mathematical models. A brief review of mathematical models depicting the behaviour of cell cycle specific anti–proliferative drugs on carcinogenic cells is discussed in Section 3.1.3. How these models can then be extended and applied to better understand how drug modulates

arterial healing is also discussed.

### 3.1.3 Mathematical models of drugs inhibiting cell cycle progression

Generally, the cell cycle (consisting of 5 phases) can be separated into two distinct phases [242, 284, 285], where the former is associated with pre–DNA synthesis, whilst the latter represents post–DNA synthesis:

$$\frac{dP_1}{dt} = 2\lambda_2 P_2 - \lambda_1 P_1, \tag{3.1}$$

$$\frac{dP_2}{dt} = -\lambda_2 P_2 + \lambda_1 P_1, \tag{3.2}$$

where $P_\chi$ describes the cell phase, and $\lambda_\chi$ is the transition rate between each phase, where $\chi = 1, 2$. Note that the factor of 2 in first term on the right–hand side of Eqn. 3.1 accounts for cell division. The model presented by Eqn. 3.1–3.2 captures cell behaviour in the absence of drug.

Roe–Dale *et al.* [242] adopted a simple model framework to explore optimal treatment strategies for breast cancer. Fig. 3.2 illustrates their control model (absence of drug) framework, where the cell cycle is divided into two stages: $P_1$ = $G_1$ and S, whilst $P_2$ = $G_2$ and M. This is quite different from the work presented in [284–286], where phase 1 does not include the S stage of the cell cycle, with it instead being captured by phase 2. However, the modelling efforts in [284–286] were supported by an experimental technique called FUCCI which was used to calibrate the authors' results. The approach suggested in [284–286] is adopted here, with a view to using a technique like FUCCI to validate the model results in the future.

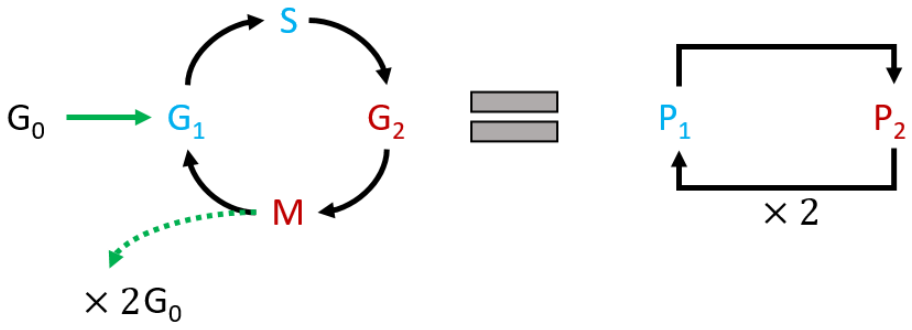


Figure 3.2: Schematic illustrating how the cell cycle is reduced from five phases to two in Roe–Dale *et al.* [242].

Nonetheless, in an attempt to influence current treatment strategies, the authors extended Eqn. 3.1–3.2 to be inclusive of drug. To do so, the authors re–wrote Eqn. 3.1–3.2 in matrix–

vector form:

$$\frac{\mathrm{d}\boldsymbol{P}}{\mathrm{d}t} = \begin{pmatrix} \frac{dP_1}{dt} \\ \frac{dP_2}{dt} \end{pmatrix} = \begin{pmatrix} -\lambda_1 & 2\lambda_2 \\ \lambda_1 & -\lambda_2 \end{pmatrix} \boldsymbol{P}. \tag{3.3}$$

Modelling the effect of two drugs, it was assumed that each would kill cells in $P_1$ and $P_2$ through different mechanisms. As such, treating the cells with the drugs in an alternating order should result in different outcomes, as illustrated by the authors. Further complexity was introduced into their model by accounting for drug resistance. Despite the differences to [284–286], the authors agreed that if the initial distribution of cells differed from one experiment to the next, the outcome may be affected as a result. They concluded that the implementation of such models could provide insight into multi–treatment chemotherapeutic strategies. However, it is clear that the modelling framework would differ when applied to the treatment of ISR, where drugs acts to reduce proliferation over inducing apoptosis through cytotoxic effects.

Other mathematical models have extended the cell cycle to account for all stages of the cell cycle when simulating tumour regression in the presence of drug [294]. As part of a highly nonlinear model, the cytotoxic effects of paclitaxel and 5–fluorouracil were simulated using Monod–type kinetics. The conclusions emphasised the significance of drug diffusion (i.e. release) and the quantification of proliferating cells in culture to enhance the models' predictive capacity. These findings emphasise the rationale for further exploration here, in the context of SMCs, where the administration and effect of drug differ to chemotherapeutic agents, and where controlled drug release is of the utmost importance to ensure optimal patient outcome [79].

Additional cell cycle models also exist in the tumour modelling literature. For example, Del Bene *et al.* [246] published a highly coupled model which emulated the progression of death as the drug induced its cytotoxic effect on the cell population. Simulating the behaviour of many drugs, the authors present their model as a possible tool to further optimize *in vitro* experimental design in the pursuit of optimal drug therapies. Various other articles [242, 247, 248] also consider ODE cell cycle models to illustrate how drug may impact the progression of cells through the cell cycle, with a particular significance on drug resistance, out with the scope of this work.

Finally, an alternative to the traditional cell cycle models has also been proposed, where different cell phenotypes are considered instead of the different stages the cell progresses through when stimulated to divide. This is interesting given that drugs such as sirolimus have been shown to possibly induce cell differentiation back to their dormant phenotype [254, 255]. In the context of cancer, such an approach was considered by Panetta *et al.* [245], where cells were deemed to be either (i) proliferating or (ii) quiescent, in an attempt to better understand how breast cancer progression was hindered following treatment with paclitaxel. Although such models emulating phenotype switching are out with the scope of this work, the authors noted an important result. They detailed the significance of drug retention on cell behaviour, where a simple on/off switch

to describe the effect of drug was inadequate. In stenting applications, Tzafriri *et al.* [79] state the importance of drug retention on inhibiting restenosis, without modelling its effect on the cell population. Although such models failed to capture *in vitro* data in Chapter 2, such models may be essential *in vivo*, where the environment is heterogeneous and less controllable.

Taken together, there has been a clear demand for simulating cell cycle behaviour when assessing the effect of chemotherapeutic agents on tumour regression. Although similar drugs are implemented in the treatment of ISR, the delivery and effect are different. Thus to fully appreciate the efficacy of these cell cycle specific drugs, models that portray the cell cycle and the precise action of such drugs in this context should be considered. Moreover, Vittadello *et al.* [284–286] demonstrated the importance of the initial distribution of cells in the absence of drug. As such, a comparison between mathematical models accounting for SMC cycle behaviour (multi–phase) and those neglecting it (single–phase) are considered, as per the first goal of this chapter. It is then expected that any discrepancies between these models will be further exacerbated when drug is introduced: the second goal of this chapter. Moreover, the models can be further extended to study the importance of attributes more unique to DES. For example, the delivery of drug from stents introduces spatiotemporal gradients of drug within the arterial wall. As such, it is likely that this may further compound the aforementioned issues with the initial distribution of cells throughout the cell cycle and is the final objective to be studied within this chapter; albeit considered within a more simplistic environment.

## 3.2 Methodology: 0D Model

### 3.2.1 Governing model equations

#### 3.2.1.1 Single–phase model

**Control model: no drug**

The single–phase model, which emulates cell proliferation when neglecting cell cycle dynamics, is given as:

$$\frac{\mathrm{d}c(t)}{\mathrm{d}t} = gc(t)\left(1-\frac{c(t)}{K}\right), \quad c(0)=c^0, \tag{3.4}$$

where $c(t)$ is the number of cells at some initial level, $c^0$, the intrinsic growth rate is given as $g$, and $K$ is the carrying capacity. This model is referred to as the control model, where drug is absent.

**Inclusion of drug**

Including the effect of drug, Eqn. 3.4 is altered to:

$$\frac{\mathrm{d}c(t)}{\mathrm{d}t} = gc(t)\left(1-\frac{c(t)}{K}\right)\underbrace{\left(1-\frac{k_{max}\,c_d^*}{c_d^*+1}\right)}_{\text{Drug Interference}}, \quad c_d^* = \frac{c_d}{k_{50}}, \quad c(0)=c^0, \tag{3.5}$$

where the expression governing the effect of drug is denoted by the underbrace, 'Drug Interference'. This follows Michaelis–Menten–like kinetics as discussed in Chapter 2. This expression is responsible for reducing the cell growth rate, where $c_d$ is the free drug concentration, $0 < k_{max} < 1$ details the maximum effect drug has on cell growth, and $k_{50}$ is drug concentration at which the effect of drug is half its maximal value. Note that $c_d$, the free drug concentration, is scaled with $k_{50}$ to give $c_d^*$. This facilitates the application of the model to a variety of different drugs and doses, simultaneously reducing the number of unknown parameters in the model. All model parameters are described in Table 3.1. In all models, unless stated otherwise, the initial number of cells ($c^0$) is assumed to be 10,000 whilst the maximum cell number ($K$) is assumed to be 100,000, in line with values presented in Chapter 2.

#### 3.2.1.2 Multi–phase model

**Control model: no drug**

The model considered here takes inspiration from Vitadello *et al.* [284]. Differently from Vitadello *et al.* [284], who considered an exponential cell growth model, a logistic cell growth model similar to earlier efforts in [285] is considered here to introduce the significance of spatial restrictions on cell proliferation [276]. Thus, the multi–phase model in the absence of drug is:

$$\begin{aligned}
\frac{\mathrm{d}c_1(t)}{\mathrm{d}t} &= 2g_2\,c_2(t)\left(1-\frac{c(t)}{K}\right) - g_1\,c_1(t), &(3.6)\\
\frac{\mathrm{d}c_2(t)}{\mathrm{d}t} &= -g_2\,c_2(t)\left(1-\frac{c(t)}{K}\right) + g_1\,c_1(t), &(3.7)\\
c(0) &= c_1^0 + c_2^0 = c^0,
\end{aligned}$$

where the cell population is divided in two, $c_1(t)$ and $c_2(t)$, referring to the number of cells in phase 1 ($G_0/G_1$) and phase 2 ($S/G_2/M$) of the cell cycle, respectively. The total number of cells, $c(t)$, is given by the addition of $c_1$ and $c_2$ at any time, initially taking the value $c^0$. Additionally, the intrinsic growth rate, $g$, present in the single–phase control model (Eqn. 3.4) is now replaced by $g_1$ and $g_2$, corresponding to the transition rates between the phases of the cell cycle. Eqn. 3.6 refers to the rate of change of cells in phase 1, where the first term on the right–hand side presents the growth of cells entering from phase 2 as they divide (hence the 2), and the second details the decline of cells in phase 1 as they progress through the cell cycle. All

model parameters are described in Table. 3.1.

| Parameter | Description | Unit |
|---|---|---|
| *Cell Related Parameters* | | |
| $c^0$ | Total initial number of cells | no. of cells |
| $c_1^0$ | Initial number of cells in phase 1 | no. of cells |
| $c_2^0$ | Initial number of cells in phase 2 | no. of cells |
| $g$ | Intrinsic growth rate (single–phase) | $\text{day}^{-1}$ |
| $g_1$ | Rate of change of cells from phase 1 to phase 2 | $\text{day}^{-1}$ |
| $g_2$ | Rate of change of cells from phase 2 to phase 1 | $\text{day}^{-1}$ |
| $K$ | Maximum cell number (Carrying capacity) | no. of cells |
| *Drug Related Parameters* | | |
| $c_d$ | Free drug concentration in the media, assumed constant | M |
| $k_{max}$ | Maximum effect drug has on cell growth | - |
| $k_{50}$ | Drug concentration at which the effect ($k_{max}$) is 50% of its maximal value | M |
| $c_d^*$ | Ratio of $c_d/k_{50}$ | - |

Table 3.1: Description of the variables and parameters used throughout the models: Eqn. 3.4–3.11.

**Drug 1, $G_1$/S transition blocker (e.g. sirolimus)**

In this section, drugs which predominantly elicit their effect prior to the first restriction checkpoint ($G_1$/S) are considered (e.g. sirolimus [80]). The following model is proposed to convey the effect of drugs of this type on cell growth:

$$\frac{\mathrm{d}c_1(t)}{\mathrm{d}t} = 2g_2\, c_2(t)\left(1-\frac{c(t)}{K}\right) - g_1\, c_1(t)\underbrace{\left(1-\frac{k_{max}\, c_d^*}{c_d^*+1}\right)}_{\text{Drug Interference}}, \tag{3.8}$$

$$\frac{\mathrm{d}c_2(t)}{\mathrm{d}t} = -g_2\, c_2(t)\left(1-\frac{c(t)}{K}\right) + g_1\, c_1(t)\underbrace{\left(1-\frac{k_{max}\, c_d^*}{c_d^*+1}\right)}_{\text{Drug Interference}}, \tag{3.9}$$

$$c(0) = c_1^0 + c_2^0 = c^0,$$

where drug acts explicitly to reduce the rate at which cells transition from phase 1 ($c_1(t)$) to phase 2 ($c_2(t)$).

**Drug 2, M Blocker (e.g. paclitaxel)**

Now drug 2 is considered, which exerts its effect on cells in phase 2, where the purpose is to

block cell division (M), inducing mitotic arrest. The model is given by:

$$\frac{dc_1(t)}{dt} = 2g_2\, c_2(t)\left(1-\frac{c}{K}\right)\underbrace{\left(1-\frac{k_{max}\, c_d^*}{c_d^*+1}\right)}_{\text{Drug Interference}} - g_1\, c_1(t), \tag{3.10}$$

$$\frac{dc_2(t)}{dt} = g_1\, c_1(t) - g_2\, c_2(t)\left(1-\frac{c}{K}\right)\underbrace{\left(1-\frac{k_{max}\, c_d^*}{c_d^*+1}\right)}_{\text{Drug Interference}}, \tag{3.11}$$

$$c(0) = c_1^0 + c_2^0 = c^0.$$

### 3.2.2 Problem workflow and model syntax

The problem is approached with the aim of comparing the behaviours between models which exclude the cell cycle dynamics (single–phase) and those which emulate the cell cycle dynamics (multi–phase).

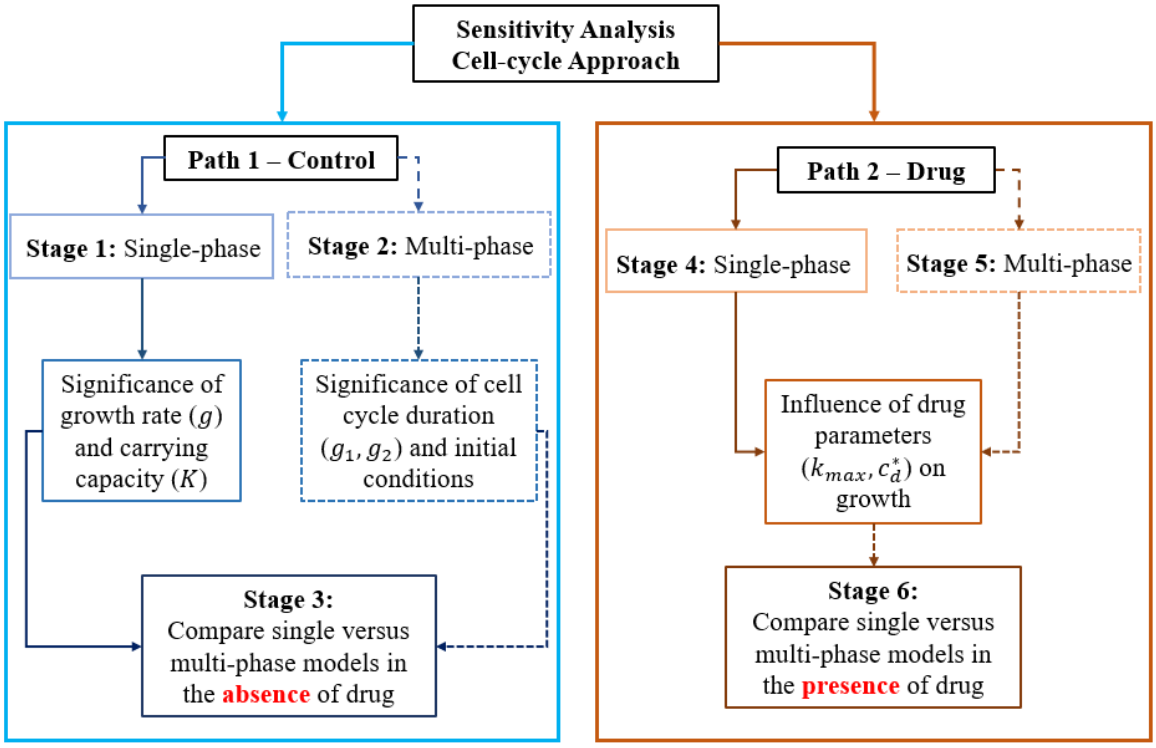


Figure 3.3: Flow chart detailing the problem approach, separated into two distinct paths which looks at models in either the absence (path 1) or presence of drug (path 2).

Fig. 3.3 demonstrates the workflow, where analysis between single and multi–phase models are placed in two distinct paths: (i) path 1: control and (ii) path 2: drug. The former investigates the parameters associated with cell proliferation, investigating the significance of growth rates

and spatial restrictions in the absence of drug. The latter, for a given growth regime, will explore the role of different drug types, assessing their efficacy through perturbations in $k_{max}$ and $c_d^*$. Looking more closely at path 2, Fig. 3.4 illustrates the parameter perturbation regime in the presence of drug for the multi–phase model, detailing the various values considered for $c_d^*$ and $k_{max}$.

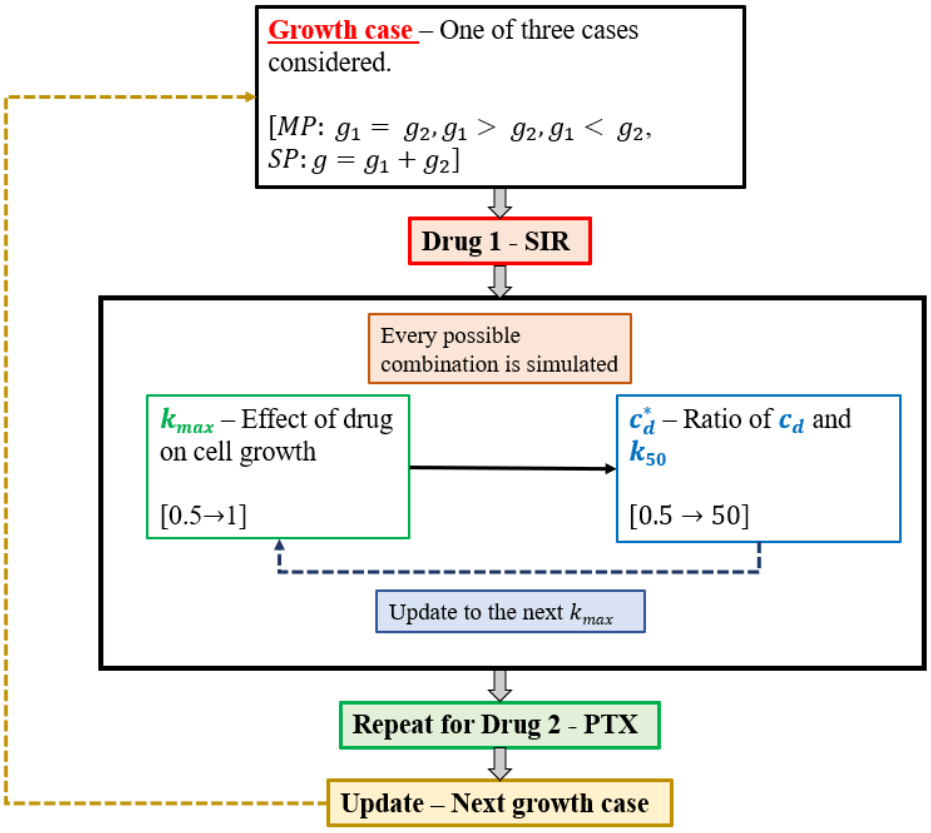


Figure 3.4: Flow chart detailing the sensitivity analysis for path 2, in the presence of drug. A particular growth regime is considered before selecting the drug: drug 1 (sirolimus, SIR) or drug 2 (paclitaxel, PTX). A series of parameter combinations are selected that begin with $k_{max}$ from which a range of $c_d^*$ values are simulated. The $k_{max}$ value is then updated and the process repeated until all combinations considered. Upon the completion of all drug 1 simulations, drug 2 is selected after which the growth regime considered is updated. Single–phase models follow a similar workflow, where for a given growth rate, $g$, the values associated with drug efficacy are perturbed, given that the model does not distinguish between the phase the drug acts in.

The process is then repeated for each drug considered and then again for the various growth regimes (lengths of the cell cycle phases). A similar workflow is adopted for the single–phase model. The value for $g$ is selected such that the turnover is comparable to the timespan of the cell cycle in the multi–phase model. In other words, the timespan details the length of the cell cycle, and the total time taken for both phases of the cell cycle to be completed. In the absence of drug specific parameters, a general sensitivity analysis is considered for all model parameters detailing drug–effectiveness.

A fundamental aspect of the multi–phase model is the choice of initial conditions for each phase. This is explored in depth within this work and thus Table 3.2 summaries the different initial conditions considered, and the syntax used within all plots that feature in the results.

| Label | Description | Number of cell per phase initially |
|---|---|---|
| SP | Single–phase | N/A |
| $MP^1$ | Multi–phase: IC 1 | All cells in phase 1 ($c_1^0 = c^0$) |
| $MP^2$ | Multi–phase: IC 2 | 75:25 split between phase 1 and phase 2 |
| $MP^3$ | Multi–phase: IC 3 | 50:50 split between phase 1 and phase 2 ($c_1^0 = c_2^0 = \frac{c^0}{2}$) |
| $MP^4$ | Multi–phase: IC 4 | 25:75 split between phase 1 and phase 2 |
| $MP^5$ | Multi–phase: IC 5 | All cells in phase 2 initially ($c_2^0 = c^0$) |

Table 3.2: Syntax for the different initial condition (IC) cases considered. Used ubiquitously in all plots within this chapter.

The numerical method employed is the same as that in Chapter 2, where the '*ode15s*' routine in MATLAB (MATLAB 2020a, The MathWorks, Inc., Natwick, MA, USA) was used to numerically integrate the differential equations over a pre–defined timespan.

## 3.3 Results & Discussion: OD Model

### 3.3.1 Path 1 (Control: no drug)

#### 3.3.1.1 Stage 1: single–phase

Considering the single–phase model first, perturbations in its model parameters illustrate behaviour that is expected. As the growth rate is increased, the cells approach the carrying capacity more quickly (Fig. 3.5a). Whereas, increasing $K$ for a fixed growth rate only alters the maximum cell number, not the time taken to reach this maximum (Fig. 3.5b). Results of simulating Eqn. 3.4 demonstrate the characteristic profiles expected from the logistic growth model. This parameter analysis presents a simplistic representation of curtailed growth through a reduction in $g$ (Fig. 3.5a), artificially mimicking the action of an anti–proliferative drug. Whereas perturbations in $K$ symbolise the response of cells in different experimental set–ups.

#### 3.3.1.2 Stage 2: multi–phase

Exploring the multi–phase model in depth, the initial conditions (Table 3.2) and cell cycle growth rates are varied. Table 3.3 summaries the different cases considered with respect to the cells growth rate: ($S2_g^1$) assumes both phases are equal in duration, ($S2_g^2$) assumes that phase 1 is shorter than phase 2, whilst ($S2_g^1$) considers the opposite to (ii).

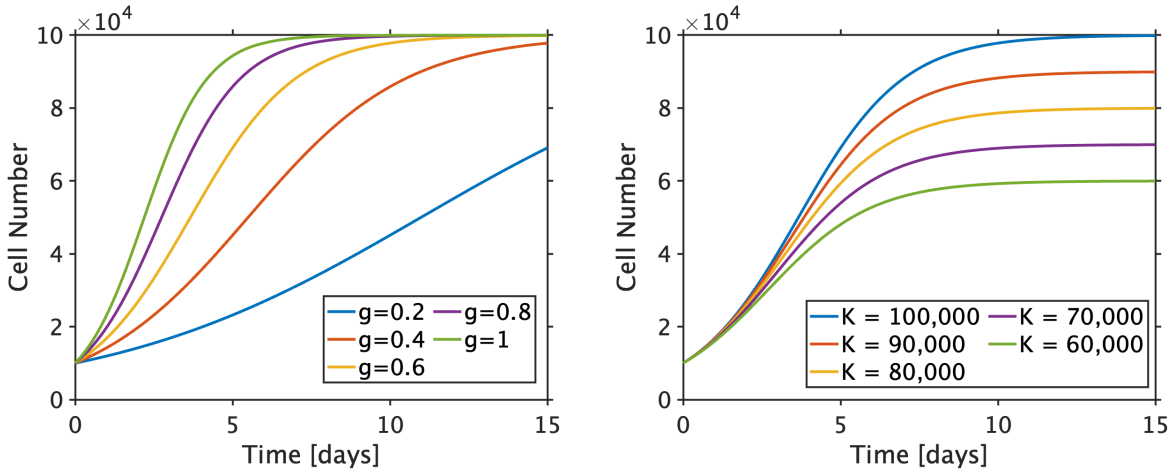


(a) Varying $g$ (b) Varying $K$

Figure 3.5: How perturbations in (a) $g$ and (b) $K$ influences cell proliferation in the single–phase model (Eqn. 3.4) in the absence of drug. In (a) $K$ is fixed to 100,000. In (b) $g$ is fixed to 0.6.

| Label | Case (Rate [ /day]) | Description |
|---|---|---|
| $S2_g^1$ | Case 1: $g_1(0.75) = g_2(0.75)$ | The rates of transition for both phases are equal |
| $S2_g^2$ | Case 2: $g_1(0.9) > g_2(0.6)$ | Phase 1 is shorter than phase 2 |
| $S2_g^3$ | Case 3: $g_1(0.6) < g_2(0.9)$ | Phase 1 is longer than phase 2 |

Table 3.3: Labels and description of each growth rate case considered. Uppercase S2 depicts the stage (2) the analysis is in per the workflow (Fig. 3.3), the superscript separates the different cases (1, 2, or 3) whilst the subscript ($g$) denotes that the analysis is with respect to the growth of cells i.e. cell cycle duration. The values have been arbitrarily selected such that cell growth concludes within 15 days for all cases.

Fig. 3.6a–3.6c illustrates how the cell response varies in time for the different initial conditions simulated. In the absence of drug, the difference between any profile is minimal across the three different cell cycle durations considered. For any given case tested ($S2_g^{1-3}$), the time taken to reach K/2 differs by approximately 1 day between the two extreme initial conditions ($MP^1$ and $MP^5$). The gap between $MP^1$ and $MP^5$ increases in $S2_g^3$, where cells can grow more freely with the inhibition by space (phase 2) reduced in time. In general, the trends presented across all scenarios are as expected such that more cells present in phase 2 initially permits a quicker growth to the maximum number, $K$.

Looking specifically at the variability present between duration of each of the cell cycle phases, Fig. 3.6d shows cell proliferation in time for a given initial condition ($MP^3$, where cells are equally divided between the two phases). Here, $S2_g^2$ gives rise to the slowest growth profile. This is expected since cells spend longer in phase 2, where spatial restrictions are influencing cell proliferation for a increased period of time; approaching the conditions of the single–phase

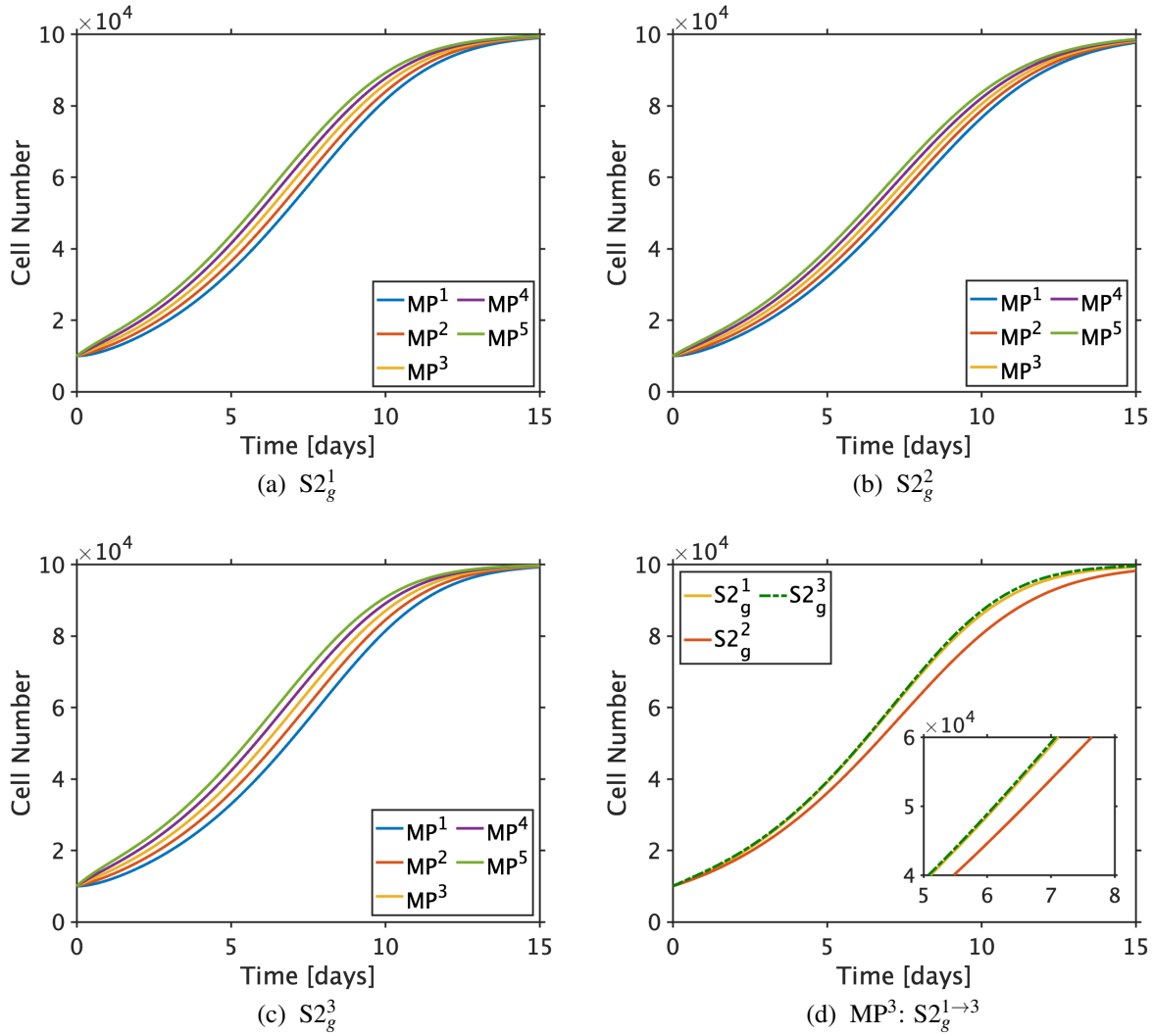


(a) $S2_g^1$ (b) $S2_g^2$

(c) $S2_g^3$ (d) $MP^3$: $S2_g^{1\rightarrow 3}$

Figure 3.6: How the initial conditions ($MP^{1-5}$) and the cell cycle durations influence the proliferative capacity of cells. (a) $S2_g^1$, (b) $S2_g^2$, (c) $S2_g^3$. Plot (d) Compares the three different cell cycle duration cases within one initial condition ($MP^3$). Inset highlights the three responses across a three day (5-8) period.

model, where spatial restrictions are always present.

#### 3.3.1.3 Stage 3: Single versus multi–phase

To explore the similarities and differences present between the singe and multi–phase models, a level of consistency is required. For example, in the single–phase model, an intrinsic growth rate ($g$) is prescribed whilst in the multi–phase model, two transition rates ($g_1, g_2$) are proposed to detail the growth of cells in each phase of the cell cycle. Thus, to ensure the two approaches are comparable, the *time to divide* between the models is set to be consistent, where a variety of different cases are considered (Table 3.4). Two of the four cases ($S3_g^1$ and $S3_g^4$) propose that the two phases of the cell cycle are equal in length, but that the total length of the cell cycle

is different. The other two cases explore the impact of different cell cycle patterns, where the transition rates favour either a longer phase one ($S3_g^2$) or phase two ($S3_g^3$). Estimates for the baseline duration ($S3_g^1$) are acquired from [67], where the duration of each phase is the same, corresponding to an approximate cell turnover of 32 hours. Other cases explore perturbations in these values, assessing the impact when simulated alongside the single–phase model. The intrinsic growth rate ($g$) in the single–phase model was estimated assuming that cells would naturally grow under exponential circumstances ($g = \frac{ln(2)}{Timespan}$). The transition rates were then trivially computed assuming that $g = g_1 + g_2$, according to the splits detailed in Table 3.4.

| Label | Case [Cell duration] | Description |
|---|---|---|
| $S3_g^1$ | Case 1: 50:50 split [32 hours] | Phase 1 and 2 are of equal length (Long time) |
| $S3_g^2$ | Case 2: 70:30 split [32 hours] | Phase 1 is longer than 2 |
| $S3_g^3$ | Case 3: 30:70 split [32 hours] | Phase 1 is shorter than 2 |
| $S3_g^4$ | Case 4: 50:50 split [26 hours] | Phase 1 and 2 are of equal length (Short time) |

Table 3.4: Labels and description of each growth case considered. Uppercase (S3) refers to stage 3 of the workflow (Fig. 3.3), the superscript ($1, 2, 3,$ or $4$) separates the different cases whilst the subscript ($g$) states that the analysis is with respect to the growth of cells i.e. cell cycle duration.

In the absence of drug, across the majority of cases considered, the single and multi–phase models are in broad agreement. In scenarios where the cell cycle length is the same between the two phases (Fig. 3.7a and 3.7d), the single–phase model is comparable to $MP^5$ at early times, and to $MP^1$ at later times, where the overall time to reach capacity is slower. This is because the single–phase model is under constant spatial restrictions. However, at early times, exponential growth is dominant since space is currently not limited, but in time, cells populate the domain and the rate of change decreases beyond the inflection point ($K/2$), hence the slower approach to capacity in the single–phase model.

When the length of each phase differs, the behaviour between the two modelling approaches changes. For a longer phase 2 (Fig. 3.7c), a very similar response is observed between the single and mulit–phase models. When phase 2 is longer, cells are exposed to spatial restrictions for prolonged periods of time, similar to the single–phase model, alluded to in Section 3.3.1.2. On the other hand, when the duration of phase 1 is longer (Fig. 3.7b), growth is notably quicker in the multi–phase modelling approach.

## 3.3.2 Path 2 (Drug)

### 3.3.2.1 Stage 4: Single–phase

Within this section, a sensitivity analysis is considered, investigating the role of cell growth in parallel with drug efficacy across a range of parameter regimes. Table 3.5 details the baseline

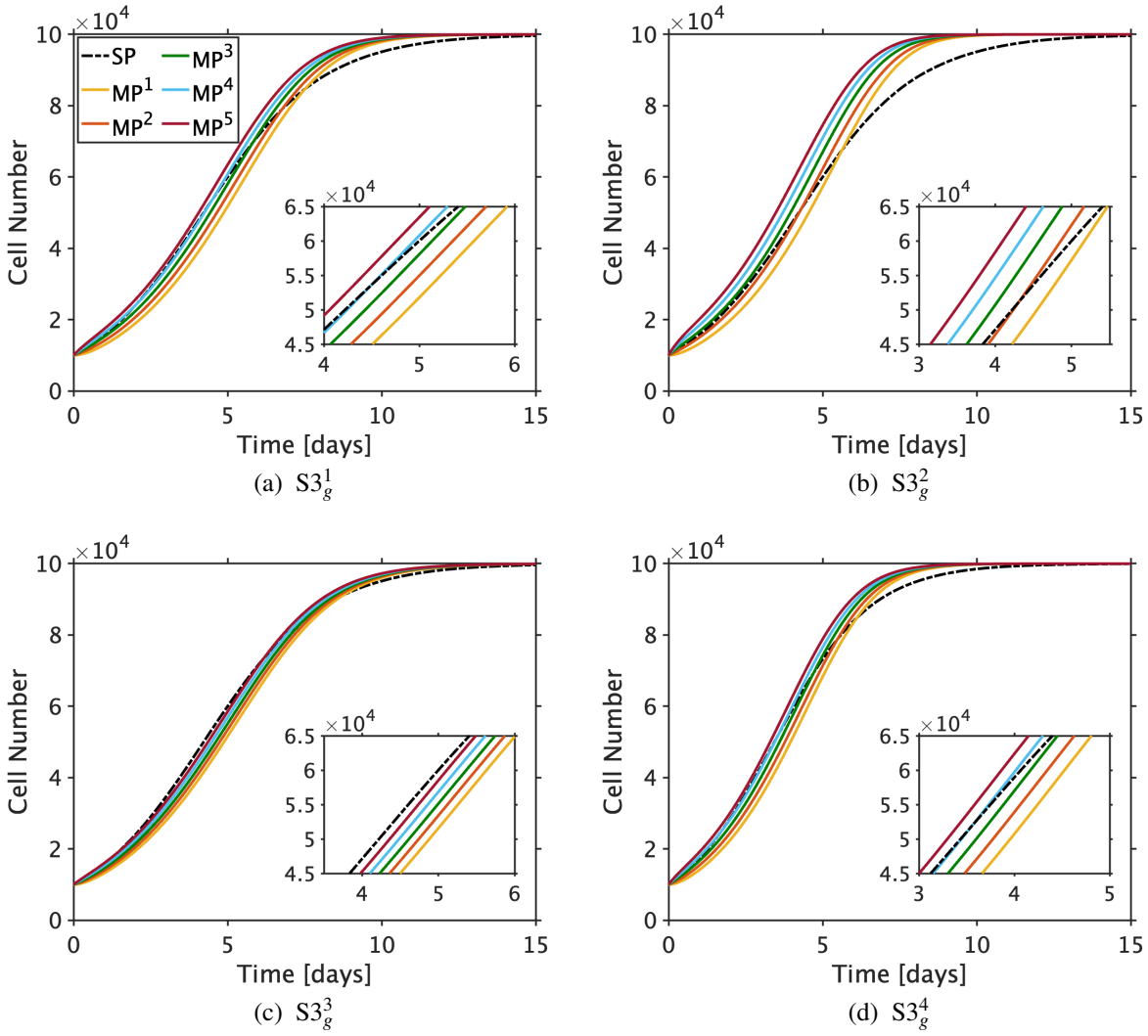


(a) $S3_g^1$ (b) $S3_g^2$

(c) $S3_g^3$ (d) $S3_g^4$

Figure 3.7: How the single (SP) and multi–phase (MP) models compare across a range of different cell duration cases (Table 3.4). (a)–(d): Presentation of the various cases in order from, $S3^{1\to4}$, respectively. All insets highlight the differences present between the initial conditions ($MP^{1\to5}$) within the multi–phase models, and how they compare to the results of the single–phase model around the inflection point of each curve ($K/2$)

values for each parameter present in the model, to which perturbations in each are assessed in turn whilst the others are fixed.

| Parameter | Baseline value [Unit] | Range of variation |
|---|---|---|
| $g$ | 0.6 [day$^{-1}$] | $[0.4 \to 0.8]$ |
| $c_d^*$ | 5 | $[0.5 \to 50]$ |
| $k_{max}$ | 0.75 | $[0.5 \to 1]$ |

Table 3.5: The baseline and range of values considered for each parameter within the single–phase drug model (Eqn. 3.5).

Observing the results, Fig. 3.8a demonstrates how an increased growth rate promotes a more prompt recovery in cell proliferation, under the assumption that both the growth serum and drug are applied constantly. The result of perturbations to $k_{max}$ is depicted in Fig. 3.8b, where an increase in its value notably curtails cell growth. However, as this value approaches zero, a behaviour similar to cell growth in the absence of drug is observed, where the Eqn. 3.5 would naturally return the logistic growth model (Eqn. 3.4). Fig. 3.8c highlights the impact of perturbations in $c_d^*$ on cell growth; previously defined as the ratio of $c_d/k_{50}$. Thus, as this ratio increases, referring to either a higher drug dose or lower $k_{50}$ value, cells exhibit a reduction in their proliferative capacity. Although free drug is considered, and binding kinetics are neglected, it is noted that the results of the model theoretically approach an upper limit. In other words, when $c_d >> k_{50}$, then negligible differences in cell behaviour are apparent.

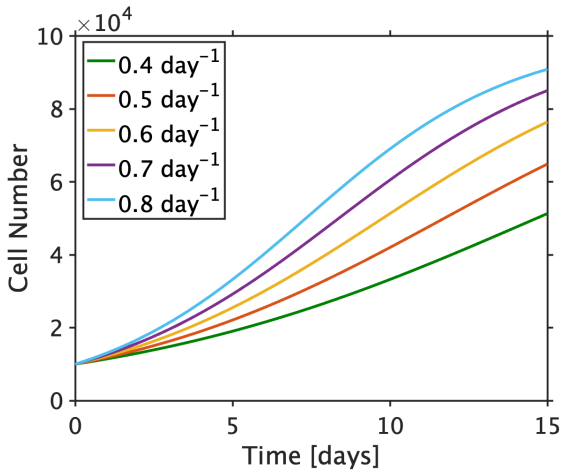


(a) Varying $g$

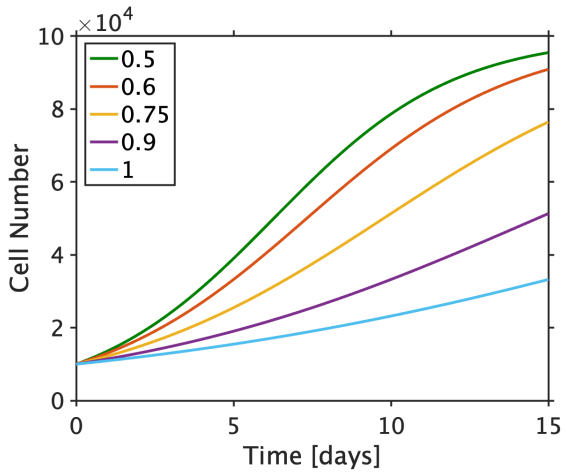


(b) Varying $k_{max}$

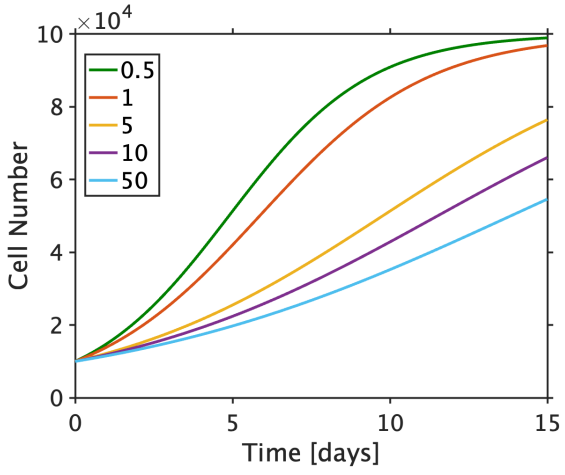


(c) Varying $c_d^*$

Figure 3.8: How perturbations to a variety of parameters (Table. 3.5) influence cell proliferation following continuous drug exposure. Variations in the following paramaters are considered: (a) $g$, (b) $c_d^*$, and (c) $k_{max}$.

Exploring this concept in more depth, a generalised response is presented in Fig. 3.9a, which illustrates how the effect of drug varies as $c_d^*$ is increased. Clearly, as the ratio $c_d^*$ is increased, the drug becomes more efficacious. However, beyond some value, the effect of drug on cell growth plateaus, highlighted at high values of $c_d^*$ which corresponds to when $c_d >> k_{50}$. Looking more closely at the response in Fig. 3.9a, the change in the value on the vertical axis (effect of drug) is approximately 8% from $c_d^*$ = 10 to 50 (effect of drug from 0.9091 to 0.9755). Thus, with approximately 90% of the response captured between $0 < c_d^* \leq 10$ (Fig. 3.9b), it can be assumed that $c_d^* \geq 10$ refers to $c_d >> k_{50}$. Moreover, when $k_{max}$ is reduced, a linear shift in the effect of drug is noted (Fig. 3.9c).

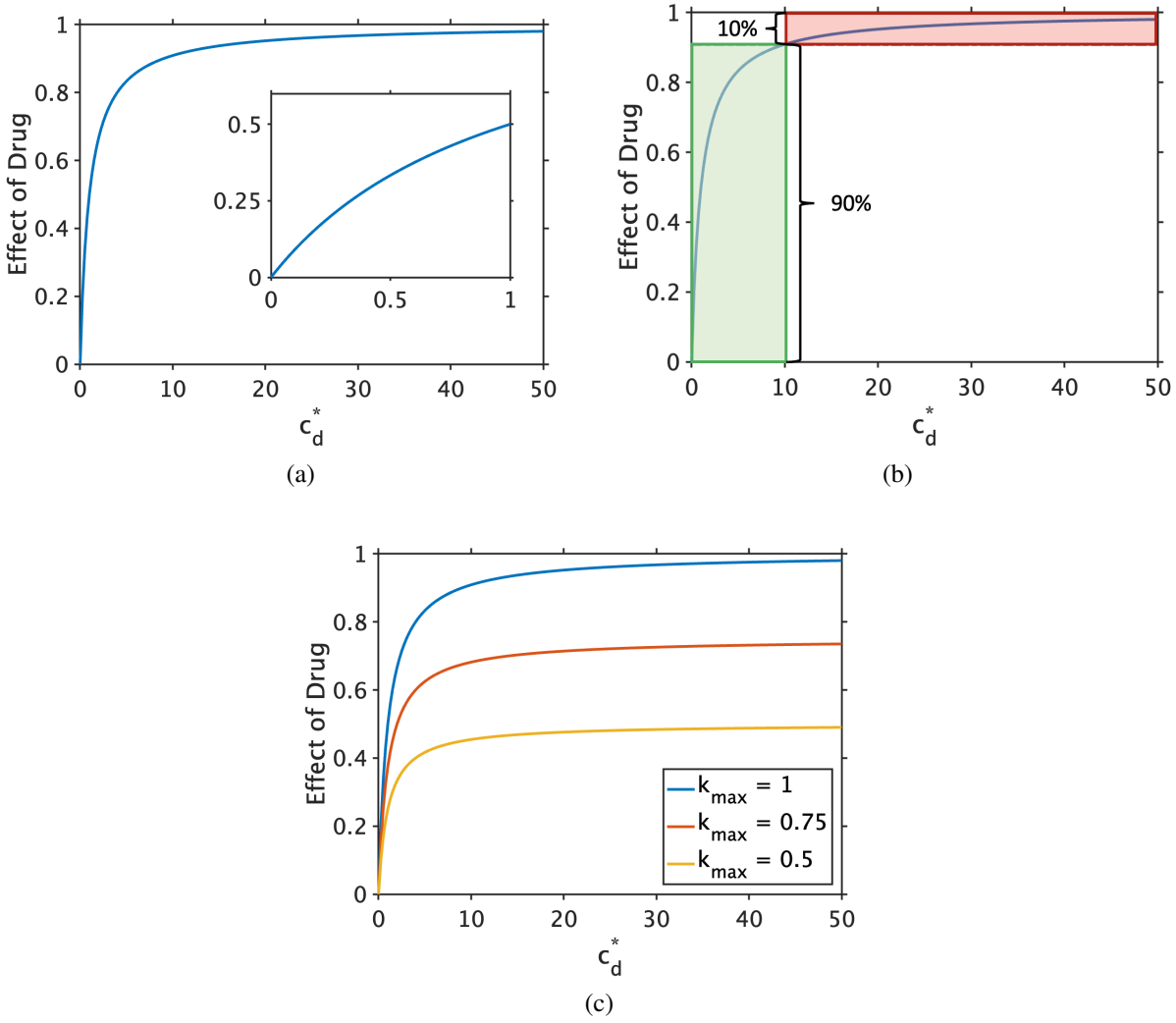


Figure 3.9: (a) Generic response of $\frac{k_{max}c_d^*}{c_d^*+1}$ to establish how perturbations in $c_d^*$ may influence cell proliferation following exposure to drug. $c_d^*$ is the ratio of $c_d/k_{50}$. *Inset:* Highlights the behaviour at lower values of $c_d^*$. (b) % of vertical axis covered by the range of $c_d^*$ simulated, denoted by the rectangular boxes. (c) How reducing $k_{max}$ influences the effect of drug.

Examining the model further, contour maps are generated which illustrate the number of

cells after 15 days for 121 different parameter combinations (Fig. 3.10), where the horizontal ($k_{max}$) and vertical ($c_d^*$) axes are consistent throughout.

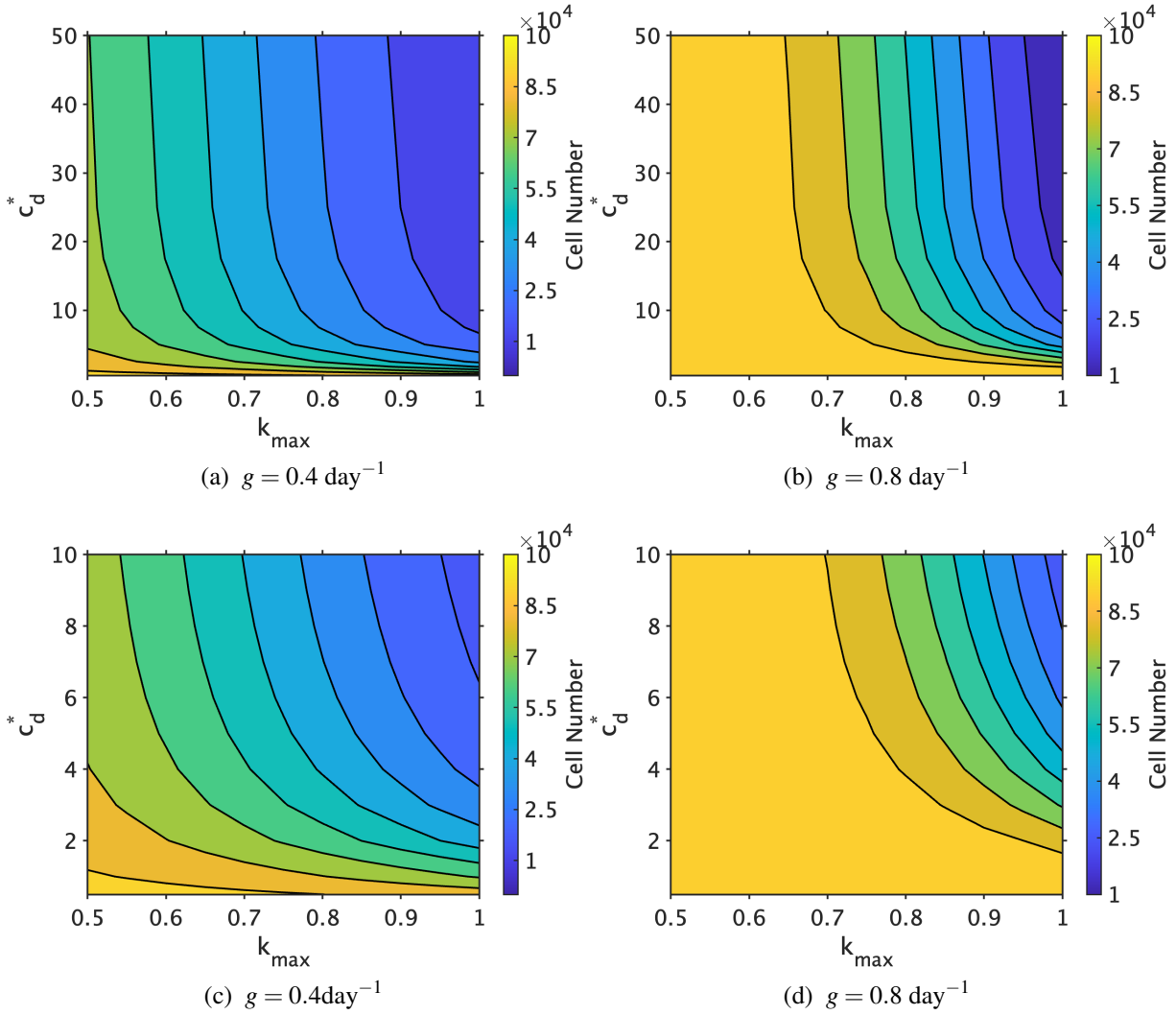


Figure 3.10: Contour maps detailing how various parameter combinations of $k_{max}$ and $c_d^*$ influence number of cells after 15 days for (a,c) g = 0.4 day$^{-1}$ and (b,c) g = 0.8 day$^{-1}$. Top row (a,b) looks at the full range ($0 < c_d^* \leq 50$) of $c_d^*$, whilst the bottom row (c,d) look at shorter range ($0 < c_d^* \leq 10$).

Fig. 3.10 clearly demonstrates the significance of all model parameters across a large range of values. Firstly, comparing Fig. 3.10a ($g = 0.4$) and 3.10b ($g = 0.8$) directly, which considers the full range of $c_d^*$, it is clear that cells are allowed to grow more quickly as a result of $g$ being higher, particularly when drug is less efficacious (low $k_{max}$ and $c_d^*$). In both plots, the choice of $k_{max}$ becomes important when $c_d^*$ is large, emphasised in Fig. 3.10b, where cell response is similar across all $k_{max}$ values when $c_d^*$ is low. This is further emphasised in Fig. 3.10c and Fig. 3.10d, where the range of $c_d^*$ considered is smaller. Moreover, it clear from Fig. 3.10b and 3.10d that in cases where cell growth is quick, the dose of drug is insignificant when $k_{max}$ is low, for

the 15–day period considered.

Within this simpler, single–phase model, a wide exploration into the parameter values present has been considered. It is clear that perturbations in not only cell growth ($g$), but also drug dependent parameters ($k_{max}$, $c_d$ and $k_{50}$) can result in a variety of different behaviours. As such, by visualising the model results through contour plots, one can identify the parameter space that achieves the primary goal of the drug: to minimise cell proliferation. This is particularly evident in Fig. 3.10d, where a large range of parameters do not achieve this goal, and cells approach their capacity (yellow area). However, the upper right corner illustrates the small range of parameters that do notably inhibit cell proliferation (blue area). Therefore, manufacturers designing novel drugs to combat cell proliferation could use such tools as a measure of identifying which drugs achieve their intended goal. This application can be extended to the multi–phase model, where the explicit action of cell cycle specific drugs can be simulated, and the action of drug is more precise.

#### 3.3.2.2 Stage 5: Multi–phase

**Drug 1, $G_1$/S transition blocker (e.g. sirolimus)**

Fig. 3.11 demonstrates the effect of drug 1 (Eqn. 3.8 & 3.9) on cell proliferation. The left–hand column illustrates simulation results assuming an initial condition of $MP^1$ (all cells initially in phase 1) whilst the figures on the right–hand side present the opposing extreme, $MP^5$ (all cells initially in phase 2). The first row (a, b) corresponds to the model results for the full range of $c_d^*$, whilst the bottom row (c, d) reduces the range ($0 < c_d^* < 10$).

Firstly, comparing tiles adjacent to one another (left versus right or $MP^1$ versus $MP^5$), it is apparent that for any $c_d^*$, the response differs when the opposing initial conditions are simulated. When drug elicits a more potent response, (high $c_d^*$ and high $k_{max}$) the difference between the initial condition cases ($MP^1$ and $MP^5$) increases, where fewer cells are present in the former, emphasised by the larger deep blue colours at the top right corner of each contour map. As to why, with drug 1 eliciting its effect at the transition point between phase 1 and 2, those cells already in phase 2 at the time of drug exposure are likely to complete their cycle and divide, before succumbing to the effects of drug. Lowering the range of $c_d^*$ (Fig. 3.11c & 3.11d) it is clear that when $c_d^*$ is high, the value of $k_{max}$ is more significant.

Looking at parameter pairs explicitly (Table 3.6), as highlighted by the different coloured markers in Fig. 3.11a–3.11b, results show that the difference in cell proliferation is most significant when the drug is most efficacious, as expected. As the drug decreases in effectiveness (Point 4: [0.6, 1]), cell behaviour tends towards its control response, where drug is absent ($c_d^* = 0$), and the percentage difference between initial conditions is notably decreased. Fig. 3.12 presents the quantitative results from Table 3.6, whilst simultaneously showing the time taken for the cell population to reach the inflection point ($K/2$); an alternative measure to highlight the differences

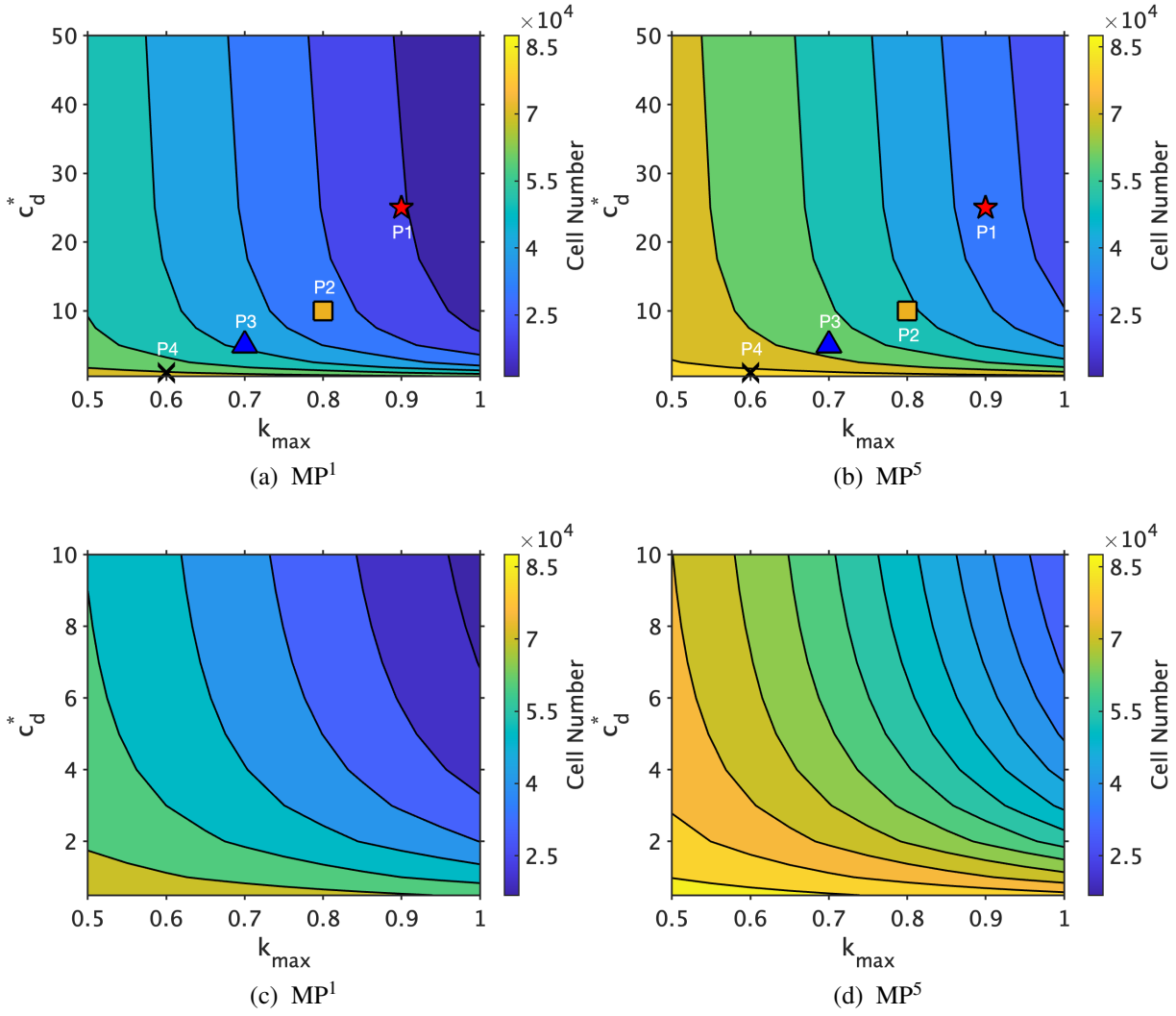


Figure 3.11: Contour maps for 121 parameter combinations of $k_{max}$ and $c_d^*$ when the action of drug 1 is considered. The first row (a,b) portrays the full range of $c_d^*$ whilst the bottom row (c,d) considers a shorter range. The left column (a,c) are the response for $MP^1$ (all cells initially in phase 1) and the right column (b,d) presents the response for $MP^5$ (all cells initially in phase 2). Markers (P1: Red star, P2: Yellow square, P3: Blue triangle, and P4: Black cross) in (a) and (b) denote parameter pairs (P) considered for subsequent analysis, as noted in Table 3.6.

between $MP^1$ and $MP^5$ across the various parameter combinations.

The results further emphasise the significance of the initial number of cells per phase within an *in vitro* setting, where drugs of type 1 inhibit cell proliferation. For example, when drug is very potent (Point 1: [0.9, 25]), the difference in the time taken to reach the inflection point is approximately 5.2 days between the two initial conditions. However, this notably decreases as the drug becomes less efficacious (Fig. 3.12).

A final interesting aspect to study is the effect of drug when the length of the cell cycle varies (Fig. 3.13), and in particular the time spent within each phase of the cell cycle. Although an approximate length for the cycle of SMCs is documented, deviations are known to exist [67].

Drug 1: Difference in number of cells ($c$) after 7.5 days

| Co–ordinate $[k_{max}, c_d^*]$ | $c$: MP$^1$ | $c$: MP$^5$ | % Difference: $\left(1 - \frac{c\text{: MP}^1}{c\text{: MP}^5}\right) \times 100$ |
|---|---|---|---|
| Point 1 (P1): [0.9, 25] | $2.06\times10^4$ | $3.547\times10^4$ | 41.9 |
| Point 2 (P2): [0.8, 10] | $3.382\times10^4$ | $5.143\times10^4$ | 34.2 |
| Point 3 (P3): [0.7, 5] | $4.807\times10^4$ | $6.55\times10^4$ | 26.6 |
| Point 4 (P4) : [0.6, 1] | $7.084\times10^4$ | $8.3\times10^4$ | 14.7 |

Drug 2: Difference in number of cells ($c$) after 7.5 days

| Co–ordinate $[k_{max}, c_d^*]$ | $c$: MP$^1$ | $c$: MP$^5$ | % Difference: $\left(1 - \frac{c\text{: MP}^1}{c\text{: MP}^5}\right) \times 100$ |
|---|---|---|---|
| Point 1 (P1): [0.9, 25] | $1.946\times10^4$ | $2.119\times10^4$ | 8.2 |
| Point 2 (P2): [0.8, 10] | $3.105\times10^4$ | $3.523\times10^4$ | 11.9 |
| Point 3 (P3): [0.7, 5] | $4.392\times10^4$ | $5.055\times10^4$ | 13.1 |
| Point 4 (P4): [0.6, 1] | $6.723\times10^4$ | $7.593\times10^4$ | 11.5 |

Table 3.6: Number of cells for two cases MP$^1$ (all cells initially in phase 1) and MP$^5$ (all cells initially in phase 2) at a series of different co-ordinates, highlighted in Fig. 3.11. Thus, $c$ : MP refers to the number of cells at 7.5 days for that initial condition: MP$^1$ or MP$^5$. Cell duration is S3$_g^1$, where phases are equal in length with both drugs 1 and 2 inhibiting cell growth. The location of all parameter pairs (P) are highlighted in Fig. 3.11a–3.11b: P1: Red star, P2: Yellow square, P3: Blue triangle, and P4: Black cross.

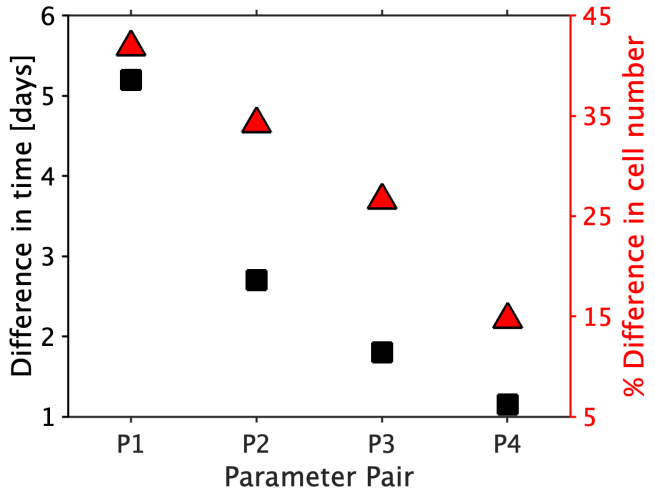


Figure 3.12: The significance of cell initial condition (MP$^1$ and MP$^5$) across different parameter pairs listed in Table 3.6. Left–hand axes: Difference in time taken for each initial condition to reach $K/2$. Right–hand axes: % Difference in number of cells between the initial condition cases after 7.5 days. Symbol colours refer to the matching coloured y–axes: black squares correspond to left–hand axes, whilst red triangle to the right–hand axes.

Adopting the different phase lengths detailed in Table 3.4 (S3$_g^1$–S3$_g^3$), the difference in model response is observed assuming drug efficacy is defined by Point 1 [0.9, 25] (Table 3.6). As

expected, cells which exist in phase 1 for the majority of their cell cycle are more notably inhibited by drugs of type 1. On the other hand, when phase 2 occupies the majority of a cells life, drug performance is at its poorest. Moreover, looking at the time taken to reach the inflection point ($K/2$), the difference between $MP^1$ and $MP^5$ is smallest (at approximately 3.3 days) when phase 2 is longest. When phase lengths are equivalent, the time taken to reach $K/2$ is approximately 5.2 days, increasing even more to 7.2 days, when phase 1 is longer than phase 2. As is shown from Fig. 3.12, the discrepancy between the two initial conditions will diminish as the drug becomes less effective (i.e. lower $c_d^*$ and/or lower $k_{max}$) across the different growth cases tested.

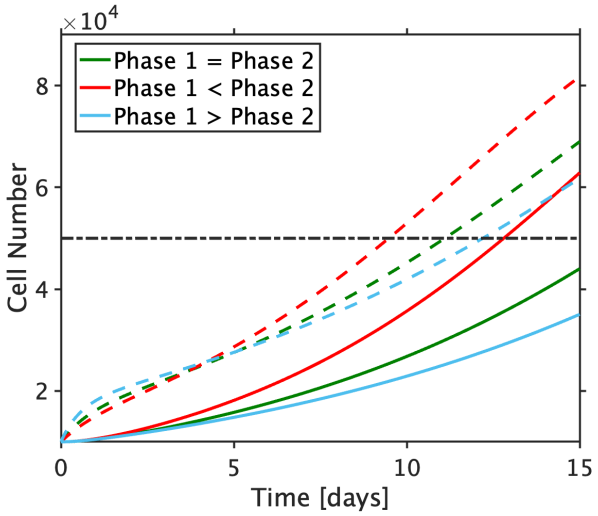


Figure 3.13: How the number of cells change in time when phase lengths differ for a single parameter co–ordinate pair, Point 1 (Table 3.6) assuming the action of drug 1. Solid lines refer to $MP^1$ (all cells initially in phase 1), and dashed lines to $MP^5$ (all cells initially in phase 2). The black dashed horizontal line corresponds to $K/2$.

In summary, it is apparent that the distribution of cells across each phase initially is critical in determining the efficacy of drugs of type 1 that block cell cycle progression at the $G_1$/S checkpoint. Additionally, the intrinsic cell cycle length has been shown to be important when exploring drug efficacy, particularly when drugs elicit their action with cell cycle specificity in mind.

**Drug 2, M Blocker (e.g. paclitaxel)**

With drug 2 (e.g paclitaxel) eliciting its action at a different location within the cell cycle, an investigation into the various parameter regimes are considered once again; with results presented in Fig. 3.14. The results demonstrate that perturbations in parameter values present less significant changes across the two initial condition cases ($MP^1$ and $MP^5$) compared with drug 1. The smaller difference between the two initial conditions is a consequence of cells in the second

phase experiencing both a reduction in growth due to spatial restrictions and as a result of drug. Additionally, when cells all exist in phase 2 initially, drug blocks proliferation before cells can divide, which is not the case when drug 1 is considered, where cells complete their cycle, divide and are then inhibited by drug as new daughter cells.

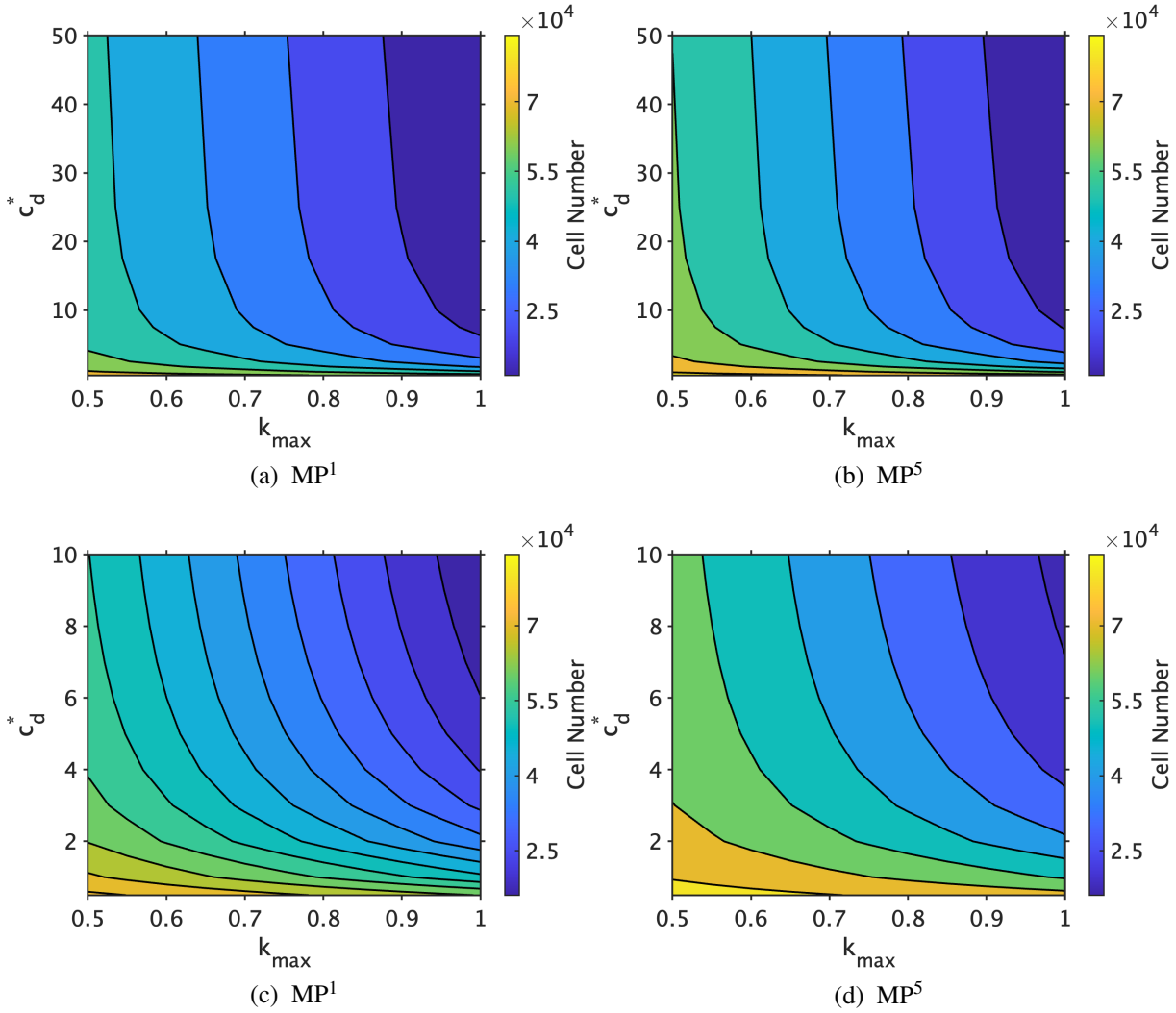


Figure 3.14: Contour maps for 121 parameter combinations of $k_{max}$ and $c_d^*$ when the action of drug 2 is considered. The first row (a,b) portray the full range of $c_d^*$ whilst the bottom row (c,d) considers a shorter range. The left column (a,c) are the responses for $MP^1$ (all cells initially in phase 1) and the right column (b,d) presents the responses for $MP^5$ (all cells initially in phase 2).

Exploring cell inhibition in more depth for drug 2, the parameter pairs in Table 3.6 are considered once again. Clearly, across all four drug parameter combinations, the number of cells in each phase is lower when drug 2 is considered over drug 1. This is emphasised in Fig. 3.14 where larger deep blue regions $(1–2.5)\times10^4$ are present for both initial conditions simulated. Moreover, the more potent the drug (higher $c_d^*$ or $k_{max}$) the smaller the difference

between the two phases for drug 2, contrary to what is observed with drug 1. The reason for this is because cells already present in phase 2 can divide prior to succumbing to the effect of drug 1, whereas regardless of the initial distribution of cells within each phase, drug 2 will elicit its inhibitory effect prior to any cell division. Although the % difference in the number of cells increases as drug 2 becomes less potent (Table 3.6) there are exceptions to the rule (Point 4: [0.6, 1]). This is simply because cells have grown significantly over the 15 days, and inhibition of growth reoccurs through logistic growth.

Moreover, when exploring the significance of the intrinsic cell cycle length, it is apparent that when phase 1 is longest, cells proliferate more quickly, whilst cell proliferation is significantly inhibited when phase 2 is longer than phase 1 (Fig. 3.15); opposing the trends present when cells are exposed to drug 1. This is expected, since drug 2 now elicits its effect in phase 2, so a prolonged duration would allow more time for the drug to act. The results generally show that the inhibition of cell growth is more substantial when drug 2 is considered over drug 1, for the same set of efficacy parameters.

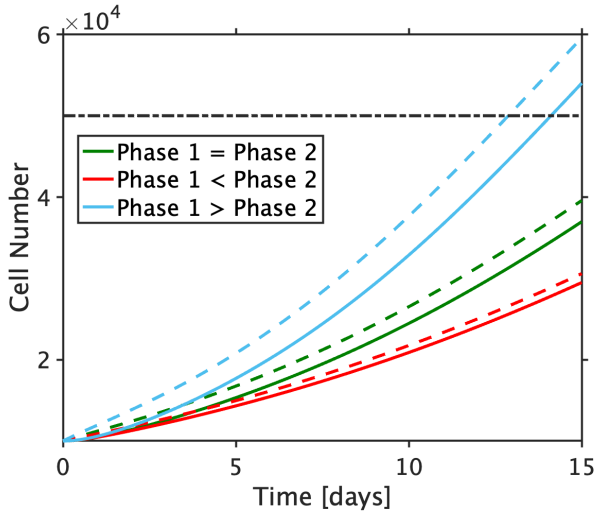


Figure 3.15: How the number of cells changes in time when phase lengths differ for a single parameter case, Point 1 (Table 3.6) assuming the action of drug 2. Solid lines refer to $MP^1$ (all cells initially in phase 1), and dashed lines to $MP^5$ (all cells initially in phase 1). The black dashed horizontal line corresponds to $K/2$.

## Drug 1 vs. Drug 2

Results have highlighted that clear differences are present between the effectiveness of drug 1 and 2, with the latter more profoundly halting cell growth for a fixed set of efficacy parameters. This was emphasised through quantitative analysis of the contour maps (Table 3.6), where the number of cells was lower following exposure to drug 2 across all parameter co–ordinates. Another significant difference between the two drugs is the discrepancy between the two initial

conditions, $MP^1$ and $MP^5$, across all parameter pairs, which is a consequence of drug 2 inhibiting all cells, regardless of their initial phase prior to division. Whereas, drug 1 will allow cells initially residing in phase 2 ($MP^5$) to divide before impeding further cell growth. As a consequence, the difference between the two initial conditions ($MP^1$ and $MP^5$) increases for drug 1 as it becomes more potent, with the opposite trends present for drug 2. This is emphasised in Fig. 3.16, where the % difference in the number of cells at 7.5 days (Fig. 3.16a) between the two initial conditions and the time taken to reach $K/2$ (Fig. 3.16b) is examined, assuming the duration of the cell cycle is equally split between the two phases (32 hours total: 16 hours per phase).

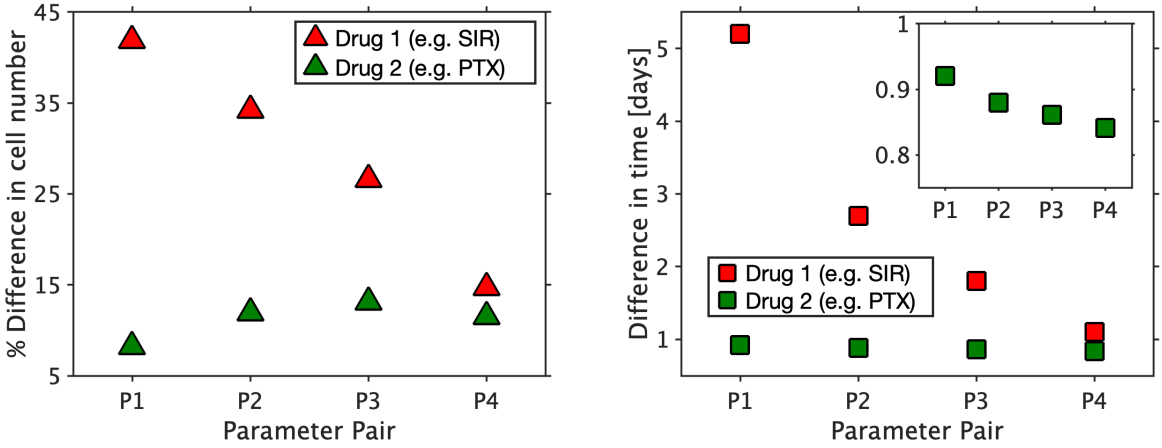


Figure 3.16: The difference between $MP^1$ and $MP^5$ across both drug types, investigating the difference in: (a) % difference in the number of cells at 7.5 days (contour maps), and (b) time taken, in days, for each case to reach the inflection point ($K/2$) , and *Inset:* Highlights a slight declining trend for drug 2.

Fig 3.16a displays the results of Table 3.6 graphically, clearly depicting the difference between $MP^1$ and $MP^5$ for drug 1 and 2. This is further emphasised in Fig. 3.16b, where the difference in time taken for both initial condition cases to reach the inflection point is significantly longer for drug 1, particularly when drug is more efficacious. However, for drugs of type 2, there is a minimal difference between each case, with a slight declining trend present (highlighted by the inset). Moreover, for both types of drug, as they become less efficacious (P4), then spatial restrictions also impede cell growth after the inflection point is passed. This will act in parallel with drug, where both will delay cell growth. Hence, this results in the % difference in the number of cells across the two initial conditions being smaller at Point 4 for drug 2 than that at point 3 (Fig. 3.16a), breaking the established trend.

Investigating the intrinsic duration of each phase within the cell cycle, it is noted that the inhibition of cell growth is more profound following exposure to drug 1 when phase 1 is longer.

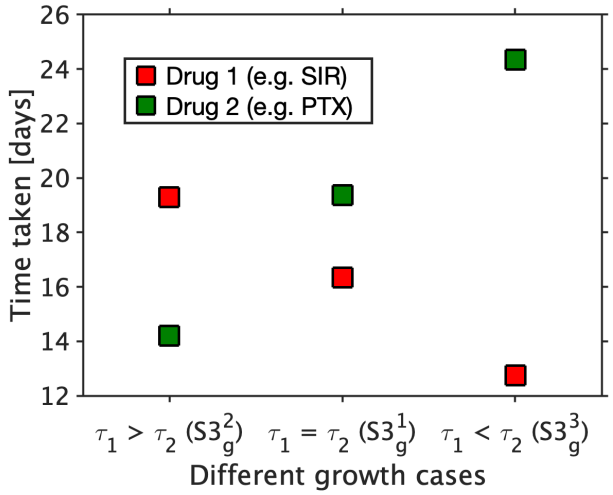


Figure 3.17: The time taken for $MP^1$ to reach the inflection point for each growth case considered (Table 3.4), where $\tau_x$ defines a given phase, where $x = 1$ or 2, for phase 1 and 2, respectively. Drug efficacy case Point 1 ([0.9, 25]) is considered (Table 3.6).

Whereas a longer phase 2 inhibits cell growth more notably when drug 2 is considered. This is emphasised in Fig. 3.17 which summarises the effect of phase length across the two different drug types assuming Point 1 (Table 3.6), by plotting the time taken for $MP^1$ (all cells initially reside in phase 1) to pass the inflection point.

#### 3.3.2.3 Stage 6: Single–phase versus multi–phase model

In the absence of drug, generally the single–phase model presents a slower approach to capacity ($K$) across all growth regimes tested (Fig. 3.7). Now, following the inclusion of drug, the difference in response between the models, differing by drug type and initial condition is compared (Fig. 3.18).

The results illustrate that for all parameter co–ordinate pairs (Table 3.6), the inhibition of cell proliferation is most profound in the single–phase (SP) model. Moreover, results again clearly demonstrate that exposure to drug 2, for the same efficacy parameters, is more inhibitory than that of drug 1. In both initial condition cases $MP^1$ (Fig. 3.18a) and $MP^5$ (Fig. 3.18b), as the drug becomes less efficacious (Point 4: P4) then all models converge to a similar result, where the time taken to reach the inflection point is negligible.

Thus, these modelling efforts demonstrate a clear difference between multi and single–phase models in the presence of drug, particularly when drug efficacy is high. Moreover, the difference in drug performance is also present between the two different drug types, which act to either block cell progression (drug 1) or cell division (drug 2). This is further mediated by the initial distribution of cells throughout the cell cycle. These results provide justification to employ experimental techniques (e.g. FUCCI) that can calibrate and validate these models. This would

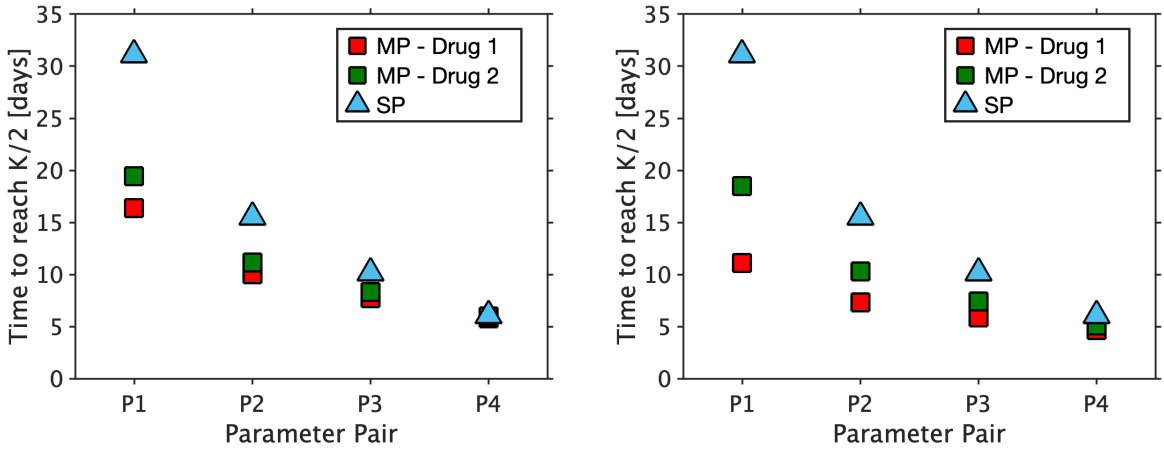


Figure 3.18: The time taken to reach $K/2$ for MP (multi–phase) drug 1 and 2 and SP (single–phase) models. (a) MP simulations adopt $MP^1$ (all cells initially in phase 1) as the initial condition. (b) MP simulations adopt $MP^5$ (all cells initially in phase 2) as the initial condition.

be to able to assess whether models accounting for cell cycle dynamics may be more predictive than those which do not, detailed in Chapter 2.

Although the results here highlight the significance of anti–proliferative drug on inhibiting cell proliferation when accounting for cell cycle dynamics, the drug is uniformly exposed to cells. However, *in vivo*, ISR is treated through the delivery of drug. In order to bridge this gap, it would be of interest to explore spatiotemporal models, making comparisons with 0D models. This is explored in more depth in Section 3.4.

## 3.4 Methodology: 1D Model

### 3.4.1 Motivation: Why the extension?

Firstly, prior to highlighting the methodology, it is necessary to further emphasise the motivation for this increase in model dimensionality. Simply, its purpose is to examine the role of cell cycle specific drugs on cell proliferation, where spatial gradients of drug are now introduced by means of drug delivery. Following stent deployment, it is known that a heterogeneous proliferation and migration of cells exist. The release of drug from the stent introduces a spatiotemporal gradient that further heightens this heterogeneity, and it is highly likely that cells within the arterial wall will exist at different stages of the cell cycle from their neighbours. In other words, the heterogeneous nature of the cell population, coupled with the spatiotemporal delivery of drug then implies that the effectiveness of the drug on a given cell will be different, depending on cell location within the arterial wall.

However, prior to exploring this phenomenon within a sophisticated *in vivo* model, it is sensible to first explore this behaviour within an *in vitro* model which can be fully controlled experimentally. As such, the model proposed emulates a simplistic 3D experimental set–up inclusive of one cell type (SMCs) that has been reduced to 1D for mathematical simplicity (Fig. 3.19); justified in subsequent sections.

### 3.4.2 Computational model

To explore the role of spatiotemporal drug gradients on cell proliferation within a multi–phase model, a simplistic 1D geometry is proposed, mimicking a prospective *in vitro* experimental set up (Fig. 3.19). A polymeric insert of some thickness (e.g. 20 $\mu$m) will be appended to the culture plate where cells reside. Drug will then be released from the coating, with the impact on cell proliferation assessed. Fig. 3.19 presents a 2D top–down view of the proposed 3D device, which dimensionally emulates a single well from a 24–well plate, with the geometry and dimensions amended accordingly to permit the addition of a polymeric insert. It is assumed that the depth of the fluid is equivalent to height of the polymer insert. Therefore, the symmetry in the set–up allows for cell behaviour to be explored in 1D, simplifying the problem. The proposed set–up is inspired by [52], where the aim there was to assess impedance of different cell lines.

The role of drug on inhibiting cell proliferation is modelled in the same way as in Section 3.2.1, however, the drug concentration ($c_d$) is now a variable in space and time ($c_d\ (x,t)$). As per the set–up (Fig. 3.19), drug initially resides on a polymer coated insert. Assuming the release of drug from this coating is a diffusion driven process, then:

$$\frac{\partial c_p(x,t)}{\partial t} = D_p \nabla^2 c_p(x,t), \quad c_p(x,0) = c_p^0, \quad 0 < x < x_p, \quad t > 0, \tag{3.12}$$

where $c_p(x,t)$ is the concentration of drug on the polymer coating, initially taking the constant value $c_p^0$. Upon leaving the coating, drug enters the domain where cells reside. To facilitate this a continuity of flux and concentration is assumed at the boundary, $\Gamma_I$, between the coating ($\Omega_p$) and the cells ($\Omega_c$). Neglecting the process of binding, it is assumed that drug transport within the culture is a diffusion dominated process:

$$\frac{\partial c_d(x,t)}{\partial t} = D_{c_d} \nabla^2 c_d(x,t), \quad c_d(x,0) = 0, \quad x_p < x < x_c + x_p, \quad t > 0, \tag{3.13}$$

where $D_{c_d}$ describes the diffusion of free drug, $c_d(x,t)$. Initially, the concentration of drug present in the cell domain is zero.

The migration of cells is ignored with the emphasis placed on proliferation in culture, as was

true for the 0D model. As such, the equation describing the effectiveness of drug is:

$$\frac{dc(x,t)}{dt} = gc(x,t)\left(1-\frac{c(x,t)}{K}\right)\left(1-\frac{k_{max}\,c_d(x,t)}{c_d(x,t)+k_{50}}\right), \quad c(0)=c^0, \quad x_p < x < x_p + x_c, \quad t>0, \tag{3.14}$$

with $c_d(x,t)$ now a variable, as opposed to a constant.

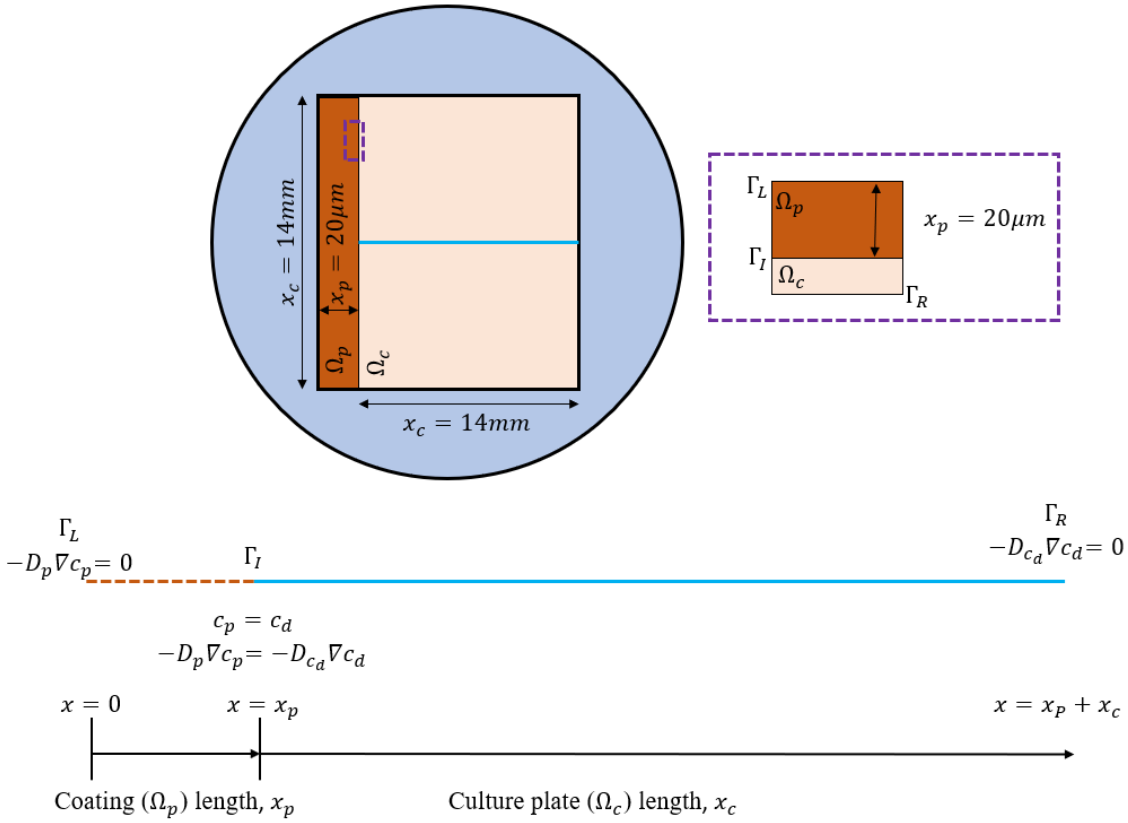


Figure 3.19: Illustration of the 1D model geometry considered in COMSOL Multiphysics 5.6a (COMSOL AB, Burlington, MA, USA), which is derived from the 2D schematic presented. The cells exist only within the square (beige) inset ($\Omega_c$), which is mounted within a larger chamber. There exists two domains and three boundaries within the 1D model, denoted by $\Omega$ and $\Gamma$, respectively. $\Omega_p$ denotes the polymer coating while $\Omega_c$ refers to the culture plate, the domain where cells reside within. The boundaries, $\Gamma_L$, $\Gamma_R$, and $\Gamma_I$ refer to the left, right, and interface, receptively and are highlighted by the inset in the 2D schematic. The lengths of each domain are $x_p$ and $x_c$, respectively. Table 3.7 provides numerical values for each aspect of the geometry.

When modelling drug release, a zero–flux condition is imposed at the left boundary ($\Gamma_L$) of the coating, assuming that all the drug is released into the culture plate. Although *in vivo* it is likely that some drug is lost to flow, within this environment, it is expected that release can sufficiently be controlled and all drug enters the domain of interest. Moreover, drug is not permitted to leave the culture plate via a zero–flux condition on the right–hand side ($\Gamma_R$). Between the two domains ($\Gamma_I$), continuity of flux and concentration is assumed. As for the cell population, a zero–flux is imposed on both sides of the cell domain ($\Gamma_I$, $\Gamma_R$), assuming cell

growth is not permitted on the insert. The 1D problem is schematically depicted in Fig. 3.19, where all boundaries ($\Gamma$) and domains ($\Omega$) are labelled.

### 3.4.3 Consistency between 0D and 1D models

In order to make comparisons between the 0D and 1D model, a degree of consistency between the model frameworks should be established. As such, several assumptions are necessary which are elaborated on within this section.

Firstly, similar to the 0D case, in an attempt to reduce the number of unknown parameters, the drug concentrations are scaled with $k_{50}$ such that:

$$c_p^* = \frac{c_p}{k_{50}}, \quad c_d^* = \frac{c_d}{k_{50}}. \tag{3.15}$$

Applying these scalings to Eqn. 3.12 and Eqn. 3.13, then:

$$\frac{\partial c_p^*}{\partial t} = D_{c_p}\nabla^2 c_p^*, \quad c_p^*(0) = c_p^{0^*}, \quad 0 < x < x_p, \quad t > 0, \tag{3.16}$$

$$\frac{\partial c_d^*}{\partial t} = D_{c_d}\nabla^2 c_d^*, \quad c_d^*(0) = 0 \quad x_p < x < x_c + x_p, \quad t > 0. \tag{3.17}$$

The scalings are then applied to the boundary conditions imposed for each variable. For free drug in the polymer, these become:

$$\frac{\partial c_p^*}{\partial x} = 0, \quad \text{at } x = 0, \tag{3.18}$$

$$c_p^* = c_d^* \quad \text{at } x = x_p, \tag{3.19}$$

$$\frac{\partial c_p^*}{\partial x} = \frac{\partial c_d^*}{\partial x}, \quad \text{at } x = x_p, \tag{3.20}$$

whereas for the free drug in culture plate where cells reside, these become:

$$\left.\frac{\partial c_d^*}{\partial x}\right|_{x=x_p+x_c} = 0 \tag{3.21}$$

Applying the scaling to Eqn. 3.14 which describes the cell population, then:

$$\frac{\partial c(x,t)}{\partial t} = g c(x,t)\left(1 - \frac{c(x,t)}{K}\right)\left(1 - \frac{k_{max}\, c_d^*(x,t)}{c_d^*(x,t)+1}\right), \quad c(0) = c^0, \quad x_p < x < x_c + x_p, \quad t > 0, \tag{3.22}$$

matching that of the 0D model. Note, the above derivation is with respect to the single–phase model. The same principle applies for the multi–phase model (Eqn. 3.8–3.11), where the same scaling is adopted.

One then has to ensure consistency between the non–dimensional drug concentration that the cells are exposed to ($c_d^*$) between the 0D and 1D model. In the former, regardless of the working volume, the cells see the same $c_d^*$ value as a consequence of the 0D implementation. Thus, in an attempt to establish consistency between 0D and 1D, the concentration of drug loaded onto the polymer coating should be sufficiently high such that upon complete release, the non–dimensional concentration ($c_d^*$) exposed to the cells is the same as present in the 0D model. To do so, a variety of assumptions are necessary. The first is to assume that the polymer insert is no higher than the cell layer ($c_h$), which is computed as:

$$c_h = \frac{V_c \times \text{Cell No.}}{SA}, \tag{3.23}$$

where $V_c$ is the volume of a SMC [55], $SA$ is the surface area (1.96 cm$^2$ [282]) hosting a total number of cells (Cell No.) of 100,000 at confluence. This results in a height close to 3.5 $\mu$m which falls close to the range of values (2.78 $\mu$m $\pm$ 0.59 $\mu$m) reported in literature [295]. The volume of the coating ($V_p$) can then be computed as $V_p = x_c\, x_p\, c_h \approx 9.8 \times 10^{-3}$ mm$^3$. Then, the volume of the cell layer in culture is given by $V_{cl} = V_c \times$ Cell No. $= 0.686$ mm$^3$.

It is assumed that the total mass of drug presented to the cells in culture between the 0D ($M_{0D}$) and the 1D ($M_{1D}$) implementation is the same. Moreover, it is also assumed that the total mass of drug present on the polymer coating ($M_p$) is equivalent to $M_{0D}$ and $M_{1D}$:

$$M_{0D} \equiv M_{1D} = c_d^*\, k_{50}\, V_{cl} \equiv M_p = c_p^{0^*}\, k_{50}\, V_p, \tag{3.24}$$

where the dimensional drug concentration ($c_d$) is replaced with the non–dimensional substitute as reported in Eqn. 3.15. The same is repeated for the mass on the polymer coating ($M_p$) where $c_p^{0^*}$ is the initial non–dimensional concentration of drug on the polymer coating. Rearranging Eqn. 3.24 for $c_p^{0^*}$ gives the following:

$$c_p^{0^*} = c_d^*\, \frac{V_{cl}}{V_p}, \tag{3.25}$$

meaning that the non–dimensional concentration of drug initially on the coating ($c_p^{0^*}$) is approximately 70 times greater than $c_d^*$ in the 0D model. However, having established the above relationship means that once drug is completely released, the values of $c_d^*$ the cells are exposed to will be the same in 0D and 1D. In other words, when all drug is released, i.e. $c_p^* \to 0$, then the non–dimensional concentration of drug ($c_d^*$) in 0D and 1D should be the same. Fig. 3.20 supports this, showing that for three different release profiles, achieved by amending the diffusion coefficient in the polymer ($R_p^1$: $D_p = 5 \times 10^{-16}$ m$^2$ s$^{-1}$, $R_p^2$: $D_p = 1 \times 10^{-15}$ m$^2$ s$^{-1}$, and $R_p^3$: $D_p = 5 \times 10^{-15}$ m$^2$ s$^{-1}$), that all points in the domain ($x = x_p$, $x = (x_p + x_c)/2$, and $x = x_p + x_c$) converge to the same non–dimensional drug concentration ($c_d^* = 25$).

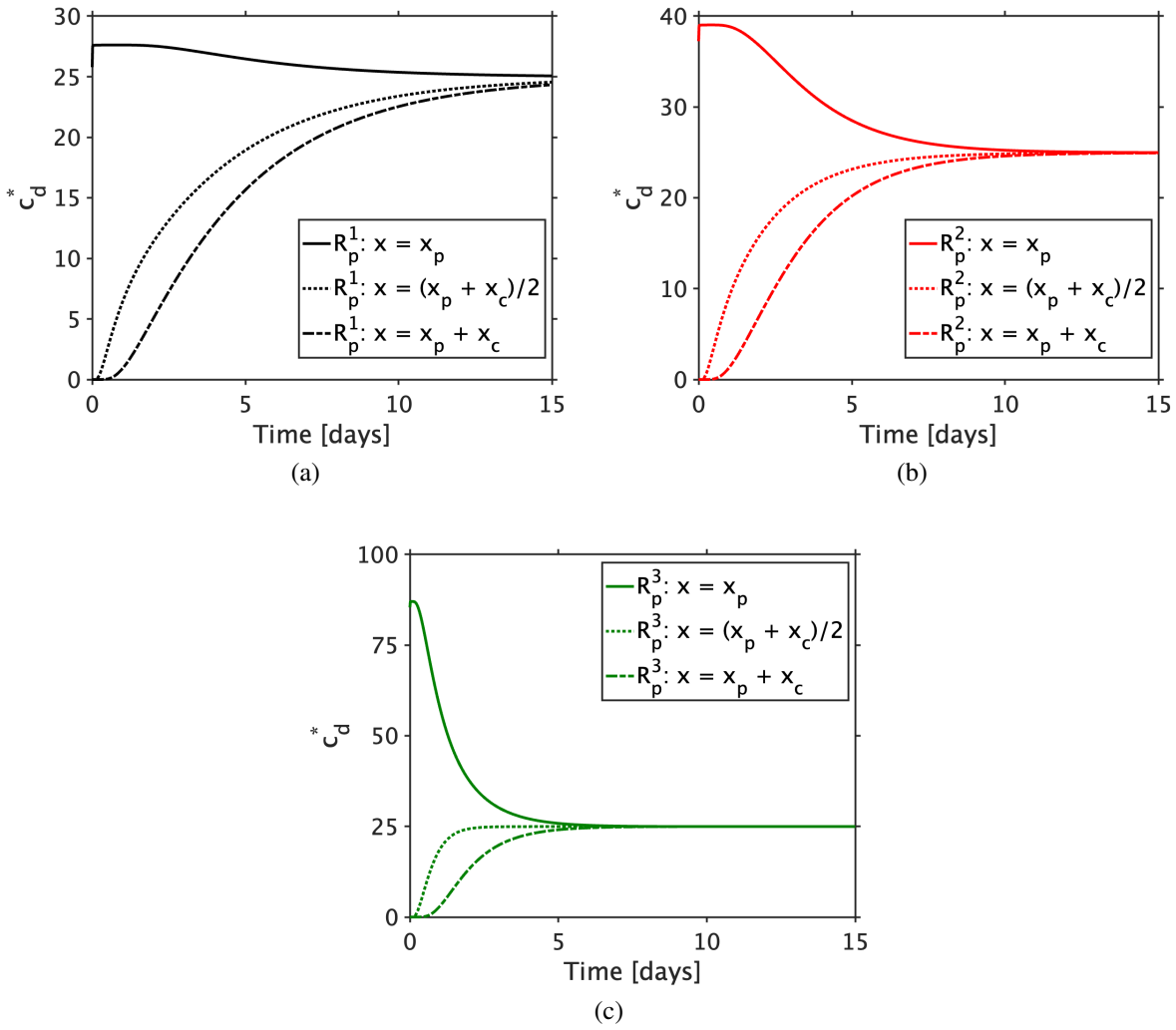


Figure 3.20: How $c_d^*$ varies in time as the drug release profile is perturbed at three points in the domain (Fig. 3.19): $x = x_p$, $x = (x_p + x_c)/2$, and $x = x_p + x_c$. (a) $R_p^1$. (b) $R_p^2$. (c) $R_p^3$. Spatial points ($x$) are in reference to the 1D geometry (Fig. 3.19).

### 3.4.4 Model parameters & Sensitivity analysis

The primary aim of this work is to assess the impact of spatiotemporal drug gradients on cell proliferation. As such, parameters which are associated with drug delivery are varied. These are $D_p$, the drug diffusion coefficient in the polymer and $c_p^{0^*}$, the initial non–dimensional coating drug concentration. An extensive analysis of other parameters associated with the cell cycle, such as the initial distribution of cells within each phase and the intrinsic growth rates have been explored in depth previously (Section 3.3).

Within this 1D framework, both a single and multi–phase model are considered. For the single–phase model, one value for $g$ is considered, corresponding to an intrinsic rate where a cell divides every 32 hours. As for the multi–phase model, a similar fixed intrinsic growth rate is implemented (50:50 split between phases) for the two extreme initial conditions, $MP^1$ (all

cells initially reside in phase 1) and MP$^5$ (all cells initially reside in phase 2). Thus, there exists three different models: SP, MP$^1$, and MP$^5$. For each of the multi–phase models, two drugs (1 and 2 from Eqn. 3.8–3.11) are again considered. Within each, perturbations in the following parameters are simulated: $D_p$, $c_p^{0^*}$, and $k_{max}$ as depicted in Fig. 3.21. Note that in the 0D model, the parameter pairs were defined as $[k_{max},\ c_d^*]$. As per Eqn. 3.25, the parameter pairs used in the 1D model are updated to $[k_{max},\ c_p^{0^*}]$, as demonstrated in Fig. 3.22b. As such, the four new parameter pairs are given as: Point 1 [0.6, 70], Point 2 [0.7, 350], Point 3 [0.8, 700], and Point 4 [0.9, 1750].

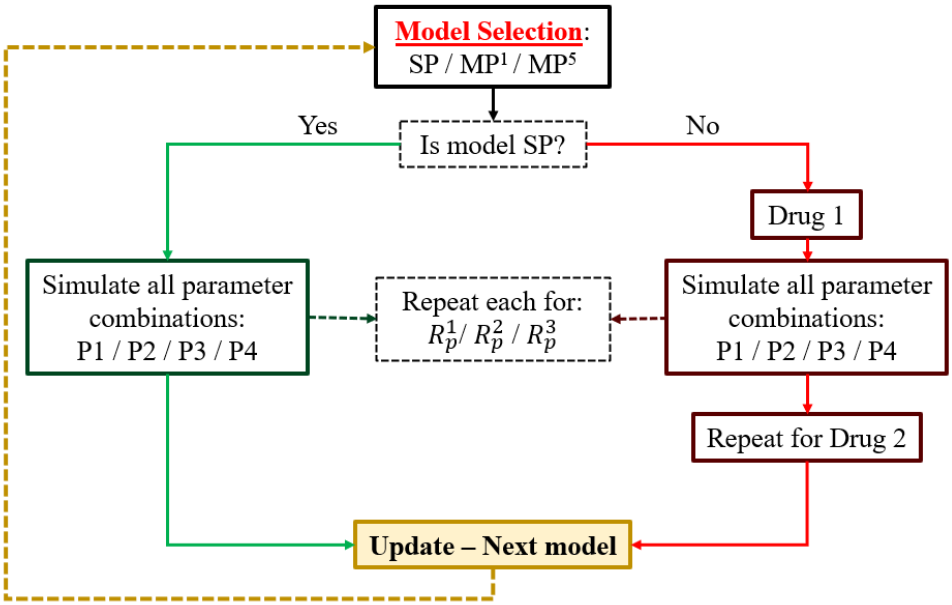


Figure 3.21: Flow chart detailing the problem approach for the 1D model. Upon selection of the model (SP: single–phase, MP$^1$: multi–phase with all cells initially in phase 1, and MP$^5$: multi–phase with all cells initially in phase 2), each of the 4 parameter combinations (P1–P4: Fig. 3.22b) are considered. For each parameter combination, three different release profiles ($R_p$) are simulated (Fig. 3.22a). The process is repeated until all models are simulated.

The various drug release profiles and parameter combinations considered are presented in Fig. 3.22a & 3.22b, respectively. The baseline drug release profile ($R_p^1$) was selected to ensure approximately all of the drug was released from the coating in the 15–day window ($D_p$ = 5 $\times$ $10^{-16}$ m$^2$s$^{-1}$). The other two drug release profiles permit a quicker release of drug, moving towards the 0D case, where drug is immediately available to the cells at a constant concentration. As for the model parameters, these are summarised in Table 3.7. The culture plate dimensions are estimated to provide a surface area comparable to a single well within a 24–well plate, whilst the breadth of the coating is estimated to be 20 $\mu$m. The diffusion coefficient for drug in the medium is acquired from [172]. All parameters associated with the cell population are as before, assuming the duration of the cell cycle is 32 hours, and that a spatially uniform initial number of cells is present on the plate initially ($c^0 = 10,000$).

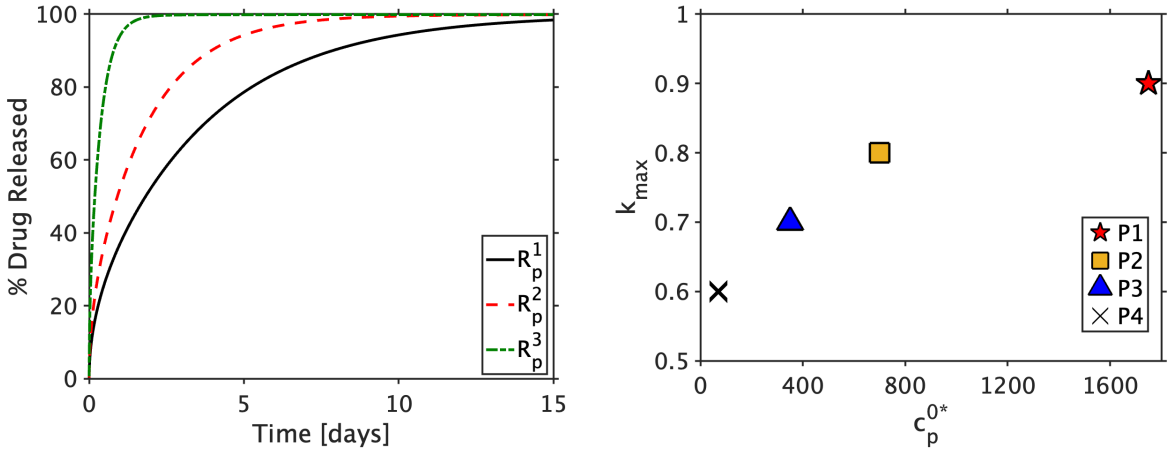


(a) (b)

Figure 3.22: (a): Different drug release profiles ($R_p$) considered. Baseline value for $D_p$ is illustrated by the solid black line. $R_p^1$: $D_p = 5 \times 10^{-16}$ m$^2$ s$^{-1}$, $R_p^2$: $D_p = 1 \times 10^{-15}$ m$^2$ s$^{-1}$, and $R_p^3$: $D_p = 5 \times 10^{-15}$ m$^2$ s$^{-1}$. (b) Different parameter pairs, [$c_p^{0*}$, $k_{max}$], considered when exploring model behaviour: Point 1 [0.6, 70], Point 2 [0.7 350], Point 3 [0.8 700], and Point 4 [0.9 1750].

| Parameter | Description | Value [Unit] | Reference |
|---|---|---|---|
| $x_c$ | Culture plate length | 14 [mm] | Estimated |
| $x_p$ | Polymer coating thickness | 20 [$\mu$m] | Estimated |
| $D_{c_d}$ | Drug diffusion coefficient | $2\times10^{-10}$ [m$^2$ s$^{-1}$] | [172] |
| $D_p$ | Polymer coating diffusion coefficient | $5\times10^{-16}$ [m$^2$ s$^{-1}$] | Estimated |

Table 3.7: Description of the parameters for the 1D model and their baseline values.

### 3.4.5 Numerical methods & Analysis of results

The commercially available software COMSOL Multiphysics 5.6a (COMSOL AB, Burlington, MA, USA) was used to mesh the 1D geometry and numerically solve the model. The mesh was chosen to host approximately 7,000 elements to ensure that error in the release of drug at $t = 0$ was less than 0.5%.

## 3.5 Results & Discussion: 1D Model

To demonstrate the difference between each of the cases presented in Fig. 3.21, the time taken for the number of cells in each model to reach $K/2$ is recorded, illustrated in Fig. 3.23. As anticipated, when the rate of drug release is increased, the time taken for cells to reach their inflection point is increased. All four figures (Fig. 3.23a–d), regardless of the parameter efficacy combination considered, illustrate this result. In other words, as the rate of drug release is

accelerated, the model results for each case (SP, MP$^1$: Drug etc.) approach the result obtained from the previous 0D simulations, where drug was exposed to the cells from $t = 0$ (Section 3.3.2).

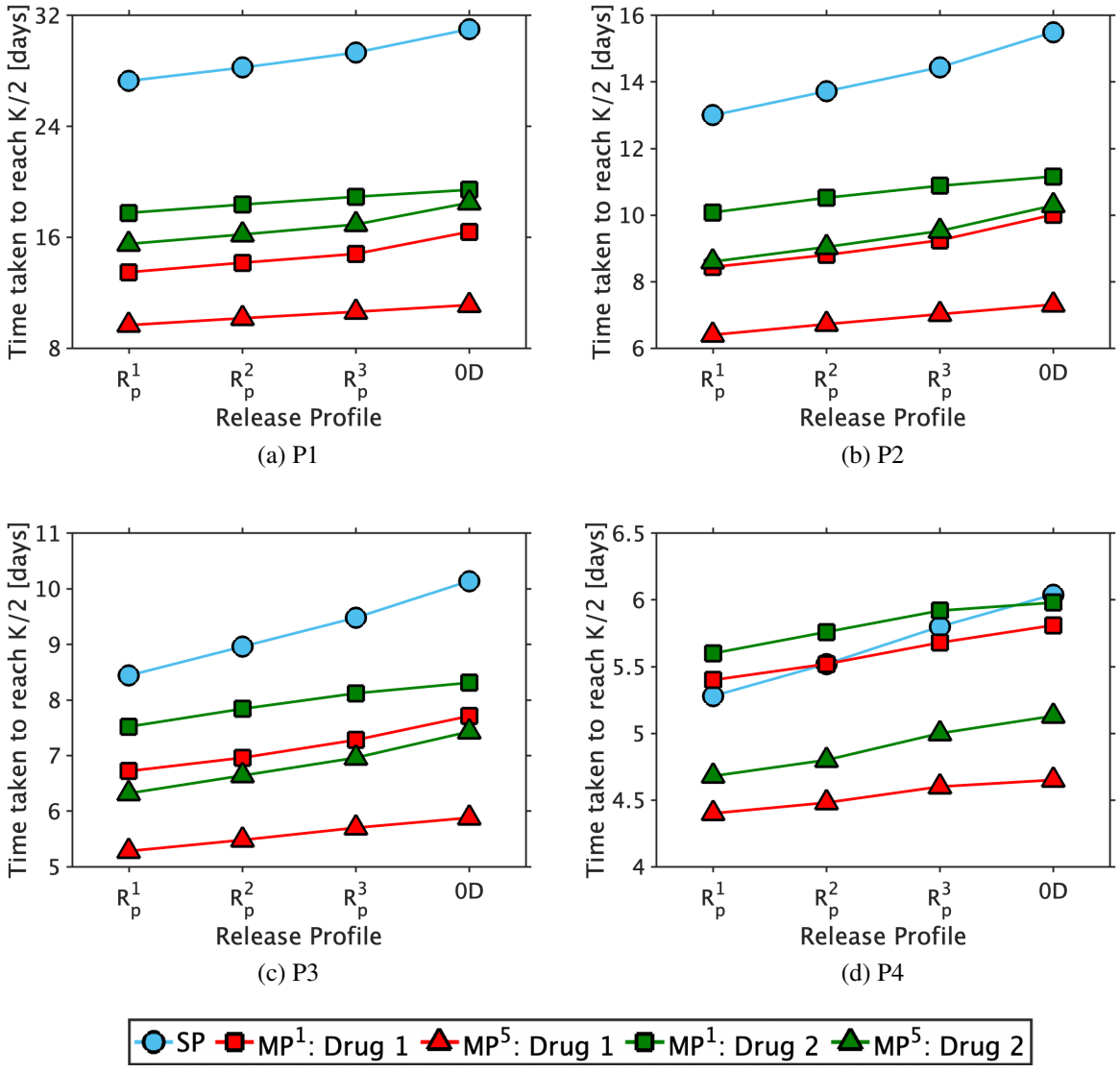


Figure 3.23: How different parameter combinations: (a) P1, (b) P2, (c) P3, and (d) P4 as defined in Fig. 3.22b influence the time taken for the cell population, computed as an average of the domain ($\Omega_c$), to reach half their carrying capacity ($K/2$) across a range of different drug release rates. $R_p^1$: $D_p = 5 \times 10^{-16}$ m$^2$ s$^{-1}$, $R_p^2$: $D_p = 1 \times 10^{-15}$ m$^2$ s$^{-1}$, and $R_p^3$: $D_p = 5 \times 10^{-15}$ m$^2$ s$^{-1}$. 0D assumes that drug is always present to cells from $t = 0$. SP = single–phase, MP$^1$ = multi–phase, all cells initially in phase 1, MP$^5$ = multi–phase, all cells initially in phase 2. Drug 1 is the $G_1$/S transition blocker and drug 2 is the mitosis (M) blocker.

All results in Fig. 3.23 present the time taken for the number of cells within the domain $\Omega_c$ to reach the inflection point. However, another interesting aspect worth exploring is how the growth of cells varies between the two extremes of the domain: $x = x_p$ and $x = x_p + x_c$. Therefore, for

the four different multi–phase models, the cell growth profile is presented in Fig. 3.24 at the two extremes under the parameter condition P2 [0.9, 700] over the original 15–day period. As expected, irrespective of the model proposed, or the initial condition of the cell population, the number of cells is insensitive to the release profile immediately adjacent to the polymer coating boundary ($x = x_p$). This result can be attributed to the drug release profiles presented back in Fig. 3.20. At $x = x_p$ the drug concentration is high, decreasing in time as it diffuses through the domain. However, at the edge of the culture dish, $x = x_p + x_c$, drug concentration is low initially before increasing towards an upper threshold, $c_d^*$ (Eqn. 3.25). Thus, the drug release profile matters most to cells at the opposite side of the domain from the drug source, which are exposed to drug much later than those at $x = x_p$.

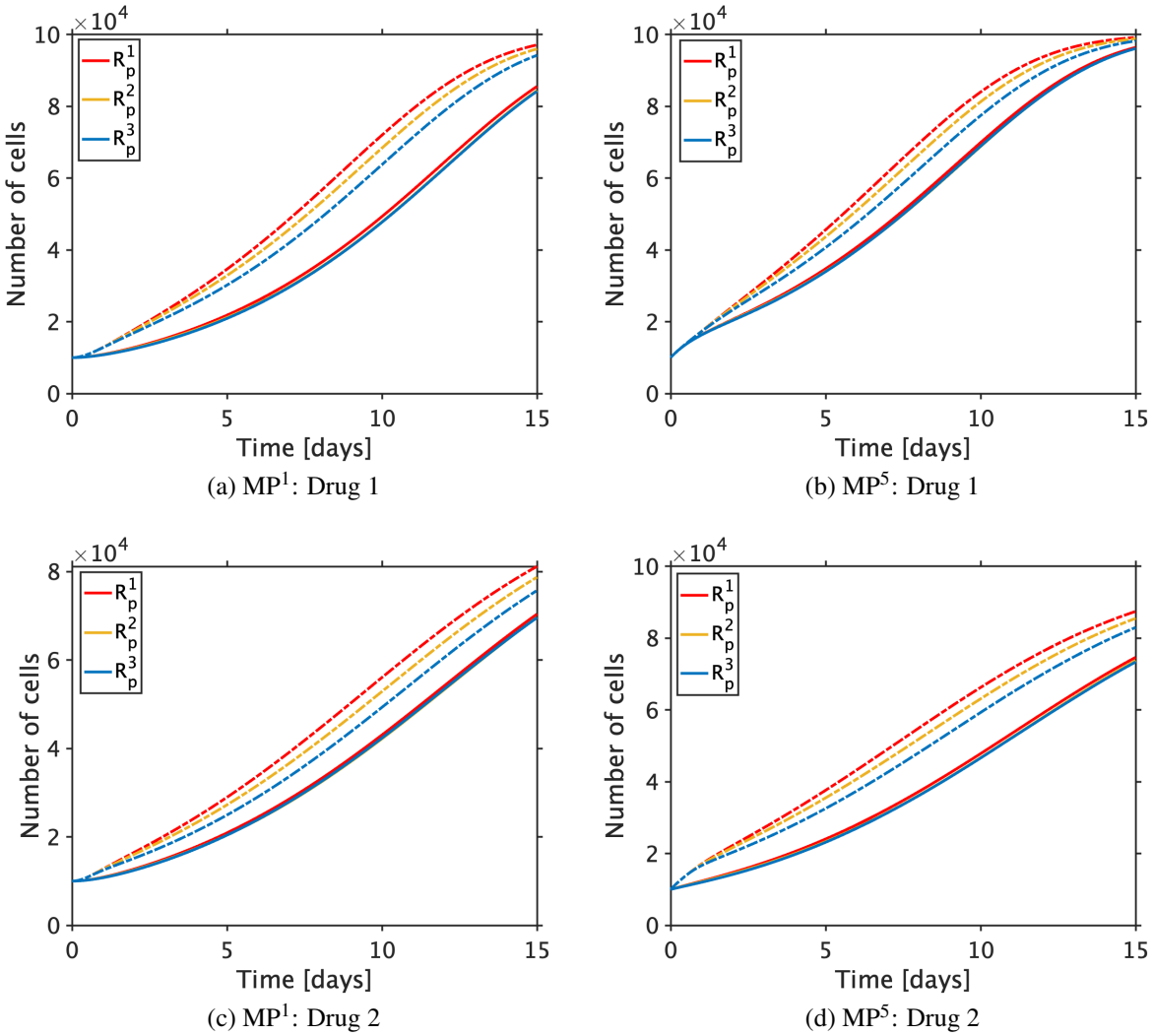


(a) MP[1]: Drug 1

(b) MP[5]: Drug 1

(c) MP[1]: Drug 2

(d) MP[5]: Drug 2

Figure 3.24: How the cell profile varies in time at either end of the domain. Cell interfacing the polymer coating ($x = x_p$) are denoted by solid lines, whilst cells at the opposite end of the domain from the drug source ($x = x_c + x_p$) by dashed lines. MP[1]: all cells initially in phase 1 and MP[5]: all cells initially in phase 2.

Although it could be argued that the difference in model response is subtle between each of the drug release profiles considered, the fact that one exists is important. Such a result may have significant implications in a setting which is more heterogeneous. For example, stents are deployed within severely diseased vessels, where the transport properties of drug are known to differ throughout [46]. Therefore, if drug is unable to reach the injured areas, where remodelling is actively present, then cells will be able to migrate and proliferate freely until drug eventually inhibits their capacity to do so. Moreover, as demonstrated in Fig. 3.23, as well as in prior 0D work (Section 3.3.2), this becomes even more significant depending upon the phase the cell resides within when drug is present, with drugs (e.g. sirolimus and paclitaxel) known to be cell cycle specific. All of this taken together suggests that spatiotemporal gradients associated with the delivery of drug could have an impact on cell proliferation *in vivo* and thus vessel re–narrowing. However, before adopting more complex *in vivo* models, subsequent efforts should explore experimental calibration and validation techniques (e.g. FUCCI) to fully assess whether these models have an advantage over traditional 'single–phase' approaches in demonstrating the dose–dependent effect of drug on cell proliferation.

## 3.6 Limitations & Future work

A number of assumptions have necessarily been made when devising the above mathematical models, which are justified in the preceding text. For example, SMC migration has been ignored throughout with the focus being on the anti–proliferative properties of drug. However, with the aid of experimental techniques (e.g. FUCCI), one can visualise the motility of cells under the effect of drug, similar to [286], and derive appropriate models that account for cell migration through a diffusive parameter; where drugs like sirolimus have demonstrated an inhibition of cell motility *in vitro* [296]. Moreover, multiple sources [240, 259] have reported that drugs of type 2 (e.g. paclitaxel) induce permanent cell senescence at high doses. In this phase, cells were unable to migrate or proliferate, but still remained viable. As such, extensions to the model proposed (Eqn. 3.10 & 3.11) could be considered to explore the possible significance of this third phase. However, this would be aided significantly by the use of experimental techniques (e.g. FUCCI), such that real time imaging of the cell population can aid in determining the experimental conditions which drive cells into this phase, and what they do once there.

Note that the effects of contact inhibition have been ignored within the current modelling framework. Although spatial restrictions are considered during mitosis, no spatial check is present in the model which halts cells from entering phase 2 if there is no space to divide. In other words, the steady state solution of Eqn. 3.6–3.7 means that all cells will be in phase 2 as $c \to K$. As such, these cells are primed to divide if space does become available. However, various articles suggest that a lack of space for cell division induces cell cycle arrest within the first phase of the cell cycle, $G_1$ ($c_1$), by means of contact inhibition, before cells fully commit

to division [297, 298]. Thus, model improvements could be considered which incorporate this behaviour. Although this is left to future work, the $g_1 c_1$ term on both Eqn. 3.6–3.7 may be improved by introducing a step function. In other words, the transition of cells from phase 1 to 2 may be blocked if space will no longer be available once the cells already within phase 2 divide. One should look at [299–303] for inspiration, where cell–to–cell adhesion is discussed in depth.

As alluded to throughout, experimental techniques should be considered to aid in model calibration and validation, assessing whether a more sophisticated iteration (multi–phase over single–phase) of the model is necessary. This could then provide justification to pursue the significance of such a model in emulating *in vivo* conditions. The improvement of the model by addressing these limitations has been left to future work.

## 3.7 Conclusions

The results of this chapter demonstrate that not only does the model description matter (single–phase versus multi–phase), but also the distribution cells throughout the cell cycle prior to being exposed to drug. Moreover, as demonstrated in the 1D model, the spatiotemporal gradients present as a consequence of drug release are important, where differences in model responses are noted. It is expected that these differences would be significantly exacerbated in scenarios where disease and other environmental factors that hinder drug transport are present. As such, vessel re–narrowing could be significantly increased as a result. Therefore, the work in this chapter has demonstrated the possible significance of modelling cell proliferation as a cyclic process. Given that drugs coated on stents are cell cycle specific, modelling the precise timing of their effect may have an importance on future modelling efforts. For example, throughout the different models proposed, the single–phase model, for the same set of efficacy parameters, has demonstrated a more profound inhibition of cell proliferation. This may allude to why the predictive capacity of such models were poor when compared with experimental data in Chapter 2, where the models may be under or over–estimating the efficacy of drug. To explore this in full, it is essential that experimental methods such as FUCCI are implemented to calibrate a cell cycle specific model [284–286]. From this, a more thorough conclusion on discrepancies with the single–phase model can be made. Although this was out with the scope of the work presented here, following the validation of these cell cycle models, implementation into capturing dynamics *in vivo* could then be attempted in the pursuit of optimal stent design.

# Chapter 4

# An *in silico* model of restenosis following stent deployment

The previous two chapters investigated the influence of drug on smooth muscle cell (SMC) proliferation alone, within an *in vitro* environment. However, it is known that these cells are fundamental to the evolution of restenosis following stent deployment, where their behaviour is mediated by many other constituents such as growth factors and extracellular matrix, in response to mechanical stimuli. Therefore, the focus of this chapter is to present a sophisticated computational model than can effectively portray this process. The subsequent chapter will then incorporate drug delivery and retention, observing how this modulates the evolution of excessive tissue growth.

The chapter begins by providing the reader with an overview of relevant mathematical models of restenosis, categorising them either as: (i) agent–based models (ABMs), or (ii) continuum models. The framework to be adopted in this work is then discussed. The model geometry and governing model equations are then described in detail before simulations are performed using COMSOL Multiphysics 5.6a (COMSOL AB, Burlington, MA, USA). The key results are presented and analysed, immediately followed by a discussion of the key limitations of the computational model.

## 4.1 Review of restenosis modelling literature

The process of in–stent restenosis (ISR) is highly heterogeneous, where a complex, multiscale network of events occur at different spatio–temporal scales to permit vessel healing within a timely manner. Nonetheless, it is stent–induced vascular damage following deployment and the subsequent alterations to vessel haemodynamics that have been found to play significant roles in the progression, and severity, of restenotic tissue. With the processes difficult to monitor directly, mechano–biological models, inspired by biological principles, have emerged to investigate the underlying mechanisms that drive ISR. Such models often employ an agent–based framework,

where constituents (e.g. cells, growth factors, and extracellular matrix) follow a set of rules in response to stent deployment, and are commonly solved in geometries of varying complexity: from simple 2D segments of an idealised artery to simulations encompassing 3D patient–specific profiles [53, 54, 57, 65–67, 206, 210–219, 225, 230]. On the other hand, a handful of continuum models also exist that implement a finite element framework to simulate restenosis [55, 115, 208, 222–224, 304]. These either describe species evolution (the variables tracked in the model) explicitly, where a series of highly nonlinear, coupled partial differential equations (PDE's) are solved to emulate restenosis [55, 222, 304], or by proposing a kinematic growth model to describe the growth in mass of tissue following stent deployment [115, 223, 224]. More recently, a hybrid methodology aiming to address the limitations of the two continuum approaches above was presented [208]. The authors utilised homogenized constrained mixture theory such that the biofidelic and kinematic growth approaches are harmonized.

### 4.1.1 ABMs of restenosis

Pioneering work by Evans *et al.* [210] introduced the idea of complex multiscale models (CxA) to describe the main physical and biological elements associated with restenosis. From this, over the last 15 years, an array of modelling literature has been published that investigates the impact of stent deployment on restenosis. Efforts have primarily focused on stent design, observing how mechanical stimuli and and subsequent fluid dynamics may hinder the remodelling process.

In the years following Evans *et al.* [210], Boyle *et al.* [211] presented a cell–centred model that encompassed multiple constituents, which followed a set of rules in response to injury and inflammation within a 2D setting. Results alluded to the significance of stent deployment, where an increased deployment depth resulted in a more aggressive healing response. Limitations associated with the model geometry were addressed in subsequent iterations [212], where the focus shifted to the simulation of clinically adopted stents with an aspiration of such models to be implemented as pre–clinical tools. A Moonley–Rivlin constitutive model was also considered, accounting for the effect of stent deployment on arterial tissue, which directly influenced the inflammatory response [57]. At a similar time, Zahedmanesh *et al.* [54, 214, 215] published a series of articles on the subject of vascular remodelling. Their preliminary models highlighted the importance of stent design, in particular strut thickness, on arterial wall stresses [214]. Assessing SMC behaviour in isolation of restenosis, their following publication demonstrated the response of SMCs to vascular injury within a tissue engineering scaffold [215]. Adding complexity to the model, a fully–coupled ABM framework was established, introducing other key constituents involved within restenosis (e.g. extracellular matrix) [54]. Albeit within a simplified environment (2D), their simulations of stent–induced vascular injury demonstrated qualitative agreement with clinical data, where increased strut thickness and deployment depth were attributed with greater levels of restenosis.

Moreover, a significant series of ABMs were developed over several years, where prelimi-

nary efforts modelled restenosis in a 2D geometry [53,65,67,206] before extending their efforts to three dimensions and emulating restenosis within patient–specific geometries [66, 217, 229]. With the clinical agenda on improving stent design, Tahir *et al.* [206] focused on the significance of stent deployment on ISR. Although proliferation of cells within their model followed logistic growth, their ability to grow was mediated by several rules which accounted for spatial restrictions (contact inhibition) and wall shear stress (WSS) levels, where blood flow was modelled using the Lattice Boltzmann method (LBM), with blood described as a Newtonian fluid. With these limitations in mind, their model demonstrated good agreement with clinical findings at the time, where a shift to a more streamlined, thinner strut design was associated with reduced rates of ISR. A key limitation, however, was the absence of the endothelial layer, which was considered in a subsequent model [53]. As such, their rule–based approach was updated to inhibit SMC proliferation following the presence of a functional endothelial cell (EC) agent. The recovery of the endothelial layer was defined by a sparse data set, existing of only two points. Thus, to probe sensitivity in this recovery, different re–endothelialzation cases were considered. Their results show the significance of this layer and its role in ISR prevention, where the authors admit that further experimental data is essential, albeit difficult to capture, to fully assess their model's potential. The authors then explored the importance of EC origin in vessel remodelling [67]. They concluded that it was most likely surviving patches around the stent struts that permitted endothelial regrowth, as opposed to migration from healthy sites adjacent to the lesion. Their final 2D efforts investigated the significance of vascular injury on ISR [65]. Here, the focus shifted away from ECs and towards SMC behaviour, where their migratory and proliferative capacities were significantly heightened following more intrusive stent deployment. As such, the cells were allowed to behave more freely as a consequence of greater exposure to circulating factors in the lumen following deep fenestrations in the internal elastic lamina (IEL). Subsequently, the authors presented the first fully–coupled 3D model of ISR, with the primary aim of it to be adopted as a pre–clinical tool to predict patient outcome [66]. Their model grouped methods from previous publications, investigating the role of vascular injury, stent design and re–endothelialization recovery speed. Although qualitative trends agreed well with experimental data, especially at early times (15 days) further advancements were necessary to depict long–term restenosis. To address these limitations, the model was extended to account for extracellular matrix (ECM) synthesis. In doing so, the results of their *in silico* model agreed well with histological data from *in vivo* models depicting restenosis over a longer duration [217, 229].

A correlation between WSS and ISR outcome has been established following stent deployment, such that low levels of WSS is a predictor of restenosis [127, 128, 227]. As a result, aforementioned articles [53, 66, 67, 217, 229] incorporated the effects of WSS on SMC proliferation through a LBM. However, more recent efforts have proposed a multiscale model that couples a finite element model of computational fluid dynamics (CFD) within an ABM framework [218,219,225,227,305]. Notably, relevant haemodynamic indices (e.g. WSS) are exported

from the CFD module and fed into the ABM, having a direct impact on constituent behaviour. For example, Corti *et al.* [226] applied this framework within simulations emulating stent deployment in human femoral arteries, where WSS directly influenced the functionality of ECs through a damage index that was directly related to WSS. Low levels of WSS ($< 0.5$ Pa) were primarily located in areas adjacent to stent struts, and stimulated vessel re–narrowing. The model was able to demonstrate good agreement with an *in vivo* patient model at a 1–month follow–up. However, limitations were present, where focal restenosis profiles present in the patient models were not captured by the *in silico* model at later times (e.g. 1–year follow–ups). In an attempt to address this, the authors proposed the inclusion of vascular injury to their model, where the arterial wall responds to stenting through a polynomial strain energy function [306]. The authors alluded to the importance of incorporating constitutive laws that describe the arterial response to stenting, where without it, focal stenosis cannot be captured which may result in a local lumen loss increasing the possibility of an adverse cardiac event.

With femoral arteries the primary focus of the models in [226, 306], efforts have recently been extended to coronary arteries. For example, Chen *et al.* [220] presented a very similar approach to Corti *et al.* [226, 306], where WSS influenced a damage index through a linear interpolation which directly mediated the behaviour of constituents present in the healing response. This is an alternative method to that present in Zahedmanesh *et al.* [54], where the linear interpolation instead encompassed shear stresses associated with arterial mechanics. In agreement with [218,219,227,305,306] greater neointimal thicknesses were observed in regions where WSS was low. However, in the absence of experimental data for validation, the model only agrees qualitatively with clinical trends. As such, Chen *et al.* [220] have indicated that further work will explore an animal model in tandem with *in silico* efforts, whilst simultaneously increasing the sophistication of the ABM of restenosis such that the phenotype of SMCs are also considered.

### 4.1.2 Continuum models of restenosis

Whilst there exists a large array of ABMs, those which adopt a continuum framework are less frequent. The continuum modelling strategy permits a more natural coupling to the mechanical aspects of the problem, whilst simultaneously modelling the explicit spatiotemporal behaviour of constituents that contribute to ISR. As such, these models tend to couple the deployment of the stent, modelled via a finite element framework, to a series of PDEs that detail constituents (e.g. smooth muscle cells, endothelial cells, growth factors, extracellular matrix, matrix–degrading metalloproteinases, and damage) interaction as tissue growth ensues. The current state–of–the–art continuum model was published by Escuer *et al.* [55]. The authors detail species evolution and tissue growth following a finite element simulation of stent expansion. To stimulate vascular healing, they propose a variable termed ‘damage’ that emulates the inflammatory response and is a consequence of arterial stresses present following stent deployment. While the model was able

to broadly capture clinical trends, it suffers from a series of limitations. In particular, excessive ECM synthesis is noted, SMC proliferation is highly simplified, EC regeneration is present in isolation from other processes, and the constitutive law used to describe arterial kinematics is simplified, failing to account for collagen fibre dispersion in the wall. Nonetheless, good qualitative agreement with clinical trends are present, where further advancements will only serve to enrich the model.

Similarly, Boland *et al.* [222] adopted a continuum based restenosis model, amending the approach published by Lally *et al.* [304] to incorporate a ghost mesh strategy that conveys restenotic tissue growth following the degradation of a magnesium stent. Unlike Escuer *et al.* [55], flow is considered within the model, highlighting the significance of both arterial stresses and WSS on patient outcome [220, 226, 306]. Although inclusive of flow, the restenosis model is highly simplified, accounting for only a single cellular species. Note, other key constituents involved (e.g. growth factors) are neglected, and the restenosis process is driven purely by arterial and wall stresses as a consequence of stent deployment and fluid flow, respectively.

Although adopting a continuum modelling framework, alternative strategies exist that model tissue growth directly within the constitutive model applied to the arterial tissue, as opposed to the modelling of species growth explicitly as present in [55, 222, 304]. To the best of the author's knowledge, Fereidoonnezhad *et al.* [224] present the first kinematic growth model in the context of balloon angioplasty in an idealised, straight geometry. Their model incorporates a growth stretch parameter that emulates lumen loss, where trends agree well with those observed clinically over the course of six months. Addressing a particular limitation, He *et al.* [223] implemented a similar growth model, but extended previous efforts to include soft tissue damage through the Mullins effect. Assessing the clinical relevance of their model, three different stent designs were simulated, where the authors focused on the significance of materials, expansion severity, and the impact of overlapping stents on restenosis. With early models simulating ISR within idealised geometries, subsequent research considered patient–specific cases, where the authors aimed to advise on possible treatment strategies for complex lesions that required overlapping stents [115]. Moreover, Gierig *et al.* [230] considered a highly coupled chemo–mechano–biological model of restenosis, where the change in mass of local constituents drives the growth of tissue at a macroscopic level, accounting for the effects from mechanical contributions of stent deployment.

Maes *et al.* [208] considered a different approach which employed a homogenized constrained mixture model, which in essence is a hybrid of the kinematic and biofidelic modelling strategies. Their primary focus was on balloons as opposed to stents, assessing the arterial response to balloon expansion. Their constitutive framework is the most sophisticated to date, allowing for the effects of mechanical stimuli on individual species (e.g. SMCs) to be considered. However, several limitations exist, most of which are a result of the simplified homogeneous 2D geometry. Further work, with the benefit of experimental data, should pursue a more complete

representation of the arterial response to vascular injury.

In light of the aforementioned efforts, [115, 208, 223, 224, 230], the authors noted the need for further experimental data. This would allow for models proposed to describe soft tissue mechanics to be validated such that their predictive capacity could be improved.

### 4.1.3 Model framework selection

A series of different modelling strategies are discussed above, where they fall into one of two categories: ABMs or continuum. Although promising and by far the most prominent choice, ABMs do not naturally lend themselves to coupling with drug transport, which ubiquitously adopts a continuum description [79, 169, 172, 188]. With the role of drug a key aspect of this thesis, then it appears more natural to adopt a framework which is consistent across the two models: restenosis and drug transport. While a coupling between models adopting separate frameworks is possible (e.g. [205]), a number of computational difficulties arise. In particular, the small time steps required for the drug transport model as a consequence of the nonlinear binding kinetics may require more coupling iterations than previously discussed in [226]; which may significantly add to an already lengthy computational time.

Of the two continuum frameworks, those which model cell behaviour explicitly are more desirable for the overall aim of this thesis. In line with previous chapters that explore the effect of drug on SMC growth, these models would permit seamless integration of a drug transport model coupled to restenosis. With Escuer *et al.* [55] publishing the current state–of–the–art for models of this type, the aim of this chapter is to then build upon this model, making notable changes that improve its realism. Prior to the inclusion of drug (Chapter 5), the restenosis model proposed is investigated, analysing how stent expansion and perturbations in strut configuration influence the restenotic response, assessing results against clinical trends. Subsequent limitations of the model are then discussed and explored in subsequent chapters, where appropriate.

## 4.2 Methodology

### 4.2.1 Overview

Illustrated in Fig. 4.1, the computational model proposed can be easily divided into three distinct steps: expansion, species evolution, and remodelling. As such, the methodology is broken down into sections, detailing the model geometry before describing the three different steps separately.

The scientific literature indicates that arterial restenosis as a consequence of injury is complex, where an abundance of species interact with one another with an aim to restore quiescence within the arterial wall [56]. This process is initiated by stent deployment (step 1). Highlighted in Fig. 4.2, the idealised geometry (a) is deformed (b) following stent expansion, where the resulting Von Mises stress field is assumed proportional to a variable termed *damage*. Devised

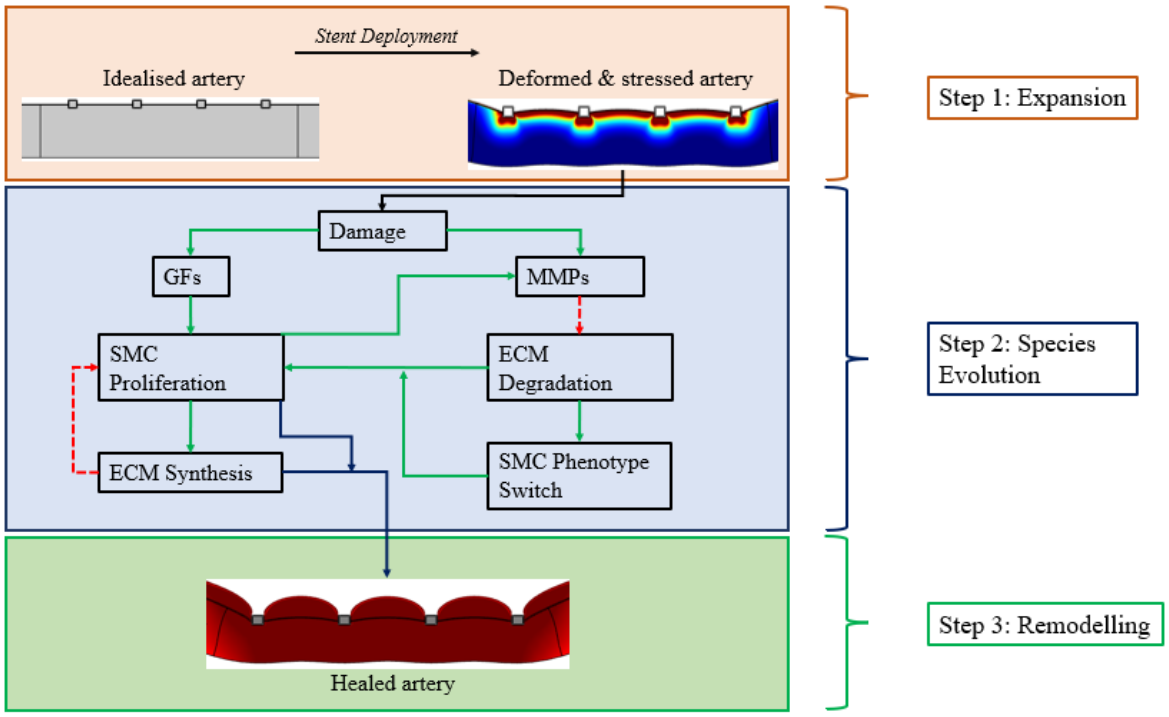


Figure 4.1: Flow chart depicting the various stages of the model. Step 1: Stent deployment deforms the artery and then triggers the restenosis model by coupling stress to damage. Step 2: Restenosis ensues, where damage upregulates species (GFs and MMPs) which interact with other constituents to drive tissue growth. Here, green solid arrows refer to stimulation, red dashed arrows to inhibition, black solid arrows as a neutral step, and blue arrows to remodelling. Step 3: Remodelling, where an increase in specific constituents gives rise to excess tissue growth.

to mimic an inflammatory response, this species is associated with the stimulation of the healing response by triggering a response from various constituents (step 2). Most notably, the production of growth factors (GFs) and matrix–degrading metalloproteinases (MMPs). Although both GFs and MMPs promote the proliferation of SMCs, they do so by different means. The former does this explicitly whilst the latter mediates ECM degradation which induces a SMC phenotype switch to an active state which can then proliferate more freely as space becomes available. Through time, these active SMCs deposit ECM, providing structural support to the vessel as it heals and remodels. As detailed ubiquitously in the literature, SMCs and ECM are the primary components that contribute to excess tissue growth [60]. At early times, SMCs populate the neointima in response to injury, with ECM dominating tissue growth at later times, providing structural support. Thus, in the model proposed, it is these two species that contribute primarily to tissue growth, covered by a thin endothelial layer (step 3).

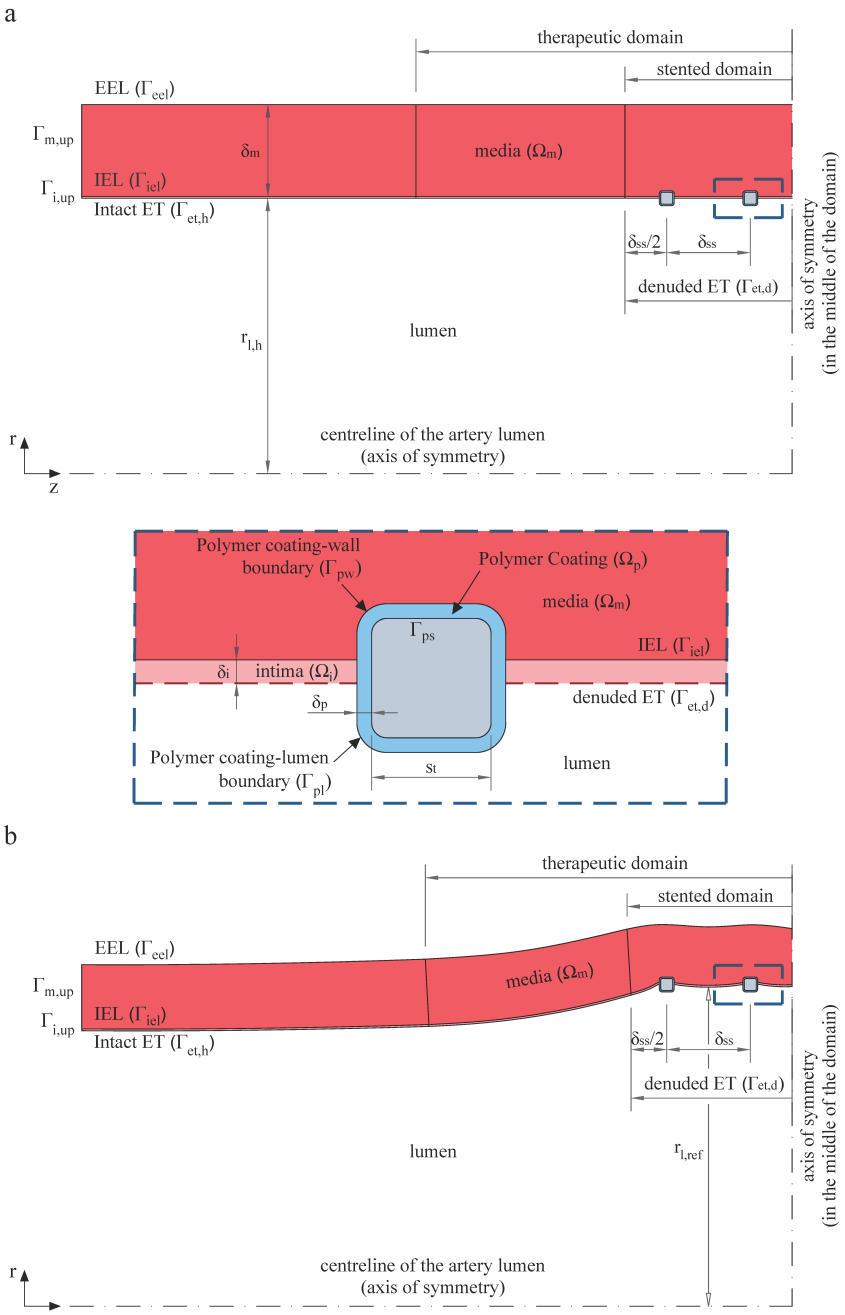


Figure 4.2: a: Longitudinal section view of the arterial wall prior to stent expansion. b: Longitudinal section view following stent expansion (20%). The inset highlights the polymer coating, intima, and denuded endothelium. $\Omega_j$ defines the various domains, where subscript $j = p, m, i$ denotes the polymer coating, media, and intima, respectively. $\Gamma$ is the symbol used to denote the different interfaces. The denuded and healthy endothelium are defined by $\Gamma_{et,d}$ and $\Gamma_{et,h}$, respectively. The polymer coating boundary is in contact with either the wall ($\Gamma_{pw}$) or lumen ($\Gamma_{pl}$), whilst $\Gamma_{ps}$ is the interface between the coating and the strut. The boundary between the intima and media is $\Gamma_{iel}$ whilst the perivascular edge is denoted $\Gamma_{eel}$. Upstream from the stent, the boundaries for the intima and media are $\Gamma_{i,up}$ and $\Gamma_{m,up}$, respectively.

### 4.2.2 Model geometry

The baseline model considers a multi–layered (intima and media), 2D–axisymmetric geometry which depicts a healthy segment of a coronary artery. In line with the newer generation of stents (e.g. Orsiro $^{TM}$ Biotronik, Bülach, Switzerland), the computational model considers a strut with a thickness in the ultra–thin range ($< 80\ \mu$m). Recently, promising results have been presented in a meta analysis against earlier devices hosting either 'thin' (80–100 $\mu$m) or 'thick' ($> 100\ \mu$m) struts [44]. The struts are coated circumferentially with a durable polymer of 8 $\mu$m in thickness, currently employed on commercial stents (e.g. Xience V $^{TM}$, Abbott Laboratories, Abbott Park, IL, USA). Moreover, an appropriate inter–strut spacing has to be defined. Various articles adopt a constant spacing of 0.7 mm between struts [55, 169, 188, 196, 307], of which the struts themselves are typically larger than those considered in this work. However, as suggested in [200], optimal inter–strut spacing for drug–eluting stents (DES) is often a consequence of the strut thickness, with the desired distance defined as $7\times T_{s_t}$, where $T_{s_t}$ is the total strut thickness. Finally, as is the case with other models of ISR, the struts are pre–embedded by 50% prior to stent expansion [55, 169]. All geometrical parameters associated with the computational model are listed in Table 4.1.

| Parameter | Description | Value / Expression | Reference(s) |
|---|---|---|---|
| $s_t$ | Strut thickness | 65 $\mu$m | [308–310]($\star$) |
| $\delta_{ss}$ | Strut spacing | $7 \times T_{s_t}$ | [200] |
| $\delta_i$ | Intima domain thickness | 0.01 mm | [55, 169] |
| $\delta_m$ | Media domain thickness | 0.5 mm | [55, 169] |
| $\delta_p$ | Polymer coating thickness | 0.008 mm | [169] |
| $r_l^h$ | Lumen radius | 1.5 mm | [188] |
| $T_{s_t}$ | Total strut thickness | 81 $\mu$m | - |

Table 4.1: Parameters of the baseline computational model. ($\star$): Representative of ultra–thin stent strut thickness range, for example: Orsiro $^{TM}$ (Biotronik, Bülach, Switzerland: 60 $\mu$m), MiStent $^{TM}$ (MiCell Technologies, Durham, NC, USA: 64 $\mu$m), and Coroflex ISAR $^{TM}$ (B. Braun Melsungen AG, Germany: 65 $\mu$m).

Fig. 4.2 schematically depicts the geometries considered: (a) a healthy and (b) a deformed artery. The lumen radii in both geometries are denoted by $r_{l,h}$ and $r_{l,ref}$, respectively. The difference in these values defines the impact of stent deployment, termed % overexpansion. Within the geometry, there exists two key areas of interest: the stented and therapeutic domain. Within the stented domain, the spatiotemporal behaviour of key model constituents are tracked. The therapeutic domain is defined as $3 \times \delta_{ss}$ from the centre of the outermost strut and tracks species behaviour either side of the stented lesion [55]. Beyond the therapeutic domain, a further extension in the model geometry is necessary such that the boundary conditions upstream/downstream from the lesion can be justified [55]. Fig. 4.2 also details the various domains ($\Omega$) and bound-

aries ($\Gamma$) present in the model. Details of these are presented in the figure, with each referenced within the text where appropriate.

In the computational model proposed, fluid flow within the lumen is not considered, with justification for neglecting the influence of fluid dynamics on restenosis provided in Section 4.4.3. Taken together with the idealised cylindrical arterial configuration, this assumption allows further reduction in the complexity of the geometry. Specifically, through symmetry, the model governing equations need only be solved on half of the arterial wall domain, with an axis of symmetry imposed between the middle two struts (Fig. 4.2). Thus, the baseline model considers 2 equally spaced struts, with symmetry implying a stent totalling 4 struts. However, the explicit number of total struts is not particularly important, where remodelling assuming a locally isotropic growth model demonstrates tissue growth profiles between struts that are identical, as noted by Escuer *et al.* [55]. Preliminary simulations supported this finding, where no difference in restenosis was observed in a stent hosting 4, 7, and 10 struts.

### 4.2.3 Step 1: stent expansion

The arterial model considered hosts two layers, the intima and media, of which both are modelled as hyperelastic, incompressible materials. The assumption of incompressibility has often been employed when analysing arterial wall elasticity [311]. Although supporting evidence is somewhat incomplete, Carew *et al.* [311] induced strains on thoracic aorta from dogs, showing that the volumetric strain was negligible, with similar studies also performed on an array of other arteries (carotid, iliac, etc.). This assumption has been supported by further evidence [312]. However, there is still some uncertainty on this topic as detailed in [313], with further work needed to explore this assumption in more detail. With the parameters of the constitutive model (Eqn. 4.1 [314]) attained under the assumption of incompressibility, the same assumption is then employed here for consistency.

Unlike the model proposed by Escuer *et al.* [55], which implements a Yeoh constitutive model, a more sophisticated model of arterial kinematics is considered. As such, the following strain energy function (SEF), devised by Gasser *et al.* [315], is considered:

$$\Psi_x = \underbrace{\mu(I_1-3)}_{\psi_{x,a}} + \overbrace{\sum_{\alpha=4,6} \frac{k_1}{2k_2}\left[\exp\left\{k_2\left[\kappa I_1 + (1-3\kappa)I_\alpha - 1\right]^2\right\} - 1\right]}^{\psi_{x,b}}, \tag{4.1}$$

where collagen fibre dispersion within each arterial layer is accounted for. The SEF ($\Psi_x$) is detailed in two parts: $\psi_{x,a}$ and $\psi_{x,b}$, where subscript $x = i,m$, for each layer present within the model. The former represents the isotropic potential of non–collagenous matrix, simulated as an incompressible isotropic material through a Neo–Hookean model. The parameter $\mu$, related only to the isotropic response of the arterial tissue, defines the shear modulus, whilst $I_1 = \mathrm{tr}(\boldsymbol{C})$, represents the first invariant of the right Cauchy–Green deformation tensor, $\boldsymbol{C}$ [316].

The second term ($\psi_{x,b}$) represents the structure tensor associated with collagen fibre distribution in each arterial layer. The key parameter here is $\kappa$, which is structural, and defines the distribution of collagen fibres such that $\kappa = 0$ and $\kappa = 1/3$ are the two extreme cases. The former ($\kappa = 0$) represents the case where fibres are perfectly aligned, and the latter ($\kappa = 1/3$) where the material is isotropic and a random distribution of collagen fibres is present [315]. Acquired from mechanical tests of tissue, $k_1$ and $k_2$ define the anisotropic contribution of collagen to the stress–strain response [314]. Anisotropy is introduced through the invariants $I_4 > 1$ and $I_6 > 1$, where fibres are active only when extended and bear no load when compressed [315, 316]. The invariants $I_4$ and $I_6$ describe the anisotropy of the arterial tissue and are measures of stretch for each family of collagen fibres. Associated with fibre stretch, $I_4$ and $I_6$ are defined as:

$$I_{4,6} = \boldsymbol{C} : \boldsymbol{M}_{4,6}, \tag{4.2}$$

where $\boldsymbol{M}_{4,6}$ is the fibre–structure tensor, such that $\boldsymbol{M}_4 = \boldsymbol{a_1} \otimes \boldsymbol{a_1}$ and $\boldsymbol{M}_6 = \boldsymbol{a_2} \otimes \boldsymbol{a_2}$ [316, 317]. The orientations of the two fibre families ($\boldsymbol{a}_{1,2}$) are given as $\boldsymbol{a_1} = [0, \cos\beta, \sin\beta]$ and $\boldsymbol{a_2} = [0, \cos\beta, -\sin\beta]$ [316, 317]. The two fibre families are aligned $\pm\beta$ with respect to the circumferential direction of the 2D–axisymmetric artery, documented schematically in Fig. 4.3 [317].

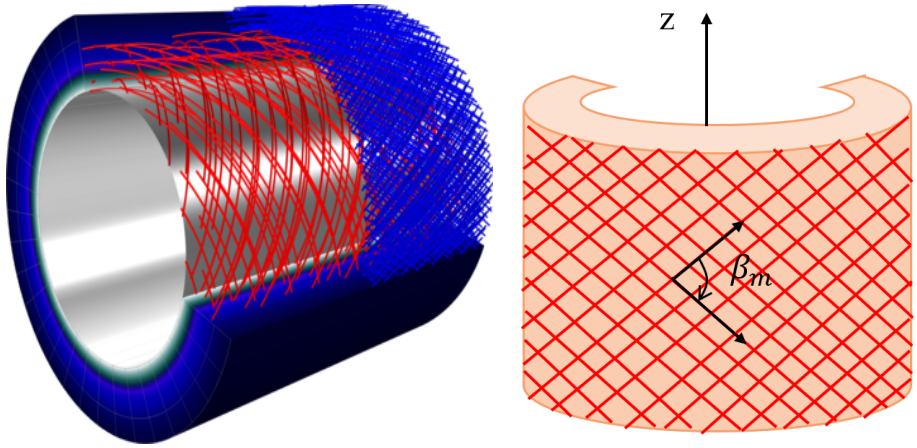


(a) (b)

Figure 4.3: Illustration of collagen fibres within the arterial wall. (a) Illustration of fibre families in the COMSOL model. Red fibres represent the media. Blue fibres represent the adventitia, discussed in Section 4.3.3. (b) Schematic representation illustrating mean angle ($\beta_m$) between the two families of collagen fibres in the media.

More details on the derivation of this constitutive model within a 2D–axisymmetric geometry can be found in [315–318]. Table 4.2 summarises the material parameters implemented within the constitutive model, acquired from [169]. The best–fitting parameters were obtained following a fit to experimental data in [314] which performed mechanical tensile tests on human coronary arteries, *in vitro*.

Mechanical models are also implemented for both the stent struts and the polymeric coating.

Newer stent designs often employ a cobalt chromium backbone (CoCr) as opposed to stainless steel, where higher radial strength and radio–opacity properties permit the adoption of these ultra–thin struts [319]. As simulated in [320], the metallic strut is modelled assuming a bilinear elastic–plastic relationship emulating the material properties of cobalt chromium alloy L6505. The mechanical properties implemented include the Young's modulus ($E$), density ($\rho$), Poisson's ratio ($\nu$), yield strength ($S_y$), and an ultimate tensile strength ($E_t$) [118, 169, 320]. Similarly, it is assumed that the stent coating considers a phosphorylcholine (PC)–based polymer and is modelled as a non–linear elastic material with bi–linear behaviour [169,320,321]. The parameter values proposed to describe the mechanical properties of the stent strut and polymer coating are detailed in Table 4.2.

M1: Arterial wall constitutive model parameters

| Layer | $\mu$ (kPa) | $k_1$ (kPa) | $k_2$ | $\kappa$ | $\beta$ (°) | Reference |
|---|---|---|---|---|---|---|
| Intima | 26.16 | 10485.2 | 20 | 0.165 | 50.02 | [169] |
| Media | 1.93 | 149.1 | 51.74 | 0.262 | 37.47 | [169] |

M2: Strut and coating model parameters

| Domain | $E$ (MPa) | $\rho$ (kg/m$^3$) | $\nu$ | $S_y$ (MPa) | $E_t$ (MPa) | Reference |
|---|---|---|---|---|---|---|
| Strut | $2.43{\cdot}10^5$ | 9700 | 0.3 | 476 | 680 | [320] |
| Coating | 240 | 1200 | 0.4975 | 16 | 7.7 | [320, 321] |

Table 4.2: (M1) Material parameters used to describe SEF (Eqn. 4.1) of the arterial wall layers. (M2) Values used to describe the mechanical properties of the polymeric coating and stent strut.

Within the 2D–axisymmetric model, the strategy for stent deployment presented in [55, 169] is implemented here. The lumen–interface boundary ($\Gamma_{et,d}$, $\Gamma_{et,h}$) is pressurised at 100 mmHg, emulating physiological conditions. A displacement condition is then prescribed on each individual strut to simulate stent deployment. Three clinically relevant levels of overexpansion (OE) are considered (10/20/30%), defined as:

$$\%OE = \left( \frac{r_{l,ref}}{r_{l,h}} - 1 \right) \times 100, \tag{4.3}$$

where $r_{l,ref}$ is the lumen radius within the stented domain, post–expansion, and $r_{l,h}$ is the lumen radius within the unstented domain, equivalent to that present pre–expansion in a healthy vessel, as detailed in Fig. 4.2. To couple the stent expansion and species evolution model, the deformed configuration (Fig. 4.2b) and the Von Mises stress ($\sigma_{vm}$) map are exported from the former and utilised within the latter to stimulate the healing response.

### 4.2.4 Step 2: species evolution

Fig. 4.1 summaries the key species implemented within the restenosis model, of which there are seven in total: damage, GFs, synthetic smooth muscle cells (sSMCs), contractile smooth muscle cells (cSMCs), ECM, MMPs, and ECs. The complexity of this process is truly immeasurable with much of the biology still unknown [56]. Thus, the species simulated are those where an understanding of the biological interactions are relatively well characterised. Within the intima and media, the proliferation, migration, differentiation and apoptotic nature of cellular species are considered with the productive and degenerative properties of non–cellular constituents also modelled. The adventitia is presented only as a boundary condition ($\Gamma_{eel}$) with the effects of flow also neglected. Details on all model limitations are discussed in more depth in Sec. 4.4. In general, the species evolution model in [55] is adopted here, with significant changes made to equations that describe the sSMC and ECM species.

#### 4.2.4.1 Damage ($d$)

The biological cascade of events which formulates excessive tissue growth is triggered via a mechanical stimulus [322, 323]. Note that the mechanical factors associated with stent deployment are not explicitly modelled within this work and the mechanotransduction of ECs, for example, are ignored [56, 61, 324]. Instead, a protocol presented in [54, 55] is considered, where a degree of injury ($0 \rightarrow 1$) is assigned to the artery in proportion to the stress ($\sigma_{vm}$) present following stent deployment. Damage, $d(r,z,t)$, is the variable implemented to emulate vascular injury. Inferior ($\sigma_{vm,inf}$) and superior ($\sigma_{vm,sup}$) stress limits which correlate to minimum (0) and maximum (1) levels of damage, respectively are acquired from [314]. As a result, the initial level of damage ($d^0$) is defined by these limits, where a linear piecewise function details the response between these upper and lower bounds:

$$d^0 = \begin{cases} 0 & \text{if} \quad \sigma_{vm} \leq \sigma_{vm,inf}, \\ \dfrac{\sigma_{vm} - \sigma_{vm,inf}}{\sigma_{vm,sup} - \sigma_{vm,inf}} & \text{if} \quad \sigma_{vm,inf} < \sigma_{vm} < \sigma_{vm,sup}, \quad \text{in } \Omega_i \,\&\, \Omega_m, \quad t = 0. \\ 1 & \text{if} \quad \sigma_{vm} \geq \sigma_{vm,sup}, \end{cases} \tag{4.4}$$

the level of damage is then assumed to decay continuously [55]:

$$\frac{\partial d}{\partial t} = -k_d \, d \, c_{mmp}, \quad \text{in } \Omega_i \,\&\, \Omega_m, \quad t > 0, \tag{4.5}$$

where $k_d$, the rate of decay of damage, is linked directly to the current MMP concentration, $c_{mmp}(r,z,t)$.

#### 4.2.4.2 Growth factors (GFs)

Upon injury, the inflammatory response involves the infiltration of leukocytes and macrophages [56]. These cells then secrete chemicals which upregulate the production of an abundance of growth factors including, but not limited to, platelet–derived GF (PDGF), epidermal GF (EGF), and transforming GF (TGF) which behave in harmony to promote healing [56]. With the specific behaviour of each still poorly understood, the efforts here encompass the behaviour of all growth factors within a single species, $c_{gf}\ (r,z,t)$. The rate of change of GFs is detailed by:

$$\frac{\partial c_{gf}}{\partial t} = D_{gf}\nabla^2 c_{gf} + g_{gf}\, d\left(1 - \frac{c_{gf}}{K_{gf}}\right) - k_{gf}\left(c_{gf} - c_{gf}^0\right), \quad \text{in } \Omega_i \,\&\, \Omega_m, \quad t > 0, \tag{4.6}$$

where $c_{gf}^0$ defines the concentration of GFs at $t = 0$, assumed constant throughout the intima and media. Moreover, the movement of growth factors is mediated by diffusion, with associated diffusion coefficient, $D_{gf}$, assumed constant and isotropic. The production of GFs to some upper limit, $K_{gf}$, is controlled by the level of injury ($d$) present within the wall at any given time. Other sources of GF production exist, where either concentration can be modelled as in–flux through the endothelium, where entry is permitted in relation to the functionality of the semi–permeable membrane, simulated recently in [221]. However, to simplify an already complex model, it is assumed that the increase in GFs is mediated by damage alone. This mimics the inflammatory response, a key event responsible for the large surplus in species that promote healing. Moreover, the degradation of GFs is assumed constant, controlled by $k_{gf}$.

#### 4.2.4.3 Smooth muscle cells (SMCs)

The heterogeneity of the vascular wall is modelled by accounting for both SMC phenotypes. Within a healthy vessel, the contractile SMCs dominate, where vessel quiescence is maintained through chemical mediators released from the endothelial layer [70]. However, following vascular injury, a phenotype switch is induced where a surge in active, synthetic SMCs is present. Various mechanisms are associated with the de–differentiation of SMCs, inclusive of: a rise in GF concentration; drop in nitric oxide concentration as a result of absent and/or dysfunctional endothelium; low vessel shear stress; and a drop in ECM concentration [54,56,70,71,325,326]. The cSMC species is given by:

$$\frac{\partial c_{csmc}}{\partial t} = -k_{csmc}^{diff}\, c_{csmc}\, K_{ssmc}^{ecm} + k_{ssmc}^{diff}\, c_{ssmc}\, K_{csmc}^{ecm}, \quad \text{in } \Omega_i \,\&\, \Omega_m, \quad t > 0, \tag{4.7}$$

where $c_{csmc}\ (r,z,t)$ defines the concentration of contractile SMCs, initially present at a concentration of $c_{csmc}^0$ within the media only, assuming that no SMCs exist in the intima prior to vascular injury. The de–differentiation ($k_{cSMC}^{diff}$) and differentiation ($k_{ssmc}^{diff}$) rates mediate phenotype conversion to a synthetic and contractile phenotype, respectively. Similar to [54, 55], the

ECM concentration is assumed to control SMC phenotype through the following expressions:

$$K_{ssmc}^{ecm} = -(e^{-((c_{ecm}^0/c_{ecm})-1)-|(c_{ecm}^0/c_{ecm})-1|} - 1), \tag{4.8}$$

$$K_{ssmc}^{ecm} = -(e^{-((c_{ecm}/c_{ecm}^0)-1)-|(c_{ecm}/c_{ecm}^0)-1|} - 1), \tag{4.9}$$

where a decrease in ECM concentration ($c_{ecm} < c_{ecm}^0$) results in a surge of sSMCs, whilst the opposite is true when ECM repopulates the domain and surpasses its initial concentration ($c_{ecm} \geq c_{ecm}^0$). It is assumed that the dormant phenotype is unperturbed by growth factors and other mediators that stimulate growth, where their migratory and proliferative capacities are notably less than that of the active phenotype, where filaments and proteins within the cell differ [71]. The more active, synthetic phenotype, $c_{ssmc}\,(r,z,t)$, is modelled as:

$$\frac{\partial c_{ssmc}}{\partial t} = D_{ssmc}\nabla^2 c_{ssmc} - \frac{\partial c_{csmc}}{\partial t} + P_{ssmc} - k_{ssmc}\, c_{ssmc} \quad \text{in } \Omega_i \;\&\; \Omega_m, \quad t > 0, \tag{4.10}$$

where the initial density is zero at $t = 0$, and only appear following vascular injury as given by $\partial c_{csmc}/\partial t$. The proliferation of synthetic SMCs ($P_{ssmc}$) is governed by:

$$P_{ssmc} = g_{ssmc}\, c_{gf}\, c_{ssmc} \left(1 - \frac{c_{ecm}}{K_{ecm}^1}\right), \tag{4.11}$$

where the increase in sSMCs is primarily a consequence of increased GF concentration, similar to what was assumed in [55]. However, differently from [55], here spatial elements are introduced, where ECM controls the rate of proliferation through a logistical expression, where the upper limit, $K_{ecm}^1$, is defined by Eqn. 4.13. Moreover, the current density of sSMCs is also accounted for, known to increase GF production as they proliferate [327]. The death of sSMCs is possible through apoptosis, described by a linear decay rate constant, $k_{ssmc}$. The migration of cells is accounted for through a diffusive term, where the diffusion coefficient, $D_{ssmc}$, is assumed constant and isotropic.

#### 4.2.4.4 Extracellular matrix (ECM)

The ECM is an essential constituent present in the arterial wall, providing structural support to the vessel; responsible for cell–matrix interactions throughout the remodelling process [60,326]. Moreover, as the restenotic tissue matures, ECM becomes its dominant constituent, and SMC proliferation is minimal. [56, 60, 76]. In the model proposed, collagen is considered to be the dominant component of ECM. The model governing ECM is:

$$\frac{\partial c_{ecm}}{\partial t} = g_{ecm} c_{ssmc} \left(1 - \frac{c_{ecm}}{K^1_{ecm}}\right) - k_{ecm} \left(c_{mmp} - c^0_{mmp}\right) \left(1 - \frac{K^2_{ecm}}{c_{ecm}}\right), \quad \text{in } \Omega_i \,\&\, \Omega_m, \quad t > 0, \tag{4.12}$$

where $c_{ecm}\,(r,z,t)$ is the ECM concentration, initially present in all domains at a healthy concentration, $c^0_{ecm}$. The synthesis of ECM is predominantly mediated by SMCs [328] at a rate $g_{ecm}$ and degraded at a rate of $k_{ecm}$ through an increase in MMP production. Improving upon the arbitrary upper limit considered in [55], ECM synthesis is now assumed to be mediated by the level of damage present in the wall following stent deployment:

$$K^1_{ecm} = c^0_{ecm}(1+\theta), \tag{4.13}$$

where $\theta$ is the mean damage ($d$) present in the stented area at $t = 0$, computed as:

$$\theta = \frac{1}{V_s} \int_{V_s} d \, \mathrm{d}V_s, \tag{4.14}$$

where $V_s$ is the volume of the stented domain.

In line with trends present clinically, the model ensures that vascular injuries of greater severity allow for increased ECM synthesis during vessel remodelling [329]. Moreover, degradation to a lower limit of $K^2_{ecm}$ ensured that negative concentrations are not possible.

#### 4.2.4.5 Matrix metalloproteinases (MMPs)

MMPs are a large family of enzymes that exist to mediate ECM degradation. Similar to [55], the model proposed specifically refers to MMP–2. This particular enzyme is responsible for cleaving a large range of ECM constituents, where elevated serum levels have been observed clinically in follow–ups where significant levels of ISR was present [56, 60, 330]. The rate of change of MMPs is described by the following equation:

$$\frac{\partial c_{mmp}}{\partial t} = D_{mmp} \nabla^2 c_{mmp} + \left(g^{ssmc}_{mmp} c_{ssmc} + g^{csmc}_{mmp} c_{csmc}\right) d \left(1 - \frac{c_{mmp}}{K_{mmp}}\right) - k_{mmp} \left(c_{mmp} - c^0_{mmp}\right), \quad \text{in } \Omega_i \,\&\, \Omega_m, \quad t > 0, \tag{4.15}$$

where $c_{mmp}\,(r,z,t)$ is the MMP concentration, initially $c^0_{mmp}$ within the arterial wall. Both SMC phenotypes ($c_{csmc}$ and $c_{ssmc}$) synthesise additional MMPs through $g^{ssmc}_{mmp}$ and $g^{csmc}_{mmp}$, respectively, further upregulated by $d$ to initiate an inflammatory response that drives healing by increasing MMP concentration to some upper limit, $K_{mmp}$. The movement of MMPs is enabled through a diffusive term, which is assumed constant and isotropic ($D_{mmp}$). The degradation of MMPs is

controlled through a linear rate constant, $k_{mmp}$.

#### 4.2.4.6 Endothelial cells (ECs)

A fully functional endothelial layer present after stent deployment represents a healed artery. Responsible for many tasks, the presence of this layer ensures natural order within the vessel, where the release of numerous chemical mediators (e.g. nitric oxide) help maintain vessel quiescence [53, 58, 331]. Moreover, ECs have established mechanotransduction capabilities, where mechanical forces influence their behaviour [322, 324]. However, vessel quiescence is absent following stent deployment, where vascular injury is apparent through the denudation of the endothelial layer. The absence of this layer triggers a series of events which stimulate the healing response through the recruitment of inflammatory cells, halted only by the presence of a fully functional sheet of ECs. Similarly to Escuer *et al.* [55], EC regeneration is modelled independently of other species such that:

$$\frac{\partial c_{ec}}{\partial t} = D_{ec}\nabla^2 c_{ec} + g_{ec}\, c_{ec}\left(1 - \frac{c_{ec}}{K_{ec}}\right), \quad \text{in } \Omega_i, \quad t > 0 \tag{4.16}$$

where $c_{ec}\,(r,z,t)$ is the density of ECs permitted to migrate via $D_{ec}$, $g_{ec}$ is the rate of EC recovery and $K_{ec}$ is the upper limit, depicting a healed endothelial layer. To elicit a healing response, it is assumed that the number of ECs residing with the stented domain initially is approximately zero, mimicking endothelial denudation as a consequence of stent deployment [53, 67]. In the domains unaffected by stenting, the initial EC concentration ($c^0_{ec}$) is equivalent to $K_{ec}$.

#### 4.2.4.7 Model parameters

The species evolution model hosts an array of parameters, describing the diffusion, production/proliferation, and death/degradation of many constituents. Most parameters have been acquired from [55], with the exception of $g_{ssmc}$ and $K^1_{ecm}$. The former exhibits different units, with sSMC equation now amended to be influenced by several species. The value was chosen such that the proliferative trends were comparable with [55]. As for the latter, its value is dictated by Eqn. 4.13, proportional to the level of damage present in the artery following stent deployment. Table 4.3 summarises all parameters and their values.

#### 4.2.4.8 Boundary conditions

For the species evolution model, constituents reside generally within two domains, the intima ($\Omega_i$) and the media ($\Omega_m$). Only $c_{ec}$ is exclusive to a single domain ($\Omega_i$). As a result, a zero–flux condition, $-\boldsymbol{n}\cdot(-D_{ec}\nabla c_{ec}) = 0$, is imposed on all relevant boundaries ($\Gamma_{et,h}, \Gamma_{et,d}, \Gamma_{i,up}$, and $\Gamma_{iel}$), where $\boldsymbol{n}$ is the unit normal vector. As for the remaining six species ($c_{ssmc}, c_{csmc}, c_{gf}, c_{mmp}, c_{ecm}$, and $d$), a zero–flux condition is imposed on all outer boundaries

| Parameter | Description | Value | Reference |
|---|---|---|---|
| $k_d$ | Damage degradation | 0.5 $m^3$ $mol^{-1}$ $s^{-1}$ | [55] |
| $g_{gf}$ | GF production | $8\times10^{-13}$ mol $m^{-3}$ $s^{-1}$ | [55] |
| $k_{gf}$ | GF degradation | $1.27\times10^{-6}$ $s^{-1}$ | [57] |
| $g_{mmp}^{csmc}$ | MMP production by cSMCs | $3\times10^{-26}$ mol $cell^{-1}$ $s^{-1}$ | [55] |
| $g_{mmp}^{ssmc}$ | MMP production by sSMCs | $6\times10^{-26}$ mol $cell^{-1}$ $s^{-1}$ | [57] |
| $k_{mmp}$ | MMP degradation | $4.63\times10^{-6}$ $s^{-1}$ | [55] |
| $g_{ecm}$ | ECM synthesis | $2.157\times10^{-11}$ g $cell^{-1}$ $s^{-1}$ | [228] |
| $k_{ecm}$ | ECM degradation | $2\times10^{3}$ $s^{-1}$ | [55] |
| $k_{csmc}^{diff}$ | cSMC differentiation | $5\times10^{-7}$ $s^{-1}$ | [211] |
| $k_{ssmc}^{diff}$ | sSMC differentiation | $2.314\times10^{-6}$ $s^{-1}$ | [211] |
| $g_{ssmc}$ $(\star)$ | sSMC proliferation rate | 3.5 $m^3$ $mol^{-1}$ $s^{-1}$ | Estimated |
| $k_{ssmc}$ | sSMC apoptosis | $2.2\times10^{-10}$ $s^{-1}$ | [183] |
| $g_{ec}$ | EC proliferation | $1\times10^{-6}$ $s^{-1}$ | [275] |
| $D_{gf}$ | GFs | $2.6\times10^{-11}$ $m^2$ $s^{-1}$ | [332] |
| $D_{mmp}$ | MMPs | $1.2\times10^{-12}$ $m^2$ $s^{-1}$ | [55] |
| $D_{ssmc}$ | sSMCs | $1.85\times10^{-13}$ $m^2$ $s^{-1}$ | [304] |
| $D_{ec}$ | ECs | $8\times10^{-14}$ $m^2$ $s^{-1}$ | [332] |
| $c_{gf}^0$ | GFs | $3.48\times10^{-7}$ mol $m^{-3}$ | [333] |
| $c_{mmp}^0$ | MMPs | $3.83\times10^{-7}$ mol $m^{-3}$ | [334] |
| $c_{ecm}^0$ | ECM | 6.67 mol $m^{-3}$ | [334] |
| $c_{csmc}^0$ | cSMCs | $3.16\times10^{13}$ cell $m^{-3}$ | [335] |
| $c_{ssmc}^0$ | sSMCs | 0 cell $m^{-3}$ | [336] |
| $c_{ec}^0$ | ECs | $5\times10^{11}$ cell $m^{-3}$ | [337] |
| $K_{gf}$ | GFs | $10\times c_{gf}^0$ | [55] |
| $K_{mmp}$ | GFs | $10\times c_{mmp}^0$ | [55] |
| $K_{ecm}^1$ $(\star)$ | ECM upper limit | $c_{ecm}^0(1+\theta)$ | Estimated |
| $K_{ecm}^2$ | ECM lower limit | $0.1\times c_{ecm}^0$ | [55] |
| $r_{ec}$ | EC radius | 17.87 $\mu$m | [54] |
| $r_{smc}$ | SMC radius | 3.75 $\mu$m | [55] |
| $l_{smc}$ | SMC length | 115 $\mu$m | [55] |
| $\rho_{ecm}$ | ECM density | 1 g $ml^{-1}$ | [334] |

Table 4.3: Model parameters for the restenosis model. Estimated parameters are denoted with a $\star$.

($\Gamma_{et,h}, \Gamma_{et,d}, \Gamma_{eel}, \Gamma_{i,up}$, and $\Gamma_{m,up}$) whilst continuity is assumed between the two layers of the artery ($\Gamma_{iel}$). The reader is referred to Fig. 4.2 where all boundaries have been defined.

### 4.2.5 Step 3: remodelling

Following the evolution of species, the depiction of excess tissue growth is necessary. Similar to [55,228,336,338] the growth of biological tissue within a continuum framework is considered. Volumetric tissue growth is simulated as an open system, where interactions between species drive a change in the geometrical configuration. Accordingly, the balance of mass within the system must satisfy:

$$\frac{\partial \rho_\eta^0}{\partial t} = \Pi_\eta - \nabla \cdot M_\eta, \tag{4.17}$$

where $\eta$ indicates the species contributing to growth. The concentration of species within the reference configuration is denoted by $\rho_\eta^0$. $M_\eta$ and $\Pi_\eta$ correspond to the mass flux and source and sink terms (e.g. proliferation, production, death, and degradation) of all model constituents, respectively.

With the model encompassing many species, the total material density ($\rho^0$) can simply be computed as the sum of all its constituents, such that $\rho^0 = \sum_\eta \rho_\eta^0$. Through the previously described species evolution model, it is known that each variable, denoting constituent behaviour, evolves in time which would consequently alter the reference configuration. In other words, the configuration will swell if the domain is populated in excess or shrink following a decrease in the concentration and/or density of its constituents. With this approach assuming that volumetric changes are locally isotropic, then the following growth deformation tensor is defined $F_\eta^g = \rho_\eta^0 / \rho_\eta^{init} \boldsymbol{I}$ [55, 338], where $\rho_\eta^{init}$ is the initial density of species $\eta$ in the reference configuration and $\boldsymbol{I}$ is the isotropic tensor of the second order. Moreover, under the small strain hypothesis, then:

$$\nabla \cdot v_\eta = \frac{\rho_\eta}{\rho_\eta^{init}}, \tag{4.18}$$

where $v_\eta$ is the velocity of material points [55, 228]. Although the remodelling process is inclusive of many cellular and non–cellular constituents, it is ECs, ECM, and SMCs (contractile and synthetic) that are the primary components of restenotic tissue [60]. As a result, isotropic tissue growth that leads to restenosis is given by:

$$\nabla \cdot v_\eta = \frac{\partial \Delta c_{ec}}{\partial t} V_{ec} + \frac{\partial \Delta c_{smc}}{\partial t} V_{smc} + \frac{\partial \Delta c_{ecm}}{\partial t} \frac{1}{\rho_{ecm}}, \tag{4.19}$$

where $\Delta c_\eta$ defines the difference in species concentration from its initial value in the reference configuration, $\rho_\eta^0$. The volume ($V_\eta$) of cellular components and the density ($\rho_\eta$) of non–cellular components give rise to tissue growth. Although more complex in shape, for simplicity, it is assumed that the volume of ECs are spherical (Eqn. 4.20) [54, 55] and SMCs ellipsoidal (Eqn.

4.21) [71]:

$$V_{ec} = \frac{4}{3}\pi r_{ec}^3, \tag{4.20}$$

$$V_{smc} = \frac{4}{3}\pi r_{smc}^2 l_{smc}, \tag{4.21}$$

where ECs have a characteristic radius, $r_{ec}$, and SMCs have a characteristic radius and length of $r_{smc}$ and $l_{smc}$, respectively.

### 4.2.6 Numerical methods

The commercially available software COMSOL Multiphysics 5.6a (COMSOL AB, Burlington, MA, USA) was used to create the finite element (FE) mesh and to numerically solve the multiscale model. The computational model proposed can be separated into three distinct steps as presented in Fig. 4.1. The initial step involves the deformation of the artery, where, through a stationary study, the stent struts are displaced into the arterial wall subjecting the geometry to high levels of stress. The second step utilises the deformed configuration and arterial stresses from step 1 to trigger the biological cascade of events which defines restenosis, simulated as a transient process. Finally, remodelling by means of volumetric tissue growth is simulated as a further stationary study. Here, the difference between the initial and final concentration/density of key species are computed to quantify the severity of excess tissue after some time.

A mesh independence study was considered to ensure results were accurate, investigating the impact of mesh coarseness on damage and % area restenosis (defined in Section 4.2.8). The computational model employs two different geometries and thus two model files, highlighted in Fig. 4.2. The initial stationary step involves stent deployment, where the damage field generated is an essential component of the subsequent species evolution model. Testing the nine different built–in mesh options within COMSOL, labelled: extremely coarse (M1), extra coarse (M2), coarser (M3), coarse (M4), normal (M5), fine (M6), finer (M7), extra fine (M8), and extremely fine (M9), the resulting damage field, along a line between the middle two struts (2 and 3) is examined within the 30% expansion case (Fig. 4.4a). The inset highlights a negligible difference in response between M5–9. However, with computational time similar across the five cases, M9 is considered moving forward to ensure the most accurate depiction of damage across the entire domain.

The next step is the species evolution model which couples together the behaviour of many species. Although many of the model constituents could be tracked to test mesh accuracy, the computation of % area restenosis is considered as the index of choice, a consequence of the interplay between all species. To ensure optimal mesh selection, a change in the index of interest below 0.5% across multiple iterations is desired. Similar to the previous step, there are nine meshes such that the labels $M_{a\rightarrow h}$ detail the difference in % area restenosis across two successive

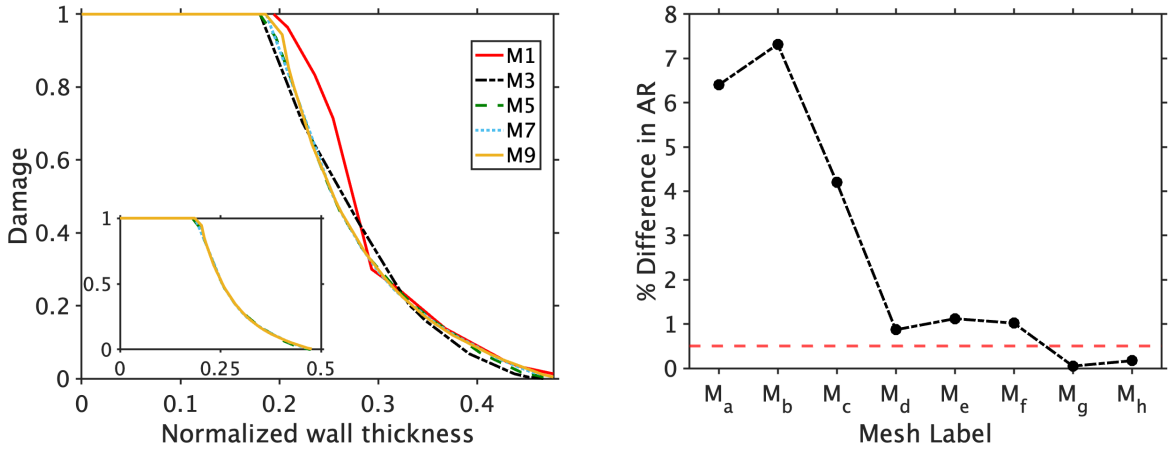


Figure 4.4: Mesh study using all of COMSOLs in–built mesh operations. (a) The damage profile directly between strut 2 and 3. The inset highlights M5/7/9. (b) % change in area restenosis (AR) values between consecutive meshes for the species evolution model (computation detailed in Section 4.2.8). Horizontal red line depicts the threshold of interest (0.5% change).

meshes, where $M_a$ is the difference between extremely and extra coarse and so on. From Fig. 5.3, it is clear that mesh labels $M_g$ and $M_h$ are sufficient which consider meshes that are finer, extra fine, and extremely fine, respectively.

Although a 'finer' mesh is adequate, with 'extremely fine' considered, the computational time is still very low, under 20 minutes for a mesh hosting approximately 32,000 elements. Moreover, further efforts (Chapter 5) will explore the role of drug on restenosis, which is known from literature [169, 196] to require particularly fine meshes as a consequence of non–linear binding. Thus, to ensure consistency between simulations employing and neglecting drug binding, the finest mesh is considered.

In all cases, the mesh discretized each domain of the model with a combination of triangular and quadrilateral elements. The baseline model hosted approximately 32,000 elements (halved geometry) and 58,000 elements in the complete model. However, the former value increased towards 75,000 elements in larger domains which explored perturbations in strut thickness and stent design. In the baseline model, the total computation time was approximately 35 minutes, increasing beyond an hour for longer domains where mesh element number was notably increased.

For all stationary problems, a direct linear solver (MUMPS) was considered with a relative error tolerance of $10^{-3}$. The implicit backward differentiation formula (BDF) method was used for the time discretization of the transient study step with a variable order of accuracy ranging from one to five in order to obtain better stability and maintain a suitable time–step size. Further stability was ensured by enabling the nonlinear controller and restricting the maximum

time–step to 10,000 seconds. The relative and absolute tolerances were set to $10^{-3}$ and $10^{-4}$, respectively. All simulations employed 16 cores of an AMD™ Ryzen 9 5950X CPU @ 3.40 GHz processor.

### 4.2.7 Summary of investigated cases

Stent design is an important factor in determining patient outcome following percutaneous coronary intervention (PCI), where strut thickness and inter–strut spacing have been focal points since bare metal stents (BMS) were first deployed [32]. Thus, a variety of different cases are considered that examine the impact of: strut thickness (ST), strut embedment (SE), and inter–strut spacing (SS) following stent deployment. Details of each of the different cases are summarised in Table 5.4.

Study A: Rationale for model changes from [55]

| Case | Name | % OE | ST [$\mu$m] | SE [%] | SS | Constitutive model(s) |
|---|---|---|---|---|---|---|
| A1 | Replication of the SEM in [55] | 10, 20, 30 | 65 | 50 | $7\times T_{s_t}$ | HGO |
| A2 | No ECM in restenotic tissue | 10, 20, 30 | 65 | 50 | $7\times T_{s_t}$ | HGO |
| A3 | New ECM threshold | 10, 20, 30 | 65 | 50 | $7\times T_{s_t}$ | HGO & Yeoh |
| A4 | New sSMC proliferation expression | 10, 20, 30 | 65 | 50 | $7\times T_{s_t}$ | HGO & Yeoh |

Study B: Impact of stent expansion and geometry

| Case | Name | % OE | ST [$\mu$m] | SE [%] | SS | Constitutive model |
|---|---|---|---|---|---|---|
| B1 | Baseline model (R4) | 10, 20, 30 | 65 | 50 | $7\times T_{s_t}$ | HGO |
| B2a | Impact of ST | 20, 30 | 65, 105, 145 | 50 | $7\times T_{s_t}$ | HGO |
| B2b | Impact of SE | 20, 30 | 65 | 30, 50, 70 | $7\times T_{s_t}$ | HGO |
| B2c | Impact of SS | 20, 30 | 65 | 50 | $SS_{small}$ & $SS_{large}$ | HGO |
| B3 | Sensitivity study | 20 | 65 | 50 | $7\times T_{s_t}$ | HGO |

Study C: Exploring further model improvements

| Case | Name | % OE | ST [$\mu$m] | SE [%] | SS | Constitutive model |
|---|---|---|---|---|---|---|
| C1 | Inclusion of adventitia | 20, 30 | 65 | 50 | $7\times T_{s_t}$ | HGO |

Table 4.4: Summary of the different cases considered. Study A: To explore rationale for model changes from [55]. SEM = Species evolution model. Study B: Investigates stent design. Case B1 investigates species behaviour across the three expansion profiles. Cases B2a-c looks at perturbations in stent design, focusing on the impact on % area restenosis. Case B3 studies the impact of perturbations in certain model parameters ($g_{ssmc}, g_{ecm}, k_{ecm}$). Study C: Investigates further model improvements in isolation of the fully coupled system. HGO = Holzapfel–Gasser–Ogden model, as defined in Eqn. 4.1.

Firstly, the previously published species evolution model by Escuer *et al.* [55] is revisited, where a new constitutive model has been implemented (A1). A series of additional cases are then considered, inclusive of: (A2) only SMCs contribute to restenotic tissue, (A3) a new ECM threshold expression, and (A4) a new sSMC proliferation term. The aim of these being to pursue a more realistic model of species evolution, and thus restenosis.

Following the derivation of the baseline model to be used in all subsequent simulations (A4), three different expansion profiles are simulated and the behaviour this has on the model constituents is explored in Study B. The importance of strut configuration is then assessed, where amendments in strut thickness (ST) and strut embedment (SE) are considered within the baseline configuration, where strut spacing (SS) follows the $7\times T_{s_t}$ expression as referred to earlier. When assessing the impact of SS, different stent designs are proposed, where the strut number varies within the stented lesion. As such, two different cases are proposed: $\mathrm{SS_{small}}$ and $\mathrm{SS_{large}}$. The former comprises of 7 struts within a fixed lesion of 5 mm, whilst the latter hosts just four struts, where SS is significantly increased as a result; an approach similar to that proposed in [101]. The final case (B3) of study B is a local sensitivity analysis of certain model parameters. With adjustments made to the sSMC and ECM species (A3, A4), the key constituents that drive restenosis, the effect of sSMC proliferation ($g_{ssmc}$), ECM synthesis ($g_{ecm}$), and ECM degradation ($k_{ecm}$) are explored where the effect on tissue growth is likely to be significant. Perturbations in all other model parameters have been discussed in depth in [55], to which the reader is referred to for further details.

Finally, a third study is proposed that investigates specific attributes of the computational model in isolation of the fully coupled system; assessing the inclusion of the adventitia layer on the stress distribution following stent deployment.

### 4.2.8 Analysis of results

To facilitate comparison between all cases within a given study, the difference in % area restenosis (% AS) is computed. With efforts focusing on an idealised, healthy artery, it is assumed that the smallest radius within the stented region defines the severity of restenosis. Therefore, assuming the geometry to be cylindrical at this point, the area which depicts growth can be considered circular. Thus, comparing the lumen radius post expansion ($r_{l,ref}$) and following remodelling ($r_{l,g}$) the severity of tissue growth is given as:

$$\%AS = \left(1 - \frac{\pi r_{l,g}^2}{\pi r_{l,ref}^2}\right) \times 100, \tag{4.22}$$

as depicted schematically in Fig. 4.5. The level of tissue growth should portray significant changes in key species behaviour, in particular SMC proliferation and ECM synthesis, covered by a fully functional endothelial layer. In addition to the computation above, constituent behaviour is tracked at various points within the domain, highlighting how their response varies following stent deployment. Unless otherwise stated, a point of interest 0.05 mm behind the second stent strut is considered to visualise the response of all medial species, whilst ECs are visualised immediately adjacent to the strut.

Initially, species evolution is simulated over a 300–day period, with tissue growth computed thereafter. However, shorter periods of growth are also considered, noting the significance of the

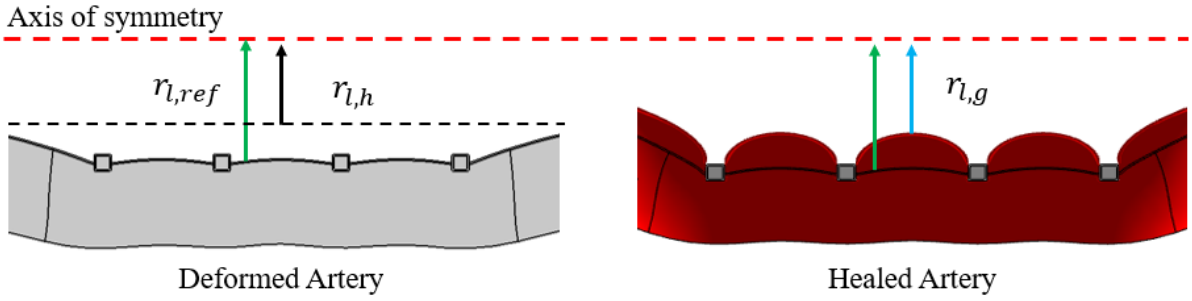


Figure 4.5: Deformed configuration depicts severity in overexpansion, highlighting difference in lumen radii pre ($r_{l,h}$) and post–expansion ($r_{l,ref}$). The geometry comprising the healed artery highlights volume of tissue growth, where severity in restenosis can be computed by the difference present between $r_{l,ref}$ and $r_{l,g}$.

healing response at early times, providing justification for computational time to be shortened in subsequent chapters inclusive of drug.

## 4.3 Results and discussion

### 4.3.1 Study A: rationale for model changes

Although the state–of–the–art continuum model of ISR published by Escuer *et al.* [55] is able to demonstrate broad agreement with clinical trends, there are notable aspects which could be improved. Firstly, case A1 replicates the species evolution model in [55] and notes an over synthesis of ECM when the HGO SEF (Eqn. 4.1) is implemented. This was further emphasised in case A2, which was purely investigatory in nature, where the contribution of ECM to restenosis was neglected. In other words, Eqn. 4.19 simplifies such that only an excess of SMCs and ECs give rise to restenotic tissue. Moreover, $K^1_{ecm}$ was chosen to be equal to $c^0_{ecm}$ in Eqn. 4.12, such that ECM was not able to synthesise in excess of its initial concentration. Following this, in an attempt to improve the realism of the species evolution model, amendments to ECM synthesis (A3) and sSMC proliferation (A4) are proposed. Note that direct comparisons cannot be made with [55] in A1 as a result of the differences in the geometrical configuration. Nonetheless, the significance of a more sophisticated constitutive law is demonstrated in A3 and A4, where two versions of the restenosis model are proposed: one which implements a Yeoh constitutive law, and the other a HGO constitutive law.

#### 4.3.1.1 Investigation of the species evolution model

In case A1, the restenosis model is updated to account for a new constitutive model of arterial kinematics, yet the species evolution model is indifferent to that in [55]. The results (Fig. 4.6) of A1 noted an excessive production of ECM within restenotic tissue as part of the vessel

remodelling process at lower stent expansions (e.g. 10%). This becomes clearer when comparing A1 and A2 simultaneously, where the former is a direct implementation of the species evolution model in [55] and the latter is the same model, but limits ECM synthesis to its initial concentration only ($c^0_{ecm}$).

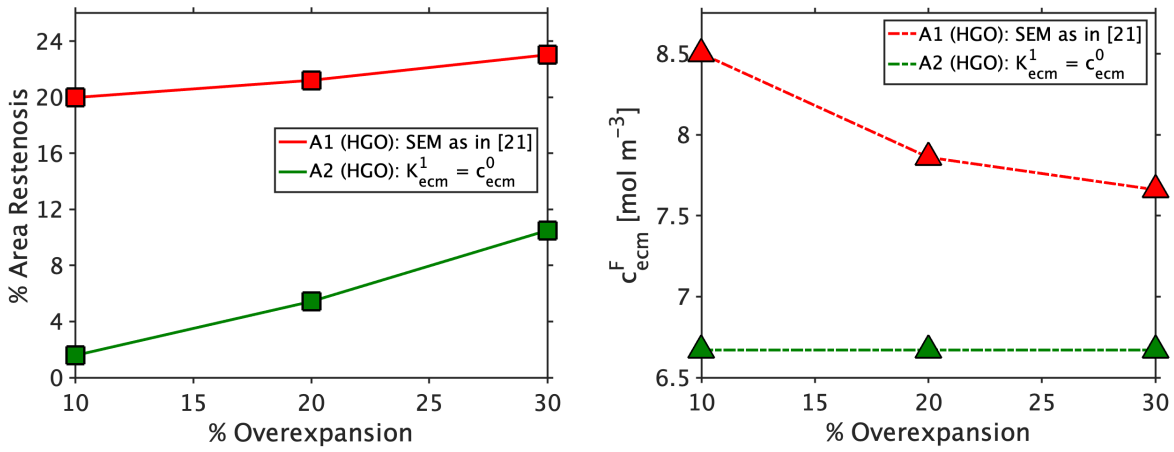


(a) A1 vs. A2: % AS

(b) A1 vs. A2: ECM

Figure 4.6: Comparing A1 and A2 across three (10/20/30%) different expansions after 300 days: (a) % Area restenosis values. (b) Final ECM concentration ($c^F_{ecm}$). Value 0.05 mm behind strut 2 (Fig. 4.2). A1 is a direct replica of the species evolution model (SEM) in [55] but uses the HGO constitutive model rather than Yeoh. A2 is the same model but changes the upper limit, $K^1_{ecm}$, of ECM synthesis to not exceed the initial concentration, $c^0_{ecm}$.

In Fig. 4.6a, significant levels of restenosis across all three expansions (10–30%) are observed in A1, which is markedly reduced in A2 when ECM contributions to restenosis are neglected. Looking at the final concentration of the ECM ($c^F_{ecm}$), at 300 days 0.05 mm behind the second strut, ECM synthesis is greatest when the expansion is lowest for A1, which is contradictory to findings in literature [56, 60]. The impact of this is further emphasised in Fig. 4.7 where the temporal behaviour of ECM at this point is presented. In Fig. 4.7a, ECM synthesis is notably more profound when stent expansion is lower, owing to the large restenosis profiles observed following an overexpansion of 10% (Fig. 4.6a), even when damage is minimal (Table 4.5). However, a more distinct difference in restenosis is observed in A2 (Fig. 4.6b), when ECM in all expansion scenarios converge to the same value (Fig. 4.7b). These results highlight two key findings. Firstly, ECM heavily contributes to restenosis, a well known phenomenon from histological evidence [60, 76]. Secondly, it also illustrates that the initial model (A1) synthesises ECM in excess, particularly in scenarios where damage following stent deployment is minimal, emphasised the $\theta$ values, representing the mean damage, in Table 4.5.

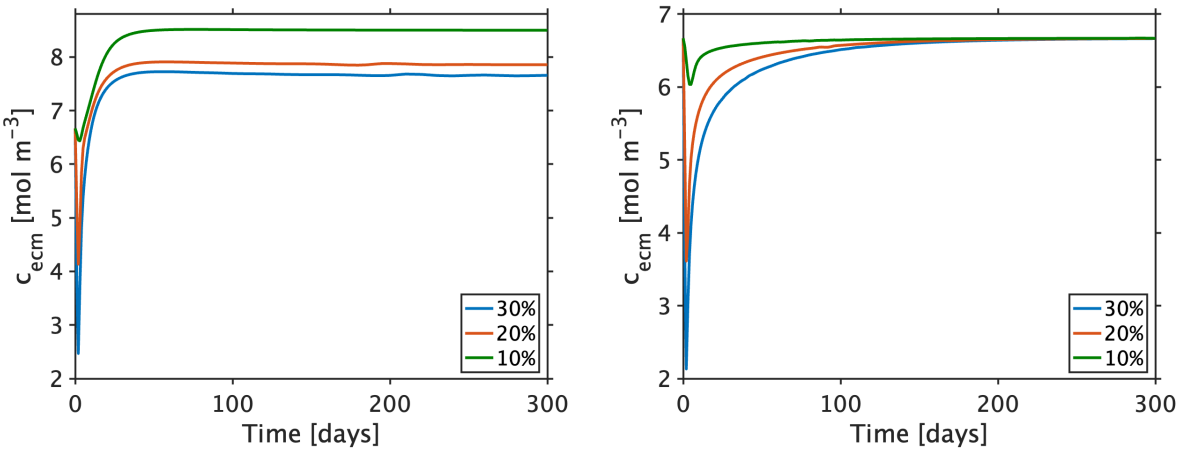


(a) A1 (b) A2

Figure 4.7: Investigating ECM concentration ($c_{ecm}$) evolution in time at a point 0.05 mm behind second stent strut. (a) A1. (b) A2.

#### 4.3.1.2 Introducing a condition for the ECM threshold concentration

In attempt to address the aforementioned issues, when further analysing [55], it was noted that an arbitrary constant threshold for ECM synthesis is proposed. In [55], the threshold condition was defined as $1.5 \times c^0_{ecm}$. Thus, when ECM degradation is less severe, more ECM is synthesised as a result, as illustrated in Fig. 4.7a. This is because there is less space to fill following stent deployment which means synthesis may be more excessive. In other words, if the parameter for the maximum ECM concentration ($K^1_{ecm}$) is an arbitrary constant, not influenced by stress or damage, the limit to which ECM synthesises towards will always be the same. However, this will be approached more quickly in situations where damage is less severe as ECM degradation is driven by MMP production, which is upregulated by damage and is more prevalent following greater stent expansion. Therefore, an alternative upper limit is proposed, case A3, where the ECM threshold condition is defined by Eqn. 4.13. To recap, this expression states that the limit of ECM synthesis is proportional to the level of damage after stent deployment. This expression, like in [55], still ensures that restenotic tissue becomes more profound as stent expansion increases (Fig. 4.8a) and that more ECM degradation following a deeper stent deployment is observed (Fig. 4.10a). However, the new expression for the ECM threshold concentration ensures ECM synthesis is also increased as stent deployment becomes more intrusive, a feature not captured in case A1 (Fig. 4.8b) nor in [55].

#### 4.3.1.3 Improving the expression for SMC proliferation

A further change made to the restenosis model is how the proliferation of sSMCs ($P_{ssmc}$) is described. In [55], cells were allowed to freely proliferate in proportion to the growth factor

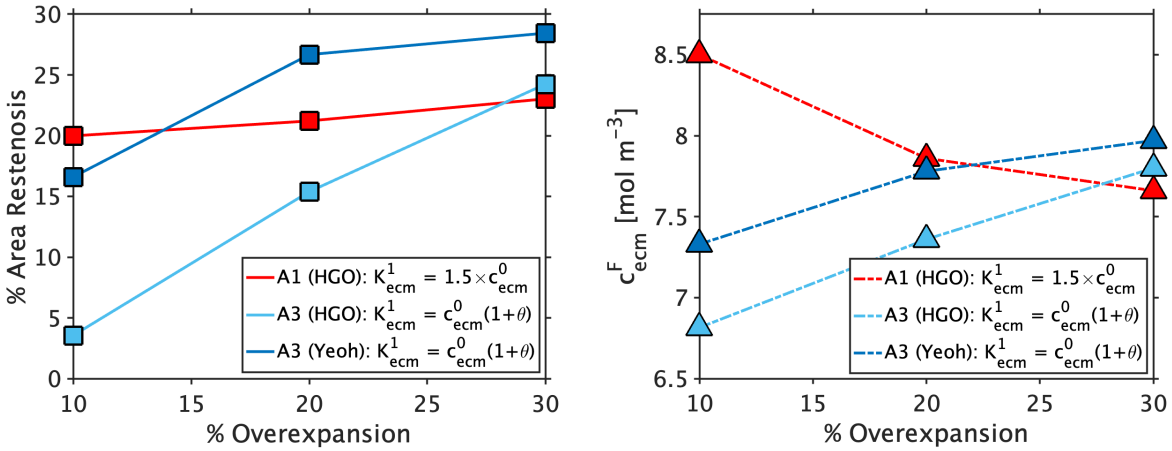


(a) A1 vs. A3: % AS

(b) A1 vs. A3: ECM

Figure 4.8: Comparing A1 and A3 across three (10/20/30%) different expansions. For A3, two different constitutive models are considered, HGO and Yeoh. (a) % Area restenosis values. (b) Final ECM concentration ($c^F_{ecm}$). A1 is the same species evolution model as [55], where the ECM threshold is given by $K^1_{ecm} = 1.5 \times c^0_{ecm}$. A3 proposes a new ECM threshold expression (Eqn. 4.13), given by $K^1_{ecm} = c^0_{ecm}(1+\theta)$.

concentration:

$$P_{ssmc} = g_{ssmc}(c_{gf} - c^0_{gf}), \tag{4.23}$$

where sSMC growth is governed by the difference between the current and initial growth factor concentration. Here it is proposed that the proliferative term (Eqn. 4.11) still accounts for the surplus in GF concentration as a result of increased damage, but also introduces mediation of cell growth through the current cell density and ECM concentration. In particular, the influence through ECM suggests that as more space becomes available then cells can grow more quickly through the logistical expression considered. Comparing how the model response varies as a result, Fig. 4.9a charts the effect on restenosis between A1 and A4, whilst Fig. 4.9b details the trend in the final ECM concentration. Across the different expansions, a much larger increase in tissue growth is noted. In other words for A1, the difference between restenosis profiles is no greater than 10% between any two expansions, yet for A4 the severity of restenosis more than triples from when expansion ratio increases from 10 to 20% and approximately doubles from 20 to 30%. Moreover, the ECM trends, as was true with A3 (Fig. 4.9), are more appropriate, where the final concentration increases alongside stent expansion severity. Finally, plotting the ECM concentration at a given point (Fig. 4.10b), the temporal trends observed are consistent with those in case A3 (Fig. 4.10a), increasing as vascular injury increases.

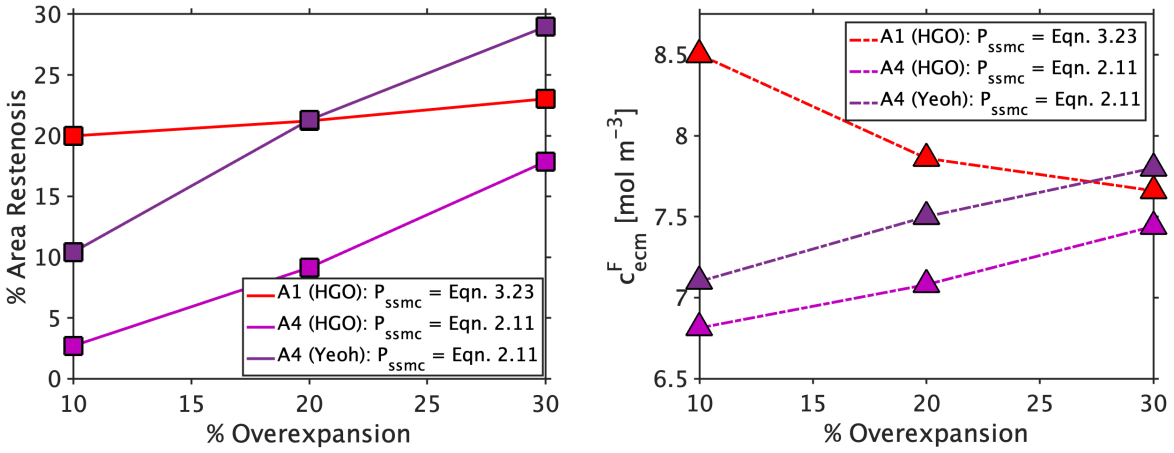


(a) A1 vs. A4: % AS (b) A1 vs. A4: ECM

Figure 4.9: Comparing A1 and A4 across three (10/20/30%) different expansions. For A4, two different constitutive models are considered, HGO and Yeoh. (a) % Area restenosis values. (b) Final ECM concentration ($c^F_{ecm}$). A1 is the same species evolution model as [55], where sSMC proliferation is given by Eqn. 4.23. A3 proposes a new expression for sSMC proliferation, given by Eqn. 4.11.

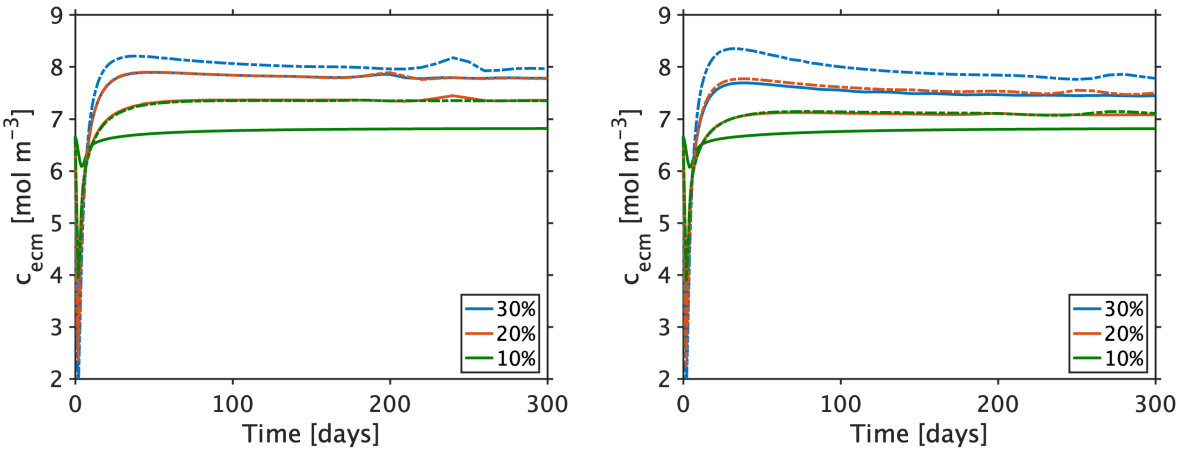


(a) R3 (b) R4

Figure 4.10: Investigating ECM concentration ($c_{ecm}$) evolution in time at a point 0.05 mm behind second stent strut. (a) A3. (b) A4. In all cases, solid lines (–) refer to simulations that employ the HGO model, whilst dash-dot (-.) lines to the Yeoh model.

#### 4.3.1.4 The significance of the constitutive model

Although alluded to in Section 4.3.1.2 and 4.3.1.3 when discussing A3 and A4, respectively, the significance of arterial kinematics is reiterated here, where two constitutive models were considered: HGO and Yeoh. The results demonstrate that with simpler arterial kinematics, the level of restenosis following a fixed expansion is more severe (Fig. 4.8 & 4.9) as a consequence

| | Expansion Profile | | | | | |
|---|---|---|---|---|---|---|
| | 10% | | 20% | | 30% | |
| Case | $\theta$ | $c^F_{ecm}$ [mol m$^{-3}$] | $\theta$ | $c^F_{ecm}$ [mol m$^{-3}$] | $\theta$ | $c^F_{ecm}$ [mol m$^{-3}$] |
| A1 | n/a | 8.5 | n/a | 7.86 | n/a | 7.66 |
| A2 | n/a | 6.67 | n/a | 6.67 | n/a | 6.67 |
| A3 – HGO | 0.023 | 6.815 | 0.234 | 7.36 | 0.612 | 7.8 |
| A3 – Yeoh | 0.222 | 7.33 | 0.636 | 7.78 | 0.959 | 7.97 |
| A4 – HGO | 0.023 | 6.813 | 0.234 | 7.08 | 0.612 | 7.44 |
| A4 – Yeoh | 0.222 | 7.1 | 0.636 | 7.5 | 0.959 | 7.8 |

Table 4.5: Comparison between $\theta$, the average damage in the stented domain and the ECM concentration at the final time, 300 days, directly behind the second strut ($c^F_{ecm}$).

of increased arterial stresses. This is further emphasised in Table 4.5 where the $\theta$ values are higher within a given expansion across the two constitutive models simulated. This alludes to the importance of arterial kinematics, where models that do not accommodate for the family of collagen fibres (e.g. Yeoh) may overestimate the effect of stent deployment by means of arterial stresses [315].

Moving forward, the computational model will implement the HGO constitutive law to describe arterial kinematics, where the dispersion of collagen fibres is accounted for. Moreover, the upper limit to ECM synthesis will be given by Eqn. 4.13, where stent deployment has a direct impact on vascular remodelling. Additionally, sSMC proliferation is inclusive of more realistic dynamics, where spatial considerations through the ECM concentration is proposed alongside the current density of sSMCs, directly mediating their proliferative capacity.

### 4.3.2 Study B: Impact of stent expansion and geometry

#### 4.3.2.1 Stent expansion

Case B1 explores the impact of stent expansion on restenosis, analysing how species behaviour varies across the different deployment depths. An important definition in the model is the initial condition for damage (Eqn. 4.4), highlighted in Fig. 4.11a. Using this definition, the species evolution model simulated within the deformed geometry can be initialised with a spatiotemporal damage field, which is a consequence of the arterial stresses present following the displacement of the struts (Fig. 4.11b).

Following stent expansion, the subsequent impact on species evolution is observed (Fig. 4.12). Across all constituents, the trends present match those expected, where an increase in damage following more intrusive stent deployment stimulates an increase in mediators associated with healing. For example, GFs and MMPs are two species which are directly upregulated

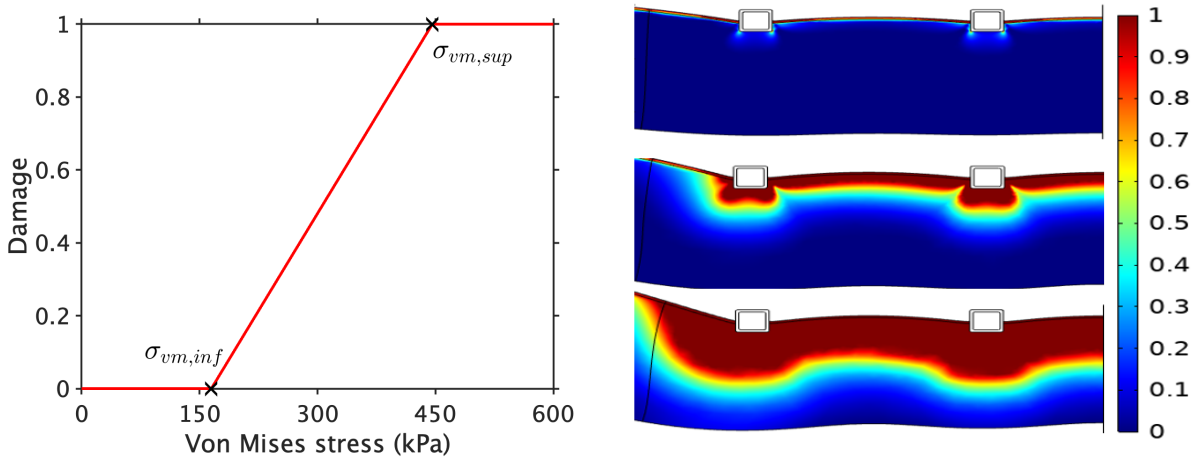


(a) (b)

Figure 4.11: (a) Definition of the damage initial condition. Linear piecewise function (Eqn. 4.4) between two limits, $\sigma_{vm,inf}$ and $\sigma_{vm,sup}$ [54, 55, 314]. (b) Initial damage following each expansion. Upper: 10% ($\theta = 0.023$), Middle: 20% ($\theta = 0.234$), and Lower: 30% ($\theta = 0.612$). All cases were simulated using the HGO constitutive model.

by damage. Thus, Fig. 4.12a and 4.12b clearly show an increase in production for each of these species as stent deployment depth is increased. With an increase in GFs and MMPs, a rise in the total SMC density is present (Fig. 4.12c & 4.12d) which in turn synthesises more ECM (Fig. 4.12e). Tissue growth is formulated as a consequence of excess SMC growth and ECM synthesis, which becomes more profound as deployment depth increases (Fig. 4.13 & 4.14a), agreeing with physiological trends present clinically [56, 60, 63, 206].

Taking a closer look at the tissue growth profiles, similar to [55], it is assumed that the minimum radius within the stented domain defines restenosis. As a result, a more schematic depiction using concentric circles can be considered to aid in the visual representation of excessive tissue growth, where direct comparisons can be made with the level of overexpansion following stent deployment (Fig. 4.13). The image on the left (a) corresponds to the change in lumen radius following expansion. The inner most circle (white) depicts the healthy artery, pre–expansion, with a radius of $r_{l,h}$. Adopting three clinically relevant expansion ratios (10/20/30%), changes in the lumen radius can then be observed (to scale with respect to $r_{l,h}$). Alluded to earlier, each expansion results in the deformation of the arterial wall, where the resultant stress field between ratios is different. As such, the growth profiles are notably different, as presented in Fig. 4.13b, where $r_{l,n}$ is the normalized lumen radius, such that $r_{l,n} = 1$ and corresponds to the lumen radius immediately after expansion, as given by $r_{l,ref(R)}$, where $R$ = 10, 20, or 30%. Therefore, although $r_{l,ref}$ differs between expansion ratios, the normalised radius means that all growth profiles can be superimposed onto a single figure, where the severity of tissue growth can be visualised graphically. With excess tissue growth computed by Eqn. 4.22, then a percentage

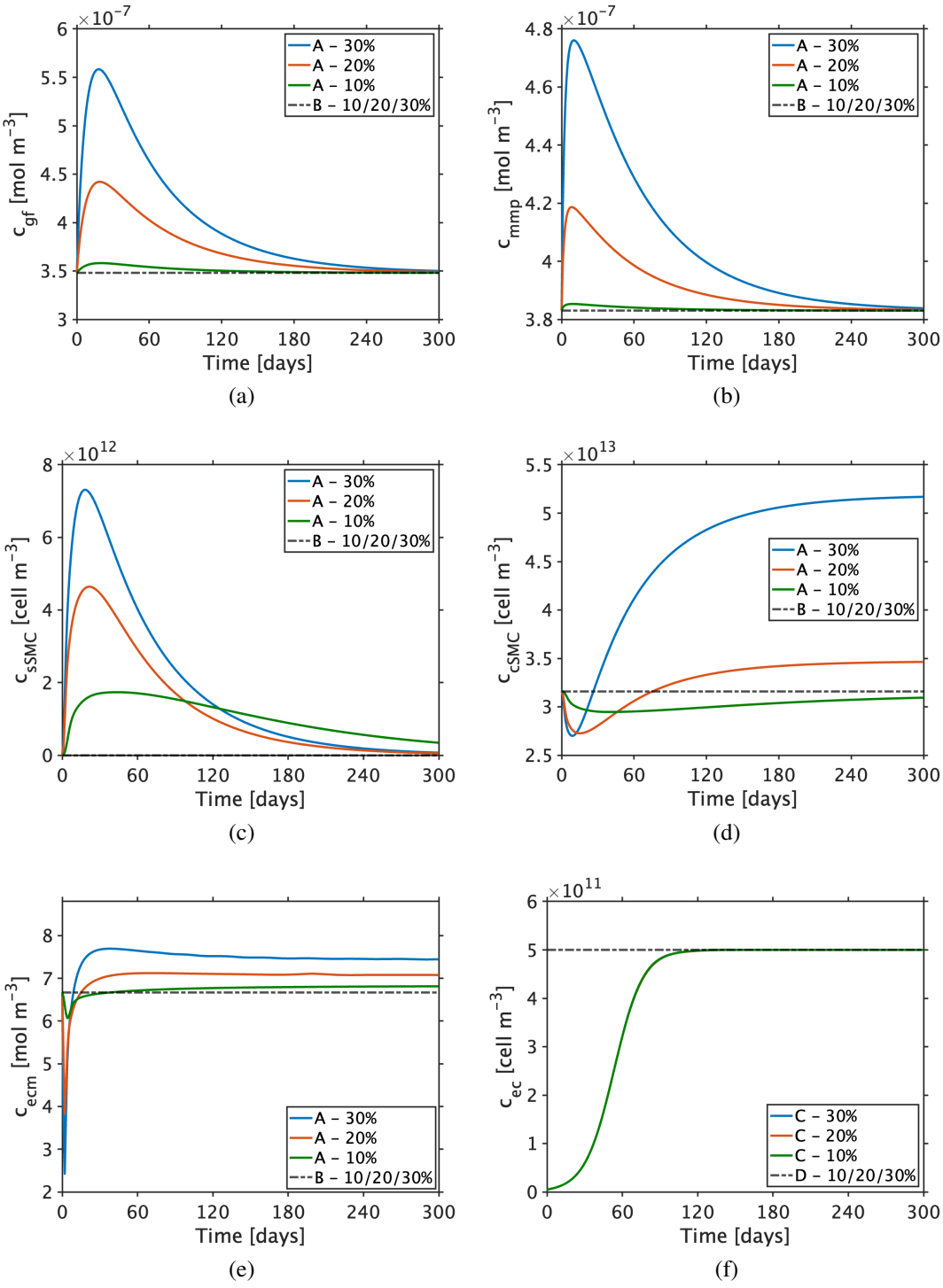


Figure 4.12: How the different species: (a) GF, (b) MMP, (c) sSMC, (d) cSMC, (e) ECM, and (f) EC vary as stent expansion is increased. Points: A is 0.05 mm behind the second strut; B is at the far edge of the domain (media, $\Gamma_{m,up}$); C is in the intima, between strut 2 and 3; and D is at the far edge of the domain (intima, $\Gamma_{i,up}$).

value is outputted. This is a percentage increase in tissue growth with respect to the expanded radius ($r_{l,ref}$), which $r_{l,n}$ has been normalized with. Thus, with the lumen radius normalised, the tissue growth profiles for each expansion scenario can be superimposed onto a single figure (Fig. 4.13b).

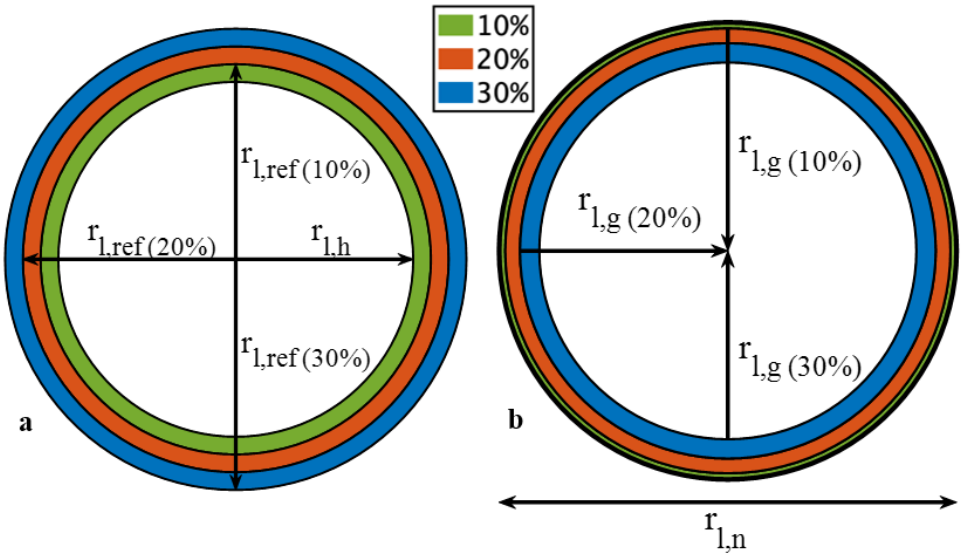


Figure 4.13: Impact of stent expansion (legend) on restenosis. (a) Schematic representation of the different lumen radii ($r_{l,ref}$) post–expansion. Healthy artery ($r_{l,h}$) = 1.5 mm. Expansions of 10, 20, and 30% result in a radius of 1.65, 1.8, and 1.95 mm, respectively. (b) Schematic representation of the different lumen radii following restenosis after 300–days ($r_{l,g}$), where $r_{l,n}$ is the normalized lumen radius, normalized with respect to the reference radius ($r_{l,ref}$) for each case and denoted the emboldened line. The normalized lumen radius in each growth case is: $r_{l,g(10\%)} = 0.9731$, $r_{l,g(20\%)} = 0.9093$, and $r_{l,g(30\%)} = 0.8235$ computed from restenosis values in Table 4.6.

As expected, a more obtrusive deployment protocol (outermost circle: Fig. 4.13a) results in an increased vessel re–narrowing (innermost circle: Fig. 4.13b) as a result of higher arterial stress.

The quantitative results are presented in Fig. 4.14a, illustrating the significance of stent expansion on excessive tissue growth. Clearly, the majority of growth occurs within the first 50 days ($\approx$ 90%), agreeing with [55], where only subtle changes in growth were present after 2 months with regeneration of the EC layer not yet complete. Note, across the three expansions, the recovery of the EC layer is indifferent (Fig. 4.12f). This is a consequence of the model formulation, where ECs behave independently of other constituents. Additional efforts in Chapter 6 explore amendments to the equation detailing the behaviour of EC species, introducing coupling with other key species in the restenosis process.

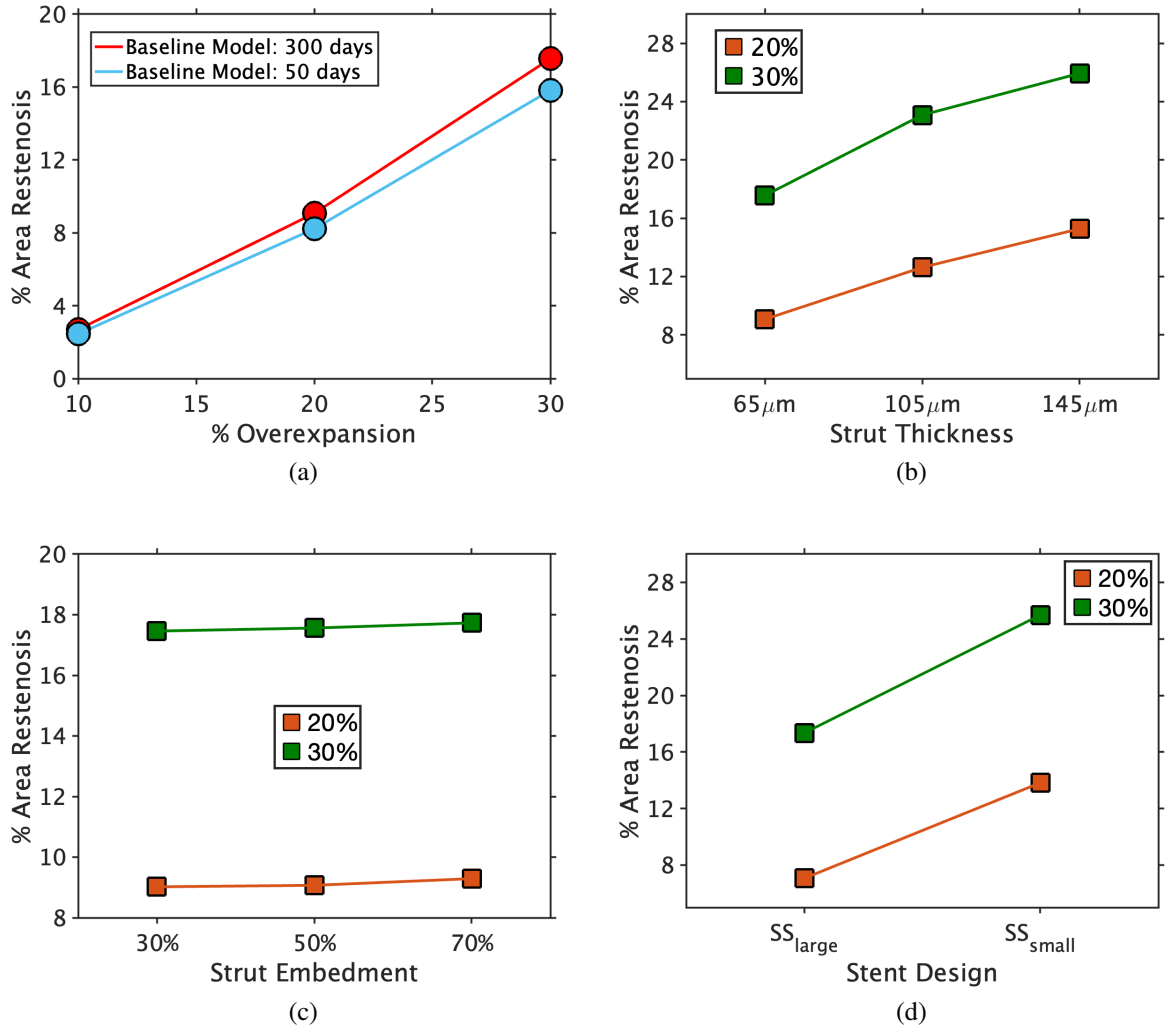


Figure 4.14: Exploring the significance of stent expansion and geometry. (a) Baseline model, parameters listed in Table 4.3, across three expansion profiles (10, 20, 30%) over a 50 and 300–day period. The impact of (b) ST, (c) SE, and (d) SS on %area restenosis over a 300 day period for two expansion profiles, 20% and 30%.

#### 4.3.2.2 Stent geometry

Cases B2a–c explore the effect of strut configuration on % area restenosis (Fig. 4.14b–4.14d), where perturbations in strut thickness, strut embedment and inter–strut spacing are analysed, respectively. Quantitative values for each of these simulations are reported in Table 4.6, where it is further emphasised that approximately 90% of growth occurs within the first 50 days across all cases simulated.

Results demonstrate qualitative agreement with trends present in both experimental and clinical literature. In particular, both an increase in strut thickness and decrease in inter–strut spacing expose the arterial wall to higher stresses following stent deployment. As a result, with how the initial condition is defined (Fig. 4.11a), the trigger of restenosis is more potent as a conse-

quence of the higher stresses, hence the more profound restenosis profiles (Fig. 4.14b & 4.14d). The impact of increased strut thickness has been extensively explored in other models of ISR ( [54, 55, 206]), which the results here agree with. Moreover, this satisfies trends present clinically, where various studies have demonstrated the superior performance of thinner struts with respect to key indices such as ISR and stent thrombosis [339–341]. Fig. 4.14b illustrates the quantitative results across the different stent expansions for each strut thickness, while Fig. 4.15 presents the direct comparisons between each of the tissue growth profiles as produced by the computational model.

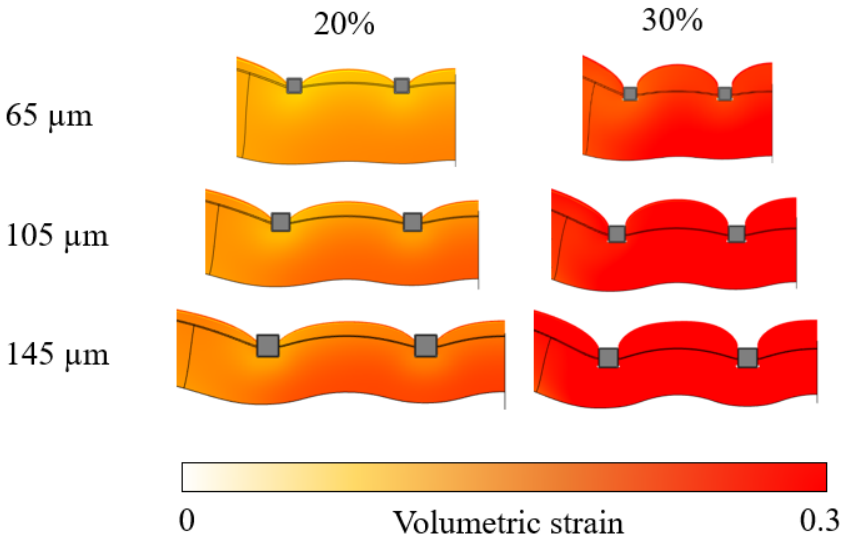


Figure 4.15: Severity of volumetric tissue growth for each strut thickness (65, 105, and 145 $\mu$m) when the stent has been expanded by 20 and 30% after 300 days. The quantitative values detailing the severity of tissue growth are reported in Table 4.6. Volumetric change is measured as the change in volume divided by the original volume of the arterial wall ($\Delta V/V$).

To assess the significance of inter–strut spacing, a comparison between different stent designs ($SS_{small}$ versus $SS_{large}$) within a fixed domain length demonstrates that an increased number of struts (reduced inter–strut spacing) produces greater levels of restenosis. This result is in agreement with Timmins *et al.* [101], who compare computational efforts with animal data, noting that an increased number of struts across a fixed lesion length subjects the artery to higher stresses, where tissue growth as a result is more prominent. Other more haemodynamically focused efforts suggest that WSS is significantly lower in configurations where inter–strut spacing is smaller, further exacerbated in cases where the struts are thicker and when inter–strut spacing is uneven [137, 342]. Thus, if the effects of flow were introduced into the model proposed, it is anticipated that greater levels of restenosis would be expected in configurations where strut spacing was reduced, where recirculation zones become more apparent [137, 343].

Finally, the pre–embedment depth was varied, assessing the impact of different, but still uni-

| Model | Expansion Profile: % Area Restenosis | | | | | |
|---|---|---|---|---|---|---|
| | 10% | | 20% | | 30% | |
| | 50 days | 300 days | 50 days | 300 days | 50 days | 300 days |
| Baseline | 2.45 | 2.69 | 8.22 | 9.07 | 15.82 | 17.58 |
| Varying ST | | | | | | |
| 65$\mu$m ($\star$) | | | 8.22 | 9.07 | 15.82 | 17.58 |
| 105$\mu$m | | | 11.23 | 12.63 | 20.29 | 23.08 |
| 145$\mu$m | | | 13.6 | 15.28 | 22.8 | 25.94 |
| Varying SE | | | | | | |
| 30% | | | 8.19 | 9.02 | 15.78 | 17.46 |
| 50% ($\star$) | | | 8.22 | 9.07 | 15.82 | 17.58 |
| 70% | | | 8.35 | 9.29 | 15.94 | 17.73 |
| Varying Stent Design | | | | | | |
| Low stress | | | 5.64 | 7.06 | 14.9 | 17.34 |
| High stress | | | 12.47 | 13.82 | 22.23 | 25.69 |

Table 4.6: How % area restenosis varies across the various cases considered in study B. The growth at both 50 and 300 days are presented. ($\star$) cases are those which overlap with the baseline geometry.

form, embedment depths on restenosis. Results illustrate that the healing response is indifferent across the various cases (Fig. 4.14c). Note, however, that the model proposed considers an idealised geometry, where deep arterial tears and malapposition are not simulated. In particular, an abundance of literature has stated the impact of malapposition on patient outcome, attributed to both ISR and stent thrombosis [32,137,344]. Future work should therefore look to simulate such cases where malapposition and/or deep arterial tears are possible. The main purpose of these different embedment profiles was to assess their impact on drug delivery, which is considered in Chapter 5.

#### 4.3.2.3 Model sensitivity study

With the effect of the stent geometry and expansion explored in depth, a local sensitivity analysis was carried out to observe the significance some of the model parameters ($g_{ssmc}, g_{ecm}, k_{ecm}$) have on tissue growth within the baseline geometrical configuration. With all model parameters explored in depth in [55], only those changed as per Study A are considered for further assessment. Fig. 4.16 demonstrates that the model results are sensitive to petrubation in all three parameters when the parameter of interest is varied by an order of magnitude that promotes growth. For ex-

ample, increasing the rate of sSMC proliferation ($g_{ssmc}$) notably increases restenosis, with these cells primarily contributing to the process. Moreover, an increase in ECM ($k_{ecm}$) degradation or decrease in ECM synthesis ($k_{ecm}$) has the same effect, with more space made available for the sSMCs to proliferate. Although the latter point may appear counter–intuitive, this is not the case. This is because of the new definition for the ECM threshold as per Eqn. 4.13, where the upper limit for ECM synthesis is now governed by stent expansion as opposed to approaching an arbitrary constant as was true in [55].

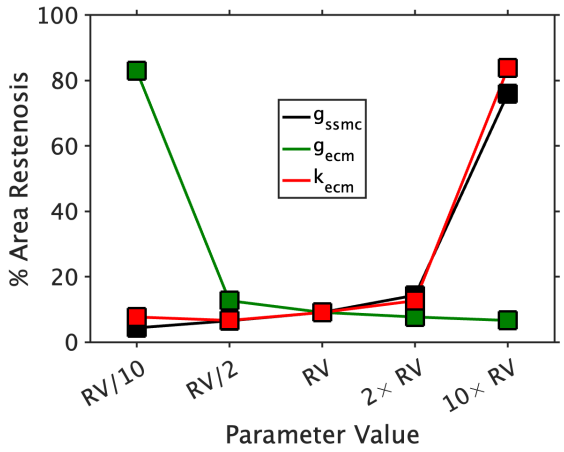


Figure 4.16: The effect varying parameters $g_{ssmc}, g_{ecm}$, and $k_{ecm}$ has on restenosis. RV = Reference value as described in Table 4.3.

With the parameters of this model acquired from a plethora of different studies (Table 4.3), additional work is necessary in acquiring a more consistent data set that aids in improving the predictability of the model. Although it is likely that the rates at which species like GFs are produced at will vary on a patient-to-patient basis (consequence of damage), the rate of sSMC proliferation and ECM synthesis are likely to be similar within a species [275], only fluctuating implicitly through an increase influx of GFs or delayed regeneration of the endothelial layer.

### 4.3.3 Study C: the effect of incorporating the adventitia

Case C1 considers the implementation of all arterial layers, accounting for the mechanical significance of the adventitia which was previously absent. The computational model (Fig. 4.2) is thus extended by 0.4 mm radially, representative of the thickness of adventitial tissue, obtained from [169], along with the constitutive model parameters. All other aspects of the mechanical model are unchanged, and stent deployment is simulated as before through the displacement of stent struts.

Observing the damage profile between two struts, it is notably reduced throughout the intima (I) and media (M) when accounting for the adventitial layer (Fig. 4.17). For lower expansions, the difference between damage profiles is less. Moreover, an interesting behaviour is observed

for more intrusive cases (30% – Fig. 4.17b), where an increase in damage is observed towards the boundary between the media and adventitia (external elastic lamina, EEL). Such intrusive stent expansion could result in the stimulation of adventitial cells (e.g. fibroblasts), which has been reported in the literature following the presence of deep arterial tears through the EEL [345, 346]. Thus, model extensions could probe the inclusion of cells residing in the adventitia where stent expansion is so profound that damage/stresses present in the adventitia stimulate deeper cell activity. Alternatively, the damage map present following deeper stent protrusion (30%) may be a consequence of the simplistic stent expansion methodology employed.

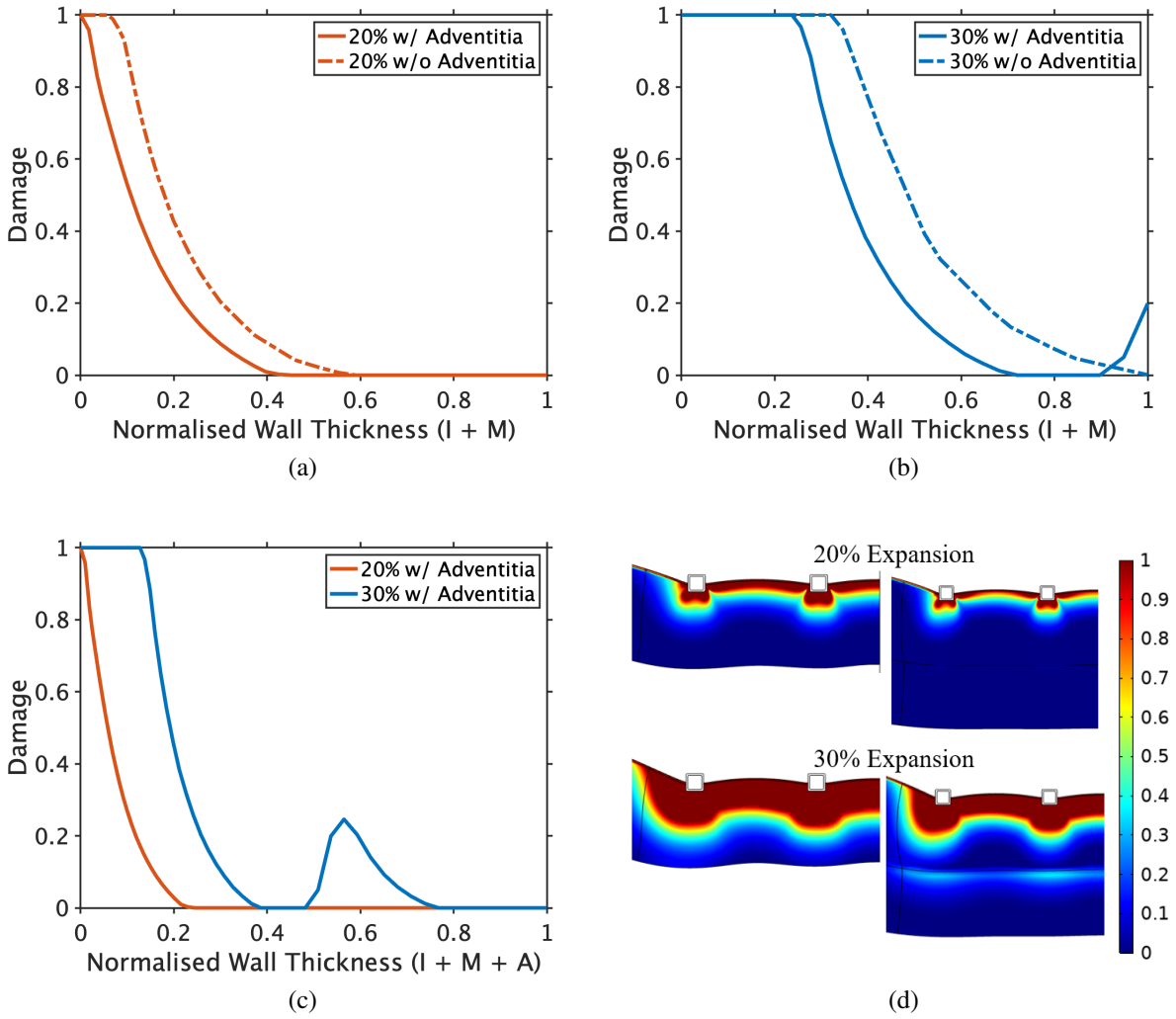


Figure 4.17: How inclusion or absence of adventitia influences the damage profile between two struts (2 and 3) following stent deployment. I = Intima, M = Media, and A = Adventitia. (a, b) How damage varies within I and M with (w/) and without (w/o) the adventitial layer following (a) 20% expansion or (b) 30% expansion. (c) How damage profiles vary across full wall thickness (I+M+A) following 20% and 30% expansions. Solid lines refer to simulations including the adventitial layer, whereas dashed lines are those which neglect it. (d) 2D representation of damage profiles within stented domain.

The reduction in damage throughout the medial layer following the implementation of the adventitia layer is explainable. Although hosting numerous responsibilities, the adventitia is essentially a sheath of connective tissue comprising of a collagen–rich ECM to provide vessel rigidity [10]. Highlighted in [315, 347], when subject to significant levels of strain, the adventitia layer stiffens which prevents the artery from overstretch or even rupture, conferring the protective function of this layer.

However, the inclusion of the adventitia significantly increases computational time. For example, the expansion process alone is increased by approximately ten fold prior to simulating species evolution and drug transport (Chapter 5). With species behaviour in this layer still poorly understood and conflicting [60], the presence of this layer is ignored, similar to [55]. Complete justification for neglecting the adventitia in the full computational model is provided in Section 4.4.

## 4.4 Limitations & Future work

As is common with computational models, a number of assumptions have necessarily been made. As justified throughout, the key limitations associated with the multiscale model relate to: (i) arterial wall complexity, (ii) stent deployment, (iii) neglecting CFD, and (iv) the restenosis and tissue growth model. The following discussion will elaborate on each in more depth, suggesting avenues for improvement as part of further work which would serve to enrich the current model.

### 4.4.1 Arterial wall complexity

The baseline 2D–axisymmetric model is comprised of only two layers, the intima and media. Study C, however, probed the role of the adventitia from a mechanical viewpoint, assessing how its presence notably reduced the arterial stress present following stent deployment, across a range of clinically relevant expansion ratios. Further work should elaborate on this, with the inclusion of adventitial cells in restenosis considered, where recent evidence has suggested the role of myofibroblasts, particularly following deep arterial tears [346]. However, with the function of such cells still poorly understood during this process, and evidence existing that contradicts this notion [56,60,348], the inclusion of the adventitia has been left to further work, where additional experimental evidence can hopefully provide more insight.

Moreover, subsequent efforts should look to explore the impact of disease on restenosis. This model, as is true for many others (e.g. [53–55, 65–67, 206, 215]), deploys the stent within a healthy, idealised vessel. However, as imaging modalities improve, better visualisation and characterisation of plaque burden is available [46, 235]. As such, the labelling of different types of plaque is possible, from regions hosting cells (fibrous cap) to those composed predominantly

of calcium (calcified plaque). However, the heterogeneous nature of atherosclerosis ensures that plaque composition differs substantially from patient–to–patient, alluded to in a recent model of atherosclerosis progression [218]. Even so, this model does not simulate a variety in plaque composition, instead just labelling the disease as a lipid core. The progression of disease is particularly difficult to emulate computationally, especially given that the process is highly time–dependent such that the lesions' cellular composition varies substantially as the disease evolves, having a demonstrable impact on computational time [349, 350]. Nonetheless, through the aid of histological data, as considered in [218], one can validate the effectiveness of their model at emulating disease progression in a once healthy vessel. Then, once the vessel is in a state that would require clinical intervention, the impact of stent deployment can be considered *in silico* initially to facilitate the optimal course of treatment *in vivo*. The natural next step would then be to assess drug release in diseased vessels, where the complex composition of plaque has been shown to influence drug transport and retention [196]. However, first an assessment of the performance of drug within a healthy vessel is needed, investigated in depth over Chapter 5–6.

### 4.4.2 Stent deployment

Although a significant improvement from [55] has been made with respect to the constitutive model that describes arterial kinematics, the process of stent deployment remains simplified. Nonetheless, the current approach simplistically captures the essence of the process, such that it produces realistic stress–distributions that trigger the restenosis model. Although the expansion process involves prescribing a simple displacement to each strut, the 50% pre–embedment profile is what presents most uncharacteristic of the true deployment process. Further work should look to implement a more sophisticated approach, where deployment is permitted by means of a balloon catheter to achieve the desired level of overexpansion. This would be a much more complex contact problem, significantly increasing computational cost. Notwithstanding, such an approach would still be limited within an idealised vessel and should be considered in tandem with progression in both model dimension (2D $\rightarrow$ 3D) and diseased state, as suggested recently [115, 122, 223].

### 4.4.3 Neglecting CFD

Probably the most prominent limitation is the lack of fluid dynamics, and its impact on the process of tissue growth. In recent years, several studies have demonstrated with the aid of experimental evidence, that low levels of WSS give rise to more severe growth profiles [218, 220, 221, 226, 227]. However, these articles all fail to simulate the explicit role of vascular injury on restenosis, where arterial stress distribution following stent deployment has been known to significantly influence tissue growth [54, 55, 65, 214]. In fact, [218, 220, 226, 227] all propose a continuous or linear piecewise function similar to Eqn. 4.4, where minimum and maximum

bounds of damage refer to WSS levels of 0 and 1 Pa, respectively. These trigger restenosis by assigning each model agent with a level of damage between 0 and 1, a method similar to the one employed here, which instead considers the Von Mises stresses present following deployment. To the best of the authors knowledge, only Jansen *et al.* [221] propose an alternative method, where WSS levels dictate the influx of growth factors through the damaged endothelial layer, for which the authors explicitly state that the precise dependence is unknown. In reality, it is likely that both WSS and arterial wall stress influence the restenosis profile, and should be considered together in future models [222,306]. The former has particularly been evidenced as a mediator in endothelial cell dysfunction [151,155,351,352], with the latter influencing constituent behaviour deeper in the arterial wall [55, 56, 65], where the role of WSS transmission into deeper arterial layers is still poorly understood [55, 218, 226]. This is particularly emphasised in [226] where a diffusion equation is employed to describe the loss of damage through the wall as a consequence of WSS at the lumen–wall interface. As such, further work should look to investigate the role of both arterial stress and WSS on restenosis, similar to [306], as the understanding of the complex phenomenon becomes more clear.

### 4.4.4 Restenosis & Tissue growth model

Aside from the inclusion of species residing within the adventitia, other limiting factors associated with the species evolution model exist, with the majority of these discussed in depth in [55]. Addressing some of these, the current model proposed amendments to the proliferation of SMCs and synthesis of ECM. The former introduced spatial restrictions, where increased space as a consequence of ECM degradation heightened the proliferative capacity of SMCs. The latter introduced an expression for the threshold associated with ECM synthesis, permitting a fair representation of remodelling in response to deeper vascular injury [56].

However, a key limitation that remains is the model proposed to detail the evolution of ECs (Eqn. 4.16). Currently, the timescale of EC regeneration is in line with the degradation of damage such that all events associated with healing occur in a timely manner. An alternative approach would be to allow the EC species to directly influence key mediators in the restenosis process, particularly the SMC population as proposed in [53, 65–67]. Thus, upon the regeneration of the endothelium, the artery can be categorised as being ‘healed’. However, with the species residing in distinct domains, a direct coupling between these two cell types is more challenging given the current framework. As such, amendments to the restenois model are probed in Chapter 6, where a direct coupling between ECs and SMCs is proposed, with the role of drug specificity also examined.

Finally, limitations are also apparent in the tissue growth model. Currently, a continuum biological tissue growth framework is proposed [55,228,336,338], where changes in the density / concentration of key species drives excessive tissue growth by means of a stationary study. Further work should look to increase the sophistication of this approach, where growth is instead

transient. Initial thoughts tend towards a moving boundary approach, where the mesh would change as the tissue swells or shrinks. Due to the complexity of such a problem, a preliminary 1D model should be considered first before extending efforts to the 2D framework presented here.

## 4.5 Conclusion

In conclusion, this chapter builds upon an already existing mathematical model [55], making significant improvements that serve to enrich it. These include amendments to the constitutive laws implemented to describe arterial kinematics, as well changes to SMC proliferation and ECM synthesis. The model involves numerous steps, most notably accounting for the mechanical damage as a consequence of stent deployment, a process known to induce the healing response. As such, species within the arterial wall respond accordingly to stimulate healing, resulting in excessive tissue growth. The results suggest good qualitative agreement with clinical trends, and thus chart responses similar to many different models of ISR [53–55, 65, 66]. Although, it should be noted that with such a complex model there exists a large number of parameters, for which estimation is needed as discussed in [55]. With the source of these ranging across animal species (e.g. rabbits, pigs, etc.), further work should look to devise a knowledgeable parameter base true to each, where perturbations in the healing process are known to vary [275].

Although several limitations are present, true to any computational model, a key limiting factor present currently is the model equation derived to describe the EC population (Eqn. 4.16). Thus, to address this, Chapter 6 investigates possible model alterations that ensure the EC population, the key marker for arterial healing, is directly linked to crucial species (e.g. SMCs) involved in tissue growth. As such, the role of drug specificity can then be analysed, where the effect on multiple cell types is simulated, and the possibility of delayed healing probed [24, 25]. Prior to this, a novel coupling must be established between the current restenosis model, and one which details the transport of drug from the stent coating through the arterial wall. This is the focus of Chapter 5, where the anti–proliferative properties of drug on SMC growth is assessed, with the subsequent effect on restenosis explored.

# Chapter 5

# An in silico model of stent–induced drug delivery and its role in the inhibition of restenosis

## 5.1 Introduction

Chapter 4 developed a novel *in silico* model of in–stent restenosis (ISR). However, a major limitation of the model, as is true in almost all models of ISR, is the absence of state–of–the–art drug transport kinetics. With drug–eluting stents (DES) known to significantly reduce the likelihood of ISR over bare metal stents (BMS), it is important for models aspiring to be adopted as pre–clinical tools to consider the delivery, and importantly, the effect of drug on vascular remodelling following stent deployment.

Computational models illustrating the performance of DES are ever pressing given that recent clinical evidence has illustrated the non–inferiority of percutaneous coronary intervention (PCI) with DES to more invasive procedures (coronary artery bypass grafting, CABG) [48]. Fearon *et al.* [48] noted that ISR is still an important clinical problem, where approximately 6% of patients required a repeat procedure after 1–year. This is expected to then increase annually at a rate of 3–5 % thereafter [353], heightened further in more complex lesions [232]. These rates equate to hundreds of thousands of patients worldwide re–visiting hospital for a repeat, invasive procedure, which has a notable impact on healthcare, resources, and cost. While many factors could be attributed to the stubbornly high number of repeat procedures needed, it is known that ISR is often the primary culprit [50]. With the stent industry focusing primarily on the materials aspect of stent design (e.g. different polymers, metal alloys, and strut thicknesses), the aspect of drug has been under–explored, except for the consideration of new limus drugs. Thus, the drug–delivery protocol is worth re–visiting as a potential target for further optimisation in stent design.

With this in mind, it is somewhat surprising that very few models exist that detail the effect

of drug on cell proliferation and subsequently restenosis [183, 205–208]. Such models were discussed in depth in Chapter 2, where the governing equations implemented to describe the action of drug were examined. These models range in complexity, from ordinary differential equations (ODE's), where drug impedes growth by different mechanisms: phenotype blocker, growth inhibitor, apoptotic inducer [183, 207], or even simpler still, where the explicit action of drug is neglected and a small sensitivity analysis on the proliferative parameter of SMCs is considered to convey the presence of drug [208]. Nonetheless, regardless of the model proposed to detail the inhibitory effect of drug, inadequate drug transport kinetics are often employed. For example, drug release into the arterial wall is either: (i) absent [208], (ii) simulated by means of an exponential condition that emulates drug release [207], or (iii) simulated assuming simpler transport kinetics, differing from the current state–of–the–art [183, 205, 206]. However, models which do employ the current state–of–the–art drug transport kinetics (e.g. [172, 178, 188, 200]) entirely neglect cellular dynamics, where the artery is assumed static (does not account for tissue growth) and constituents (e.g. cells) that are influenced by drug ignored. Therefore, the focus of this chapter is to develop a novel computational model which simulates restenosis subject to the spatiotemporal delivery of drug, assessing the impact of features associated with the design of DES on patient outcome.

The methodology immediately follows, focusing on the drug transport model and its explicit coupling to smooth muscle cell (SMC) function within the spatiotemporal framework of restenosis presented in Chapter 4. Efforts are then separated into two studies: examining the impact of stent design and different models of drug–effectiveness. As part of the latter, the validity of the static artery assumption in an environment that is naturally heterogeneous and time–dependent is tested. The results are discussed extensively before addressing the key limitations, where further work suggests possible improvements to the current model.

## 5.2 Methodology

To assess the impact of spatiotemporal drug delivery on cell proliferation and thus restenosis, the multi–step computational model implemented in Chapter 4 is adjusted accordingly. To do so, step 2 detailing species evolution is extended to integrate a drug transport model within the framework. This is highlighted in Fig. 5.1, which is an amendment to Fig. 4.1: Chapter 4, emphasising the process of drug release and how it subsequently modulates restenosis through the inhibition of SMC proliferation. The geometry of the model is unchanged from Chapter 4 (Fig. 2) which defines all boundaries and domains. Moreover, the first and last step, detailing stent expansion and tissue growth, respectively are also indifferent from Chapter 4, where the reader is again referred to for more details on these aspects.

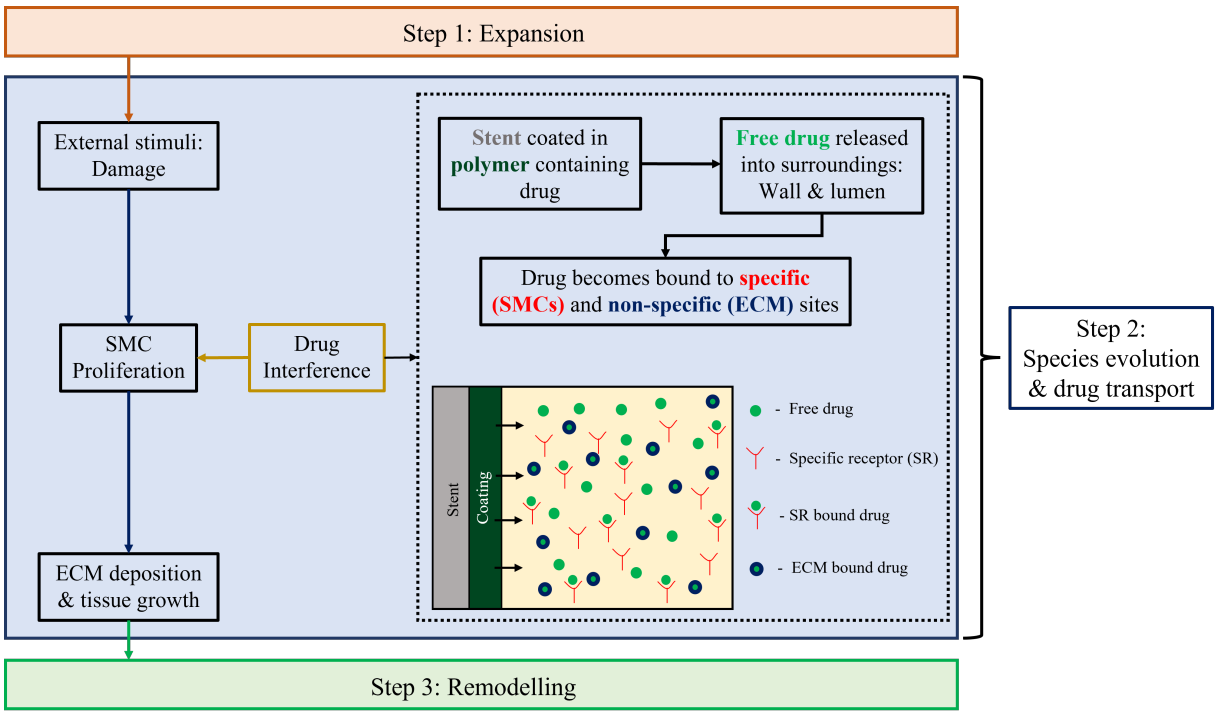


Figure 5.1: Schematic highlighting the action of drug subsequent to release from the polymer–coated stent and how it is integrated into the multi–step model of restenosis.

### 5.2.1 Drug transport model

Drug release from a durable polymer coating is considered, which is commonly described in the literature as a diffusion driven process [78]:

$$\frac{\partial c_p}{\partial t} = D_p \nabla^2 c_p, \quad \text{in } \Omega_p, \quad t > 0, \tag{5.1}$$

where $c_p\,(r,z,t)$ is the free drug concentration in the polymer coating, with an effective constant diffusion coefficient of $D_p$. The initial coating concentration ($c_p^0$) is computed by dividing the initial mass of drug per strut ($M_0$) by the volume of the coating ($V_p$) per strut. The domains ($\Omega$) and boundaries ($\Gamma$) are presented in Chapter 4: Fig. 4.2. Following release from the coating, the free drug enters the arterial wall, denoted by $c_w\,(r,z,t)$, and is described by means of a reaction–diffusion equation:

$$\frac{\partial c_w}{\partial t} = \nabla \cdot (\boldsymbol{D}_w \nabla c_w) - \frac{\partial b^{ns}}{\partial t} - \frac{\partial b^{s}}{\partial t}, \quad \text{in } \Omega_i \;\&\; \Omega_m, \quad t > 0, \tag{5.2}$$

where $c_w$ is initially zero. With the arterial wall heterogeneous, diffusion of free drug is governed by the following diffusivity tensor, $\boldsymbol{D_w}$:

$$\boldsymbol{D}_w = \begin{pmatrix} D_r & 0 \\ 0 & D_z \end{pmatrix}, \tag{5.3}$$

noting that diffusion in the radial ($D_r$) and axial ($D_z$) directions differ. The second and third term on the right–hand side of Eqn. 5.2 detail the depletion of free drug as a consequence of binding. The former denotes non–specifically bound drug, $b^{ns}\ (r,z,t)$, which binds to constituents such as extracellular matrix (ECM). The latter details specifically bound drug, $b^{s}\ (r,z,t)$, which is assumed to bind to intracellular receptors present within SMCs. The rate of change of concentration of specific and non–specific bound drug are governed by:

$$\frac{\partial b^s}{\partial t} = k^s_{on}\, c_w (B^s_c - b^s) - k^s_{off}\, b^s, \tag{5.4}$$

$$\frac{\partial b^{ns}}{\partial t} = k^{ns}_{on}\, c_w (B^{ns}_c - b^{ns}) - k^{ns}_{off}\, b^{ns}, \tag{5.5}$$

where $k^i_{on}$ and $k^i_{off}$ $(i = s, ns)$ denote the binding on and off rates whilst $B^i_c$ $(i = s, ns)$ refers to the maximum local density of binding sites present, which is assumed constant in the baseline model, in keeping with the current state–of–the–art models [78, 79, 178].

In the computational model proposed, only the action of sirolimus is considered. Of all drugs used clinically for DES, this is the most widely studied in the context of drug transport and retention following the release from endovascular devices. As such, there exists a full set of parameters available in the literature, displayed in Table 5.1 [79, 170, 172, 188, 196]. Moreover, further motivation exists, where several models that assess sirolimus drug efficacy neglect to consider how the drug interferes with cell proliferation [79, 172]. Additionally, most drugs coated on modern generation stents are derivatives of sirolimus [22], further emphasising the relevance of its selection here.

| Parameter | Description | Value | Reference |
|---|---|---|---|
| $D_r$ | Radial drug diffusion coefficient | $7\times10^{-12}$ m$^2$ s$^{-1}$ | [197] |
| $D_z$ | Axial drug diffusion coefficient | $4\times10^{-11}$ m$^2$ s$^{-1}$ | [197] |
| $k^s_{on}$ | Specific binding on rate | 800 m$^3$ mol$^{-1}$ s$^{-1}$ | [79] |
| $k^s_{off}$ | Specific binding off rate | $1.6\times10^{-4}$ s$^{-1}$ | [79] |
| $B^s$ | Specific binding site density | $3.3\times10^{-3}$ mol m$^{-3}$ | [79] |
| $k^{ns}_{on}$ | Non–specific binding on rate | 2 m$^3$ mol$^{-1}$ s$^{-1}$ | [79] |
| $k^{ns}_{off}$ | Non–specific binding off rate | $5.2\times10^{-3}$ s$^{-1}$ | [79] |
| $B^{ns}$ | Non–specific binding site density | 0.366 mol m$^{-3}$ | [79] |
| $M_w$ | Sirolimus molecular weight | 914.172 g mol$^{-1}$ | [197] |
| $\rho_t$ | Density of wet arterial tissue | 0.983 g ml$^{-1}$ | [79] |

Table 5.1: List of model parameters that depict the behaviour of sirolimus.

To ensure no drug enters the metallic strut, a zero–flux condition is imposed at the interface between the coating and the stent strut ($\Gamma_{ps}$) [55, 188]. With the domain sufficiently large in the axial direction, a zero–flux condition is imposed upstream/downstream from the stent ($\Gamma_{i,up}$,

$\Gamma_{m,up}$) similar to [169, 170, 188, 189, 196]. To permit the transport of drug through the wall, continuity of flux and concentration is assumed between the coating and the wall ($\Gamma_{pw}$) and between the two layers of the artery considered ($\Gamma_{iel}$). As published by Escuer *et al.* [170], free drug concentrations in the lumen were very low as a consequence of blood flow. Thus, an infinite sink is imposed on the lumen–coating interface ($\Gamma_{pl}$) and the boundary that interfaces the lumen and the wall ($\Gamma_{et,h}$, $\Gamma_{et,d}$). An infinite sink condition is also imposed at the interface between the media and adventitia ($\Gamma_{eel}$), with the latter neglected in the current modelling framework [169, 188]. Table 5.2 summarises all the relevant boundary conditions imposed within the drug transport model as well as a description of where they are imposed within the geometry (Fig. 4.2: Chapter 4).

| Boundary | Description | Condition |
|---|---|---|
| $\Gamma_{ps}$ | Polymer–strut interface | Zero–flux |
| $\Gamma_{i,up}$ / $\Gamma_{m,up}$ | Up–stream boundaries: Intima (i), Media (m) | Zero–flux |
| $\Gamma_{pw}$ | Polymer–wall interface | Continuity |
| $\Gamma_{iel}$ | IEL: Interface between intima and media | Continuity |
| $\Gamma_{pl}$ | Polymer–lumen interface | Infinite sink |
| $\Gamma_{et,h}$ $\Gamma_{et,d}$ | Healthy (h) and damaged (d) endothelium: Lumen–wall interface | Infinite sink |
| $\Gamma_{eel}$ | EEL: Interface between media and adventitia | Infinite sink |

Table 5.2: List of all boundary conditions imposed in the drug transport model. Please refer to Fig. 2: Chapter 4 for a schematic presentation of all boundary locations. Boundary conditions are consistent with the existing literature [169,170,188,196,307]. Continuity refers to continuity of both concentration and flux.

### 5.2.2 Coupling drug release and transport to restenosis

The key novelty associated with this work is the coupling of drug transport directly to cellular function, which in turn modulates restenosis. In Chapter 2, where the influence of drug on cell proliferation *in vitro* was considered, the validity of various models were tested. These models adopted either Michaelis–Menten kinetics to detail the effectiveness of drug, or assumed that saturated receptors through bound drug directly mediated the proliferative capacity of SMCs. In Chapter 2, it was noted that the former performed best, particularly when binding kinetics were neglected. However, it is not clear that this will be the case *in vivo*, particularly where the environment is significantly more heterogeneous. As such, this chapter proposes four distinct approaches to modelling the effect of drug on cell proliferation. These are: $RS^c$–Receptor saturation by bound drug, assuming a constant binding site density; $MM^f$–Michaelis–Menten kinetics neglecting drug binding; $MM^b$–Michaelis–Menten kinetics accounting for drug binding; and $RS^v$–Receptor saturation by bound drug, assuming a variable binding site density. To simulate these different models, the proliferative capacity of sSMCs ($P_{ssmc}$), presented in Chapter 4

(Eqn. 2.11), is amended accordingly.

#### 5.2.2.1 Model 1: RS$^{c}$

The efficacy associated with sirolimus is attributed to the sustained saturation of specific binding sites [79, 172]. Thus, the baseline drug model assumes that sSMC proliferation is reduced in proportion to the fraction of specific binding sites ($B_c^s$) that are bound by drug ($b^s$):

$$P_{sSMC} = g_{sSMC}\, c_{gf}\, c_{sSMC} \left(1 - \frac{c_{ecm}}{K_{ecm}^1}\right) \underbrace{\left(1 - \frac{b^s}{B_c^s}\right)}_{\text{Drug Interference}}, \tag{5.6}$$

where complete efficacy is assumed when $b^s = B_c^s$ and all specific binding sites are occupied such that sSMC proliferation is ceased. Note, in the preliminary model, it is assumed that the number of available binding sites is constant, hence the $c$ subscript. This is in agreement with the static artery assumption adopted ubiquitously in drug transport models in this field [78, 79].

#### 5.2.2.2 Model 2: MM$^{f}$

The first alternative model of drug effectiveness neglects binding kinetics completely, where the drug transport model (Eqn. 5.2) in the arterial wall reduces to a simple anisotropic diffusion equation, and free drug ($c_w$) mediates cell growth via:

$$P_{sSMC} = g_{sSMC}\, c_{gf}\, c_{sSMC} \left(1 - \frac{c_{ecm}}{K_{ecm}^1}\right) \underbrace{\left(1 - \frac{k_{max}\, c_w}{c_w + k_{50}}\right)}_{\text{Drug Interference}}, \tag{5.7}$$

where $k_{max}$ and $k_{50}$ are parameters that correspond to drug performance, with the former detailing the maximum effect of drug on cell proliferation and the latter the drug dose at which this effect is 50% of its maximum. With the bound drug population ignored, such a model is unable to capture the lasting effects of drug retention on cellular function. Hence, only the free drug present to cells at any given time mediates the proliferative capacity of sSMCs.

#### 5.2.2.3 Drug Model 3: MM$^{b}$

To assess the significance of free versus bound drug, Eqn. 5.7 is amended such that specifically bound drug ($b^s$) replaces free drug ($c_w$):

$$P_{sSMC} = g_{sSMC}\, c_{gf}\, c_{sSMC} \left(1 - \frac{c_{ecm}}{K_{ecm}^1}\right) \underbrace{\left(1 - \frac{k_{max}\, b^s}{b^s + k_{50}}\right)}_{\text{Drug Interference}}, \tag{5.8}$$

where binding kinetics are detailed by Eqn. 5.4. Here, the model, like RS$^{c}$, accounts for the importance of receptor saturation. However, it does so implicitly through Eqn. 5.4, where the

term detailing the effectiveness of drug is now more complex, inclusive of additional parameters not present in Model 1: $RS^c$.

#### 5.2.2.4 Drug Model 4: $RS^v$

In all previous models, where binding kinetics are considered, specifically bound drug ($b^s$) approaches an upper limit ($B^s$) which is assumed constant, while the artery remodels. In other words, models which detail drug effectiveness assume a static artery [78,79,172] where the number of cells and binding sites do not change with time and are unperturbed by vascular injury. However, it is known that sirolimus exerts its effect on cellular function by binding to FKBP12, a cytosolic protein located within SMCs. As such, histological evidence has suggested that an increase in FKBP12 expression is present at early times, where sSMC proliferation dominates, decreasing in time as the neointima matures, becoming hypocellular [60,354,355]. Therefore, a new binding site density, $B^s_v$, is proposed, which is dynamic, varying in proportion to the number of sSMCs:

$$B^s_v(c) = R_c \times c_{ssmc}, \tag{5.9}$$

where $R_c$ is a non–dimensional quantity that captures the receptor expression per cell. Naturally, this expression replaces $B^s_c$ in Eqn. 5.6. Although an issue arises, where a singularity is present if the density of sSMCs is assumed zero. To overcome this, a small density ($10^{-3}$) of sSMCs is assumed to exist initially in all domains of the arterial wall. The value was chosen to correspond to a density an order of magnitude below that present in the drug–free simulations after 5 seconds. Assessing the validity of this assumption, no difference in model response was observed when values two orders of magnitude below were considered. Differences present were only in relation to the initial peak (Fig. 5.2a), a consequence of this assumption. Moreover, in the absence of reliable estimates for $R_c$, it is assumed that:

$$R_c = \frac{B^s_c}{X_{ssmc}}, \tag{5.10}$$

where $X_{ssmc}$ corresponds to one of three values associated with the spatially–averaged sSMC concentration across the therapeutic domain: (i) maximum in time (ii) time–averaged over 50 days or (iii) time–averaged over 21 days. Note, the therapeutic domain is defined in Fig. 4.2: Chapter 4, given as $3 \times \delta_{ss}$ ($\delta_{ss}$ is the inter–strut spacing) from the centre of the outermost strut in the stented lesion [169]. The corresponding values for $R_c$ for each case (i–iii) is presented in Table 5.3. Note, these values are computed only for the sSMC profile following an expansion of 20%. These are likely to vary as the expansion ratio changes, owing to the complex heterogeneity of arterial healing.

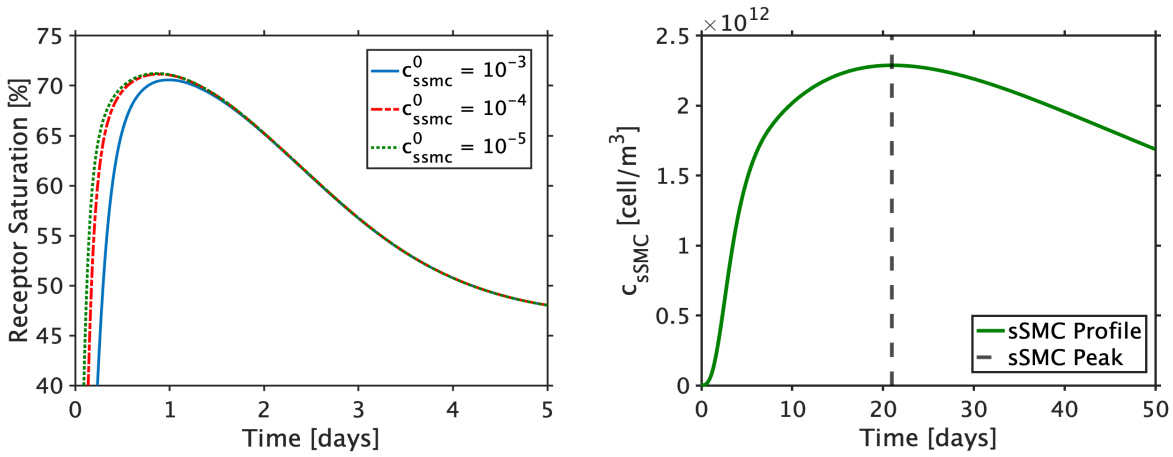


(a) (b)

Figure 5.2: (a) How the initial condition of sSMCs influences the receptor saturation curve. (b) sSMC mean concentration within the therapeutic domain. Vertical dashed line corresponds to the profile peak (21 days).

| Label | $X_{ssmc}$ value used to compute $R_c$ | $R_c$ Value |
|---|---|---|
| $R_c^1$ | (i) Maximum sSMC density in time – 50 days | $1.435\times10^{-3}$ |
| $R_c^2$ | (ii) Time–averaged sSMC concentration – 50 days | $1.72\times10^{-3}$ |
| $R_c^3$ | (iii) Time–averaged sSMC concentration – 21 days | $2.163\times10^{-3}$ |

Table 5.3: Investigating different variable binding site densities ($B_v^s = R_c \times c_{ssmc}$) through different $R_c$ values. The various $X_{ssmc}$ behaviours make reference to the sSMC profile in Fig. 5.2b, illustrating the spatially–averaged concentration throughout the therapeutic domain.

### 5.2.3 Numerical methods

The numerical method employed is similar to that considered within Chapter 4. However, the inclusion of drug transport is associated with increased computational demands [170]. With large concentration gradients present, and rapid binding kinetics, mesh amendments were necessary to achieve reliable results. Using the 'extremely fine' mesh option as a foundation, additional refinements were implemented that reduced mesh size, whilst ensuring a consistent mesh both radially and axially through the wall. Moreover, a number of boundary layers (8) were required at the interface between the coating, lumen and wall ($\Gamma_{pw}, \Gamma_{pl}, \Gamma_{et,h}$, and $\Gamma_{et,d}$). Fig. 5.3 illustrates the mesh of the baseline model, where further reductions in mesh element size presented no significant change in % area restenosis. However, further improvements in mesh quality were necessary in scenarios where gradients were larger as a consequence of the larger inter–strut spacing (i.e. $SS_{large}$). Thus, as a consequence of the various strut configurations, the total number of mesh elements varied significantly from 55,000–150,000 elements whilst still achieving an average element quality $\geq 0.91$. Note, as a result of the highly variable geometries and

meshes, computational time varied from 2–23 hours.

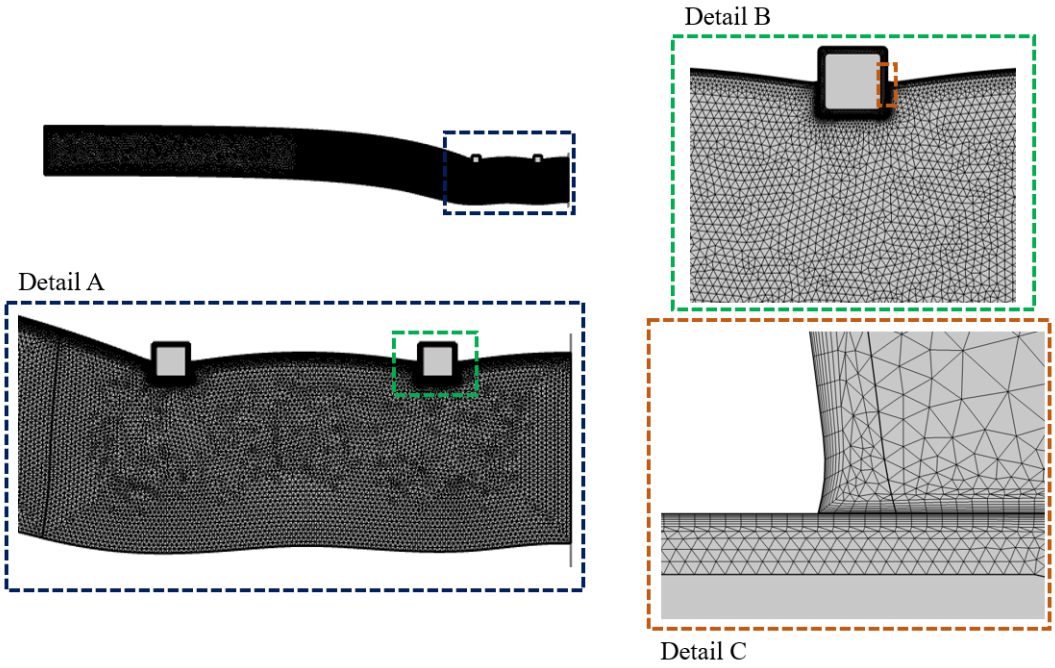


Figure 5.3: An illustration of the mesh considered for the baseline drug model: RS$^{c}$. Detail A: Stented domain. Detail B: Stent strut. Detail C: Boundary layers.

### 5.2.4 Summary of investigated cases

To explore the effect of drug on vessel re–narrowing thoroughly, a variety of different cases are considered, as presented in Table 5.4. Description of the geometrical set–up has been reduced to a single column displaying the information in the form of a matrix, where each entry defines the (range of) values considered for each aspect: % Overexpansion (OE), strut thickness (ST), strut embedment (SE), and inter–strut spacing (SS).

In addition to perturbation in physical design, parameters unique to DES are varied, including the initial drug loading per strut (DM) and the drug release rate (RP), influenced by the polymer diffusion coefficient ($D_p$). Thus, unless otherwise stated, all simulations use the respective values presented in Table 5.5. The default drug release profile (RP2) is selected as it emulates the moderate release of drug from a Xience$^{TM}$ (Abbott Vascular, Santa Clara, CA, USA) stent, where approximately 80% drug is eluted within 30 days. RP1 and RP3 vary the polymer diffusion coefficient ($D_p$) an order of magnitude either side of this value. All release profiles are illustrated in Fig. 5.4. The initial drug masses are quoted per strut (Table 5.5). To be consistent with commercially used stents, the largest drug mass (DM3) considered is taken from [170]. Since this value is at the higher end for drug loadings on commercial stents, three smaller, arbitrary values (DM0–2) are proposed to assess the possibility of DES hosting

Study A: Impact of stent expansion and geometry

| Case | Drug Model | Description | Model configuration [% OE; ST; SE; SS] |
|---|---|---|---|
| A1 | RS[c] | Impact of stent expansion | [20/30; 65 $\mu$m; 50%; 7 $\times$ $T_{s_t}$] |
| A2 | RS[c] | Impact of strut thickness (ST) | [20; 65/105/145 $\mu$m; 50%; 7 $\times$ $T_{s_t}$] |
| A3 | RS[c] | Impact of strut embedment (SE) | [20; 65 $\mu$m; 30/50/70%; 7 $\times$ $T_{s_t}$] |
| A4 | RS[c] | Impact of inter–strut spacing (SS) | [30; 65 $\mu$m; 50%; $SS_{large}$/$SS_{small}$] |

Study B: Exploring alternative models of drug effectiveness

| Case | Drug Model | Description | Model configuration [% OE; ST; SE; SS] |
|---|---|---|---|
| B1 | MM[f] | Free drug MM model | [20; 65 $\mu$m; 50%; 7 $\times$ $T_{s_t}$] |
| B2 | MM[b] | Bound drug MM model | [20; 65 $\mu$m; 50%; 7 $\times$ $T_{s_t}$] |
| B3 | RS[v] | Variable binding site density model | [20; 65 $\mu$m; 50%; 7 $\times$ $T_{s_t}$] |

Table 5.4: Summary of the different cases considered. Study A: to explore how stent design coupled with spatiotemporal drug delivery influence restenosis. Study B: to investigate a variety of different models that detail the effectiveness of drug.

lower initial drug loadings. Such a notion has been proposed in recent clinical studies involving sirolimus [356, 357] and paclitaxel [358, 359], where the drug loadings are comparable to the values proposed in this study.

| RP | $D_p$ [m$^2$/s] | DM | $M_0$ [$\mu$g] |
|---|---|---|---|
| 1 | $1.5 \times 10^{-18}$ | 0 | 0.05 |
| 2$^\dagger$ | $1.5 \times 10^{-17}$ | 1$^\dagger$ | 0.1 |
| 3 | $1.5 \times 10^{-16}$ | 2 | 1 |
| | | 3 | 5 |

Table 5.5: Different parameter values for the effective diffusion coefficient of the polymer coating ($D_p$), which govern the different drug release profiles (RP) and the initial drug mass present in each strut (DM). The baseline parameters are denoted by a $^\dagger$ symbol.

In total, there exists two studies (A and B). The first explores stent design changes coupled with spatiotemporal drug delivery, and the subsequent impact on restenosis. To do so, the study is separated into four cases that examine: (A1) two clinically relevant stent expansions (20 and 30%); (A2) the impact of ST; (A3) the impact of SE; and (A4) the impact of SS by means of different stent designs. Study B then assesses the effect of different models of drug effectiveness on restenosis within the baseline geometrical configuration: Case A1, Table 5.4. As per Section 5.2.2, three alternative models of drug effectiveness are considered. For each case in study A and B, the impact of drug mass and release rate is assessed (Table 5.5).

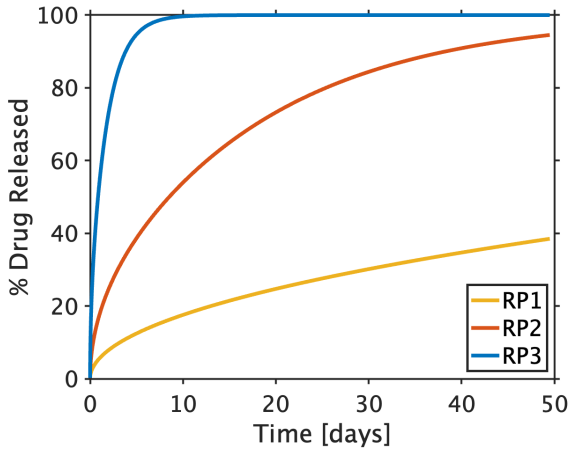


Figure 5.4: Sirolimus release profile for various polymer diffusion coefficients ($D_p$).

### 5.2.5 Analysis of results

In addition to monitoring % area restenosis as defined in Chapter 4, further indicators, measured within the therapeutic domain, are introduced which are linked with the safety and efficacy of DES. Firstly, drug content (DC, $\mu$g drug/g tissue), associated with safety, is given by:

$$DC(t) = \frac{M_w}{\rho_t V_w} \int_{V_w} \left(c_w + b^s + b^{ns}\right)\, dV_w, \tag{5.11}$$

where $V_w$ denotes the volume of the arterial wall, $\rho_t$ is the density of wet arterial tissue, and $M_w$ is the molecular weight of drug.

Moreover, drug efficacy is assessed by observing the saturation of specific receptors, in line with various articles that assume static arteries [79, 172]. It is this variable which influences the proliferative capacity of cells in models which consider binding, and is computed as:

$$\%RS^s = \frac{100}{V_w} \int_{V_w} \frac{b^s}{B^s_T}\, dV_w, \tag{5.12}$$

where $\%RS^s$ is the percentage of saturated specific binding sites and subscript $T$ denotes the different binding site considerations, either constant ($T = c$) or variable ($T = v$).

Additionally, Chapter 4 demonstrated that over 90% of tissue growth occurred within the first 50 days. As a result, unless otherwise stated, all results depict model behaviour after a 50–day period.

## 5.3 Results & Discussion

### 5.3.1 Study A: RS$^c$ Model

Case A1 examines the role of stent expansion on restenosis following drug release, with the key results presented in Fig. 5.5. Focusing on a single expansion scenario first (20%), it is clear that the choice of both the initial drug mass (DM) and drug release rate (RP) are important.

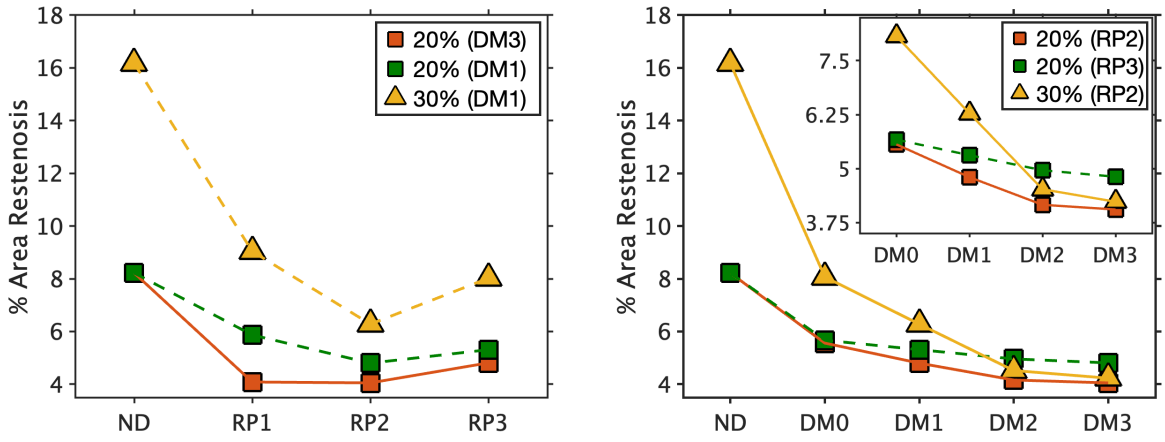


(a) Study A1–RP

(b) Study A1–DM

Figure 5.5: Significance of drug release profile (RP) and initial drug mass per strut (DM) on restenosis across two different expansion profiles (20/30%) for a period of 50 days. (a) Study A1–RP: Solid lines refer to DM3 whilst dashed lines to DM1. (b) Study A1–DM: Solid lines correspond to RP2, whilst dashed lines refer to RP3. *Inset:* Highlights the differences between cases where only drug is considered. In all cases, ND corresponds to the drug–free simulation.

Firstly, Fig. 5.5a demonstrates that although the moderate drug release profile (RP2) performs best across the drug masses considered, the choice of a slower or quicker release is heavily influenced by the initial drug loading. For example, the slow release profile (RP1) performs well when the initial drug mass is high (DM3). However, this would be at the cost of elevated tissue drug content for a long period of time, where safety may be compromised as a result (Fig. 5.6). When a lower drug mass is considered (DM1), then a quicker release of drug is more desirable, ensuring that cells are exposed to sufficient drug concentrations during the active phase of remodelling. If the release of drug is too slow (RP1), then restenosis is notably higher (Fig. 5.5a). Taken together, this suggests an intricate balance between design parameters for DES, where an increase in drug mass and drug release rate is not always the best approach. Furthermore, it is apparent that as stent expansion is increased (30%), higher masses than DM1 would be required to combat excessive tissue growth to the same degree as an expansion ratio of 20%. This is a result of increased vessel stress, heightening *damage* throughout the arterial wall, stimulating a surplus of constituents (e.g. GFs) that contribute to cell proliferation and excessive remodelling.

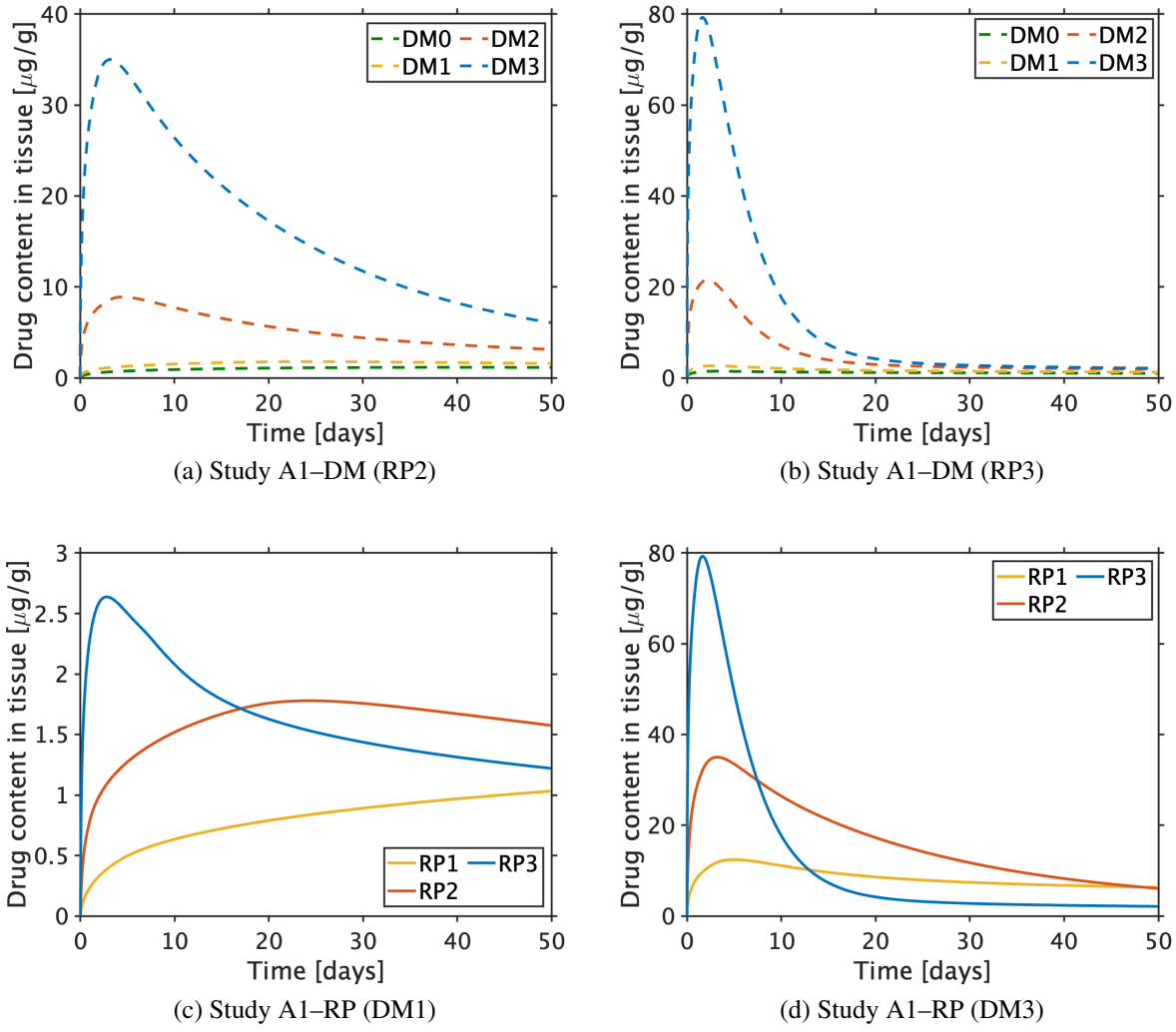


(a) Study A1–DM (RP2)

(b) Study A1–DM (RP3)

(c) Study A1–RP (DM1)

(d) Study A1–RP (DM3)

Figure 5.6: How tissue drug content varies across the different parameter cases simulated. Impact of different DMs for a fixed drug release profile: (a) RP2 and (b) RP3. Impact of different RPs for a fixed initial drug mass: (c) DM1 and (d) DM3. Drug content in tissue is computed by Eqn. 5.11.

Next, perturbations in the initial drug loading across multiple release rates are explored (Fig. 5.5b), again highlighting an intricate interplay between RP and DM. Analysing the results of the 20% expansion ratio first, as drug mass is increased, restenosis decreases towards some threshold value, where further increase in mass would present negligible changes to vessel restenosis. However, the threshold this value approaches differs depending upon the drug release rate selected. If drug is released and washed away to quickly (RP3), the threshold value is notably higher as a consequence of increased cell proliferation, where specific receptors are not completely saturated across the active period of cell growth (Fig. 5.7). At lower drug masses (DM0/1), the difference in vessel response is significant between the 20 and 30% expansion ratios. However, as the mass of drug is increased, values approach a similar threshold value, made

clear by the inset in Fig. 5.5b. This is interesting, suggesting that lower drug doses may be applicable in cases where stent expansion inflicts lower levels of injury within the vessel wall. Thus, in time, through the aid of complex models acting as pre–clinical tools, clinicians may be able to tailor treatment on a patient–by–patient basis if the level of injury the patient is subject to following stent deployment may be predicted *a priori*.

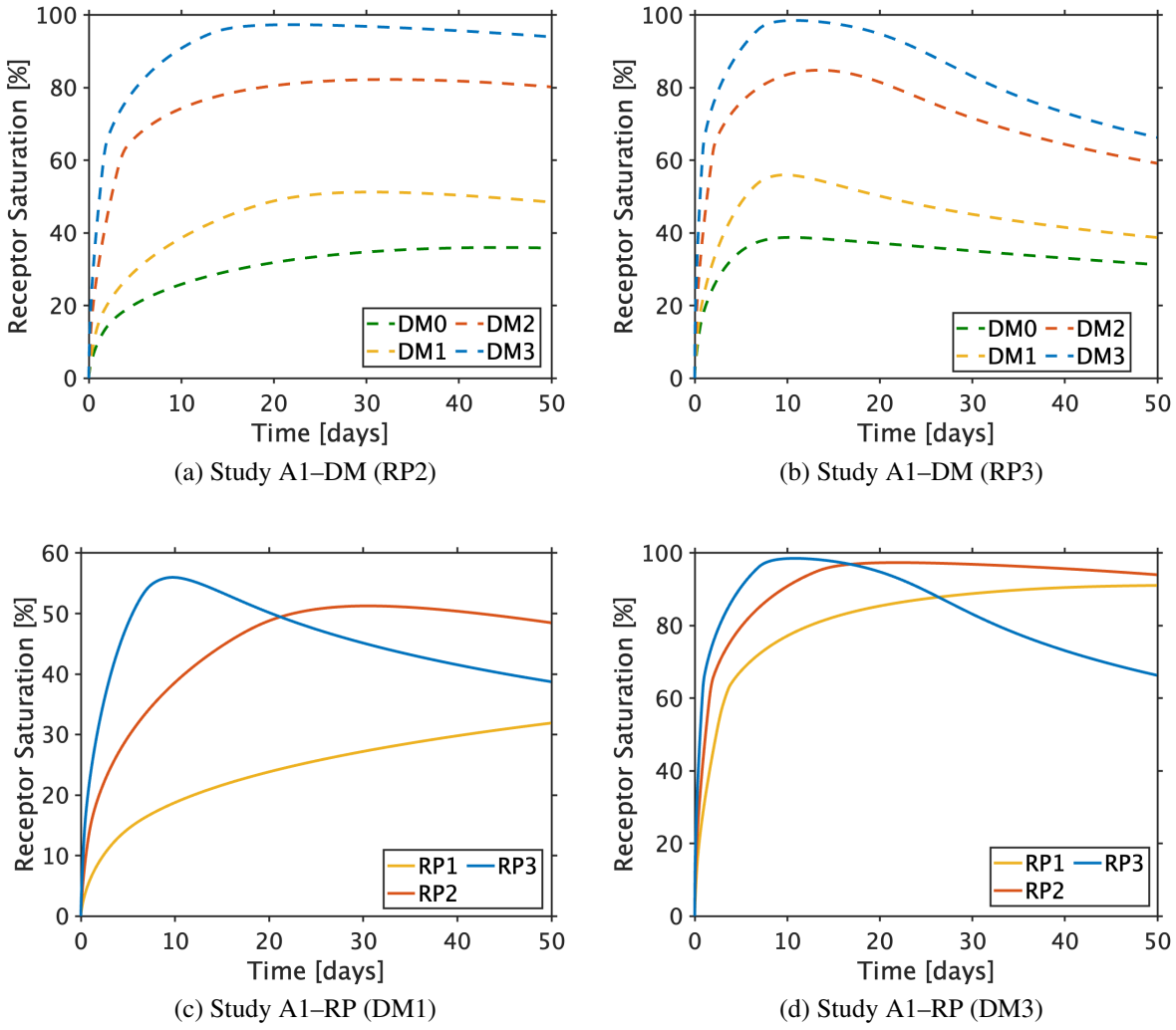


(a) Study A1–DM (RP2)

(b) Study A1–DM (RP3)

(c) Study A1–RP (DM1)

(d) Study A1–RP (DM3)

Figure 5.7: How specific receptor saturation varies across the different parameter cases simulated. Impact of different DMs for a fixed drug release profile: (a) RP2 and (b) RP3. Impact of different RPs for a fixed initial drug mass: (c) DM1 and (d) DM3. Specific receptor saturation is computed by Eqn. 6.12 and is the same across 20 and 30% expansions when binding site density is assumed constant.

Subsequent efforts (Case A2–4) explore the impact of stent geometry on % area restenosis. First, the impact of strut thickness (ST) is analysed. Across the various release profiles, it is apparent that as the strut thickness is increased, more drug is required to combat the higher levels of vascular injury present following stent expansion (Fig 5.8a & 5.8b).

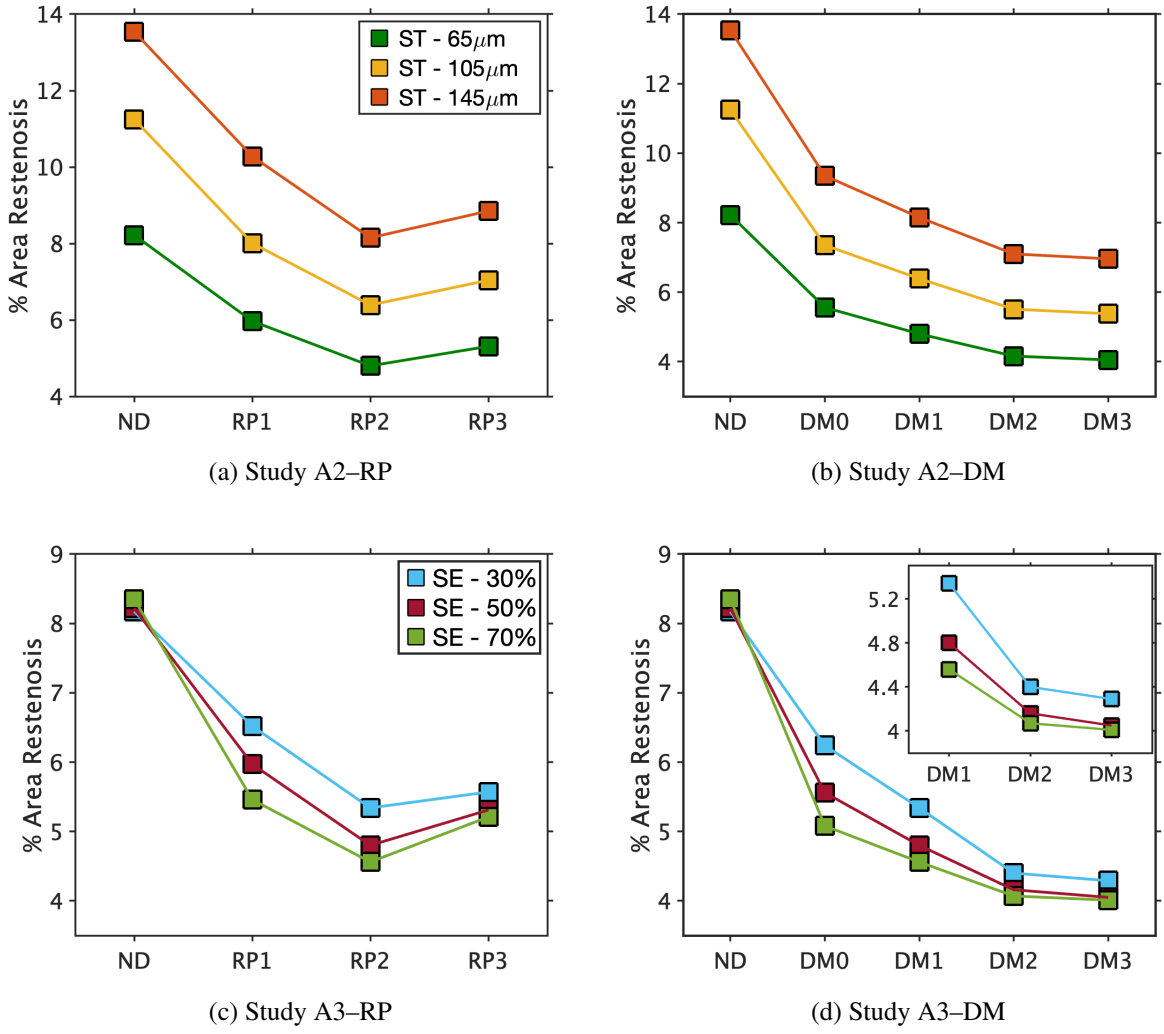


(a) Study A2–RP

(b) Study A2–DM

(c) Study A3–RP

(d) Study A3–DM

Figure 5.8: Significance of drug release profile (RP) and initial drug mass per strut (DM) on restenosis across different stent configuration regimes: variation in strut thickness (ST) or variation in strut embedment (SE) for a period of 50 days. All simulations are conducted within the 20% expansion profile. (a) Study A2 - RP. (b) Study A2 - DM. (c) Study A3 - RP. (d) Study A3 - DM. *Inset:* Highlights the differences between cases at higher drug masses. In all studies, when varying RP the mass is fixed at DM1 and when varying DM, the release profile is fixed to RP2. In all cases, ND corresponds to the drug-free simulation.

Simulating a lower fixed mass (DM1), trends follow those charted in Fig. 5.5, where a sustained release of drug (RP2) is most desirable (Fig. 5.8a). Moreover, as drug mass is increased, each strut thickness geometry approaches a local plateau, which varies across the different configurations. In other words, further increase in drug mass will have a minimal effect on the inhibition of restenosis. This is most likely a consequence of the inter–strut spacing condition ($7 \times T_{s_t}$) which means the distance between two adjacent struts varies as as a consequence of strut thickness. Thus, the results suggest that more mass, or indeed more tailored release kinetics would be required in such a case. Another (although unlikely) reason is the assumption of

a constant binding site density, where the current model is unable to account for the increase in receptors as a result of cell proliferation.

Perturbations in strut embedment are also assessed (Fig. 5.8c & 5.8d). Although in the absence of drug (ND), the restenotic profile is comparable across all cases, the inclusion of drug demonstrates different trends, where deeper strut protrusion reduces excessive tissue growth at the cost of elevated tissue drug content levels. At lower drug masses, the difference between the embedment profiles is exacerbated, diminishing as the mass of drug entering the artery increases. Thus, similar to the case investigating different expansion profiles, lower masses of drug may be appropriate when strut protrusion is deeper, assuming the level of injury caused following stent deployment is not significantly increased, as the mass of drug entering the tissue is increased.

The final case (A4) considers the impact of inter–strut spacing by means of different stent designs, where lesion length is fixed (5 mm) and the stent hosts either 4 ($SS_{large}$) or 7 struts ($SS_{small}$). In agreement with all other cases, the sustained release of drug (RP2) is optimal (Fig. 5.9a). Moreover, as was true in earlier cases which exhibited increased vascular injury across stent designs, more drug is required to combat tissue growth in scenarios where arterial stress is heightened: in this case, as a consequence of the increased strut number (Fig. 5.9b).

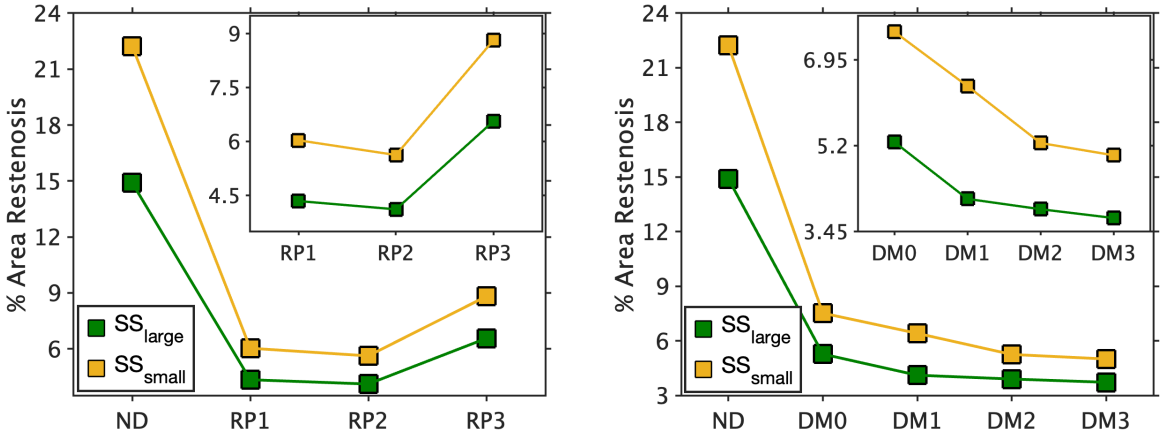


(a) Study A4–RP

(b) Study A4–DM

Figure 5.9: Significance of drug release profile (RP) and initial drug mass per strut (DM) on restenosis when inter-strut spacing (SS) is varied. All simulations are conducted within the 30% expansion profile for a period of 50 days. (a) Study A4–RP. *Inset:* Highlights the differences between release profiles. (b) Study A4–DM. *Inset:* Highlights the differences between cases at higher drug masses. In all studies, when varying RP the mass is fixed at DM1 and when varying DM, the release profile is fixed to RP2. In all cases, ND corresponds to the drug-free simulation. The key associated with DM differs here from Table 5.5, where masses are reported with respect to the full stent length: DM0 = 1 $\mu$g, DM1 = 5 $\mu$g, DM2 = 10 $\mu$g, and DM3 = 25 $\mu$g.

All cases taken together, it is clear that the parameters associated with stent design (RP, DM) are important to consider for the success of DES. Throughout the various cases, the stent con-

figurations which increase vessel stress, and thus damage following stent expansion appear to require higher masses of drug to combat excessive tissue growth. Moreover, although a sustained release (RP2) is desirable, the choice of a faster or slower release may be applicable, but is dependent upon the initial coating mass. In agreement with state–of–the–art drug transport models that assume static arteries [79, 172, 178, 188], results of this model allude to the importance of controlled release kinetics and sustained saturation of specific receptors in ensuring the optimal inhibition of restenosis.

### 5.3.2 Study B

The results of study B are divided into two parts. The first explores, in depth, alternate models of drug effectiveness in depth (Case B1 & B2). The second part investigates the validity of the assumption of a constant binding site density (Case B3), replacing the static approach considered in many drug transport models with a dynamic term that evolves in space and time as a consequence of SMC phenotype change and proliferation.

#### 5.3.2.1 Case B1 & B2: MM$^{\mathbf{f}}$ Model

In addition to varying parameters associated with stent design (DM & RP), parameters detailing the effectiveness of drug ($k_{max}$ and $k_{50}$) are perturbed (Eqn. 5.7 & 5.8). As such, a local sensitivity analysis is performed, where the range of values considered is presented in Table 5.6.

Case B1: Free-drug MM model

| Parameter | Value range |
|---|---|
| $k_{max}$ | 1, 0.5 |
| $k_{50}^1$ | $2.5\times10^{-5}$ |
| $k_{50}^2$ | $2.5\times10^{-6}$ |
| $k_{50}^3$ | $2.5\times10^{-7}$ |

Case B2: Bound-drug MM model

| Parameter | Value range |
|---|---|
| $k_{max}$ | 1 |
| $k_{50}^1$ | $B_c^s/2$ |
| $k_{50}^2$ | $B_c^s/5$ |

Table 5.6: Study B: Different parameter values $k_{max}$ and $k_{50}$ used within a given global parameter regime, defined by Table 5.5.

Assessing model MM$^{\mathrm{f}}$ first (Case B1), it is observed that as the drug mass is increased within a given set of parameters, $k_{max} = 1$ (Fig. 5.10a) or when $k_{max} = 0.5$ (Fig. 5.10b), the inhibition

of restenosis is more profound. In the absence of drug binding, where the effectiveness of drug approaches an upper limit, it is both the initial drug mass and the efficacy parameters ($k_{max}$, $k_{50}$) that define drug performance, alongside the drug release rate. Elaborating on this, at higher drug masses, the difference between successive $k_{50}$ values is minimal, and it is likely the model approaches some upper value. Similarly, it is noted that for $k_{50}^3$ that a further increase in mass would also have negligible difference in arterial response.

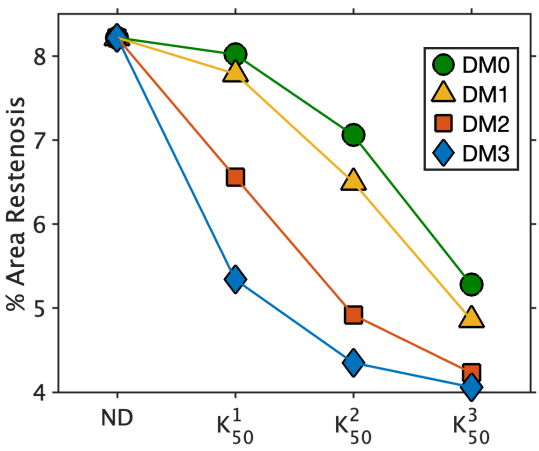


(a) Study B1 - DM: $k_{max} = 1$

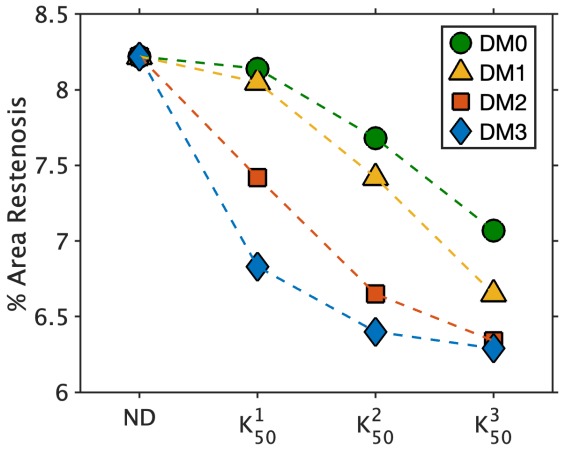


(b) Study B1 - DM: $k_{max} = 0.5$

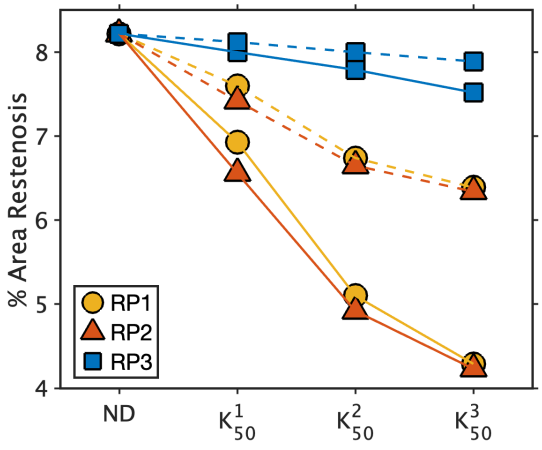


(c) Study B1 - RP

Figure 5.10: How % area restenosis varies across the different parameter regimes. Markers and colours highlight the different initial drug masses or release profiles simulated. Line styles separate the different $k_{max}$ values such that: Solid lines = $k_{max} = 1$ and Dashed lines = $k_{max} = 0.5$. (a): How drug mass influences % area restenosis for $k_{max} = 1$. (b): How drug mass influences % area restenosis for $k_{max} = 0.5$. (c): How drug release profile influences % area restenosis for $k_{max} = 1$ and $k_{max} = 0.5$. All simulations were run over a period of 50 days.

In addition to assessment of the initial drug mass, perturbations in drug release rates were considered. Results (Fig. 5.10c) show that the quickest drug release rate (RP3) is by far the worst, giving rise to the highest levels of restenosis. With drug released from the coating in

less than 10 days, and in the absence of drug retention, the drug is readily removed from the artery prior to the peak of cell proliferation (Fig. 5.2b). The other release profiles chart similar responses, with the performance of drug improving as $k_{50}$ decreases, towards some threshold value.

Case B2 introduced an alternative model (Eqn. 5.8), where specifically bound drug mediates cell proliferation. Adopting the Michaelis–Menten–like term introduces additional parameters that control drug performance whilst receptor saturation still influences drug effectiveness through non–linear binding kinetics (Eqn. 5.4). Assessing the performance of Case B2 in isolation first (Fig. 5.11a and 5.11b) it is apparent that an upper limit on % area restenosis is approached for each $k_{50}$ considered. This is particularly prominent in Fig. 5.11a where, depending upon the value of $k_{50}$, the threshold value approached changes as the drug mass is increased. Compared with the free drug model ($MM^f$), particularly when drug mass is varied (Fig. 5.11c), a limiting behaviour is more notable in the bound drug case ($MM^b$), a consequence of receptor saturation, which is non–existent in the free drug model. Moreover, as expected, the adoption of RP3 drastically increases the severity of restenosis when free drug mediates cell function, where drug binding and retention in tissue is neglected.

In summary, although the free drug Michaelis–Menten model performed well when compared with *in vitro* proliferation data, it is unlikely that such an approach can be implemented within a model depicting *in vivo* conditions without adequate amendments to account for drug retention, a feature that is present in the bound drug Michaelis–Menten model. Thus, the receptor saturation (RS, baseline model: $RS^c$) and Michaelis–Menten ($MM^b$) bound drug models present themselves as possible options to detail the effect of drug on sSMC proliferation *in vivo*, where trends present are broadly similar across the two. The key difference being that the latter introduces additional unknown parameters that aid in the definition of drug efficacy.

#### 5.3.2.2 Case B3: $RS^v$ Model

With various mathematical models of drug transport adopting static arteries [79, 172, 178], the validity of this assumption is examined, assessing how the definition of a variable binding density compares with the constant one. In the absence of reliable estimates for the FKBP12 receptor expression per cell, three different values are considered for $R_c$ (Table 5.3). These are non–dimensional quantities estimated with respect to the average sSMC density within the therapeutic domain (Fig. 5.2b). Note, the computation of these estimates are naturally biased towards the constant assumption (Eqn. 5.10), with numerical and experimental evidence suggesting that $B_c^s$ is an adequate steady state assumption of the specific receptor density [79, 233].

The results of the model equations simulating $B_v^s$ are presented in Fig. 5.12a–5.12c, each considering different $R_c$ values. Although only the spatially–averaged temporal behaviour of $B_v^s$ across the therapeutic domain is illustrated in these figures, it is noted that the concentration of binding sites is highest directly behind the stent struts where damage following stent deployment

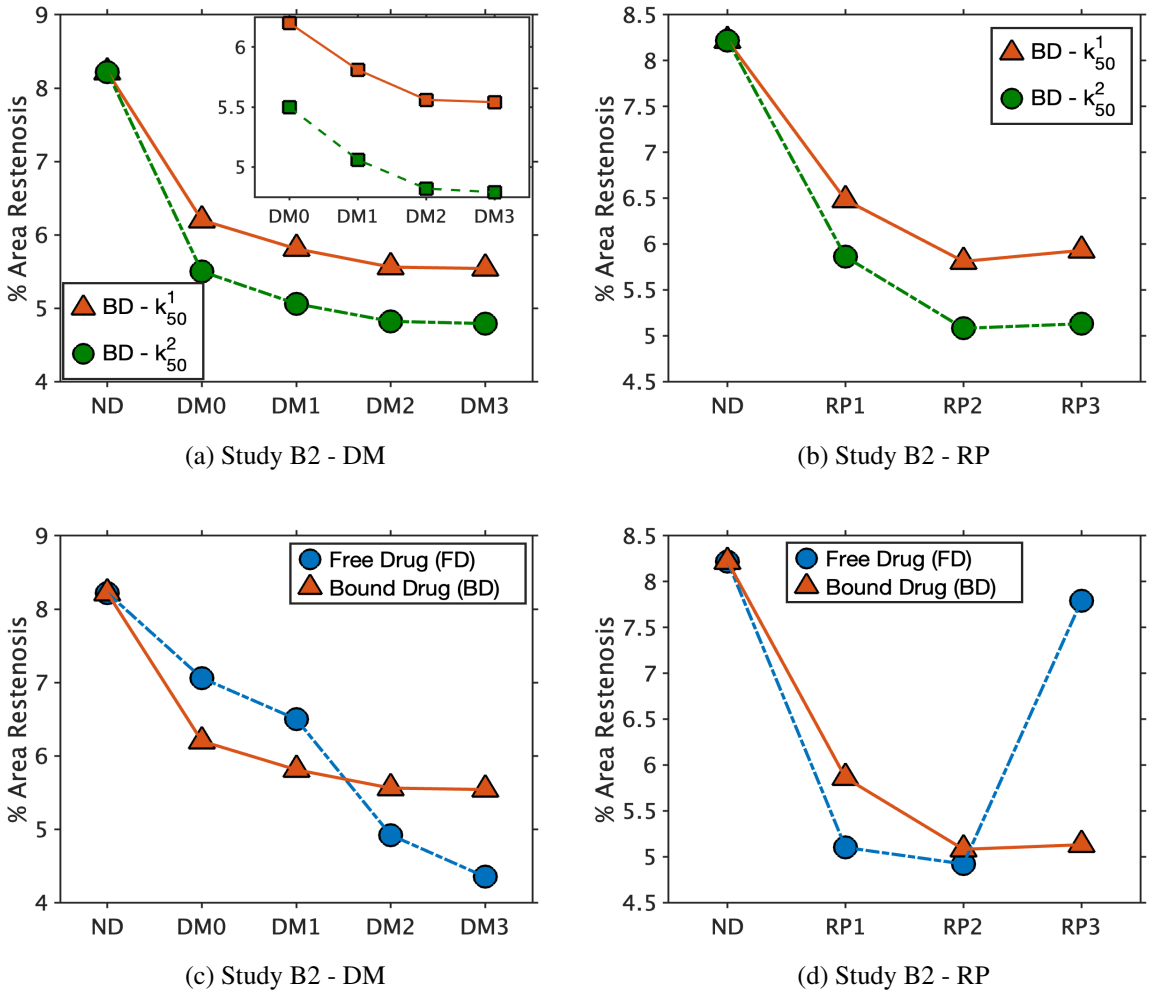


(a) Study B2 - DM

(b) Study B2 - RP

(c) Study B2 - DM

(d) Study B2 - RP

Figure 5.11: How % area restenosis varies across different parameter regimes for $MM^b$, compared directly to the free drug model ($MM^f$). (a) How different $k_{50}$ values influence response across the different initial drug masses assuming RP2. (b) Repeat of (a) for different drug release rates assuming DM1. (c) Trend comparison between free drug and bound drug MM model for the different initial drug masses assuming RP2. The free drug model employs $k_{50}^2$ whilst the bound drug model considers $k_{50}^1$. Both models employ maximal value for $k_{max} = 1$. (d) Repeat of (c) for different drug release rates assuming DM1. In both (c) and (d), the solid lines denote bound drug model response and dashed lines correspond to the free drug iteration. All simulations were run over a period of 50 days.

is most profound, declining as the outward edge of the therapeutic domain is approached and the severity of damage diminishes (Fig. 5.13).

To assess the binding site density assumption in depth, a dose–dependent study is performed for each $R_c$ value. Across all simulations, the receptor density increases as the value of $R_c$ increases. Of the three estimates considered, all with the exception of $R_c^1$ peak above the steady–state value of $B_c^s$; suggesting that this may underestimate the receptor expression per cell. Somewhat unsurprising is that regardless of the $R_c$ value considered, as the drug dose is increased

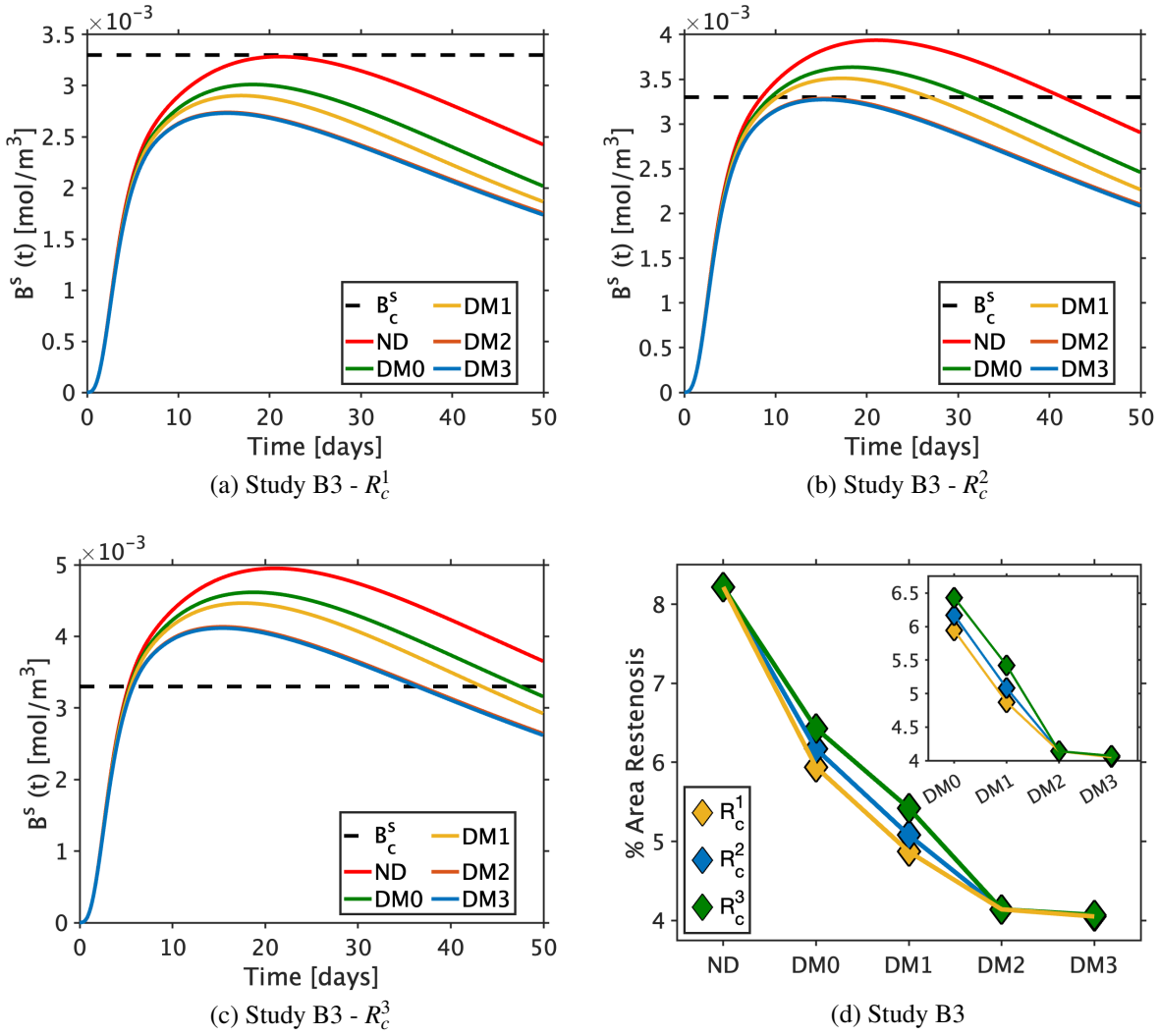


(a) Study B3 - $R_c^1$

(b) Study B3 - $R_c^2$

(c) Study B3 - $R_c^3$

(d) Study B3

Figure 5.12: Analysis of different receptor per cell ($R_c$) values. (a)-(c): How the receptor density ($B^s(t)$) varies as a function of time, compared directly to the constant assumption ($B_c^s$ – dashed black line) for each $R_c$ value: (a) $R_c^1$=1.435×10$^{-3}$, (b) $R_c^2$=1.72×10$^{-3}$, (c) $R_c^3$=2.163×10$^{-3}$. (d) Compares % area restenosis values between the three approaches across the 50 day time period. *Inset:* Focused on the different drug masses. All simulations were performed on 20% expansion profile and used RP2 release profile of the baseline stent configuration. In all cases, ND corresponds to the drug–free simulation.

a decrease in receptor density is observed, alluding to the idea that the expression of FKBP12 is dose–dependent. Thus, it would appear to be more physiologically representative of what occurs in reality, where the elution of anti–proliferative drug reduces cell growth, which in turn would decrease the specific receptor density. Of all values tested, only $R_c^3$ peaks above $B_s^c$ in all simulations. Moreover, the general trends of the dynamic receptor density ($B_v^s$) are in agreement with [354, 355], where receptor expression peaks when cell proliferation dominates, declining thereafter as ECM synthesis takes over and cells differentiate back to their dormant phenotype. Finally, Fig. 5.12d documents how % area restenosis varies across the different $R_c$ values as the

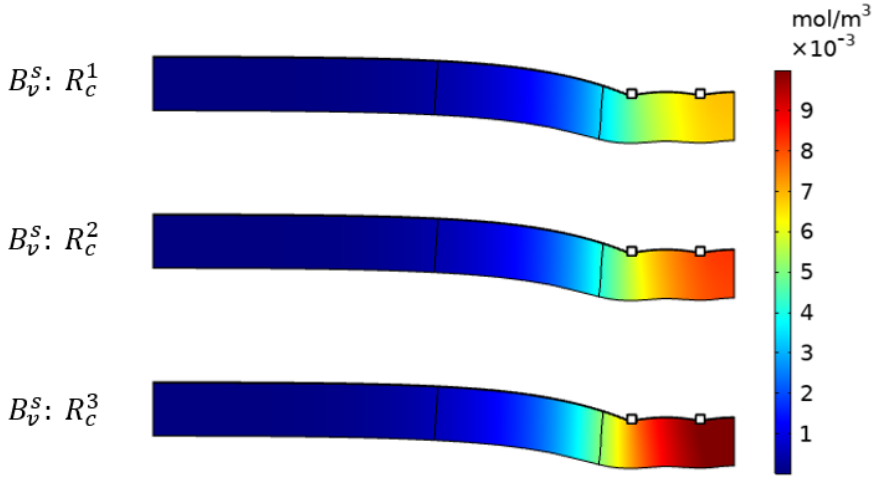


Figure 5.13: How the variable binding site density ($B_v^s$) varies spatially throughout the domain at 21 days, the approximate peak of proliferation within the 20% expansion profile. From top to bottom: $R_c^1$=1.435×10$^{-3}$, $R_c^2$=1.72×10$^{-3}$, and then $R_c^3$=2.163×10$^{-3}$.

drug dose is increased. At lower doses, $R_c^3$ presents with the most profound restenotic profile. This is understandable, as with an increase in receptor number, then cell proliferation must also increase in cases where drug is unable to fully saturate all of the binding sites. This is emphasised in Fig. 5.14 which illustrates the saturation of specific receptors assuming $B_c^s$ (Fig. 5.14a) or $B_v^s$ (Fig. 5.14b). However, as the initial drug loading is increased, the difference between the $R_c^{1\to3}$ cases is negligible as specific receptors are quickly saturated regardless of the receptor expression per cell (Fig. 5.14b).

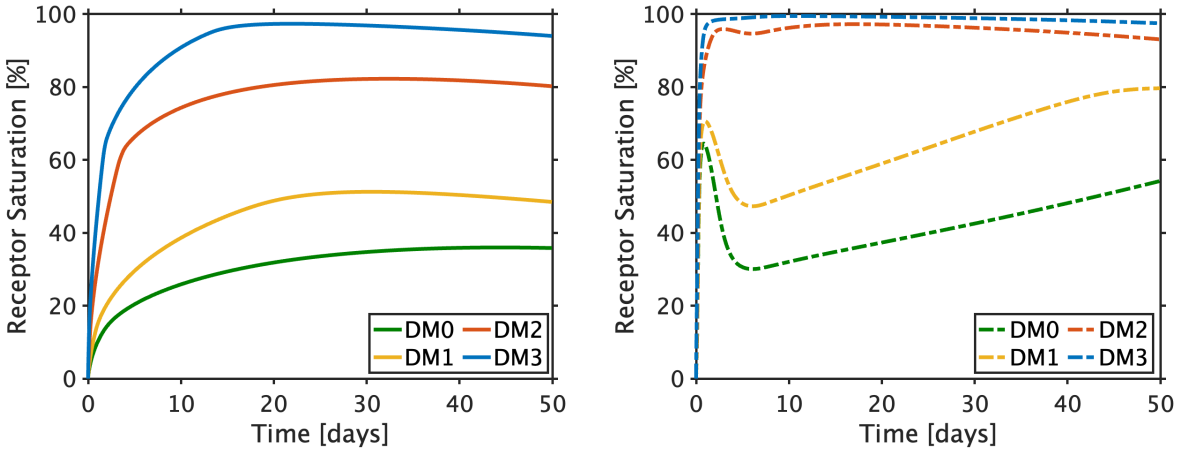


(a) Study A

(b) Study B3

Figure 5.14: How receptor saturation varies between the two binding site density approaches: (a) $B_c^s$ (solid lines) and (b) $B_v^s = R_c^2\ c_{ssmc}$ (dashed/dotted lines). Simulations are considered across various drug masses where RP2 is considered within the 20% expansion ratio of the baseline stent configuration.

Investigating the receptor saturation curves in more detail, it becomes apparent that under the assumption of a constant binding site density ($B_c^s$), the curves rise steeply at early times before a slower incline towards peak saturation. Following this, a gradual decline ensues as the free drug concentration source depletes (Fig. 5.14a). Trivially, the steepness of the curve and height of the peak are greater when the initial drug loading is higher. These trends are reciprocated in models that adopt the variable binding site ($B_v^s$) assumption (Fig. 5.14b). However, a more peculiar profile is present, particularly evident at lower drug masses. Fig. 5.15 elaborates on these profiles in depth, taking DM1 from Fig. 5.14b as an example, where sections of the receptor saturation (RS) curve are colour–coded as so: RS1 (blue), RS2 (red), and RS3 (green). RS1 has been alluded to earlier as it highlights the initial peak in the saturation of receptors, a consequence of the initial condition prescribed for the sSMC population. RS2 denotes the decline in receptor saturation, where the transition of cells from contractile to synthetic occurs on a quicker timescale than the release and binding of drug, highlighted in the red box where the gradients of $B_v^s$ and $b^s$ are shown. Finally, RS3 analyses the long linear region, which in some cases is met with a plateau. The linear region is a consequence of the rate of change of $B_v^s$ and $b^s$ being similar, noted towards the end of curves presented in RS2. For lower masses (DM1: Fig. 5.14b), the plateau occurs following a decline in the cell population as $b^s \rightarrow B_v^s$. At higher masses this peculiar profile is less prominent due to the large amount of drug entering the artery, where receptors are quickly bound with drug as a result.

In addition to perturbations in the initial drug mass, similar trends are apparent following analysis into the different release rates (Fig. 5.16). Interestingly, when adopting the variable binding site density ($B_v^s$), the quicker release rate (RP3) approaches levels of inhibition similar to RP2, overtaking it when the receptor expression per cell is equivalent to $R_c^3$. This implies that when the number of binding sites per cell is increased, drug needs to be released more quickly during the active phase of remodelling to combat restenosis. This is emphasised in Fig. 5.16a, where the crossover between RP2 and RP3 occurs later as $R_c$ is increased. This may suggest that $R_c^3$ is an over–estimate, since literature has illustrated that a sustained release (RP2) is the optimal selection for the design of DES [79]. Moreover, taken together with previous efforts, this study heightens the need for further exploration into the drug delivery aspect of stenting, particularly when coupled directly to cell functionality. Results suggest that the definition of binding site density has a clear impact on the overall performance of the stent within this model of restenosis. Experimental data would provide further insight, where the validity of the estimates for $R_c$ can be probed in depth.

Summarising this study, regardless of whether $B_c^s$ or $B_v^s$ is considered, the correct trends with respect to receptor saturation and restenosis are observed. Both show, as Eqn. 5.6 suggests, that the saturation of specific receptors defines drug efficacy, and thus more profoundly inhibits excessive tissue growth.

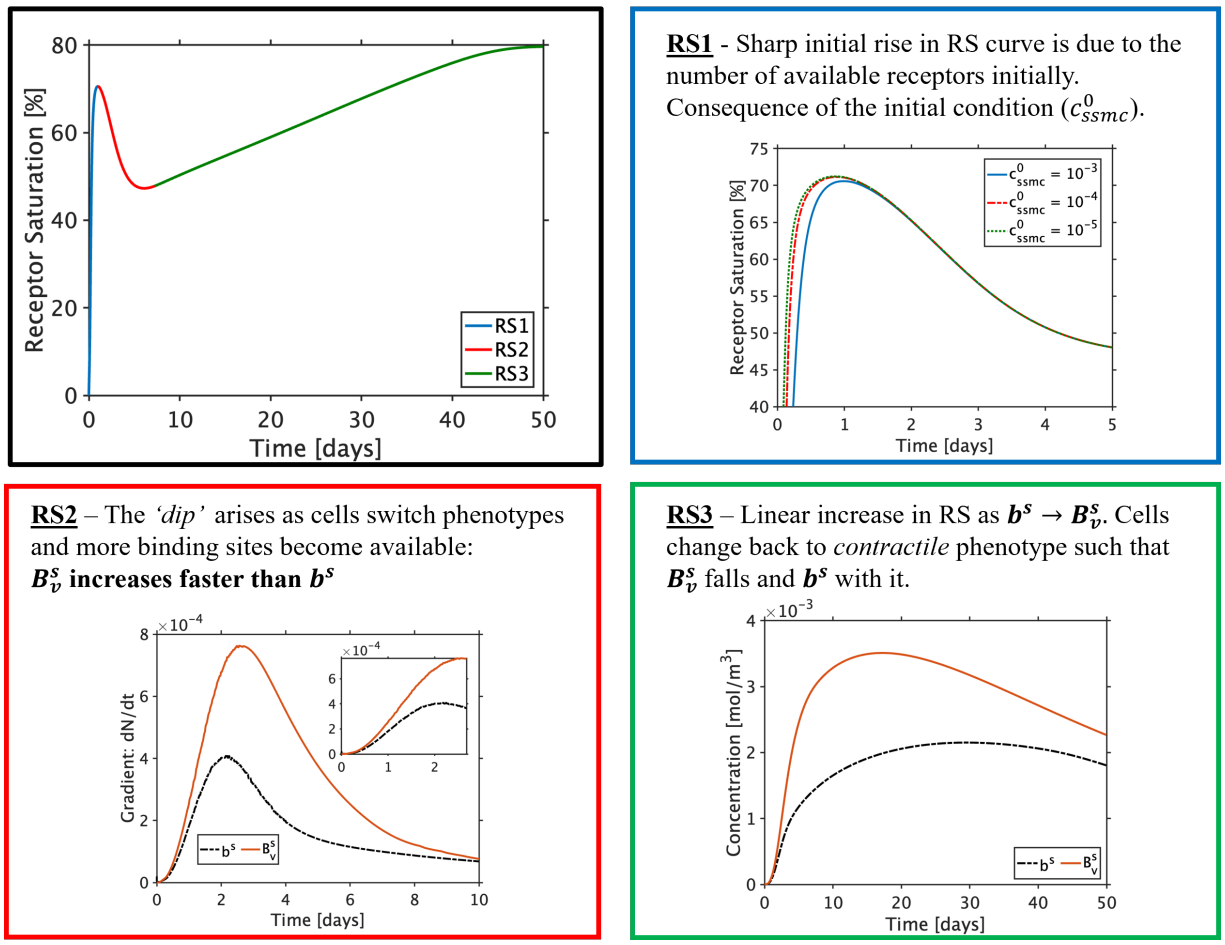


Figure 5.15: A schematic breakdown of the receptor saturation curve (DM1: Fig. 5.14b) under the assumption of a variable binding site density, $B^s_c$. RS1 – Impact of the initial condition for $c^0_{ssmc}$. RS2 – Why the dip in RS occurs. N = $b^s$ or $B^s_v$. RS3 – The linear increase in the RS plot.

## 5.4 Limitations & Future work

With limitations of the restenosis model discussed in depth in Chapter 4, the limitations associated with the drug transport model and how it couples to the tissue growth model are discussed in depth here. There are three key limitations present: (i) the complexity of the drug transport model, (ii) lack of an investigation into additional drug compounds, and (iii) the influence of drug on other key cell types is neglected. Each of these is elaborated on within the following sections.

### 5.4.1 Complexity of the drug transport model

Addressing the key limitation first, it is clear that the model lacks complete realism by neglecting flow. Although state–of–the–art drug transport models assume steady Navier Stokes [78, 169, 188, 189, 196], recent efforts have shown that in idealised cases, free drug concentrations in the lumen are several orders of magnitude lower than in the tissue, meaning that the lumen

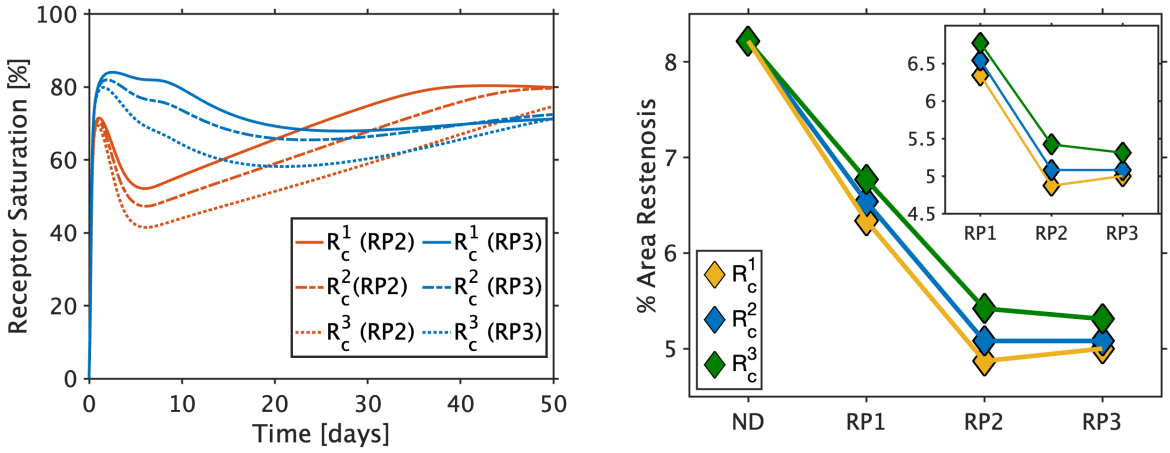


(a) Study B3 (b) Study B3

Figure 5.16: Analysis of receptor saturation curves for different drug release profiles (RP) for each $R_c$ value when drug mass is fixed at DM1. (a) Receptor saturation curves for RP2 (orange) and RP3 (blue) across the different $R_c$ values. (b) % Area restenosis values across all $R_c$ values and drug release profiles (RP) across a simulation time of 50 days.

essentially acts as a sink for the drug [170]. However, other models have simulated fluid flow within the tissue [169,170,188,196]. This is typically considered through the implementation of Darcy's law, which can contribute towards the speeding up of drug transport depending upon the magnitude of the velocity field. As such, drug may become available to the binding sites more quickly, where receptor saturation profiles will likely peak earlier as a result. Sophistication of the model can then be further increased by making necessary changes to the geometrical model. For example, the transport properties of drug in each layer should be different, aided by the implementation of Kedem–Katchalsky equations which describe the flux of species transport across the boundaries within the arterial wall [169, 170]. These improvements are discussed in Chapter 7 (Conclusions and further work), where the drug–transport model is coupled to an ABM of restenosis.

However, the key rationale for neglecting flow here was a result of its absence from the restenosis model in Chapter 4. With the underlying effect of flow, and particularly WSS on cell function deep into the wall (e.g. SMCs) still absent [55, 226], it was deemed inappropriate to include its effect on drug–transport when missing from the tissue growth model. Moreover, the assumption of neglecting advection is valid in cases where the arterial Peclet number (Pe) is less than 1, in which cases diffusion dominates over advection.

However, upon introducing flow into the model, as an immediate next–step, one could consider how WSS influences EC recovery mathematically, in line with articles present in the literature [152, 154, 155], whilst mechanical induced arterial stresses mediate cell behaviour deep within the wall through a damage index, as currently proposed. Further model enhancements

could ensure that SMCs exposed to blood–flow are also influenced by WSS levels, with the subsequent effects deeper into the wall only considered as the understanding of the complex phenomena improves.

Moreover, further experimental evidence on specific receptor expression per cell should be made available to fully assess the implications of a constant versus dynamic binding site density. For example, [354, 355] qualitatively depict the evolution of FKBP12 in time, but provide no physical data on the possible values that can be used for $R_c$ in this model. As such, further *in vitro* and/or *ex vivo* data may aid in improving the estimate of $R_c$ and thus the predictive capabilities of this model.

### 5.4.2 Lack of additional drug compounds

This model considers the effect of just one drug, sirolimus, as a consequence of insufficient data detailing the binding kinetics of other drugs. For example, although there is data available for paclitaxel [169, 188, 194, 360], the binding parameters reported vary quite significantly, where recent data has even presented binding on and off rates similar to sirolimus [360]. Moreover, as stents shift to the adoption of alternative drugs (analogues of sirolimus, e.g. biolimus), data on their binding kinetics is needed to permit a comparative analysis between the drug considered in this computational model.

### 5.4.3 Neglecting the effect of drug on additional cell types

Delayed arterial healing is a recurring problem, particularly prevalent in arteries receiving DES [24, 25]. For example, in an animal study involving rabbits, Nakawza *et al.* [25] was able to demonstrate poor endothelial strut coverage for a variety of different DES over the traditional BMS. Initially, the hypersensitive reaction associated with the long–term presence of the polymer coating was perceived to be the primary culprit of delayed healing [24]. However, a series of studies have since demonstrated non–inferiority between durable stent coatings with enhanced bicompatibility versus those which host biodegradable properties [33–35] or neglect the coating entirely [39, 40]. Therefore, in an attempt to better understand the concept of delayed arterial healing, the computational model developed here should be extended to consider the effect of drug on multiple cell types, especially ECs. For example, *in vitro* data exists that charts similar responses with respect to the inhibition of proliferation between ECs and SMCs when sirolimus is considered [31]. Moreover, various 2D–axisymmetric computational models emulating drug release have demonstrated the presence of high concentrations of drug present in the endothelial layer, particularly at early times, establishing the importance of stent design when defining stent efficacy and safety [189, 361]. Such efforts focused on CFD, where stent design has been known to influence the size and location of recirculation zones at stent struts which may prolong the length of time the endothelial surface is exposed to increased drug concentrations. Therefore,

further efforts should initially explore how drug mediates the EC population; the topic of Chapter 6. With data associated with binding kinetics on the EC population unavailable, this will be proof of concept in an attempt to demonstrate the significance of delayed arterial healing. To do so, the methodology is amended from the current model to ensure that the EC and SMC population are explicitly coupled such that EC regrowth has a direct impact on key species involved in excessive tissue growth. Following this, sophisticated co–culture experiments can then be used to provide data that may help validate such a model. Then, in time, efforts should also be extended to be inclusive of CFD, where the impact of recirculation zones and low WSS on drug distribution and thus EC function can be assessed.

## 5.5 Conclusion

In conclusion, this chapter presents a novel computational model, explicitly coupling drug transport kinetics with cell behaviour, and thus tissue growth as a consequence of spatiotemporal drug delivery from a stent. Results highlight that an intricate interplay in the initial coating drug dose and release rate exists, and that the choice of these parameters are important when optimising the design of DES. Despite the aforementioned limitations, the model charts expected trends, highlighting that in scenarios where arterial stress is greater following stent deployment, an increase in drug dose should be considered to combat the heightened healing response. This suggests that different stent designs could incorporate different drug release rates and initial drug loadings. Further work should explore the role of drug across multiple cell types whilst also increasing model sophistication to be inclusive of flow, observing its impact on both drug transport and cellular functionality in harmony.

# Chapter 6

# An improved model of restenosis: Understanding the possible implications of delayed arterial healing

## 6.1 Introduction

The computational model in Chapter 5 demonstrated the role of anti–proliferative drug on the inhibition of restenosis. However, a limitation of the model in Chapter 5 was that it did not incorporate the effect of anti–proliferative drug on the endothelial cell (EC) population. This is particularly important given that clinical and experimental evidence has highlighted the occurrence of delayed arterial healing, the inhibition of EC recovery, following the deployment of drug–eluting stents (DES) [24,25,362]. From preliminary bare metal designs, initial DES hosted two significant differences: the inclusion of a polymer coating and drug. As such, these were noted as the two possible explanations for the occurrence of delayed arterial healing following the deployment of DES.

The first was associated with physical stent design, where the permanence of the polymer coating and/or device subjected the patient to a hypersensitive reaction, prolonging inflammation [24]. As such, stent design shifted to devices absent of a polymer coating or the employment of biodegradable materials and resorbable structures [22]. However, clinical studies have since highlighted that with increased biocompatibility, adverse patient outcome was indifferent between these newer devices versus the traditional durable, polymer coated approach [33–35, 39, 40].

The second proposed explanation for delayed arterial healing was associated with the drug delivery strategy. Evidence has shown that drugs coated on stents inhibit the proliferation of both ECs and smooth muscle cells (SMCs). For example, Nakawaza *et al.* [25] illustrated poor endothelial strut coverage across a range of commercial DES when deployed in rabbit iliac arteries. Additionally, Matter *et al.* [31] noted within an *in vitro* study that the proliferative

capacity of ECs were hindered to an extent similar to SMCs, when exposed to the same dose of drug (sirolimus and tacrolimus).

Elaborating further on the drug delivery strategy, despite the large array of drug transport models discussed in Chapter 1 and 2, it is to the best of the author's knowledge that none of those models account for the impact of drug on the explicit function of cells. In other words, these models adopted static arteries, where tissue remodelling through cell proliferation was not considered. Nonetheless, the importance of the drug delivery strategy was highlighted by Tzafriri *et al.* [79, 194], where the sustained release of drug over the course of 30 days reduced the occurrence of in–stent restenosis (ISR). However, here the focus was primarily on drug binding to SMCs and to non–specific sites (e.g. extracellular matrix), with drug's effect on ECs not considered. Drug delivery was further analysed by Bozsak *et al.* [188] who were pursuing the optimal design of DES. Following the derivation of a 2D–axisymmetric drug delivery model, their results demonstrated how the transport kinetics of different drugs varied within the arterial wall. With these drugs coated on commercial stents, the study suggested that the release kinetics of DES should be tailored to the drug used. This was further emphasised in their subsequent paper, where the optimal course of drug release was found to be markedly different between paclitaxel and sirolimus–eluting stents [189]. The former involved depositing drug very quickly, or over the course of months to a year. Whereas sirolimus–eluting stents performed best only when drug release was slow. The importance of stent design was then explored by Seo *et al.* [361], investigating its impact on flow disturbance and the concentration of drug at the interface between the lumen and the intima. The results of this study did indeed show that stent design was an important factor on the concentration of drug that ECs were exposed too. Although consideration has been given to the optimum duration and conditions for drug delivery to ensure the sufficient recovery of the endothelial layer [189, 361, 363], the explicit behaviour of drug on EC functionality does not appear to have been modelled to date.

Despite re–endothelialization rates improving in newer generation devices [364], repeat procedures remain unsatisfactory at 1–year follow–ups [48], with ISR known to be the primary culprit [50]. The re–endothelialization process is crucial to vessel re–narrowing, given that the presence of a fully functional endothelium is known to halt further SMC proliferation and thus tissue growth [62, 66, 67]. Thus, motivation for an improved restenosis model exists, where the original model in Chapter 4 assumes that the EC population behaves independently of the other model constituents. However, it is known from literature that EC recovery is directly impeded by vascular injury as a result of stent expansion (Fig. 6.1a) [62]. As such, justification exists for coupling EC recovery to *damage*, a variable associated with vessel injury in the model.

Moreover, it has been well documented in both experimental and modelling literature that increased vascular injury stimulates a more aggressive healing response [56, 60, 62, 65, 66]. For example, Zun *et al.* [66] produced the model data presented in Fig. 6.1b, which demonstrated the effect of stent deployment on restenosis (neointima thickness). Within their framework, re–

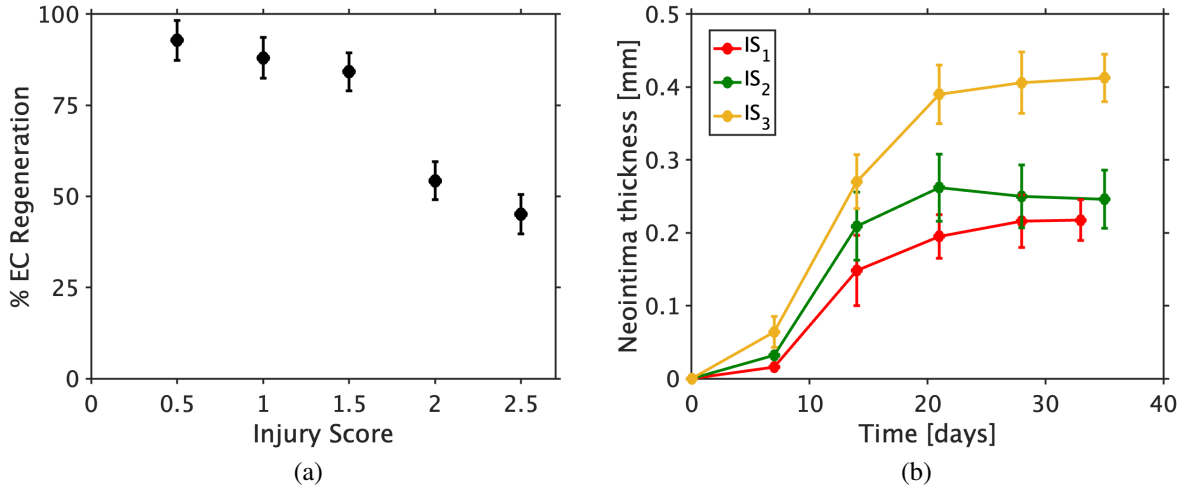


Figure 6.1: (a) How vascular injury impedes EC regeneration in rabbit iliac arteries. Data reproduced from [62]. (b) Increase in tissue growth (neointima thickness) following more intrusive stent deployment. IS = Injury score. $IS_1$: Stent only touches the internal elastic lamina (IEL), $IS_2$: Stent minimally pressed into IEL at angle of less than 45°, and $IS_3$: Stent is further pressed into IEL at angle of greater than 45°. Full details on the injury score can be found in [63]. Data reproduced from [66].

endothelialization is a key marker of healing, where upon the regeneration of a fully functional endothelium, the healing process is stopped. To the best of the author's knowledge, such an approach has not yet been considered within a continuum framework. Although the restenosis model in Chapter 4 has previously demonstrated more profound healing profiles when stent deployment is more intrusive, it fails to synchronously capture the behaviour of both ECs and SMCs as the artery heals. Therefore, in order to be able to fully capture the implications of delayed arterial healing following drug delivery, it is necessary to explore a coupling where the regrowth of the endothelial layer limits the proliferative capacity of SMCs.

The notion of delayed arterial healing is made particularly interesting following drug delivery, where the competition of drug between different cell types (ECs and SMCs [31]) is crucial. This is important given that a trade–off following drug delivery exists. For example, in Chapter 5 an intricate interplay was revealed between parameters associated with the design of DES when the inhibition of only one cell type (SMCs) was considered. However, in reality, this intricate interplay is further compounded by the fact that drug needs to be delivered in high enough concentrations to inhibit SMC growth without adversely impeding EC functionality. This balance suggests that an optimal drug delivery strategy exists which warrants further investigation.

Thus, the aim of this chapter is to devise a computational model which simulates the effect of drug on both ECs and SMCs in an attempt to better understand how the drug delivery strategy has an impact on delayed arterial healing. Prior to the inclusion of drug, the first objective is to propose changes to the restenosis model from Chapter 4 such that ECs have a direct influence

on the behaviour of key model constituents. To enable the success of this objective, two key model changes are proposed. The first model change establishes a coupling between *damage* and ECs, such that vascular injury has a direct impact on the time taken for the artery to heal. Following this, the second change to the restenosis model proposes a coupling between ECs and SMCs. Therefore, the recovery of the EC layer, directly mediated by vascular injury as per model change 1, will have a notable impact on the proliferative capacity of SMCs. In other words, a delay in re–endothelialization should promote a prolonged period of active SMC behaviour [65, 67]. Direct comparisons are made with the original restenosis model proposed in Chapter 4 for both of these model changes. The second key objective is to then test different drug transport models, assessing the effect of drug on the proliferation of ECs and SMCs and the possible implications on patient outcome. Following a description of the computational model, each of the aforementioned objectives are considered in turn.

## 6.2 Computational model

### 6.2.1 Geometry, assumptions and simplifications

With the present study more focused on EC and SMC behaviour, and to reduce computational time, the full geometry implemented in previous chapters (4 and 5) is reduced in length, (Fig. 6.2), equivalent to an inter–strut space ($\delta_{ss} = 7 \times T_{s_t}; T_{s_t} = 81 \mu m$), hosting just a single strut. This is considered for two stent expansion scenarios (20 and 30%) to capture the impact of damage induced by stress within the model. The expansion step considers the full geometrical model (Chapter 4), from which the slice in Fig. 6.2 was exported along with the spatiotemporal Von Mises stress map. For clarity, all boundaries and domains are highlighted in Fig. 6.2, of which all except $\Gamma_l$ and $\Gamma_r$ are the same as in Chapter 4. All boundary conditions implemented within the species evolution and drug transport models are detailed in Table 6.1.

To ensure the time–course of the re–endothelialzation process is similar to that proposed in [53,66], various parameter values ($g_{ec}$ and $k_d$) are amended (Table 6.2) following the coupling of ECs with *damage* and SMCs. The rate of these parameters have been increased such that healing, described as the degradation of damage and recovery of ECs, occurs over a 50–day period following an expansion of 30%. However, with drug likely to further delay EC recovery, simulation time will be extended towards 80 days when drug delivery is considered. This is to assess the longer term effects of drug on the EC and SMC populations. Moreover, as a consequence of the simplified geometry, restenosis is not evaluated. However, it is known from Chapter 4, that with increased SMC number and ECM concentration, a rise in restenosis severity would be observed.

As in Chapter 4 and 5, the commercially available software COMSOL Multiphysics 5.6a (COMSOL AB, Burlington, MA, USA) was used to mesh and numerically solve the compu-

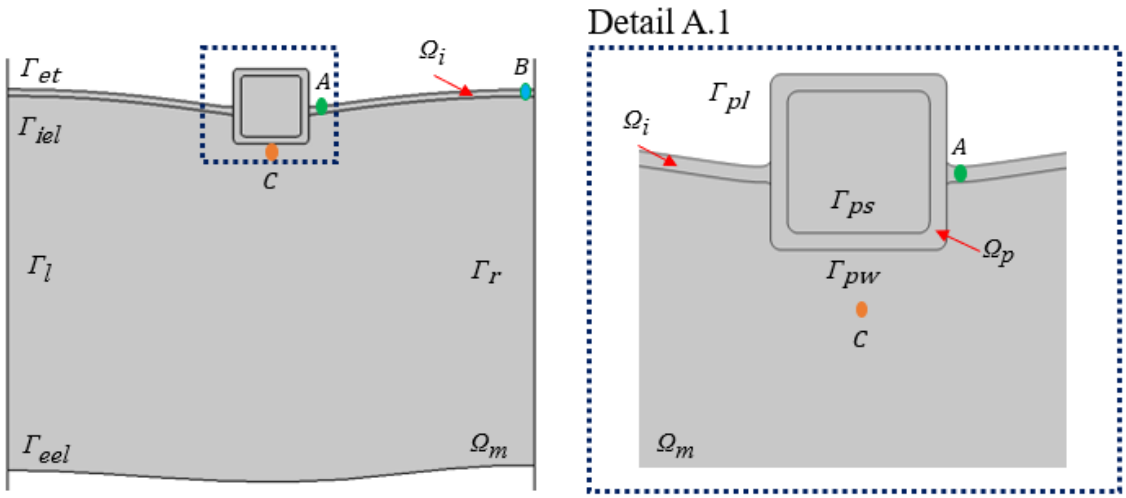


Figure 6.2: Simplified geometry (20% expansion) hosting a single strut with a domain length of a single inter-strut space ($\delta_{ss}$). The 30% geometry (not shown) is of identical length. All domains are denoted by $\Omega$ ($\Omega_p$: polymer coating, $\Omega_m$: media, and $\Omega_i$: intima). All boundaries are denoted by $\Gamma$ ($\Gamma_{et}$: endothelium, $\Gamma_{iel}$: internal elastic lamina, $\Gamma_{eel}$: external elastic lamina, $\Gamma_l$: left–wall, $\Gamma_r$: right–wall, $\Gamma_{pw}$: polymer–wall interface, $\Gamma_{pl}$: polymer–lumen interface, and $\Gamma_{ps}$: polymer–strut interface). Detail A.1 highlights the intima and polymer coating. Various points of interest include: A (green)–intima adjacent to the strut, B(blue)–far end of the domain ($\Gamma_r$), and C (orange)–media 0.05 mm behind the stent strut.

| | | Boundary condition | |
|---|---|---|---|
| Boundary | Location | Species evolution model | Drug transport model |
| $\Gamma_{pw}$ | Polymer–wall interface | Zero–flux | Continuity |
| $\Gamma_{ps}$ | Polymer–strut interface | N/A | Zero–flux |
| $\Gamma_{ps}$ | Polymer–lumen interface | N/A | Infinite sink |
| $\Gamma_{et}$ | Endothelium | Zero–flux | Infinite sink |
| $\Gamma_{iel}$ | IEL | Zero–flux$^{\dagger}$ / Continuity$^{\ddagger}$ | Continuity |
| $\Gamma_{eel}$ | EEL | N/A$^{\dagger}$ / Continuity$^{\ddagger}$ | Infinite sink |
| $\Gamma_l$ & $\Gamma_r$ | Left and right | Zero–flux | Zero–flux |

Table 6.1: List of all boundary conditions imposed in the species evolution and drug transport model. Please refer to Fig. 6.2 for a schematic presentation of all boundary locations. In the species evolution model, boundary conditions vary between the ECs, existing only in the intima ($\Omega_i$) and species residing in the intima and media (e.g. SMCs and ECM). The boundary conditions imposed on ECs are denoted by a † whilst all other species are represented by a ‡. If symbol not shown then the BC is the same for all species. Continuity refers to a continuity of flux and concentration.

tational model. The reader is referred to Chapter 4 (Section 4.2.6) for a discussion on the numerical implementation and to Chapter 5 (Fig. 5.3) for an illustration of the mesh considered,

particularly detail B.

| Parameter | Description | Previous Value (Chapter 4) | New Value |
|---|---|---|---|
| $g_{ec}$ | EC proliferation | $1\times10^{-6}$ [$s^{-1}$] | $2.5\times10^{-6}$ [$s^{-1}$] |
| $k_d$ | Degradation of *damage* | 0.5 [$m^3$ $mol^{-1}$ $s^{-1}$] | 2.5 [$m^3$ $mol^{-1}$ $s^{-1}$] |
| $k_{csmc}^{diff}$ | Differentiation: Contractile to synthetic | 5e-7 [$s^{-1}$] | 3.5e-7 [$m^3$ $mol^{-1}$ $s^{-1}$] |
| $k_{ecm}$ | ECM synthesis | 7.19e-5 [$s^{-1}$] | 3.2e-5 [$s^{-1}$] |
| $k_{20\%}^1$ | $\theta^e$ 20% decay constant | N/A | $8.58\times10^{-2}$ [$s^{-1}$] |
| $k_{30\%}^2$ | $\theta^e$ 30% decay constant | N/A | $9.3\times10^{-2}$ [$s^{-1}$] |
| $\theta_{20\%}^0$ | Initial mean *damage*: 20% | N/A | 0.2489 |
| $\theta_{30\%}^0$ | Initial mean *damage*: 30% | N/A | 0.5789 |

Table 6.2: New model parameters associated with the updated restenosis model. New parameter values for $g_{ec}, k_d, k_{csmc}^{diff}$, and $k_{ecm}$ are estimated such that the time–course of endothelial cell recovery occurs within 50 days. The other parameters, not previously considered in Chapter 4 are detailed in depth in Section 6.3.

## 6.3 Model change 1: Vascular injury influences endothelial cell recovery

The first model change from Chapter 4 considers an amendment to the equation describing the rate of change of the EC population such that vascular injury mediates its recovery [62]. To facilitate this, a direct coupling is established between ECs and the artificial construct *damage*, emulating the inflammatory response that stimulates arterial healing. From amendments made to the ECM species in Chapter 4, it is noted that the mean *damage* ($\theta$) within the stented domain differs significantly across the expansion ratios. Thus, it is this measure which is considered to ensure that EC recovery differs as stent deployment varies. In particular, it is the depreciation of this variable ($\theta$) in time that is of interest (Fig. 6.3a).

A disadvantage to this approach is that computing $\theta$ at every time–step increases computational time, significantly. In an attempt to find an alternative strategy, it is clear that the response presented in Fig. 6.3a produces a curve which closely matches exponential decay. As such, the mean *damage* is instead computed through the following expression:

$$\theta^e(t) = \theta_{P\%}^0 \, e^{-k_{P\%}^1 t}, \tag{6.1}$$

where $\theta_{P\%}^0$ is the initial mean *damage* present following stent expansion and $k_{P\%}^1$ is a linear decay constant that adequately emulates how $\theta$ changes in time throughout the healing process. The subscript, $P\%$, in each term refers to the expansion ratio present following stent deployment. By interpolating a series of points across the line which conveys the change in $\theta$ through time (Fig. 6.3b), a best–fitting parameter can be obtained for $k_{P\%}^1$ in Eqn. 6.1 by using the least

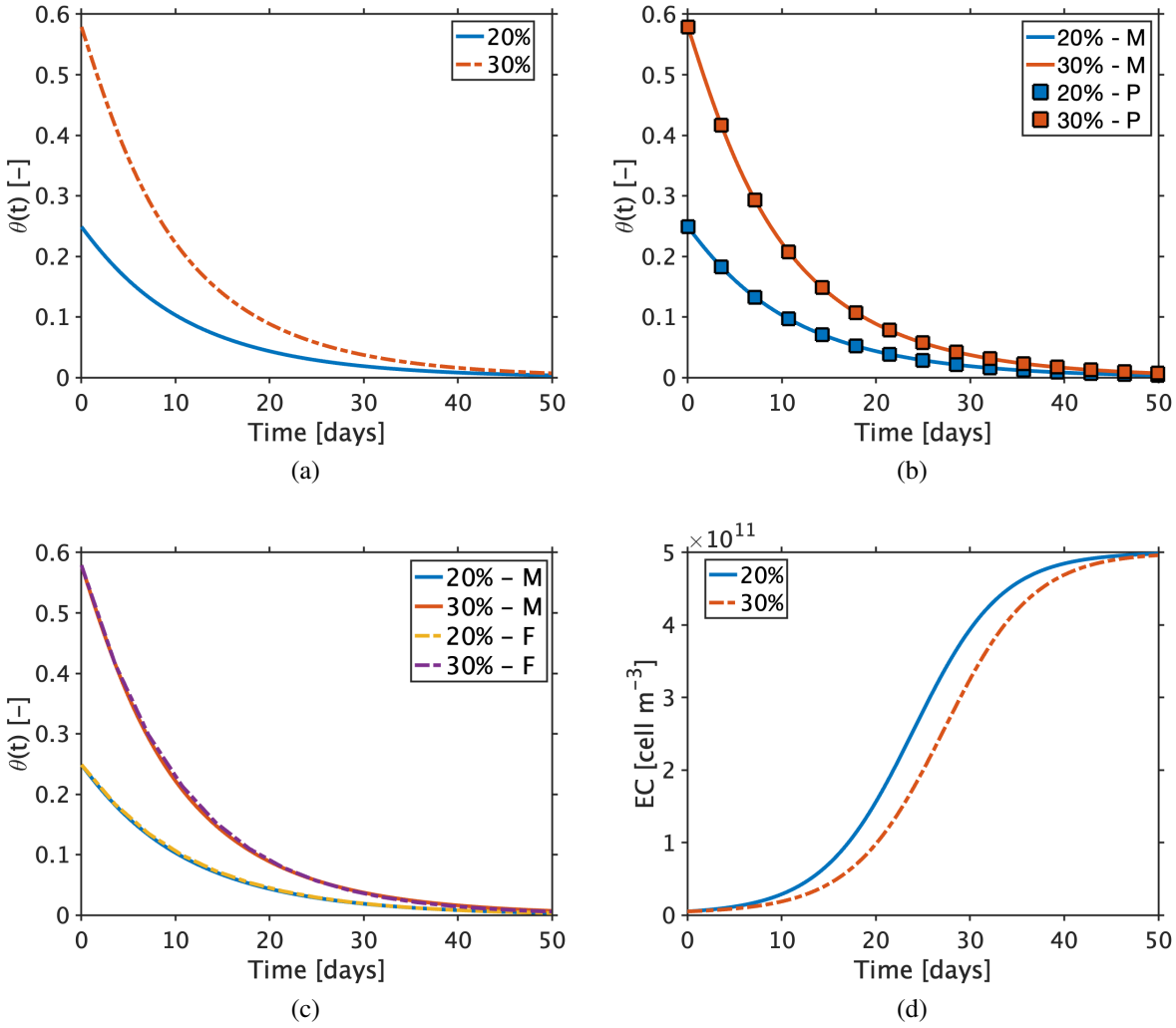


Figure 6.3: (a): How mean *damage* ($\theta\ (t)$) varies in time across the domain. (b): Interpolating a series of points (P) through the model (M). Where M is how the mean *damage* ($\theta$) depreciates in time using COMSOLs in–built average function. (c): Agreement between the original model (M) data using COMSOLs average function and the estimation of this data (F) provided by Eqn. 6.1. (d): How mean *damage* through an exponential interpretation ($\theta^e$) impacts EC proliferation for different expansions ratios.

squares method. Fig. 6.3c demonstrates the quality of the estimation, where the result of $\theta^e$ (F) is indifferent to the curve generated by COMSOL (M) which computes the average at every time step. Note, the values for the best–fitting parameters obtained for $k^1_{P\%}$ are presented in Table 6.2.

With distinct *damage* profiles now present between the expansion ratios, a link between *damage*, $d$, and EC regeneration can be established such that:

$$\frac{\partial c_{ec}}{\partial t} = D_{ec}\nabla^2 c_{ec} + g_{ec}\, c_{ec}\left(1 - \frac{c_{ec}}{K_{ec}}\right)\left(1 - \theta^e\ (t)\right), \quad \text{in } \Omega_i, \quad t > 0, \tag{6.2}$$

where the proliferative capacity of ECs ($c_{ec}$) is now hindered by *damage*. This is emphasised in

Fig. 6.3d which demonstrates the impact that *damage* has on EC recovery through the different expansion ratios; where it is known from Chapter 4 that increased stent expansion results in higher levels of stress and thus *damage*, heightening the healing response. Such a result qualitatively agrees with the trends discussed in Kipshidze *et al.* [62], as documented in Fig. 6.1a. Whereas, when considering the original restenosis model from Chapter 4, it is noted there is no distinction in EC recovery between the two expansion profiles (Fig 6.4). Although the original model is used, the new values in Table 6.2 are considered except for $k_{csmc}^{diff}$, where the units differ due to differences in governing equations that describe ECM synthesis in the original model (Chapter 4: Eqn. 4.8).

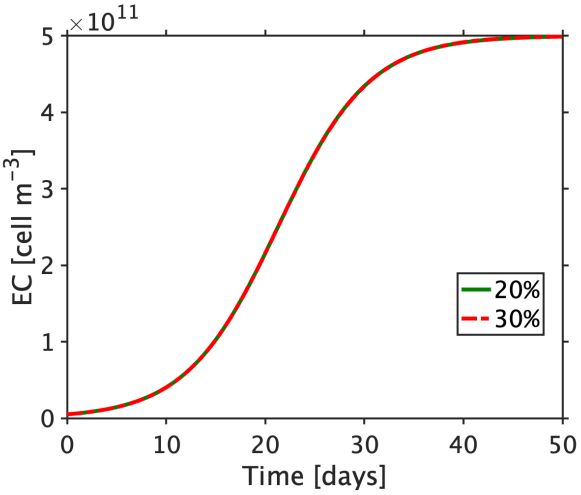


Figure 6.4: EC density at Point A (Fig. 6.2) when adopting the governing equations of the original model from Chapter 3.

## 6.4 Model change 2: ECs influence the proliferation of SMCs

### 6.4.1 Model formulation

With a coupling between vascular injury and EC regeneration established, a natural next step is to propose a model amendment such that EC recovery directly influences SMC behaviour. With stent expansion, and thus *damage* explicitly impeding growth of the former, sufficient coupling between ECs and SMCs will ensure that the proliferative capacity of SMCs is directly controlled by the regeneration of the endothelium [53,67]. To facilitate this, assumptions are required such that the growth of endothelial cells, present only in the intima ($\Omega_i$), influences the growth of SMCs present in all wall domains ($\Omega_i$ and $\Omega_m$).

As was present in the baseline model (Chapter 4), it is assumed that ECs initially exist at a small, uniform density throughout the intima, allowed to migrate through a diffusive term ($D_{ec}$). However, the timescale of EC migration is very quick due to the intima dimensions being

comparatively small. Thus, the density of these cells varies very little spatially throughout the domain. In an attempt to reduce model complexity, the density of the ECs ($c^{\star}_{ec}(t)$) is observed at just a single point, A (Fig. 6.2), immediately adjacent to the stent strut. To support this assumption, Fig. 6.5 depicts the EC response at Point A and B, where the latter is at the edge of the domain (Fig. 6.2), where no difference in cell density is noted.

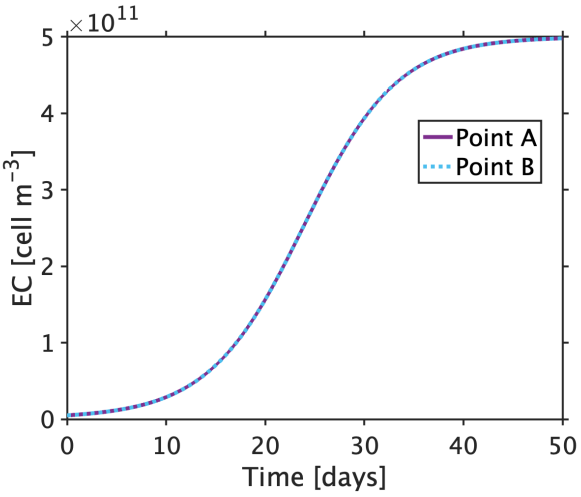


Figure 6.5: EC density at Point A and B, as detailed in Fig. 6.2.

Chapter 4 elucidated the role of ECs in maintaining vessel quiescence, where numerous chemicals (e.g. nitric oxide) are released to regulate vascular tone [53, 58, 331]. However, following stent deployment, this protective endothelial layer is often completely denuded, exposing the underlying tissue to circulating factors present in the blood [53, 56]. This is studied in depth in [53, 65–67], where the authors acknowledge that damage to this layer is what initiates the healing response, becoming more aggressive as the fenestrations in the IEL increase in severity [65]. Nonetheless, similar to [54, 55], the phenotype behaviour of SMCs in the initial restenosis model (Chapter 4) was controlled by ECM concentration, another aspect known to mediate the proliferative capacity of SMCs [54, 56, 70, 71, 325, 326]. However, to establish a direct coupling between ECs and SMCs, the terms associated with cell differentiation have been amended. Now cell differentiation, and thus the contractile SMC population is modelled via:

$$\frac{\partial c_{csmc}}{\partial t} = -k^{diff}_{csmc}\, c_{csmc}\left(K_{ec} - c^{\star}_{ec}\right) + k^{diff}_{ssmc}\, c_{ssmc}\left(c^{\star}_{ec} - c^{0}_{ec}\right), \quad \text{in } \Omega_i \;\&\; \Omega_m, \quad t > 0, \tag{6.3}$$

which replaces the equation describing the contractile SMC (cSMC) population in the original restenosis model (Chapter 4: Eqn. 4.8), with $k^{diff}_{csmc}$ and $k^{diff}_{ssmc}$ still dictating the rate of differentiation to and from the synthetic phenotype, respectively. The switch from contractile to synthetic is fast initially where the current EC density is close to zero following stent expansion ($c_{ec} = c^{0}_{ec} \approx 0$). As the species regenerates, $c^{\star}_{ec} \to K_{ec}$ and the differentiation back to the con-

tractile phenotype from synthetic dominates. To ensure trends were somewhat comparable with the baseline model, multiple parameters ($k_{csmc}^{diff}$ and $k_{ecm}$) were amended, with the previous and new values stated in Table 6.2.

### 6.4.2 Results

Model change 1 ensured that *damage*, as a consequence of stent deployment (20 versus 30% expansion), directly influenced the recovery of ECs. With a coupling now also established between ECs and SMCs (Section 6.4.1), an examination of the effect on key model constituents is necessary before further extending the model to account for drug transport. With only species evolution simulated, and tissue growth not calculated as a consequence of the geometry, the behaviour of SMCs (particularly sSMCs) and ECM are presented, species known to directly influence vessel re–narrowing (Fig. 6.6). Note that the response of ECs across different stent expansions have been shown previously (Fig. 6.3d).

Fig. 6.6a charts a significant change in sSMC behaviour from the original model (Fig. 6.6c), where the peak is not only heightened following increased arterial stress but also shifted such that the 'active' cells remain in their proliferative state for longer. The higher peak is associated with increased GF production as a consequence of *damage*, a behaviour illustrated in Chapter 4. However, the temporal peak shift is new and is a consequence of the delay to re–endothelialization following more intrusive stent deployment (Fig. 6.3d). Within the original model (shown in Chapter 4), the sSMC population is uncoupled from the re–endothelialization and thus only the height of the peak varies between expansions (Fig. 6.6c). With re–endothelialization delayed in the updated model of arterial healing, and the sSMC profile influenced, a significant impact on ECM synthesis is apparent (Fig. 6.6b). Here, the initial degradation is not only more profound, but occurs more quickly as a consequence of the increased synthetic SMC density. Thus, the new model is able to qualitatively agree with the trends illustrated in Fig. 6.1b, where a more intrusive stent deployment results in a more profound restenotic profile. Within the original model, similar to the sSMC population, only a change in the minimum peak of ECM is observed (Fig. 6.6d).

Summarising, a clear benefit of the updated model of arterial healing from the original one in Chapter 4 is that the healing is ceased as a consequence of the endothelial layer recovering. This feature was absent in Chapter 4, where the ECs acted independently of all other model constituents. Such a result alludes to the possible significance of delayed arterial healing, where an impairment to the recovery of ECs (through the delivery of anti–proliferative drug or increased vessel injury) could have a significant impact on patient outcome.

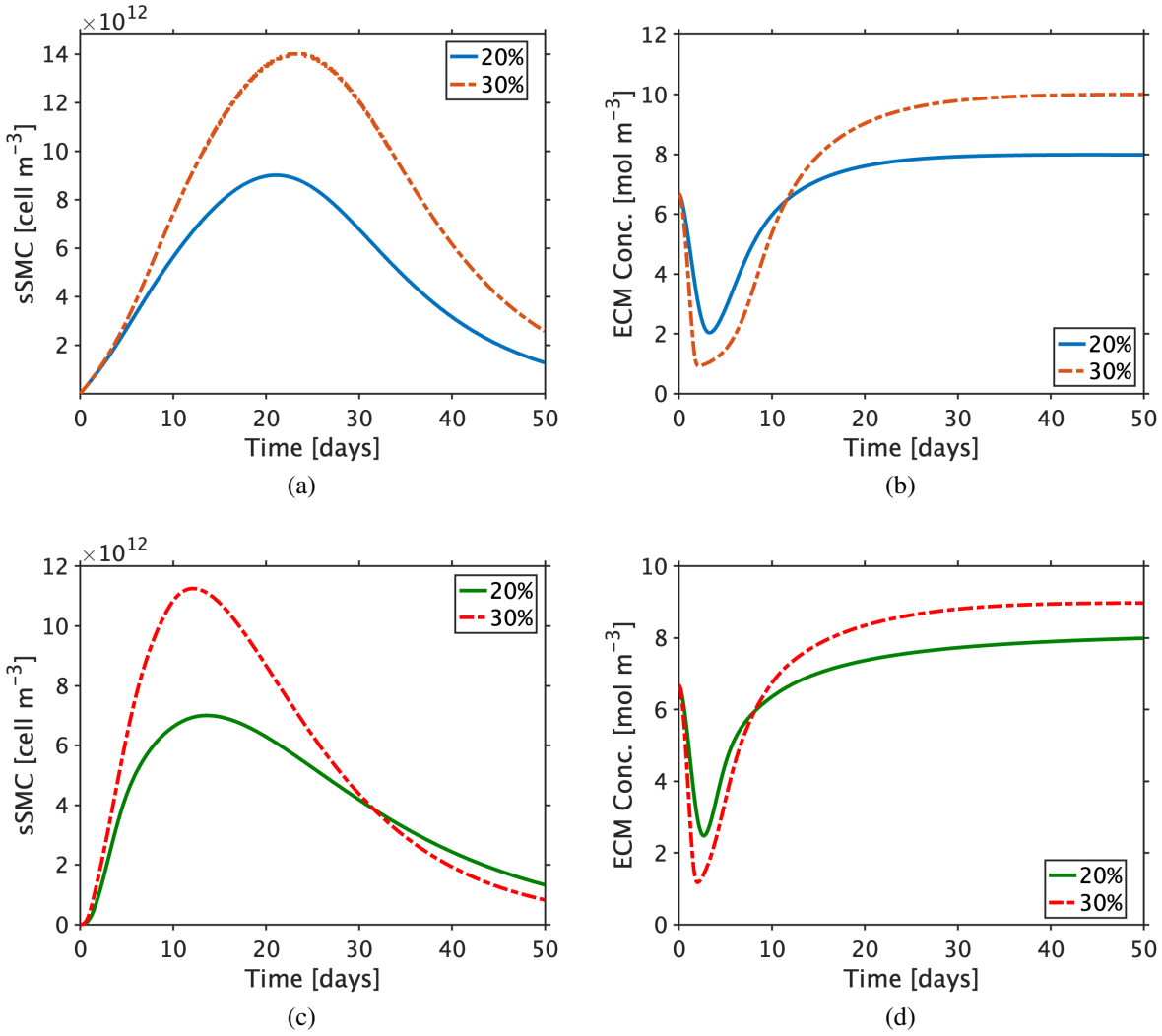


Figure 6.6: (a)–(b) How coupling EC and SMC species influences the behaviour of key species involved in restenosis within the updated model of arterial healing. (a) sSMC density. (b) ECM concentration. (c)–(d) Results adopting the restenosis model governing equations from Chapter 4. New parameter values (Table 6.2) are used for this model except for $k_{csmc}^{diff}$ where the units differ. (c) sSMC density. (d) ECM concentration. Results of all species behaviour are presented at Point C (Fig. 6.2).

#### 6.4.2.1 Impact of EC regeneration

With the results of the various couplings established (*damage* with ECs, and then ECs with SMCs), it is apparent that as a consequence of stent deployment, increased *damage* permits a delay in EC regeneration which has a subsequent impact on the proliferative profile of sSMCs. The next step is to then further analyse the possible implications of delayed arterial healing as a consequence of drug delivered from DES. Clinical and experimental data [25,27] has noted that re–endothelialization is impaired following the delivery of drug. However, to explore the justification for the inclusion of a drug transport model, a small sensitivity analysis is considered. The

purpose of this being to observe the impact of perturbations in the EC proliferation parameter ($g_{ec}$) on key model species: SMCs and ECM (Fig. 6.7). Given that the effect of stent expansion has already been assessed, the following sensitivity analysis is conducted for a single expansion ratio (20%).

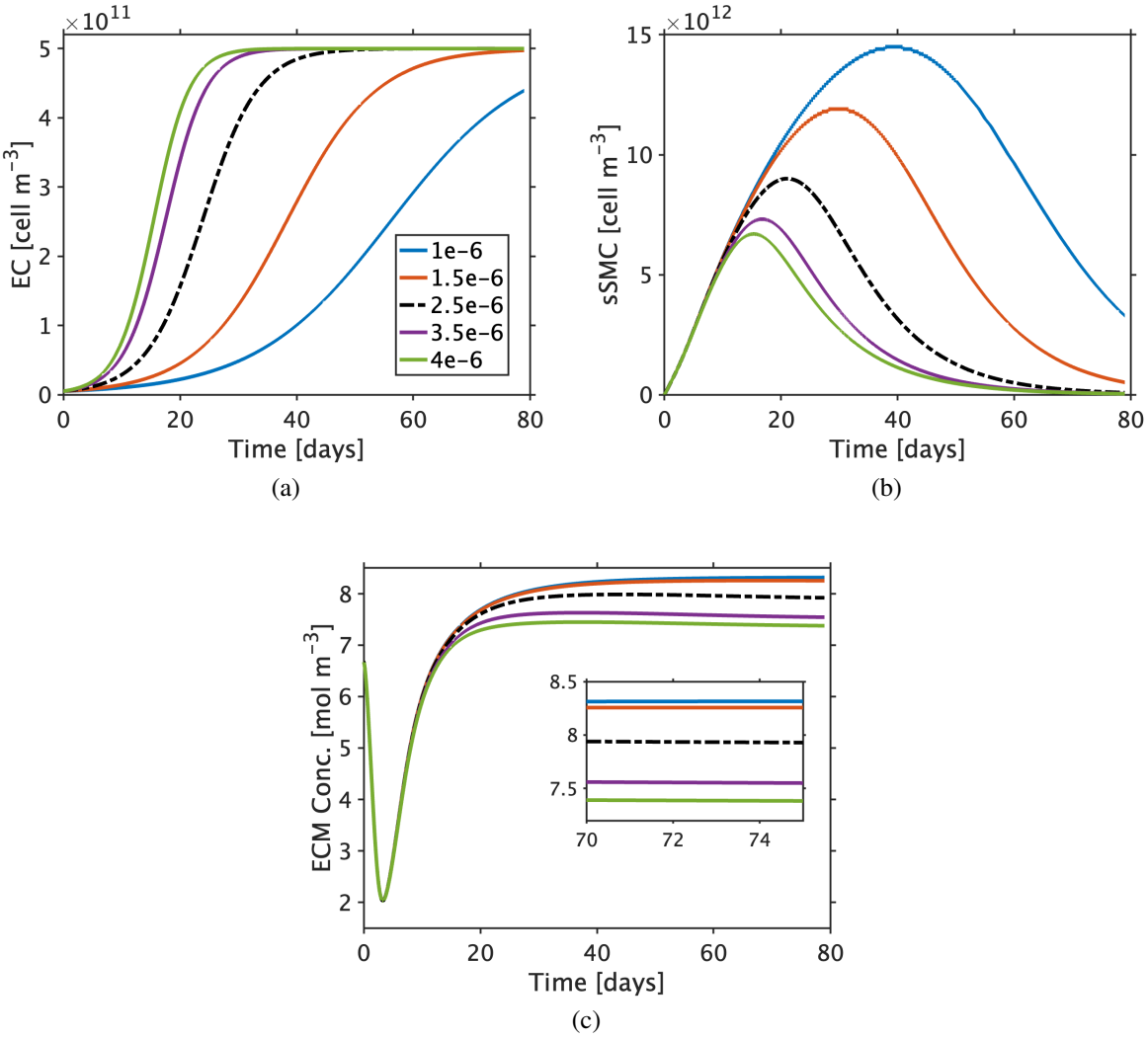


Figure 6.7: Investigating how EC proliferation ($g_{ec}$) influences the response of other species contributing to restenosis following a 20% stent expansion. (a) EC. (b) sSMC. (c) ECM. All species profiles illustrate the behaviour at point C (Fig. 6.2).

Fig. 6.7 presents the behaviour of three key species (EC, sSMC, and ECM) across a range of values for $g_{ec}$. Trivially, as the parameter is increased, the recovery of the ECs is faster, with the proliferative capacity of sSMCs hindered and ECM synthesis reduced. However, as EC recovery reduces, artificially emulating the presence of drug, more sSMCs proliferate, with the peak more profound in height and width, synthesising additional ECM as a result. Hence, with the new coupling term proposed between ECs and *damage* (Eqn. 6.2), and then ECs and SMCs (Eqn. 6.3), the endothelial barrier which interfaces the arterial wall is now intrinsically linked

to arterial healing. In other words, the healing process is halted as the number of ECs approach their healthy value ($c_{ec} \rightarrow K_{ec}$), and any delay in that would result in additional neointimal tissue being produced.

With the importance of EC regeneration demonstrated, the next stage is to explicitly account for drug, and its impact on EC recovery. Note, importantly, that drug will also be inhibiting the proliferation of SMCs. As such, the model proposed (Section 6.5) will explore the effect of drug on multiple cell types, investigating the possible implications of delayed arterial healing following treatment with DES [24, 25, 27, 362].

## 6.5 Accounting for the impact of drug on multiple cell types: ECs and SMCs

### 6.5.1 Governing equations

The drug transport model introduced in Chapter 5 is considered here, where drug resides initially within a polymer coating before diffusing into the arterial wall, binding to sites which are either specific or non–specific. To explore the effect of drug on the EC population and as a result arterial healing, additions and changes are made to the drug transport model, summarised in the list below:

- The introduction of a third bound drug phase (EC bound).
- Amendment to drug transport kinetics: diffusion in the intima ($\Omega_i$) and media ($\Omega_m$) now differ, as suggested in [170, 196].
- Amendments to the proliferative term for ECs (Eqn. 6.2) such that saturation of their receptors by drug mediates their growth.

The transport of drug in the polymer coating is identical to that proposed in Chapter 5, Eqn. 5.1. To account for the layer–specific transport properties, the free drug concentration in the wall ($c_w\ (r,z,t)$) is now amended to:

$$\frac{\partial c_x}{\partial t} = \nabla \cdot (D_x \nabla c_w) - R_x, \quad \text{in } \Omega_x, \quad t > 0, x = i, m, \tag{6.4}$$

where free drug ($c_x$) is present in all domains, differing in its transport properties ($D_x$) and reaction kinetics ($R_x$) between each of the layers, where superscript $x$ denotes the layer, either intima ($i$) or media ($m$). As in Chapter 5 (Eqn. 5.3), diffusion of free drug in the media is assumed to be anisotropic. As for the intima ($\Omega_i$), an isotropic effective diffusion coefficient is acquired from literature such that $D_i = 1.67 \times 10^{-11}$ m$^2$ s$^{-1}$. The reaction kinetics, $R_x$, differ on a layer–by–layer basis and are governed by the following expressions:

$$R_i = \frac{\partial b^s}{\partial t} + \frac{\partial b^{ns}}{\partial t} + \frac{\partial b^{ec}}{\partial t} \quad \text{in } \Omega_i, \quad t > 0, \tag{6.5}$$

$$R_m = \frac{\partial b^s}{\partial t} + \frac{\partial b^{ns}}{\partial t} \quad \text{in } \Omega_m, \quad t > 0, \tag{6.6}$$

where there now exists a total of three bound drug concentrations: $b^s\ (r,z,t)$, $b^{ns}\ (r,z,t)$, and $b^{ec}\ (r,z,t)$ which represent specifically bound drug to SMCs, non–specifically bound drug to ECM and drug bound to ECs, respectively. The first two types exist in all domains, whilst the EC bound drug exists only within the intima. The rate of change of each of these species is presented below:

$$\frac{\partial b^s}{\partial t} = k^s_{on} c_x (B^s - b^s) - k^s_{off} b^s, \quad \text{in } \Omega_x, \quad t > 0, \tag{6.7}$$

$$\frac{\partial b^{ns}}{\partial t} = k^{ns}_{on} c_x (B^{ns} - b^{ns}) - k^{ns}_{off} b^{ns}, \quad \text{in } \Omega_x, \quad t > 0, \tag{6.8}$$

$$\frac{\partial b^{ec}}{\partial t} = k^{ec}_{on} c_i (B^{ec} - b^{ec}) - k^{ec}_{off} b^{ec}, \quad \text{in } \Omega_i, \quad t > 0, \tag{6.9}$$

where all binding parameters ($k_{on}$, $k_{off}$, $B$) are as before (Chapter 5: Table 5.1), differing in value for each different phase of binding. The selection of binding parameters for the ECs is discussed in Section 6.5.2.

The final consideration of the computational model is the impact of drug on the EC population. Prior efforts, assessing the effect of drug on SMCs, implemented a range of models. Here, to provide focus, only a single model is considered, assuming that receptor saturation mediates the proliferative capacity of both ECs and SMCs. Thus, the equation corresponding to EC growth (Eqn. 6.2) is amended as so:

$$\frac{\partial c_{ec}}{\partial t} = D_{ec} \nabla^2 c_{ec} + g_{ec}\, c_{ec} \left(1 - \frac{c_{ec}}{K_{ec}}\right) (1 - \theta^e(t)) \underbrace{\left(1 - \frac{b^{ec}}{B^{ec}}\right)}_{\text{Drug interference}}, \quad \text{in } \Omega_i, \quad t > 0, \tag{6.10}$$

where EC proliferation is naturally impeded by space and vascular injury, as if drug was absent. The new term, labelled *drug interference*, further inhibits EC growth following drug delivery by means of receptor saturation; similarly to how drug hinders SMC proliferation in the model (Chapter 5: Eqn. 5.6).

### 6.5.2 Summary of cases

State–of–the–art drug transport models in static arteries have accounted for two binding phases, specific and non–specific, for which binding parameters exist assuming the action of sirolimus [79, 170, 188]. Clinical and experimental literature has also suggested that drug impedes the functionality of ECs, delaying the regeneration of the endothelium, where strut coverage is significantly impaired following the deployment of DES [27, 75]. However, to the best of the authors knowledge, there has been no distinction made between drug that is specifically bound to either SMCs or ECs. As such, the parameters of the drug binding model (Eqn. 6.8) associated with the binding of drug to ECs are undocumented and do not appear in the literature. Studies that do provide such parameters focus on the action of sirolimus or paclitaxel on SMCs [79,194]. It may be the case that the binding parameters are similar between these two cell types, given that the target receptors are the same [365]. Nonetheless, perturbations in $k_{on}$, $k_{off}$, and $B$ are considered, such that the rate of drug binding to ECs matches specific, non–specific or some intermediate value (Table 6.3). In permitting the binding of drug to ECs, the simultaneous effect on the SMC population is also assessed, exploring the implications of delayed healing on other model constituents.

| Case | Description | Binding Parameters | Value [Unit] |
|---|---|---|---|
| A1 | EC binding parameters match non–specific binding parameters | $k_{on}^{ec} \equiv k_{on}^{ns}$ | 2 $m^3$ $mol^{-1}$ $s^{-1}$ |
| | | $k_{off}^{ec} \equiv k_{off}^{ns}$ | $5.2\times10^{-3}$ $s^{-1}$ |
| | | $B^{ec} \equiv B^{ns}$ | 0.366 mol $m^{-3}$ |
| A2 | EC binding parameters are the mean of specific and non–specific binding parameters | $k_{on}^{ec} = \frac{k_{on}^{s}+k_{on}^{ns}}{2}$ | 401 $m^3$ $mol^{-1}$ $s^{-1}$ |
| | | $k_{off}^{ec} = \frac{k_{off}^{s}+k_{off}^{ns}}{2}$ | $2.68\times10^{-3}$ $s^{-1}$ |
| | | $B^{ec} = \frac{B^{s}+B^{ns}}{2}$ | 0.185 mol $m^{-3}$ |
| A3 | EC binding parameters match SMC specific binding parameters | $k_{on}^{ec} \equiv k_{on}^{s}$ | 800 $m^3$ $mol^{-1}$ $s^{-1}$ |
| | | $k_{off}^{ec} \equiv k_{off}^{s}$ | $1.6\times10^{-4}$ $s^{-1}$ |
| | | $B^{ec} \equiv B^{s}$ | $3.3\times10^{-3}$ mol $m^{-3}$ |

Table 6.3: Different parameter cases considered when simulating the binding of drug to ECs.

Similar to work in Chapter 5, the impact of stent design parameters (the initial drug mass, DM) is considered in parallel with changes to the binding parameters. The different initial drug masses selected are displayed in Table 6.4. Moreover, with the impact of vascular injury by stent deployment demonstrated, this analysis considers a single expansion ratio (20%). In all simulations, the drug release rate is fixed, where the diffusion coefficient in the polymer is given as $D_p = 1.5 \times 10^{-17}$ $m^2 s^{-1}$.

| Parameter | Key | Value [Unit] |
|---|---|---|
| Initial drug mass (DM) | 0 | 0.05 [$\mu$g] |
| | 1 | 0.1 [$\mu$g] |
| | 2 | 1 [$\mu$g] |
| | 3 | 5 [$\mu$g] |

Table 6.4: Parameter values corresponding to the different drug masses initially coated on the polymer coating of the stent strut ($M_0$).

### 6.5.3 Analysis of results

With the effect of drug on cell proliferation mediated by the saturation of receptors, the percentage of receptors occupied by drug with respect to time is expected to be a key indicator of drug efficacy. Thus, receptor saturation is computed via:

$$\%RS^s = \frac{100}{V_x}\int_{V_x}\frac{b^s}{B^s}\,dV_x, \tag{6.11}$$

$$\%RS^{ec} = \frac{100}{V_i}\int_{V_i}\frac{b^{ec}}{B^{ec}}\,dV_i, \tag{6.12}$$

where $\%RS^s$ and $\%RS^{ec}$ are the percentage of specifically SMC and specifically EC receptors saturated by drug, respectively. The SMC specific receptor saturation is computed in all domains, hence the $x$ subscript, where $x = i,m$, and the volume ($V$) corresponds to the entire arterial wall. As for the saturation of EC receptors, these cells exist only within the intima, hence the $i$ subscript.

In addition to receptor saturation, the EC and sSMC species will be tracked at Point A and C (Fig. 6.2), respectively, with the possible implications on patient outcome discussed. Therefore, for each case (Table 6.3), four plots will be illustrated: sSMC, EC, $\%RS^s$, and $\%RS^{ec}$.

### 6.5.4 Results & Discussion

With a modelling framework established that permits the binding of drug to both ECs and SMCs, the purpose is now to assess the significance of drug delivery on arterial healing, and whether it may have implications on patient outcome. Other factors such as stent thrombosis are not considered within this model and are left to future work.

As per Table 6.3, Case A1 assumes that drug binds to ECs with the same affinity as non–specific binding sites. The results of this are presented in Fig. 6.8. Following the release of drug from the polymer coating, drug is initially at high concentrations within the intima before quickly depleting towards zero [188, 189]. This is reiterated in Fig. 6.8a, where across the different drug masses proposed, the difference in EC recovery is negligible. This is supported

by Fig. 6.8c, where the peak of saturated endothelial receptors is minimal, and only present within the first few days post stent deployment. Therefore, as the density of EC binding sites is assumed to be so high, then the level of drug delivered to the artery is unable to come close to complete saturation of EC receptors. As such, EC regeneration is unaffected by drug, and only the peak of SMC proliferation is altered as a consequence of drug binding to specific receptors, inhibiting their proliferative capacity (Fig. 6.8b). The inhibition of SMCs is supported by Fig. 6.8d, where a clear saturation of specific receptors is present, particularly at higher drug masses (DM2 and DM3). Although DM2 falls away from its peak value more quickly than DM3, the SMC response is almost identical between the two. This is because drug saturates the specific receptors for long enough during the active phase of remodelling (3 weeks), where depreciation from this value after that has no consequence on the outcome. The findings of case A1 seem to suggest that delayed arterial healing would be minimal to non–existent and do not agree with trends present in [25], assuming the density of EC binding sites is similar to that of the non–specific sites.

Considering Case A2, it is assumed that the rate at which drug binds to ECs is equivalent to the mean of the specific and non–specific binding parameters. A limitation of this approach is that the parameters are biased towards the non–specific case due to the parameter values being over an order of magnitude higher (Table 6.3). Nonetheless, Fig. 6.9 illustrates how ECs and thus the sSMC population are affected when adopting these binding parameters.

At lower drug masses (DM0 and DM1), akin to Case A1, the endothelial population recovers at a rate similar to when drug is absent (Fig. 6.9a). Here, the saturation of endothelial receptors again peaks at early times before tending towards zero (Fig. 6.9c). However, as there is a slight inhibition in EC recovery, the peak of SMCs is not only reduced as a result of drug but is also inhibited temporally, where the peak is shifted to the right. This suggests that SMCs remain in their active, proliferative state for longer as a consequence of the delayed re–endothelialization. However, as the mass of drug is increased (DM2 and DM3), the recovery of ECs becomes significantly impaired, where the time to reach its healthy value ($K_{ec}$) is almost doubled for the highest drug mass considered. Here, the percentage of drug bound to endothelial receptors is notably increased (Fig. 6.9c). Although $\%RS^{ec}$ still quickly depreciates from its peak value, it never reaches zero within the 80–days considered for this simulation when DM3 is proposed. As such, the duration SMCs spend in their active, proliferative state is notably increased (Fig. 6.9b). Although drug specifically bound to specific SMC receptors is still high (Fig. 6.9d), the role of drug is to only inhibit proliferation and not to induce differentiation back to the quiescent, contractile phenotype in this model. Therefore, when drug mass is increased (DM3), the peak of SMC is not only shifted temporally to the right but also upwards. In other words, although drug is inhibiting the proliferation of sSMCs, with the recovery of the endothelial population delayed, more SMCs are permitted to transition from their contractile to synthetic phenotypes, as demonstrated by the significant peak in Fig. 6.9b for DM3. This is alluded to in more depth

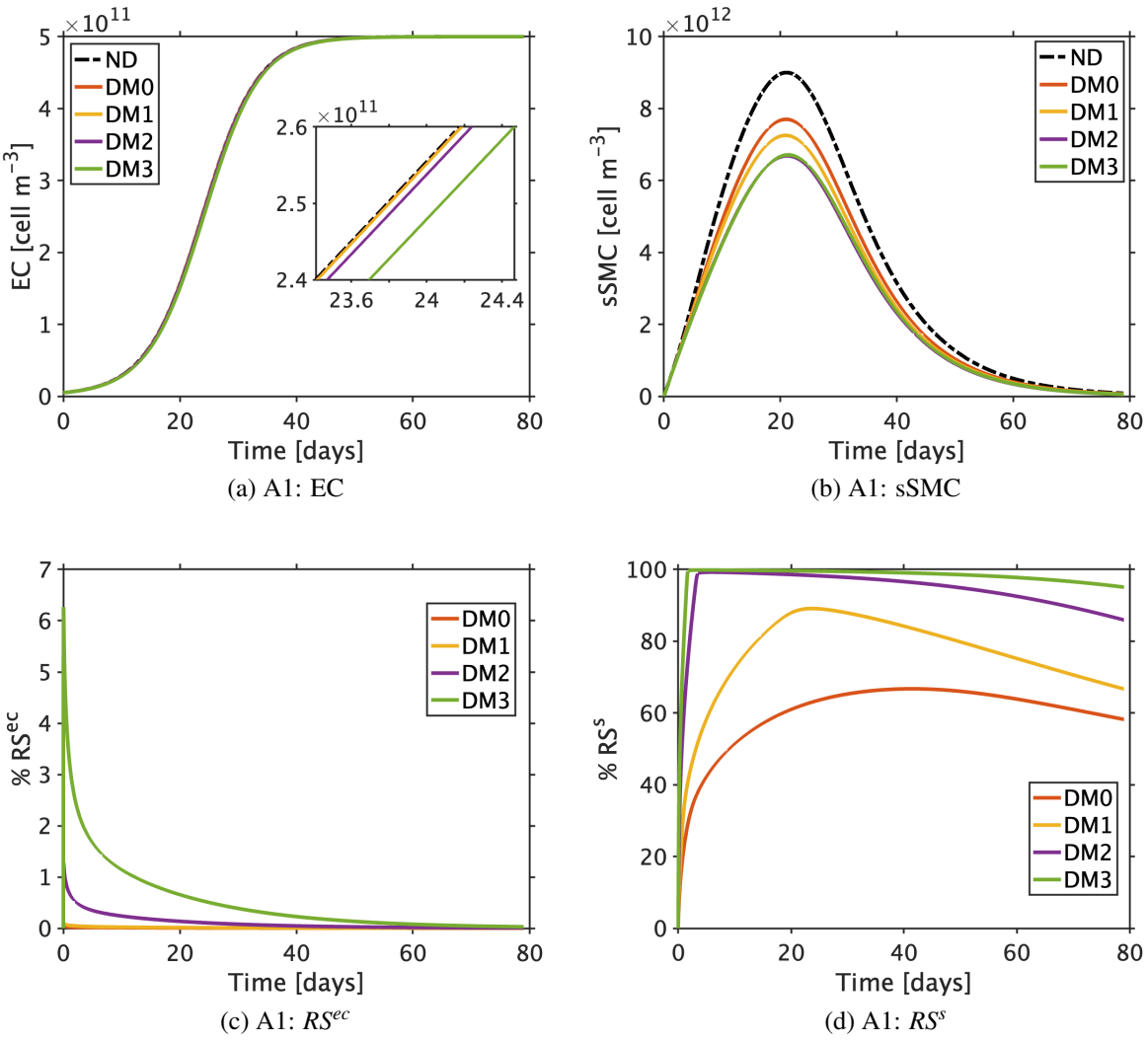


(a) A1: EC

(b) A1: sSMC

(c) A1: $RS^{ec}$

(d) A1: $RS^{s}$

Figure 6.8: Results of the drug transport model coupled with re–endothelialization: Case A1. (a) EC. (b) sSMC. (c) Endothelial receptor saturation ($RS^{ec}$). (d) Specific receptor saturation ($RS^{s}$). ND = No drug. DM0–3 are the various drug masses, reported in Table 6.4. All species profiles (EC and sSMC) illustrate the behaviour at point C (Fig. 6.2).

following the results of Case A3. Although the total SMC density does not increase, with more sSMCs now present, then ECM synthesis is increased, where vessel re–narrowing is likely to be more profound as a result (Fig. 6.7).

Assuming that drug binds to ECs with the parameters proposed in Case A2, then the effects of delayed arterial healing are noteworthy. Although SMC proliferation is still significantly inhibited by drug, the number of active, synthetic SMCs is drastically increased when the recovery of ECs is impaired, which may have implications on patient outcome with respect to the volume of ECM synthesised.

Finally, the most extreme scenario is considered: Case A3. Here, it is assumed that drug will bind to both ECs and SMCs with the same affinity. This, of all the cases, is likely to

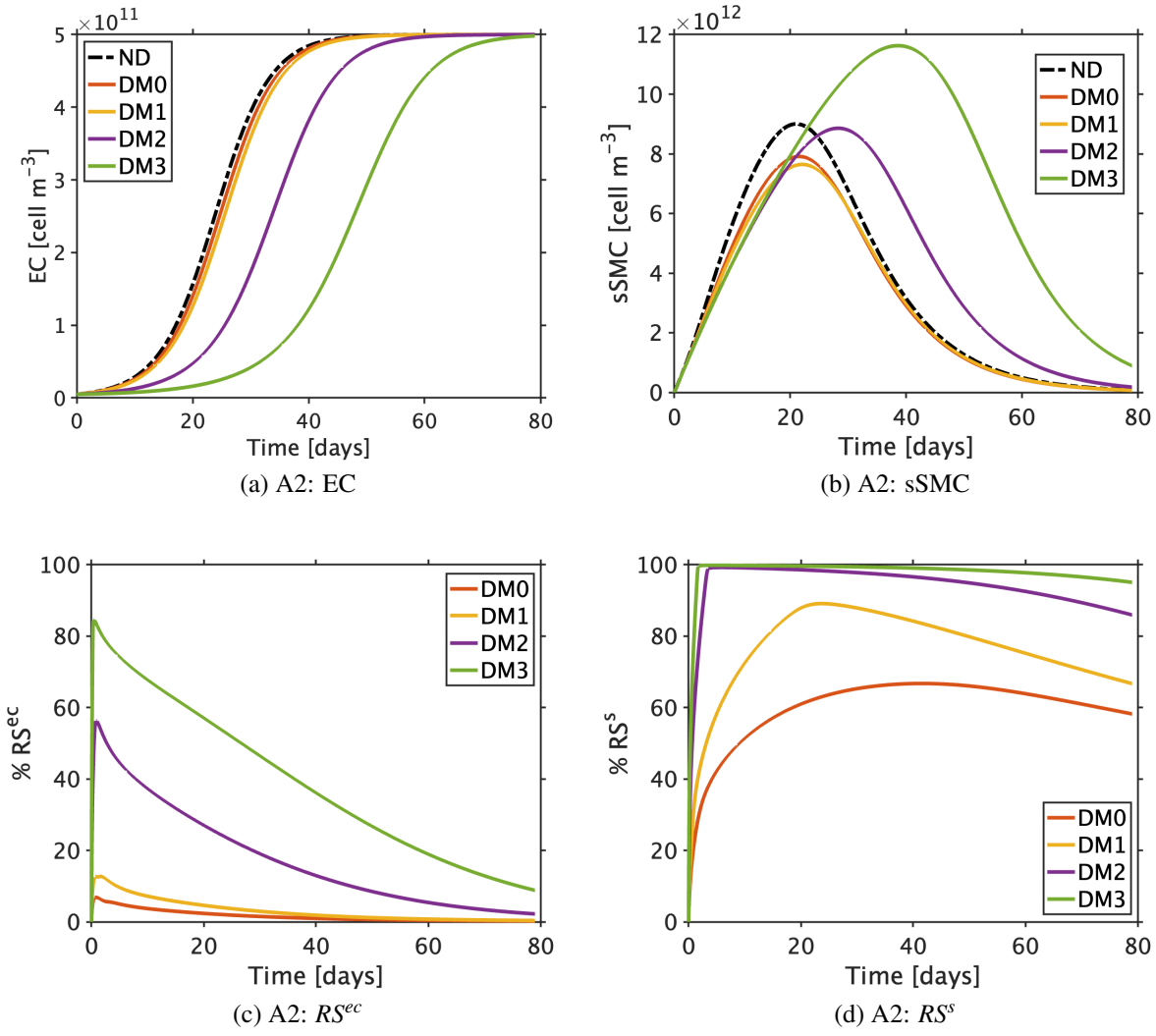


(a) A2: EC (b) A2: sSMC

(c) A2: $RS^{ec}$ (d) A2: $RS^{s}$

Figure 6.9: Results of the drug transport model coupled with re–endothelialization: Case A2. (a) EC. (b) sSMC. (c) Endothelial receptor saturation ($RS^{ec}$). (d) Specific receptor saturation ($RS^{s}$). ND = No drug. DM0–3 are the various drug masses, reported in Table 6.4. All species profiles (EC and sSMC) illustrate the behaviour at point C (Fig. 6.2).

be the closest to reality given that both cell types possess the same intracellular receptors for drug [365]. Moreover, by means of an *in vitro* proliferation assay, Matter *et al.* [31] demonstrated that sirolimus elicited a similar dose–dependent response on ECs and SMCs in separate cultures.

Unsurprisingly, EC proliferation is significantly curtailed for all drug doses considered (Fig. 6.10a). This is reinforced by the receptor saturation curves (Fig. 6.10c). At higher drug masses (DM2 and DM3), the saturation of receptors is close to 100% at early times before slowly declining from its peak across the 80–day period of interest. As such, EC proliferation is minimal, particularly at DM3, where growth barely exceeds the initial value. Alluded to in Case A2, this has a significant impact on the sSMC curves (Fig. 6.10b). For all doses, the peak of each curve exceeds the height of the drug–free scenario. Moreover, there is also a temporal shift for each

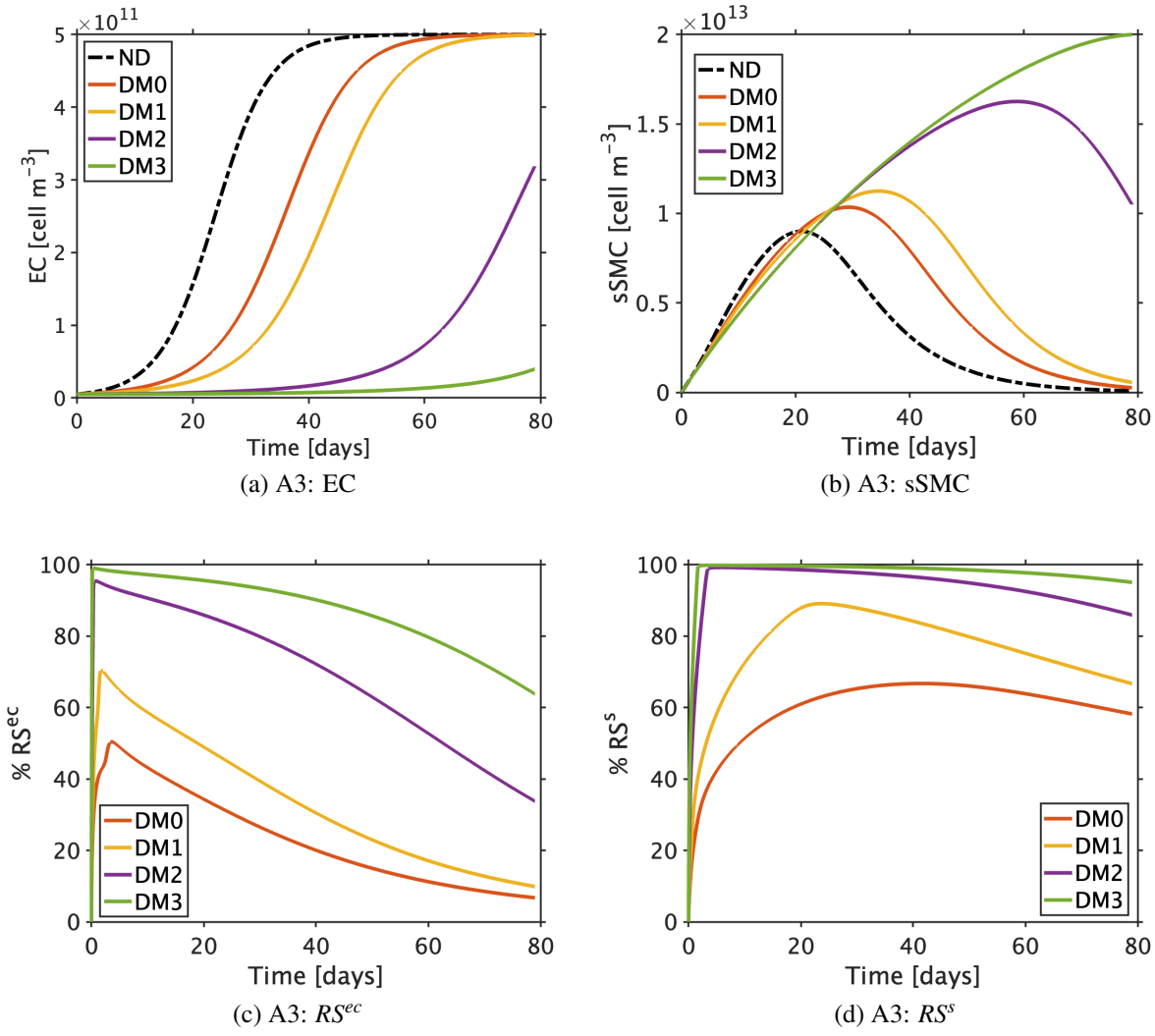


(a) A3: EC

(b) A3: sSMC

(c) A3: $RS^{ec}$

(d) A3: $RS^{s}$

Figure 6.10: Results of the drug transport model coupled with re–endothelialization: Case A3. (a) EC. (b) sSMC. (c) Endothelial receptor saturation ($RS^{ec}$). (d) Specific receptor saturation ($RS^{s}$). ND = No drug. DM0-3 are the various drug masses, reported in Table 6.4. All species profiles (EC and sSMC) illustrate the behaviour at point C (Fig. 6.2).

curve, where the time taken to reach the peak is a direct consequence of the time taken for the EC species to reach the inflection point (Fig. 6.10a). At higher drug masses, as was true in Case A2, sSMC proliferation is minimal, and the increase in sSMC density is a consequence of predominantly phenotype switching. However, for lower drug masses (DM0 and DM1), complete saturation of specific (SMC) receptors is not achieved. Thus, it is likely that the increase in SMC density (Fig. 6.9b) is a result of proliferation and phenotype switching. To examine this further, a direct comparison is made between the synthetic and contractile curves when no drug (ND) is considered as well as at the two mass extremes, DM0 and DM3 (Fig. 6.11).

Fig. 6.11a presents each of the contractile SMC curves, which can be directly compared with the sSMC curves in Fig. 6.10b. However, to visualise differences between these curves

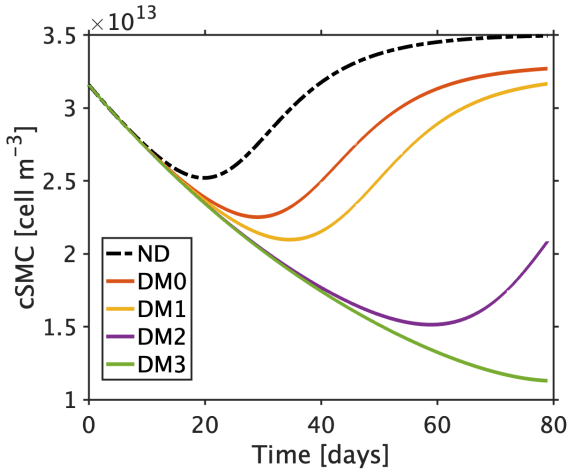


(a) A3: cSMC

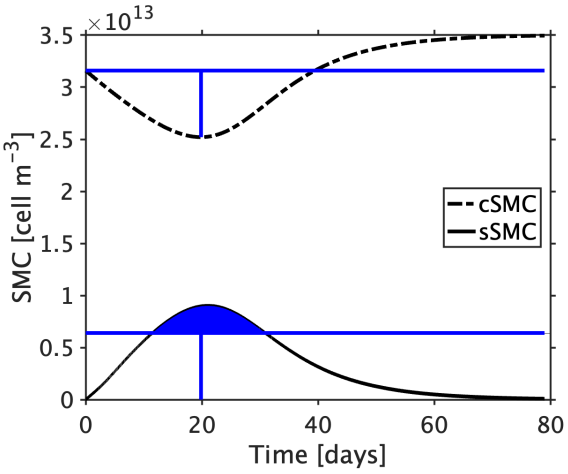


(b) A3: cSMC versus sSMC (ND)

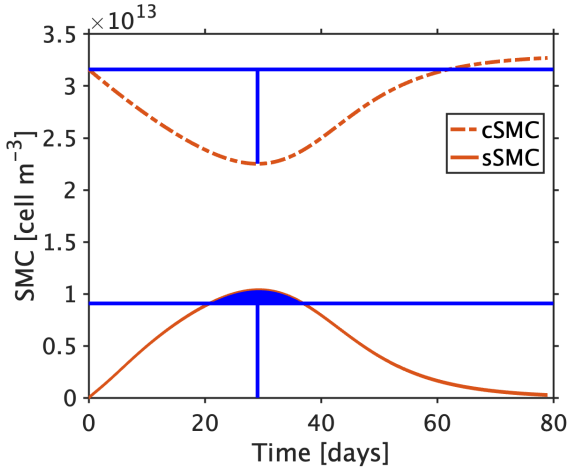


(c) A3: cSMC versus sSMC (DM0)

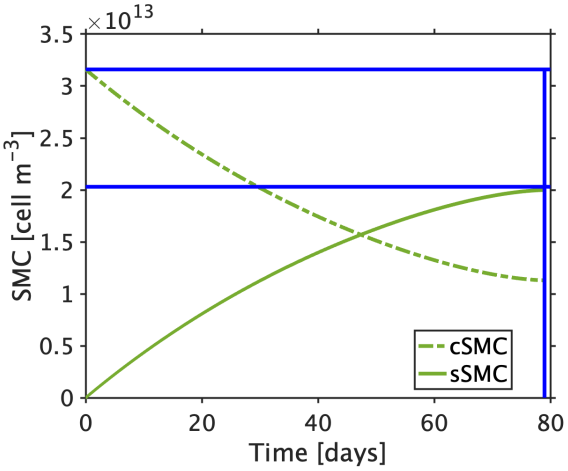


(d) A3: cSMC versus sSMC (DM3)

Figure 6.11: Results of the drug transport model coupled with re–endothelialization: Case A3. (a) cSMC. (b)–(d) cSMC versus sSMC for (b) ND, (c) DM0, and (d) DM3. Here, the magnitude of the cSMC minimum has been computed, and superimposed onto the sSMC curve. Difference between the sSMC curve and this value are denoted by a shaded blue region, highlighting the change in cell density as a result of proliferation. Solid lines refer the sSMC species, whilst dashed lines to the cSMC one. ND = No drug. DM0–3 are the various drug masses, reported in Table 6.4

simultaneously, Fig. 6.11b–6.11d was devised. To facilitate this comparison, the minimum peak of the cSMC curve was identified (vertical blue line) from the initial density of cells, $c^0_{csmc}$ (horizontal blue line). The magnitude of this peak ($P^v$) was computed by, $P^v = c^0_{csmc} - \min(c_{csmc})$. The height of $P^v$ was then superimposed onto the sSMC profile by adding it from zero. To further emphasise the density of proliferating cells, the areas of the sSMC curve which surpass $P^v$ are shaded in blue. Unsurprisingly, the shaded area is most profound in the case where drug is absent (Fig. 6.11b). For lower drug masses, DM0, a small shaded area exists (Fig. 6.11c), illustrating that because EC recovery is notably delayed (Fig. 6.10a), and the sSMC

specific receptors are not completely saturated (Fig. 6.10d), then excess SMC proliferation is enabled. Although much of the increase in sSMC density following exposure to DM0 is a result of an increased number of cells differentiating from contractile to synthetic, it is clear that the rise in sSMC peak is also a consequence of sSMC proliferation. Finally, no shaded area exists following exposure to DM3 (Fig. 6.11d). This suggests that the increase in sSMC density is predominantly a consequence of phenotype conversion from cSMCs, where proliferation is minimal (Fig. 6.11b).

Summarising, if it is assumed that drug binds to ECs and SMCs with the same affinity, then the drug delivery strategy has the potential to have a notable impact on the timeline of arterial healing. Although sSMC proliferation is minimal, particularly at higher masses (Fig. 6.10b, 6.10d, and 6.11d), increased vessel re–narrowing is likely to occur with ECM synthesis increased as a result of the increased density of sSMCs. On the other hand, at lower masses (DM0), where the proliferation of both cell types is impeded but not halted, then an increase in sSMC also occurs through proliferation due to a delay in the recovery of the endothelial layer; an important implication of delayed arterial healing.

The model presented here is the first of its kind to explore the effect of drug on multiple cell types (ECs and SMCs) within the context of arterial healing. Whilst the results presented are interesting, additional work is necessary to fully appreciate the implications of drug on ECs and the subsequent impact on patient outcome. These aspects are discussed in Section 6.6.

## 6.6 Limitations & Future work

With the model presented in this chapter being preliminary, limitations are evident. One key limitation is with respect to the model geometry proposed. A simple, shorter geometry was considered to focus closely on EC and SMC behaviour. However, subsequent efforts should implement a geometry like that in Chapter 4. This would represent a more realistic environment and enable measures such as % area restenosis to be calculated.

Although the results of the model proposed here demonstrate that drug has an impact on EC recovery, there are other factors that undoubtedly contribute to the process of delayed arterial healing. One of these being low wall shear stress (WSS) as a consequence of disturbed blood flow following stent deployment. Various models of ISR have recently emerged that correlate this index (WSS) with patient outcome [220, 221, 226]. Moreover, other models, where tissue growth is absent, have highlighted importance of stent design features (deployment depth, strut shape, and strut thickness) on disturbed flow profiles adjacent to the stent struts [361, 366]. Additionally, the inclusion of fluid dynamics would also permit the assessment of recirculation zones on drug deposition, and its impact EC functionality and thus patient outcome [200, 361, 366]. Taken together, in time, one can begin to explore other aspects associated with poor patient outcome as a consequence of disturbed flow profiles such as stent thrombosis, commonly linked

with delayed arterial healing [24, 362].

Finally, the purpose of this chapter was to consider a direct coupling between ECs and SMCs: inspired from agent–based models (ABMs) which follow a rule based approach [53, 65–67]. To the best of the authors knowledge, this is the first model that proposes such an idea within a continuum modelling framework. To facilitate the coupling between ECs and SMCs, the term associated with the phenotype switch of SMCs was updated (Eqn. 6.3). This new term dictates the number of active, synthetic SMCs depending on whether ECs have surpassed their inflection point of the logistic growth profile or not. It would be beneficial to test the validity of this mathematical expression, perhaps through the aid of *in vitro* co–culture proliferation assays comprising of both cell types, where experimental data could help calibrate and validate the model proposed.

## 6.7 Conclusions

In conclusion, amendments to the original restenosis model in Chapter 4 have been proposed that consider the impact of *damage* on endothelial recovery [62], and the subsequent effect a delay in re–endothelialization may have on patient outcome through an increase in SMC number and proliferation [53, 65–67]. With DES the focus of this work, the drug transport model was also extended to explore the effect of drug on multiple cell types: SMCs and ECs. As such, the model was able to illustrate delayed arterial healing as a consequence of drug binding to sites within ECs. Through a series of cases, results suggested that this could possibly have an impact on patient outcome through an increase in SMC number, primarily a consequence of phenotype switching as opposed to proliferation, but that the results are drug dose–dependent.

Further work should aim to address the limitations proposed in an attempt to enrich the computational model. In doing so, one can begin to examine the implications of DES more thoroughly, assessing the impact of drug possibly being present in the intima for prolonged periods of time [361], where fenestrations in the IEL through a dysfunctional endothelium may promote vessel remodelling that could result in patient complications: all a consequence of delayed arterial healing. Moreover, the effect of different drug release rates should also be considered as in Chapter 5, where it is likely that the release of drug more slowly or quickly into the artery will have implications on both EC recovery and SMC proliferation through a range of different drug masses. Finally, upon the inclusion of fluid dynamics, a more thorough investigation into adverse outcomes associated with stent–induced flow disturbances can be considered [24, 25, 27, 361].

# Chapter 7

# Conclusions and future work

This chapter summarises the key conclusions of this thesis, proposing possible avenues for further work. The chapter is broken into two distinct sections. The first details the importance of the *in vitro* models presented in Chapters 2 and 3. These models were then built upon in complexity to simulate the role of anti–proliferative drug within an *in vivo* environment: the focus of the second section, making reference to Chapters 4–6.

## Mathematical models calibrated and validated from *in vitro* experimental data

Chapters 2 and 3, through a series of mathematical models, demonstrated the effect of anti–proliferative drug on smooth muscle cell (SMC) proliferation within an *in vitro* environment. The importance of such experimental methods cannot be underestimated to appreciate the pharmacodynamic effects of drug on cellular function, which in turn drives therapeutic dose ranges *in vivo* [22,78]. In Chapter 2, the models varied in complexity, where somewhat surprisingly, the ubiquitously used, nonlinear saturable binding model was unable to capture the dose–dependent effect of drug on SMC growth unless the best–fitting parameters used to detail drug binding kinetics varied on a dose–by–dose basis, meaning its predictive capacity was significantly limited. Models depicting simpler kinetics were able to effectively capture all of the experimental data, where subsequent predictions were adequate. These results suggest that, when available in large enough concentrations, drugs like paclitaxel are able to elicit their effect very quickly (complete inhibition of cell proliferation following 3–60 minute exposure); perhaps explaining the success of such drugs on drug–coated balloon devices [22, 170, 360], where the is only a very short window to delivery the drug. Moreover, the models were able to capture the differences in the lipophillic properties of two drugs (paclitaxel and sodium salicylate), simulating cell recovery, or lack thereof, following the removal of the supernatant. Although the model which neglected binding performed best, its predictive capabilities were limited by the data available, where additional data is necessary to fully validate the model. Moreover, the poor quality of predictions

of these models could also be attributed to a number of factors. Possible explanations include the best–fitting parameter protocol perhaps being sub–optimal, or that the parameters detailing the binding kinetics were drug and/or dose dependent. However, an alternative explanation is that an inadequate model description was proposed in Chapter 2, where the precise action of the drugs was not considered. In other words, the models assumed the drug acts without regard for the cyclic behaviour of a proliferating cell: ignoring the cell cycle specificity of such drugs. Chapter 3 addressed these issues, simulating the cell cycle as the population of cells proliferated to capacity. As such, two different drugs were tested: (i) $G_1$/S transition blocker (e.g. sirolimus) and (ii) a mitosis, M, blocker (e.g. paclitaxel). Thus, the models derived for each drug ensured the timing of its action within the cell cycle was different. The results of these efforts concluded the following:

- Differences were noted when cell cycle dynamics were neglected (single–phase) or considered (multi–phase). As anticipated, the former inhibited cell proliferation more profoundly.
- When simulating cell cycle dynamics, the initial distribution of cells throughout the cell cycle has a direct impact on drug efficacy.
- The effect of drug is further exacerbated when spatiotemporal gradients of drug are introduced, i.e. drug delivery.

These appear to be the first modelling strategies that have explored this concept within the context of SMC proliferation. To fully appreciate the benefits of considering cell cycle behaviour within mathematical models, further work should explore sophisticated experimental techniques (e.g. fluorescent universal cell cycle indicator, FUCCI [284–286]) to calibrate and validate the mathematical models. Such experimental data has been known to inform clinicians of the optimal treatment strategies for chemotherapy [287, 288], and could thus be applied within the context of in–stent restenosis (ISR) in the pursuit of optimal stent design.

Moreover, although Chapter 3 highlighted the importance of spatiotemporal drug delivery on the efficacy of drug, it is clear that a translation into an *in vivo* environment is needed. With anti–proliferative drug known to elicit its effect on the cell (e.g. SMC) population, these *in vivo* models will aid in understanding the subsequent impact on patient outcome through restenosis; where SMCs are known to be the driving force in its evolution. With stent–induced vascular injury known to trigger a heterogeneous healing response, one can explore the impact of stent design on patient outcome, with a particular emphasis placed on the drug delivery strategy.

## *In vivo* modelling reveals an intricate interplay between drug release rate and dose on arterial restenosis

Chapter 4 derived a novel, multiscale model of ISR, illustrating the impact of stent design on patient outcome, where trends agreed with those present in the modelling, clinical, and experimental literature [53, 65–67, 101]. The model illustrated that increased vascular injury, as a consequence of increased strut thickness or reduced inter–strut spacing, resulted in more profound tissue growth profiles. However, a notable limitation of the model, as is true with many models of ISR [53–55, 57, 65–67, 101, 211, 220, 221, 226], was that the role of anti–proliferative drug was neglected. Moreover, state–of–the–art drug transport models assume static arteries, where the remodelling process of the artery following stent deployment is neglected [78, 79, 172, 178]. With this in mind, Chapter 5 built upon the model proposed in Chapter 4, explicitly coupling a sophisticated model of drug transport with cellular function. The results revealed an intricate interplay between the rate at which drug was delivered and the initial coating drug mass on vessel re–narrowing, where simply increasing either did not always improve patient outcome. This was explored across a range of stent designs proposed in Chapter 5, demonstrating that in situations where vascular injury was more profound, higher masses of drug were necessary to combat a more aggressive healing response. With drug release dictating the rate at which the mass of drug in tissue changed, the optimal patient outcome was achieved following an intermediate rate of drug delivery. This achieved a sustained saturation of binding site receptors across the active phase of remodelling [79]. However, faster or slower rates of delivery were acceptable when the initial drug loading varied from high to low, respectively.

Moreover, with the *in vivo* environment naturally heterogeneous, the model proposed in Chapter 5 assessed the validity of a constant binding site density, adopted ubiquitously in drug transport models. In such situations, the artery is assumed static, where cell proliferation is ignored and the number of binding sites does not change in space or time [78, 79]. Alternatively, based upon histological evidence [60, 354, 355], Chapter 5 proposed a variable binding site density that was regulated by the density of active, proliferating cells. In other words, the density of drug binding sites increased early in response to injury and depreciated in time as the artery healed, and the neointima matured, becoming hypocellular [56, 60]. Although reliable data on the average receptor expression per cell was absent, the model demonstrated similar trends to the constant binding assumption, again emphasising the importance of stent design parameters on patient outcome. Furthermore, it is likely that the variable binding site density would be further heightened in diseased vessels, where the morphology is significantly more heterogeneous.

Nonetheless, the models proposed in both Chapters 4 and 5 have limitations. Firstly, in Chapter 4, the recovery of the endothelial cell (EC) population was simulated in isolation of all other model constituents. Thus, in Chapter 5, the implications of delayed arterial healing could not be fully assessed. As such, Chapter 6 proposed an alternative approach to modelling arterial healing, where the recovery of ECs was directly influenced by vascular injury [62], and

that the ECs were directly responsible for the proliferative capacity of SMCs [65, 67]. The drug transport model in Chapter 5 was then extended to enable the binding of drug to ECs. With data on the binding kinetics of drug to ECs absent, a series of cases were simulated which illustrated the possible implications of delayed arterial healing on patient outcome. To reduce computational time, these simulations were considered within a shortened segment of the full geometrical model in Chapter 4 and 5. As such, the immediate next step should be to simulate this effect within the full computational model. Nonetheless, following an examination of key model species (extracellular matrix, ECM and SMCs) within the model, the results alluded to the possible significance of delayed arterial healing through the inhibition of EC recovery following the delivery of drug.

The models proposed in Chapters 4–6 are limited by other factors which should be explored in further research. Firstly, the role of the adventitia on restenosis was ignored. Although its significance in stent deployment was highlighted, with the function of the cells residing in the adventitia still poorly understood [56, 348] its inclusion within the restenosis model is left to future work, where it is hoped that experimental evidence may provide more insight. Secondly, the complexity of the geometrical model could be increased. In the first instance, this could include disease, where imaging modalities like virtual histology–intravascular ultrasound (VH–IVUS) could be considered to characterise the severity of disease within the blood vessel. Upon the derivation of a computational model which depicts this disease profile, the impact on drug transport and thus restenosis could be assessed. On the other hand, the dimensionality of the model geometry could be extended to 3D, allowing one to explore the possible implications of deep arterial tears and strut malapposition on patient outcome in depth. Additionally, patient–specific geometries could also be explored with 3D geometries introduced.

Moreover, the restenosis model in particular is limited by the fact that the tissue growth profile is computed in a separate, stationary study. To improve the realism of the model, a moving boundary problem could be considered, where the leading front of the restenosis profile is dynamic, transgressing through the lumen as cells proliferate and synthesise ECM. It remains unclear how such a model would be derived and implemented, but initial efforts should strip back model complexity to 1D before introducing it within a more complex environment (2D or 3D).

Lastly, a limitation present within all models in Chapters 4–6 is the absence of flow, and its effect on both tissue growth and drug transport. Although its effect on the latter has been well characterised, its contribution to tissue growth is still poorly understood [55]. Several models of ISR have established a link between wall–shear stress (WSS) and ISR [219, 220, 225, 305], where efforts often propose a linear or continuous piecewise function to assign levels of damage to agents in their model, an approach similar in principle to the definition of *damage* in Chapter 4 (Eqn. 2.5). In such models, the role of vascular injury is notably absent, only introduced recently in [306], who highlighted its significance in focal lumen loss. Although the importance of WSS

on EC functionality has been studied extensively [200, 361], with a particular focus on strut design, its underlying effect deeper into the arterial wall is still poorly understood [55,225,226]. In particular, [226], the most sophisticated agent–based model (ABM) of ISR to date simulated the transmission of WSS through the artery by a simple diffusion equation to assign each agent with its own level of damage. Moreover, Jansen *et al.* [221] also noted that the effects of WSS on growth factor influx within their model was purely theoretical and that further evidence was needed. Thus, with the effects of flow absent in the tissue growth model, its contribution to drug transport was neglected, where the magnitude of the advective velocity field is expected to only decrease the time taken for binding sites to be saturated.

The majority of drug transport models which do not account for arterial remodelling assume steady Navier Stokes when modelling blood flow in the lumen [78, 188, 189, 196]. However, in idealised vessels, Escuer *et al.* [170] demonstrated that free drug concentrations in the lumen were orders of magnitude below those in the tissue due to clearance by blood flow. Therefore, in an attempt to reduce model complexity, only fluid flow in tissue was simulated through the implementation of Darcy's Law [169, 170, 188, 189, 196].

## Derivation of a multiscale model of ISR subject to drug delivery: ABM of restenosis coupled with a continuum model of drug transport

In an attempt to address the limitations associated with the lack of flow, a collaborative project with a research group in Politecinico di Milano was devised. The primary aim of this work was to develop a novel multiscale model of ISR which coupled an ABM of restenosis within a continuum model of drug transport. The former was derived and simulated by colleagues from Politecinico di Milano, where fluid flow was known to mediate tissue growth as in [226, 306]. As such, the drug transport model introduced fluid flow within the tissue through Darcy's law, where each layer of the arterial wall possesses its own unique transport properties. The method adopted is discussed extensively in [170]. Not detailed in depth here, the reader is referred to [170] for full details on the drug transport model, where subtle simplifications have been made, as discussed in the following text.

Fig. 7.1 presents the geometry implemented within COMSOL Multiphysics 5.6a (COMSOL AB, Burlington, MA, USA), with Fig. 7.2 noting some preliminary results. To be consistent with the ABM in [226,306], a 2D cross–sectional geometry is proposed for the drug transport model. Emulating the design of a shorter Xience V $^{\text{TM}}$ stent, 12 equally spaced struts ($\theta_{ss} = 30^{\circ}$) are considered, with a strut thickness ($s_t$) of 81 $\mu$m and a coating thickness ($\delta_p$) of 8 $\mu$m. The arterial wall comprises of three layers: intima, media, and adventitia. However, with the former notably thin (10 $\mu$m), then distinction from the media is challenging within the ABM of ISR. Thus, it is assumed that the transport properties of these two layers are identical, emulating that of the medial layer. Layer thickness are taken from literature [169], and summarised in Table

7.1 along with the other parameters associated with the geometrical configuration.

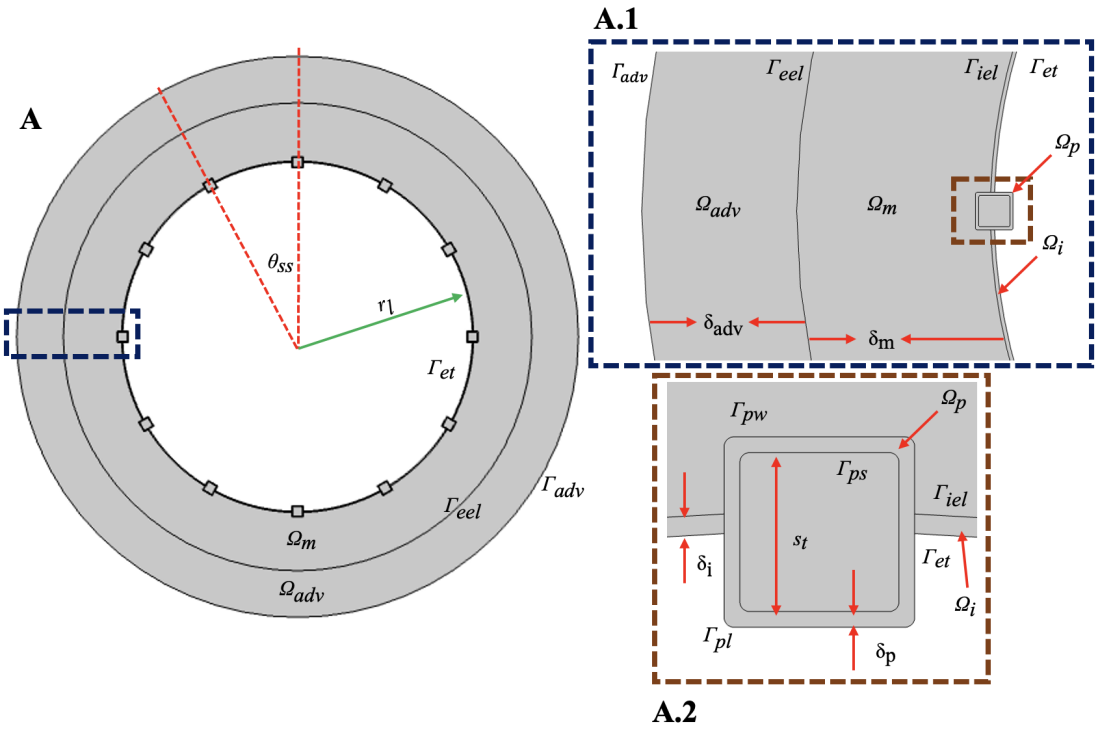


Figure 7.1: A: Illustrates the entire 2D geometry, where struts are separated by an angle of 30° ($\theta_{ss}$). A.1: Shows a single strut and surrounding layers. A.2: Focuses in on the stent strut. All domains and boundaries are denoted $\Omega$ and $\Gamma$, respectively. Domains include: polymer coating ($\Omega_p$), media ($\Omega_m$), and the adventitia ($\Omega_{adv}$). The boundaries include: endothelium ($\Gamma_{et}$), internal elastic lamina ($\Gamma_{iel}$), external elastic lamina ($\Gamma_{eel}$), perviascular edge ($\Gamma_{adv}$), polymer-lumen interface ($\Gamma_{pl}$), polymer-wall interface ($\Gamma_{pw}$), and polymer-strut interface ($\Gamma_{ps}$).

| Parameter | Description | Value | Reference(s) |
|---|---|---|---|
| $s_t$ | Strut thickness | 81 $\mu$m | [170] |
| $\delta_p$ | Polymer coating thickness | 8 $\mu$m | [169, 170] |
| $\theta_{ss}$ | Strut spacing | 30° | † |
| $\delta_i$ | Intima domain thickness | 0.01 mm | [55, 169] |
| $\delta_m$ | Media domain thickness | 0.5 mm | [55, 169] |
| $\delta_{adv}$ | Adventitia domain thickness | 0.4 mm | [169, 170] |
| $r_l$ | Lumen radius | 1.5 mm | [188] |

Table 7.1: Parameters of the baseline computational model. References denoted by a † are estimated assuming that the stent struts are uniformly separated.

Fig 7.2a again illustrates the baseline geometry imposed for the drug transport model. However, Fig. 7.2b portrays an example of a geometry after some time where growth has occurred, as a consequence of the ABM. Fig. 7.3 presents a high–level presentation of the work flow

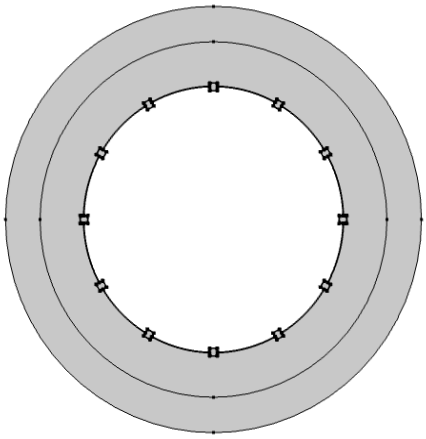

(a) Baseline geometry

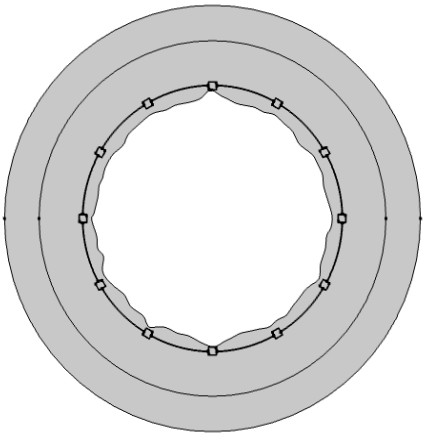

(b) Geometry following growth

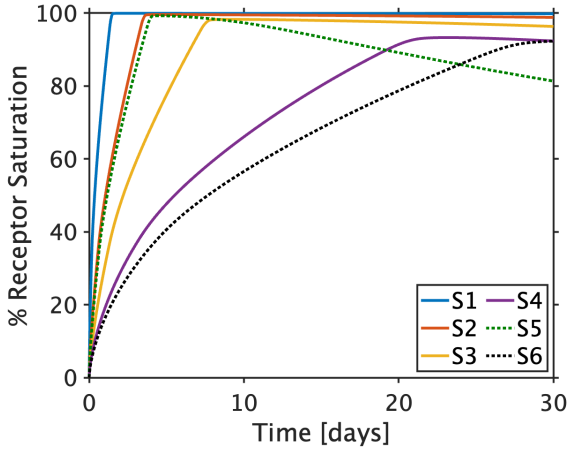


(c) RS curves

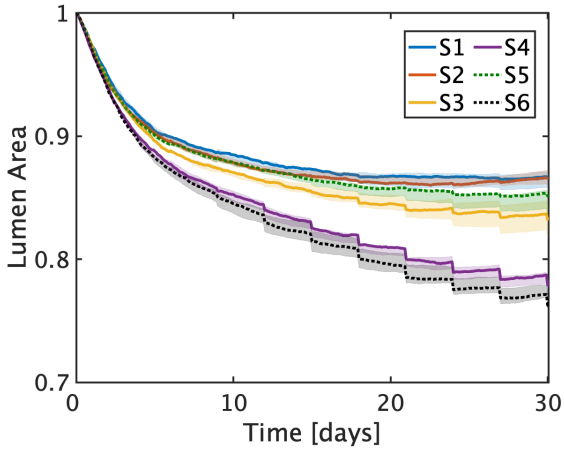


(d) Lumen area

Figure 7.2: (a) Baseline geometry as detailed in Fig. 7.1. (b) A geometric profile where tissue growth has occurred. (c) Receptor saturation (RS) curves from the drug transport model for a range of cases, S1–S6 (Table 7.2). (d) Lumen area curves from the drug transport model for a range of cases, S1–S6 (Table 7.2). The shaded areas adjacent to the curves represent uncertainty, with the ABM stochastic in nature. Results of (c) and (d) assume a single coupling between the drug transport and agent–based models (Fig. 7.3.

to be considered in future work. Initially, a 3D geometry is obtained from optical coherence tomography (OCT) images and meshed within ANSYS FLUENT (ANSYS Canonsburg, PA, USA). Here, a computational fluid dynamics (CFD) simulation is performed to obtain WSS values along the lumen interface. A 2D slice of one of the planes highlighted in the CFD simulation is created in COMSOLMultiphysics 5.6a (COMSOL AB, Burlington, MA, USA) (Fig. 7.2a), where a drug transport simulation (detailed in [170]) is performed. In the initial study, a series of receptor saturation curves (Fig. 7.2c) are plotted across a 30–day period. These are exported and treated as inputs into the ABM simulated in MATLAB (MATLAB 2020a, The MathWorks, Inc., Natwick, MA, USA). In such a study, the coupling is just one–way between the drug transport

and ABM frameworks, where the relevant lumen areas are as shown in Fig. 7.2d. Similarly to Chapter 5, it is clear that the choice of both drug release rate and initial drug loading are important mediators of outcome. Details of each of the simulations (S1–S6) are discussed in Table 7.2. In subsequent efforts, a more iterative coupling between the drug transport and agent–based model should be considered, where the 'new' geometry (i.e. Fig. 7.2b) is fed back into the drug transport model, with the simulation continued. The methodological process for this is highlighted in Fig. 7.3 by the optional step process (dashed lines) which makes use of Rhinoceros (Rhinoceros 3D, Version 6.0, Seattle, WA, USA) for manipulation of the geometry.

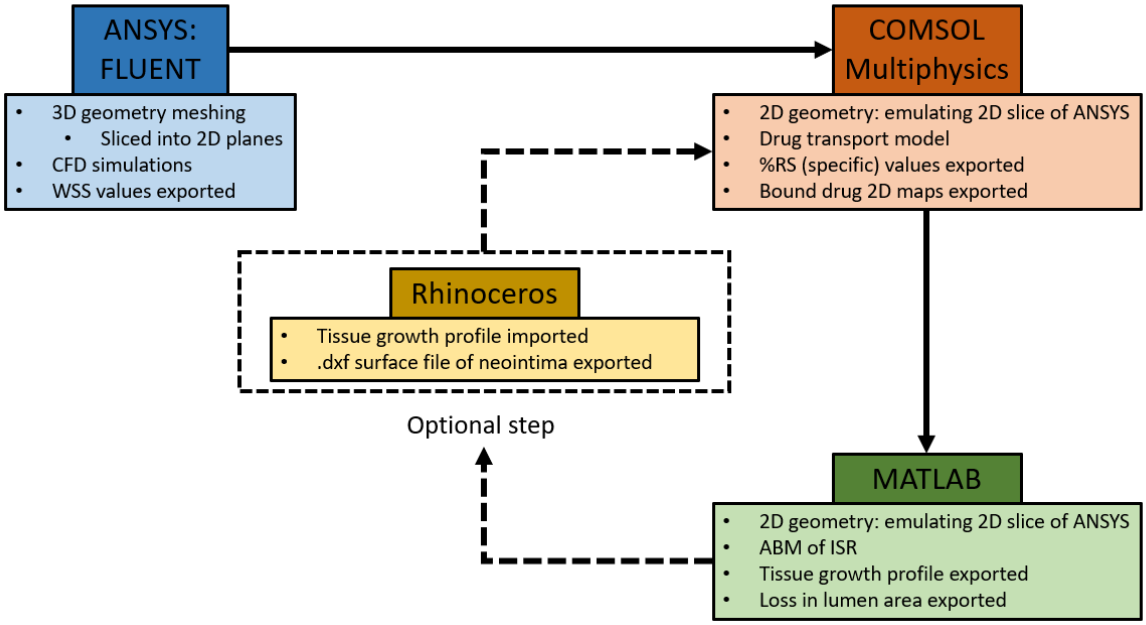


Figure 7.3: Flowchart of methodology established in a collaborative effort with Milan research group. A combination of four software packages are used: ANSYS FLUENT (ANSYS Canonsburg, PA, USA), COMSOL Multiphysics 5.6a (COMSOL AB, Burlington, MA, USA), MATLAB (MATLAB 2020a, The MathWorks, Inc., Natwick, MA, USA), and Rhinoceros (Rhinoceros 3D, Version 6.0, Seattle, WA, USA).

Within the preliminary work of this novel, multiscale, hybrid model of ISR subject to drug delivery, the results chart trends present in Chapter 5. Although vascular injury is absent from the ABM (see [226]), as the initial drug mass loading is increased, the resultant loss in lumen area is reduced (Fig. 7.2b). Moreover, the choice of the drug release rate is important, where all profiles are notably different. In future work, efforts should establish the importance of iterative coupling as the drug dose and release rate are perturbed. It is anticipated that as the drug coating dose is decreased, the need for more frequent coupling steps is increased as the tissue growth profile is likely to be more severe with the number of saturated receptors decreased. Furthermore, additional work should investigate the impact of vessel heterogeneity on the type of coupling considered: (i) time–dependent receptor saturation curves or (ii) 2D spatial maps of bound drug

| Label (Fig. 7.2) | Description | Drug mass [$\mu$g cm$^{-2}$] | Polymer coating diffusion coefficient [m$^2$ s$^{-1}$] |
|---|---|---|---|
| S1 | Drug mass 1 (†) | 100 | $1.5\times10^{-17}$ |
| S2 | Drug mass 2 | 10 | $1.5\times10^{-17}$ |
| S3 | Drug mass 3 | 2.5 | $1.5\times10^{-17}$ |
| S4 | Drug mass 4 | 1 | $1.5\times10^{-17}$ |
| S5 | Fast drug release | 2.5 | $1.5\times10^{-16}$ |
| S6 | Slow drug release | 2.5 | $1.5\times10^{-18}$ |

Table 7.2: Different cases explored in the initial collaboration with Milan research group. Drug mass 1, denoted by †, is acquired from FDA document on Xience V $^{TM}$ eluting stents [187]. Other drug masses are selected to pursue the possibility of future stents employing lower initial drug loadings [358, 359]. Different drug release rates are consistent with those presented in Chapter 5 (Fig. 5.4).

concentration (Fig. 7.3).

## Concluding remarks and next steps

Despite the key insights the models in Chapter 4–6 have provided, there is clear scope to extend the work further to ensure that the model devised is as realistic as possible. As such, further work should firstly look to build upon the novel multiscale model of ISR subject to the delivery of drug. Immediately thereafter, subsequent iterations should explore possible improvements that enrich the computational model, such as the inclusion of: (i) disease, (ii) increased model dimensionality, (iii) cell cycle behaviour on vessel re–narrowing, and (iv) stent–induced flow disturbances (i.e. possibility of stent thrombosis on patient outcome). Then, in time, model sophistication can be further increased to be inclusive of time–dependent tissue growth.

For example, addressing (i) first, the *in vivo* environment is notably heterogeneous following stent deployment, further exacerbated when disease is present, where the transport properties of drug are known to differ from healthy tissue throughout the lesion: particularly in necrotic and calcified regions [46]. As such, focal vessel re–narrowing may occur where drug is unable to reach proliferating SMCs in a timely manner following vascular injury as a consequence of stent deployment. Moreover, if the components of plaque which drug struggles to diffuse through directly interface the lumen, then drug concentrations may be sufficiently large at this boundary. This is likely to then have a negative impact on the regeneration of the endothelial layer, possibly contributing to the occurrence of delayed arterial healing [24, 25].

Model dimensionality (ii) could be improved by extending the computational models in Chapter 4–6 to 3D. This would be met with drastically increased computational costs, but would allow for simulations to emulate a more realistic setting.

The importance of cell cycle behaviour (iii) was demonstrated in Chapter 3. Following calibration and validation of those models, a natural next step would be to observe the impact of such models within an *in vivo* environment. As such, SMC proliferation in either restenosis

model (Chapter 4 or 6) could be extended to introduce the role of anti–proliferative drug when cell cycle specificity is accounted for. Particularly when the effect of drug on multiple cell types is considered, further insight could be gained from such models in the pursuit of the optimal drug delivery strategy.

Finally, inclusion of CFD (iv) within the lumen could further enrich the model. This would facilitate the inclusion of stent–induced flow disturbances into the model, where consideration of the importance of stent thrombosis could be analysed within a tissue remodelling framework. Furthermore, as detailed in [200, 361], the impact of flow disturbances on drug deposition could be assessed, particularly in highly deformed arteries where recirculation zones are known to exist. Such modelling may allude to events that increase the probability of delayed arterial healing.

It is clear that there are several avenues to pursue in future work, all which only serve to improve the models detailed within this thesis. Each studied in isolation should enable researchers to improve their understanding of the performance of drug–eluting stents (DES). However, taken together, it is likely that, in time, such a model could be incorporated as a pre–clinical tool to aid in the optimal course of treatment in the clinic. With ISR still the primary culprit associated with the need for repeat procedures [48, 50], more sophisticated computational models of the process can only serve to improve one's understanding, and highlight the possible pitfalls in stent design and/or procedure that promote its prevalence.

# Appendix A

# Appendix

## A.1 Supplemental Equations: Non-dimensional analysis

### A.1.1 Non-dimensionalisation of Model D1

The dimensional model equations are given by Eqn. 2.6–2.7 in the main text. These equations are non-dimensionalised using the scalings:

$$t^* = gt, \qquad c^* = \frac{c}{K}, \qquad b^* = \frac{b}{BK}. \tag{A.1}$$

Applying Eqn. A.1 to Eqn. 2.6–2.7 results in the following equations, where asterisks have been omitted from variables for convenience:

$$\frac{\mathrm{d}b(t)}{\mathrm{d}t} = \beta_1^{D1}\left(c(t)-b(t)\right) - \beta_2^{D1} b(t), \quad t>0, \quad b(0)=0, \tag{A.2}$$

$$\frac{\mathrm{d}c(t)}{\mathrm{d}t} = c(t)\left(1-c(t)\right)\left(1-\frac{b(t)}{c(t)}\right), \quad t>0, \quad c(0)=C^0. \tag{A.3}$$

The three non-dimensional constants appearing in Eqn. A.2–A.3 are given by:

$$\beta_1^{D1} = \frac{k_{on}\, c_d}{g}, \quad \beta_2^{D1} = \frac{k_{off}}{g}, \quad C^0 = \frac{c_0}{K}. \tag{A.4}$$

### A.1.2 Non-dimensionalisation of Model D2

The dimensional equations are given by Eqn. 2.9–2.10 in the main text. These equations are non-dimensionalised using the scalings:

$$t^* = gt, \qquad c^* = \frac{c}{K}, \qquad b^{I*} = \frac{b^I}{k_{50}}. \tag{A.5}$$

Applying Eqn. A.5 to Eqn. 2.9–2.10 results in the following equations, where asterisks have been omitted from variables for convenience:

$$\frac{\mathrm{d}b^I(t)}{\mathrm{d}t} = \beta_1^{D2} - \beta_2^{D2}\, b^I(t), \quad t > 0, \quad b^I(0) = 0, \tag{A.6}$$

$$\frac{\mathrm{d}c(t)}{\mathrm{d}t} = c(t)\,(1-c(t))\left(1 - \frac{k_{max}\, b^I(t)}{b^I(t)+1}\right), \quad t > 0, \quad c(0) = C^0, \tag{A.7}$$

The three new non-dimensional constants appearing in Eqn. A.6–A.7 are given by

$$\beta_1^{D2} = \frac{\alpha c_d}{g k_{50}}, \quad \beta_2^{D2} = \frac{\alpha}{g K_p}, \quad C^0 = \frac{c_0}{K}. \tag{A.8}$$

### A.1.3 Non-dimensionalisation of Model D3

The dimensional model equations are given by Eqn. 2.11a–2.11b in the main text. These equations are non-dimensionalised using the scalings:

$$t^* = gt, \qquad \tau^* = g\tau, \qquad c^* = \frac{c}{K}, \qquad c_d^* = \frac{c_d}{k_{50}}. \tag{A.9}$$

Applying Eqn. A.9 to Eqn. 2.11a–2.11b results in the following equations, where asterisks have been omitted from variables for convenience:

$$\frac{\mathrm{d}c(t)}{\mathrm{d}t} = \begin{cases} c(t)\,(1-c(t))\left(1 - \dfrac{k_{max}\, c_d^*}{c_d^*+1}\right), & 0 < t \le \tau, \quad c(0) = C^0, \quad \text{(A.10a)} \\ c(t)\,(1-c(t))\left(1 - \dfrac{k_{max}\, c_d^*\, e^{(-\beta_1^{D3}(t-\tau))}}{c_d^*\, e^{(-\beta_1^{D3}(t-\tau))}+1}\right), & t > \tau. \quad \text{(A.10b)} \end{cases}$$

The two new non-dimensional constants appearing in Eqn. A.10a–A.10b are given by

$$\beta_1^{D3} = \frac{k_d}{g}, \quad C^0 = \frac{c_0}{K}. \tag{A.11}$$

## A.2 Supplemental Tables

Table A.1–A.4 presents information associated with the Marra data set. In order: Table A.1 documents the best–fitting paramaters following an individual fit to each data set; Table A.2 compares the error of model D1 and D2 for two different fitting protocols; Table A.3 presents the various error values when one data set is used to predict all remaining response; and Table A.4 documents the best–fitting parameters and associated error values following the optimal fitting regime (Step 3, Fig. 2.7). Table A.5–A.7 presents the same information but for the Scheller data set, excluding a repeat of Table A.2, since continuous exposure is absent in the

Scheller study.

| | **Best-fitting Parameter(s)** | | | | | | |
|---|---|---|---|---|---|---|---|
| | Model D1 | | Model D2 | | | Model D3 | |
| Data set | $k_{on}$ | $k_{off}$ | $k_{max}^{D2}$ | $\frac{\alpha}{k_{50}}$ | $\frac{\alpha}{K_P}$ | $k_{max}^{D3}$ | $k_{50}$ |
| $H_{12}^m$ | 596.16 | 0.021 | 1.127 | 1.31e3 | 0.922 | 14.416 | 0.0706 |
| $M_{12}^m$ | 142.35 | 0.117 | 17.077 | 9.407 | 0.344 | 10.4171 | 0.0347 |
| $L_{12}^m$ | 1.96e-6 | 0.0021 | 0.4 | 6.16e-2 | 0.542 | 5.266 | 0.1906 |

Table A.1: Inversely estimated parameters of models D1, D2 and D3 when fitting is performed against each individual data set of Marra *et al.* [269] The best fitting parameters vary not only across the different doses for a given model, but also between the models (e.g. $k_{max}$).

| | **Model response following washing**: Quality of fit / prediction ($\varepsilon$) | | | |
|---|---|---|---|---|
| | $H_{12}^m$ Fit / $H_4^m$ Prediction | | Multi-fit: $H_{12}^m$ Fit and $H_4^m$ | |
| Model | $\varepsilon_{H_{12}^m}$ | $\varepsilon_{H_4^m}$ | $\varepsilon_{H_{12}^m}$ | $\varepsilon_{H_4^m}$ |
| D1 | 0.0229 | 0.6174 | 0.0257 | 0.0126 |
| D2 | 0.0235 | 0.0603 | 0.062 | 0.062 |

Table A.2: The table presents the series of cases from Fig. 2.9. Divided into two, where the left shows how fitting to $H_{12}^m$ can predict $H_4^m$ for model D1 and D2 (Fig. a & c). Note, here the column ($\varepsilon_{H_{12}^m}$) is the same values as Table A.1. The right–hand column presents the results following a multi–fit to both of the aforementioned data sets (Fig. b & d).

| | | Quality of Predictions - $\varepsilon$ | | |
|---|---|---|---|---|
| ***Model D1*** | | | | |
| **F** | **P** | $\varepsilon_{H_{12}^m}$ | $\varepsilon_{M_{12}^m}$ | $\varepsilon_{L_{12}^m}$ |
| $H_{12}^m$ | $L_{12}^m$ & $M_{12}^m$ | 0.0229 | 0.551 | 0.111 |
| $M_{12}^m$ | $L_{12}^m$ & $H_{12}^m$ | 0.912 | 0.0238 | 0.052 |
| $L_{12}^m$ | $M_{12}^m$ & $H_{12}^m$ | 26.57 | 0.427 | 0.0455 |
| ***Model D2*** | | | | |
| **F** | **P** | $\varepsilon_{H_{12}^m}$ | $\varepsilon_{M_{12}^m}$ | $\varepsilon_{L_{12}^m}$ |
| $H_{12}^m$ | $L_{12}^m$ & $M_{12}^m$ | 0.0235 | 0.8243 | 0.4637 |
| $M_{12}^m$ | $L_{12}^m$ & $H_{12}^m$ | 1.3106 | 0.0163 | 0.0521 |
| $L_{12}^m$ | $M_{12}^m$ & $H_{12}^m$ | 26.5717 | 0.4287 | 0.0455 |
| ***Model D3*** | | | | |
| **F** | **P** | $\varepsilon_{H_{12}^m}$ | $\varepsilon_{M_{12}^m}$ | $\varepsilon_{L_{12}^m}$ |
| $H_{12}^m$ | $L_{12}^m$ & $M_{12}^m$ | 0.0273 | 0.0652 | 0.05 |
| $M_{12}^m$ | $L_{12}^m$ & $H_{12}^m$ | 0.9015 | 0.0294 | 0.0529 |
| $L_{12}^m$ | $M_{12}^m$ & $H_{12}^m$ | 18.3403 | 0.3537 | 0.046 |

Table A.3: Quality of predictions when best–fitting model parameters based on a single Marra *et al.* [269] data set are used in the prediction of the other Marra *et al.* [269] data sets. Coloured cells correspond to the error value ($\varepsilon$) of the data set on which the fit was performed. **F** and **P** refer to the fitted and predicted data set(s), respectively.

| | Parameter | | | Error - $\varepsilon$ | | | |
|---|---|---|---|---|---|---|---|
| Model | $k_{on}$ | $k_{off}$ | - | $\varepsilon_{H_{12}^m}$ | $\varepsilon_{M_{12}^m}$ | $\varepsilon_{L_{12}^m}$ | $\varepsilon_{H_4^m}$ |
| D1 | 4.31e2 | 0.283 | - | 0.17 | 0.158 | 0.074 | 0.076 |
| | $k_{max}^{D2}$ | $\frac{\alpha}{k_{50}}$ | $\frac{\alpha}{K_P}$ | $\varepsilon_{H_{12}^m}$ | $\varepsilon_{M_{12}^m}$ | $\varepsilon_{L_{12}^m}$ | $\varepsilon_{H_4^m}$ |
| D2 | 1.79 | 2.088e2 | 0.828 | 0.051 | 0.021 | 0.055 | 0.078 |
| | $k_{max}^{D3}$ | $k_{50}$ | $k_d$ | $\varepsilon_{H_{12}^m}$ | $\varepsilon_{M_{12}^m}$ | $\varepsilon_{L_{12}^m}$ | $\varepsilon_{H_4^m}$ |
| D3 | 2.65 | 8.54e-3 | 0.253 | 0.035 | 0.03 | 0.053 | 0.038 |

Table A.4: Best–fitting parameters and associated error for each of three models D1, D2 and D3, when a multi–fit is used to inversely estimate the model parameters before the effect of the low dose drug $L_{12}^m$ is predicted to the Marra *et al.* [269] dataset. For Models D1 and D2, the $M_{12}^m$, $H_{12}^m$ and $H_4^m$ data sets were used in the multi-fit. For Model D3, the $M_{12}^m$ and $H_{12}^m$ data sets were used in the multi-fit with a subsequent fitting step using the $H_4^m$ data set required to estimate the parameter associated with drug retention ($k_d$).

| | Best-fitting Parameter(s) | | | | | | | |
|---|---|---|---|---|---|---|---|---|
| | Model D1 | | Model D2 | | | Model D3 | | |
| Data set | $k_{on}$ | $k_{off}$ | $k_{max}^{D2}$ | $\frac{\alpha}{k_{50}}$ | $\frac{\alpha}{K_P}$ | $k_{max}^{D3}$ | $k_{50}$ | $k_d$ |
| $H_{60}^s$ | 8.87e6 | 1.61e-4 | 0.977 | 1.027e7 | 7.38e-4 | 2.65 | 3.01e-5 | 1.25e-4 |
| $H_{10}^s$ | 5.059e7 | 8.02e-5 | 1.979 | 8.135e6 | 1.24e-2 | 2.72 | 2.98e-5 | 1.27e-4 |
| $H_3^s$ | 2.078e8 | 8.68e-4 | 1.823 | 3.27e7 | 6.37e-4 | 1.58 | 1.01e-5 | 2.54e-8 |
| $L_{60}^s$ | 2.028e7 | 1.41e-4 | 2.569 | 3.32e6 | 2.3e-3 | 3.61 | 1.08e-5 | 1.52e-4 |

Table A.5: Inversely estimated parameters of models D1, D2 and D3 when fitting is performed against each individual data set of Scheller *et al.* [81] The best fitting parameters vary not only across the different doses for a given model, but also between the models.

| | | Quality of Predictions - $\varepsilon$ | | | |
|---|---|---|---|---|---|
| | | ***Model D1*** | | | |
| **F** | **P** | $\varepsilon_{H_{60}^s}$ | $\varepsilon_{H_{10}^s}$ | $\varepsilon_{H_3^s}$ | $\varepsilon_{L_{60}^s}$ |
| $H_{60}^s$ | $H_{10}^s$, $H_3^s$ & $L_{60}^s$ | 0.2649 | 18.66 | 36.38 | 0.2746 |
| $H_{10}^s$ | $H_{60}^s$, $H_3^s$ & $L_{60}^s$ | 0.531 | 0.096 | 20.23 | 0.725 |
| $H_3^s$ | $H_{60}^s$, $H_{10}^s$ & $L_{60}^s$ | 0.529 | 0.482 | 0.173 | 2.07 |
| $L_{60}^s$ | $H_{60}^s$, $H_{10}^s$ & $H_3^s$ | 0.509 | 7.83 | 31.77 | 0.057 |
| | | ***Model D2*** | | | |
| **F** | **P** | $\varepsilon_{H_{60}^s}$ | $\varepsilon_{H_{10}^s}$ | $\varepsilon_{H_3^s}$ | $\varepsilon_{L_{60}^s}$ |
| $H_{60}^s$ | $H_{10}^s$, $H_3^s$ & $L_{60}^s$ | 0.0786 | 8.3835 | 30.1301 | 0.0248 |
| $H_{10}^s$ | $H_{60}^s$, $H_3^s$ & $L_{60}^s$ | 3.1154 | 0.0284 | 21.88 | 0.322 |
| $H_3^s$ | $H_{60}^s$, $H_{10}^s$ & $L_{60}^s$ | 3.2635 | 2.5687 | 0.0356 | 2.8331 |
| $L_{60}^s$ | $H_{60}^s$, $H_{10}^s$ & $H_3^s$ | 3.2313 | 2.9855 | 30.065 | 0.0052 |
| | | ***Model D3*** | | | |
| **F** | **P** | $\varepsilon_{H_{60}^s}$ | $\varepsilon_{H_{10}^s}$ | $\varepsilon_{H_3^s}$ | $\varepsilon_{L_{60}^s}$ |
| $H_{60}^s$ | $H_{10}^s$, $H_3^s$ & $L_{60}^s$ | 0.0549 | 0.0304 | 0.1378 | 0.4848 |
| $H_{10}^s$ | $H_{60}^s$, $H_3^s$ & $L_{60}^s$ | 0.0863 | 0.0593 | 0.0463 | 0.4729 |
| $H_3^s$ | $H_{60}^s$, $H_{10}^s$ & $L_{60}^s$ | 0.1259 | 0.0967 | 0.0346 | 0.3062 |
| $L_{60}^s$ | $H_{60}^s$, $H_{10}^s$ & $H_3^s$ | 3.5872 | 3.6166 | 3.6055 | 0.0048 |

Table A.6: Quality of predictions when best-fitting model parameters based on a single Scheller *et al.* [81] data set are used in the prediction of the other Scheller *et al.* [81] data sets. Coloured cells correspond to the error value ($\varepsilon$) of the data set on which the fit was performed. **F** and **P** refer to the fitted and predicted data set(s), respectively.

| | Parameter | | | Error - $\varepsilon$ | | | |
|---|---|---|---|---|---|---|---|
| Model | $k_{on}$ | $k_{off}$ | - | $\varepsilon_{H^s_{60}}$ | $\varepsilon_{H^s_{10}}$ | $\varepsilon_{H^s_3}$ | $\varepsilon_{L^s_{60}}$ |
| D1 | 1.642e7 | 3.01e-3 | - | 0.33 | 11.01 | 33.33 | 0.083 |
| | $k^{D2}_{max}$ | $\frac{\alpha}{k_{50}}$ | $\frac{\alpha}{K_P}$ | $\varepsilon_{H^s_{60}}$ | $\varepsilon_{H^s_{10}}$ | $\varepsilon_{H^s_3}$ | $\varepsilon_{L^s_{60}}$ |
| D2 | 0.95 | 1.13e7 | 2.3e-3 | 0.13 | 8.2 | 29.75 | 0.02 |
| | $k^{D3}_{max}$ | $k_{50}$ | $k_d$ | $\varepsilon_{H^s_{60}}$ | $\varepsilon_{H^s_{10}}$ | $\varepsilon_{H^s_3}$ | $\varepsilon_{L^s_{60}}$ |
| D3 | 0.95 | 2.14e-5 | 2.14e-4 | 0.13 | 0.10 | 0.45 | 0.019 |

Table A.7: Best-fitting parameters and associated error for each of three models D1, D2 and D3, when a multi-fit is used to inversely estimate the model parameters to the Scheller *et al.* [81] dataset. The 60 min exposure of low and high drug dose data sets were used simultaneously to find the best fitting parameters, with the effect of the shorter exposure times of the high drug dose predicted.

# Bibliography

[1] "CHD Statistics bhf." https://www.bhf.org.uk/what-we-do/our-research/heart-statistics. Accessed: 2021-07-19.

[2] "CVD Statistic bhf." https://www.bhf.org.uk/informationsupport/publications/statistics/trends-in-coronary-heart-disease-1961-2011. Accessed: 2021-07-19.

[3] A. Lusis, "Atherosclerosis," *Nature*, vol. 407, no. 6801, pp. 233–41, 2000.

[4] M. Rafieian-kopaei, M. Setorki, M. Doudi, M. Khodai, and H. Nasri, "Atherosclerosis: Process, indicators, risk factors and new hopes," *International Journal of Preventive Medicine*, vol. 5, no. 8, pp. 927–946, 2014.

[5] N. R. Aggarwal, H. N. Patel, L. S. Mehta, R. M. Sanghani, G. P. Lundberg, S. J. Lewis, M. A. Mendelson, M. J. Wood, A. S. Volgman, and J. H. Mieres, "Sex differences in ischemic heart disease," *Circulation: Cardiovascular Quality and Outcomes*, vol. 11, no. 2, p. e004437, 2018.

[6] A. Sandoo, J. Veldhuijzen van Zanten, G. Metsios, D. Carroll, and G. Kitas, "The endothelium and its role in regulating vascular tone," *The open cardiovascular medicine journal*, vol. 4, pp. 302–12, 2010.

[7] J. Davignon and P. Ganz, "Role of endothelial dysfunction in atherosclerosis," *Circulation*, vol. 109, no. 23, pp. III–27–III–32, 2004.

[8] B. A. Brown, H. Williams, and S. J. George, "Evidence for the involvement of matrix-degrading metalloproteinases (mmps) in atherosclerosis," *Progress in Molecular Biology and Translational Science*, vol. 147, pp. 197 – 237, 2017.

[9] A. Milutinovic, D. Suput, and R. Zorc-Pleskovic, "Pathogenesis of atherosclerosis in the tunica intima, media, and adventitia of coronary arteries: An updated review," *Bosnian Journal of Basic Medical Sciences*, vol. 20, no. 1, pp. 21–30, 2020.

[10] R. Mazurek, J. M. Dave, R. R. Cahndran, A. Misra, A. Q. Sheikh, and D. M. Greif, "Vascular cells in blood vessel wall development and disease," *Advanced Pharmacology*, vol. 78, pp. 323–50, 2017.

[11] M. W. Majesky, X. R. Dong, V. Hoglund, W. M. Mahoney, and G. Daum, "The adventitia: a dynamic interface containing resident progenitor cells," *Arteriosclerosis, Thrombosis, and Vascular Biology*, vol. 31, no. 7, pp. 1530–539, 2011.

[12] K. J. Moore and I. Tabas, "Macrophages in the pathogenesis of atherosclerosis," *Cell*, vol. 145, no. 3, pp. 341–55, 2011.

[13] P. Libby, P. Ridker, and A. Maseri, "Inflammation and atherosclerosis," *Circulation*, vol. 105, no. 9, pp. 1135–43, 2002.

[14] G. P. Kwon, J. L. Schroeder, M. J. Amar, A. T. Remaley, and R. S. Balaban, "Contribution of macromolecular structure to the retention of low-density lipoprotein at arterial branch points," *Circulation*, vol. 117, no. 22, pp. 2919–927, 2008.

[15] G. Basatemur, H. Jørgensen, M. Clarke, M. Bennett, and Z. Mallat, "Vascular smooth muscle cells in atherosclerosis," *Nature Reviews Cardiology*, vol. 16, pp. 727–44, 2019.

[16] J. L. Harman and H. F. Jørgensen, "The role of smooth muscle cells in plaque stability: Therapeutic targeting potential," *British Journal of Pharmacology*, vol. 176, no. 19, pp. 3741–3753, 2019.

[17] J. Iqbal, J. Gunn, and P. W. Serruys, "Coronary stents: historical development, current status and future directions," *British Medical Bulletin*, vol. 106, pp. 193–211, 2013.

[18] J. Y. Moon, F. Franchi, F. Rollini, and D. J. Angiolillo, "Evolution of coronary stent technology and implications for duration of dual antiplatelet therapy," *Progress in Cardiovascular Diseases*, vol. 60, no. 4, pp. 478–490, 2018.

[19] J. Canfield and H. Totary-Jain, "40 years of percutaneous coronary intervention: History and future directions," *Journal of Personalized Medicine*, vol. 8, no. 4, p. 33, 2018.

[20] G. N. Levine, A. P. Chodos, and J. Loscalzo, "Restenosis following coronary angioplasty: Clinical presentations and therapeutic options," *Clinical Cardiology*, vol. 18, no. 12, pp. 693–703, 1995.

[21] P. Leva, P. Kukla, and O. Hlinomaz, "Treatment of coronary in-stent restenosis: a systematic review," *Journal of Geriatric Cardiology*, vol. 15, no. 2, pp. 173–84, 2018.

[22] C. McCormick and C. M. McKittrick, "Chapter 6 - coronary drug-eluting stents: Still room for improvement?," in *Drug Delivery Devices and Therapeutic Systems* (E. Chappel, ed.), Developments in Biomedical Engineering and Bioelectronics, pp. 107–127, Academic Press, 2021.

[23] L. Holmvang, H. Kelbæk, A. Kaltoft, L. Thuesen, J. F. Lassen, P. Clemmensen, L. Kløvgaard, T. Engstrøm, H. E. Bøtker, K. Saunamäki, L. R. Krusell, E. Jørgensen, H.-H. Tilsted, E. H. Christiansen, J. Ravkilde, L. Køber, K. F. Kofoed, C. J. Terkelsen, and S. Helqvist, "Long-term outcome after drug-eluting versus bare-metal stent implantation in patients with st-segment elevation myocardial infarction: 5 years follow-up from the randomized dedication trial (drug elution and distal protection in acute myocardial infarction)," *JACC: Cardiovascular Interventions*, vol. 6, no. 6, pp. 548–553, 2013.

[24] M. Joner, A. V. Finn, A. Farb, E. K. Mont, F. D. Kolodgie, E. Ladich, R. Kutys, K. Skorija, H. K. Gold, and R. Virmani, "Pathology of drug-eluting stents in humans: Delayed healing and late thrombotic risk," *Journal of the American College of Cardiology*, vol. 48, no. 1, pp. 193–202, 2006.

[25] G. Nakazawa, A. V. Finn, M. Joner, E. Ladich, R. Kutys, E. K. Mont, H. K. Gold, A. P. Burke, F. D. Kolodgie, and R. Virmani, "Delayed arterial healing and increased late stent thrombosis at culprit sites after drug-eluting stent placement for acute myocardial infarction patients," *Circulation*, vol. 118, no. 11, pp. 1138–1145, 2008.

[26] A. Curcio, D. Torella, and C. Indolfi, "Mechanisms of smooth muscle cell proliferation and endothelial regeneration after vascular injury and stenting - approach to therapy," *Circulation journal: official journal of the Japanese Circulation Society*, vol. 75, no. 6, pp. 1287–96, 2011.

[27] G. Nakazawa, M. Nakano, F. Otsuka, J. N. Wilcox, R. Melder, S. Pruitt, F. D. Kolodgie, and R. Virmani, "Evaluation of polymer-based comparator drug-eluting stents using a rabbit model of iliac artery atherosclerosis," *Circulation: Cardiovascular Interventions*, vol. 4, no. 1, pp. 38–46, 2011.

[28] G. P. Talarico, F. Burzotta, C. Trani, *et al.*, "One-year outcomes of consecutive patients treated by endeavor zotarolimus and resolute zotarolimus stents: The impact of polymer coating in drug-eluting stent technology," *Cathererization and Cardiovascular Interventions*, vol. 81, no. 2, pp. 268–73, 2013.

[29] D. Matsumoto, T. Shinke, T. Nakamura, *et al.*, "Optical coherence tomography and histopathological assessment of delayed arterial healing after drug-eluting stent implant in a pig coronary model," *International Journal of Cardiology*, vol. 170, no. 2, pp. 152–59, 2013.

[30] H. M. van Beusekom, O. Sorop, M. can den Heuvel, *et al.*, "Endothelial function rather than endothelial restoration is altered in paclitaxel- as compared to bare metal-, sirolimus- and tacrolimus-eluting stents," *Eurointervention*, vol. 6, no. 1, pp. 117–25, 2010.

[31] C. Matter, I. Rozenberg, A. Jaschko, H. Greutert, D. Kurz, S. Wnendt, B. Kuttler, H. Joch, J. Grünenfelder, G. Zünd, F. Tanner, and T. Lüscher, "Effects of tacrolimus or sirolimus on proliferation of vascular smooth muscle and endothelial cells," *Journal of cardiovascular pharmacology*, vol. 48, no. 6, pp. 286–92, 2007.

[32] D. Buccheri, D. Piraino, G. Andolina, and B. Cortese, "Understanding and managing in-stent restenosis: a review of clinical data, from pathogenesis to treatment," *Journal of Thoracic Disease*, vol. 8, no. 10, pp. E1150–E1162, 2016.

[33] S. Bangalore, B. Toklu, N. Amoroso, M. Fusaro, S. Kumar, E. L. Hannan, D. P. Faxon, and F. Feit, "Bare metal stents, durable polymer drug eluting stents, and biodegradable polymer drug eluting stents for coronary artery disease: mixed treatment comparison meta-analysis," *BMJ*, vol. 347, 2013.

[34] S.-H. Kang, K. W. Park, D.-Y. Kang, W.-H. Lim, K. T. Park, J.-K. Han, H.-J. Kang, B.-K. Koo, B.-H. Oh, Y.-B. Park, D. E. Kandzari, D. J. Cohen, S.-S. Hwang, and H.-S. Kim, "Biodegradable-polymer drug-eluting stents vs. bare metal stents vs. durable-polymer drug-eluting stents: a systematic review and Bayesian approach network meta-analysis," *European Heart Journal*, vol. 35, no. 17, pp. 1147–1158, 2014.

[35] R. A. Buiten, E. H. Ploumen, P. Zocca, C. J. Doggen, P. W. Danse, C. E. Schotborgh, M. Scholte, K. G. van Houwelingen, M. G. Stoel, M. Hartmann, R. M. T. J. Gin, S. Somi, G. C. Linssen, M. M. Kok, and C. von Birgelen, "Thin, very thin, or ultrathin strut biodegradable or durable polymer-coated drug-eluting stents," *JACC: Cardiovascular Interventions*, vol. 12, no. 17, pp. 1650–1660, 2019.

[36] E. P. Navarese, M. Kowalewski, D. Kandzari, A. Lansky, B. Górny, Ł. Kołtowski, R. Waksman, S. Berti, G. Musumeci, U. Limbruno, R. J. van der Schaaf, M. Kelm, J. Kubica, and H. Suryapranata, "First-generation versus second-generation drug-eluting stents in current clinical practice: updated evidence from a comprehensive meta-analysis of randomised clinical trials comprising 31 379 patients," *Open Heart*, vol. 1, no. 1, 2014.

[37] C. Stettler, S. Wandel, S. Allemann, A. Kastrati, M. C. Morice, A. Schömig, M. E. Pfisterer, G. W. Stone, M. B. Leon, J. S. de Lezo, J.-J. Goy, S.-J. Park, M. Sabaté, M. J. Suttorp, H. Kelbaek, C. Spaulding, M. Menichelli, P. Vermeersch, M. T. Dirksen, P. Cervinka, A. S. Petronio, A. J. Nordmann, P. Diem, B. Meier, M. Zwahlen, S. Reichenbach, S. Trelle, S. Windecker, and P. Jüni, "Outcomes associated with drug-eluting and

bare-metal stents: a collaborative network meta-analysis," *The Lancet*, vol. 370, no. 9591, pp. 937–948, 2007.

[38] M. Chiarito, G. Sardella, A. Colombo, C. Briguori, L. Testa, F. Bedogni, F. Fabbiocchi, A. Paggi, A. Palloshi, C. Tamburino, A. Margonato, C. A. Pivato, U. Baber, S. Calcagno, A. Giordano, C. Godino, G. G. Stefanini, and null null, "Safety and efficacy of polymer-free drug-eluting stents," *Circulation: Cardiovascular Interventions*, vol. 12, no. 2, p. e007311, 2019.

[39] J. Wu, J. Way, L. Kritharides, and D. Brieger, "Polymer-free versus durable polymer drug-eluting stents in patients with coronary artery disease: A meta-analysis," *Annals of Medicine and Surgery*, vol. 38, pp. 13–21, 2018.

[40] S. Altoukhy, A. Rezq, B. Anany, W. Elhamady, M. Metwally, and M. Taher, "Polymer free drug-eluting stents versus durable polymer drug-eluting stents in elective percutaneous coronary interventions in patients with stable coronary artery disease patients," *QJM: An International Journal of Medicine*, vol. 113, 2020.

[41] D. Hoare, A. Bussooa, S. Neale, N. Mirzai, and J. Mercer, "The future of cardiovascular stents: Bioresorbable and integrated biosensor technology," *Advanced Science*, vol. 6, no. 20, p. 1900856, 2019.

[42] C. Tamburino, P. Capranzano, T. Gori, A. Latib, M. Lesiak, H. Nef, G. Caramanno, C. Naber, J. Mehilli, C. D. Mario, M. Sabaté, T. Münzel, A. Colombo, A. Araszkiewicz, J. Wiebe, S. Geraci, C. Jensen, A. Mattesini, S. Brugaletta, and D. Capodanno, "1-year outcomes of everolimus-eluting bioresorbable scaffolds versus everolimus-eluting stents," *JACC: Cardiovascular Interventions*, vol. 9, no. 5, pp. 440–449, 2016.

[43] Z. A. Ali, R. Gao, T. Kimura, Y. Onuma, D. J. Kereiakes, S. G. Ellis, B. Chevalier, M. thien Vu, Z. Zhang, C. A. Simonton, P. W. Serruys, and G. W. Stone, "Three-year outcomes with the absorb bioresorbable scaffold," *Circulation*, vol. 137, no. 5, pp. 464–479, 2018.

[44] S. Bangalore, B. Toklu, N. Patel, F. Feit, and G. W. Stone, "Newer-generation ultrathin strut drug-eluting stents versus older second-generation thicker strut drug-eluting stents for coronary artery disease," *Circulation*, vol. 138, no. 20, pp. 2216–2226, 2018.

[45] M. Ono, H. Kawashima, H. Hara, C. Gao, R. Wang, N. Kogame, K. Takahashi, P. Chichareon, R. Modolo, M. Tomaniak, J. J. Wykrzykowska, J. J. Piek, I. Mori, B. K. Courtney, W. Wijns, F. Sharif, C. Bourantas, Y. Onuma, and P. W. Serruys, "Advances in ivus/oct and future clinical perspective of novel hybrid catheter system in coronary imaging," *Frontiers in Cardiovascular Medicine*, vol. 7, no. 119, 2020.

[46] P. Mandal, Sarifuddin, and V. Kolachalama, "Computational model of drug-coated balloon delivery in a patient-specific arterial vessel with heterogeneous tissue composition," *Cardiovascular Engineering and Technology*, vol. 7, no. 4, pp. 406–419, 2016.

[47] A. Maehara, M. Matsumura, Z. A. Ali, G. S. Mintz, and G. W. Stone, "Ivus-guided versus oct-guided coronary stent implantation: A critical appraisal," *JACC: Cardiovascular Imaging*, vol. 10, no. 12, pp. 1487–1503, 2017.

[48] W. F. Fearon, F. M. Zimmermann, B. De Bruyne, Z. Piroth, A. H. van Straten, L. Szekely, G. Davidavičius, G. Kalinauskas, S. Mansour, R. Kharbanda, N. Östlund Papadogeorgos, A. Aminian, K. G. Oldroyd, N. Al-Attar, N. Jagic, J.-H. E. Dambrink, P. Kala, O. Angerås, P. MacCarthy, O. Wendler, F. Casselman, N. Witt, K. Mavromatis, S. E. Miner, J. Sarma, T. Engstrøm, E. H. Christiansen, P. A. Tonino, M. J. Reardon, D. Lu, V. Y. Ding, Y. Kobayashi, M. A. Hlatky, K. W. Mahaffey, M. Desai, Y. J. Woo, A. C. Yeung, and N. H. Pijls, "Fractional flow reserve–guided pci as compared with coronary bypass surgery," *New England Journal of Medicine*, vol. 386, no. 2, pp. 128–137, 2022.

[49] S. K. Arramraju, R. K. Janapati, E. Sanjeeva Kumar, and G. R. Mandala, "National interventional council data for the year 2018-india," *Indian Heart Journal*, vol. 72, no. 5, pp. 351–355, 2020.

[50] F. Alfonso, J. Coughlan, D. Giacoppo, A. Kastrati, and R. Byrne, "Management of in-stent restenosis," *EuroIntervention*, vol. 18, pp. e103–e123, 2022.

[51] E. E. Antoine, F. P. Cornat, and A. I. Barakat, "The stentable *in vitro* artery: an instrumented platform for endovascular device development and optimization," *Journal of The Royal Society Interface*, vol. 13, no. 125, p. 20160834, 2016.

[52] I. Holland, C. McCormick, and P. Connolly, "Towards non-invasive characterisation of coronary stent re-endothelialisation – an in-vitro, electrical impedance study," *PLOS ONE*, vol. 13, no. 11, pp. 1–17, 2018.

[53] H. Tahir, C. Bona-Casas, and A. G. Hoekstra, "Modelling the effect of a functional endothelium on the development of in-stent restenosis," *PLoS One*, vol. 8, no. 6, p. e66138, 2013.

[54] H. Zahedmanesh, H. Oosterwyck, and C. Lally, "A multi-scale mechanobiological model of in-stent restenosis: deciphering the role of matrix metalloproteinase and extracellular matrix changes," *Computer methods in biomechanics and biomedical engineering*, vol. 17, no. 8, pp. 813–828, 2014.

[55] J. Escuer, M. A. Martínez, S. McGinty, and E. Peña, "Mathematical modelling of the restenosis process after stent implantation," *Journal of The Royal Society Interface*, vol. 16, no. 157, p. 20190313, 2019.

[56] C. Chaabane, F. Otsuka, R. Virmani, and M.-L. Bochaton-Piallat, "Biological responses in stented arteries," *Cardiovascular Research*, vol. 99, no. 2, pp. 353–63, 2013.

[57] C. J. Boyle, A. B. Lennon, and P. J. Prendergast, "In silico prediction of the mechanobiological response of arterial tissue: Application to angioplasty and stenting," *Journal of Biomechanical Engineering*, vol. 133, no. 8, pp. 081001–1, 2011.

[58] J. Y. Jeremy, D. Rowe, A. M. Emsley, and A. C. Newby, "Nitric oxide and the proliferation of vascular smooth muscle cells," *Cardiovascular Research*, vol. 43, no. 3, pp. 580–594, 1999.

[59] N. D. Tsihlis *et al.*, "Nitric oxide inhibits vascular smooth muscle cell proliferation and neointimal hyperplasia by increasing the ubiquitination and degradation of ubch10," *Cell Biochemistry and Biophysics*, vol. 60, no. 1-2, pp. 89–97, 2011.

[60] R. Fitridge and M. Thompson, *Mechanisms of Vascular Disease: A Reference Book for Vascular Specialists*. The University of Adelaide Press, 2011.

[61] K. van der Heiden, F. J. H. Gijsen, A. Narracott, *et al.*, "The effects of stenting on shear stress: relevance to endothelial injury and repair," *Cardiovacular Research*, vol. 99, no. 2, pp. 269–75, 2013.

[62] N. N. Kipshidze *et al.*, "Role of the endothelium in modulating neointimal formation - vasculoprotective approaches to attenuate restenosis after percutaneous coronary interventions," *Journal of the American College of Cardiology*, vol. 44, no. 4, pp. 733–39, 2004.

[63] J. Gunn *et al.*, "Coronary artery stretch versus deep injury in the development of in-stent neointima," *Heart*, vol. 88, no. 4, pp. 401–05, 2002.

[64] E. Tenekecioglu, Y. Sotomi, R. Torii, C. Bourantas, Y. Miyazaki, C. Collet, T. Crake, S. Su, Y. Onuma, and P. Serruys, "Strut protrusion and shape impact on endothelial shear stress: insights from pre-clinical study comparing mirage and absorb bioresorbable scaffolds," *The international journal of cardiovascular imaging*, vol. 33, no. 9, pp. 1313–1322, 2017.

[65] H. Tahir, I. Niculescu, C. Bona-Casas, R. M. H. Merks, and A. G. Hoekstra, "An *in silico* study on the role of smooth muscle cell migration in neointimal formation after coronary stenting," *Journal of The Royal Society Interface*, vol. 12, no. 108, p. 20150358, 2015.

[66] P. S. Zun, T. Anikina, A. Svitenkov, and A. G. Hoekstra, "A comparison of fully-coupled 3d in-stent restenosis simulations to in-vivo data," *Frontiers in Physiology*, vol. 8, p. 284 eCollection, 2017.

[67] H. Tahir, C. Bona-Casas, A. J. Narracott, *et al.*, "Endothelial repair process and its relevance to longitudinal neointimal tissue patterns: comparing histology with in silico modelling," *Journal of Royal Society Interface*, vol. 11, no. 94, p. 20140022, 2014.

[68] S. Sartore *et al.*, "Contribution of adventitial fibroblasts to neointima formation and vascular remodeling: from innocent bystander to active participant," *Circulation Research*, vol. 89, no. 12, pp. 1111–121, 2001.

[69] R. C. M. Siow, C. M. Mallawaarachchi, and P. L. Weissberg, "Migration of adventitial myofibroblasts following vascular balloon injury: insights from in vivo gene transfer to rat carotid arteries," *Cardiovascular Research*, vol. 59, no. 1, pp. 212–21, 2003.

[70] S. O. Marx, H. Totary-Jain, and A. R. Marks, "Vascular smooth muscle cell proliferation in restenosis," *Circulation: Cardiovascular Interventions*, vol. 4, no. 1, pp. 104–111, 2011.

[71] S. Rensen, P. Doevendans, and G. Eys, "Regulation and characteristics of vascular smooth muscle cell phenotypic diversity," *Netherlands heart journal : monthly journal of the Netherlands Society of Cardiology and the Netherlands Heart Foundation*, vol. 15, no. 3, pp. 100–8, 2007.

[72] R. S. Schwartz *et al.*, "The restenosis paradigm revisited: an alternative proposal for cellular mechanisms," *Journal of the American College of Cardiology*, vol. 19, no. 2, pp. 267–74, 1992.

[73] I.-M. Chung, H. K. Gold, S. M. Schwartz, Y. Ikari, M. A. Reidy, and T. N. Wight, "Enhanced extracellular matrix accumulation in restenosis of coronary arteries after stent deployment," *Journal of the American College of Cardiology*, vol. 40, no. 12, pp. 2072–2081, 2002.

[74] D. W. Leung *et al.*, "Vascular endothelial growth factor is a secreted angiogenic mitogen," *Science*, vol. 246, no. 4935, pp. 1306–309, 1989.

[75] T. F. Lüscher, J. Steffel, F. R. Eberli, M. Joner, G. Nakazawa, F. C. Tanner, and R. Virmani, "Drug-eluting stent and coronary thrombosis," *Circulation*, vol. 115, no. 8, pp. 1051–1058, 2007.

[76] M. A. Costa and D. I. Simon, "Molecular basis of restenosis and drug-eluting stents," *Circulation*, vol. 111, no. 17, pp. 2257–2273, 2005.

[77] W. S. Weintraub, "The pathophysiology and burden of restenosis," *The American Journal of Cardiology*, vol. 100, no. 5, Supplement, pp. S3–S9, 2007.

[78] S. McGinty, "A decade of modelling drug release from arterial stents," *Mathematical Biosciences*, vol. 257, pp. 80–90, 2014.

[79] A. R. Tzafriri, A. Groothuis, G. S. Price, and E. R. Edelman, "Stent elution rate determines drug deposition and receptor-mediated effects," *Journal of Controlled Release*, vol. 161, no. 3, pp. 918–926, 2012.

[80] M. Oberhoff *et al.*, "Stent-based antirestenotic coatings (sirolimus/paclitaxel)," *Catheterization, Cardiovascular Interventions*, vol. 55, no. 3, pp. 404–408, 2002.

[81] B. Scheller, U. Speck, A. Schmitt, M. Böhm, and G. Nickenig, "Addition of paclitaxel to contrast media prevents restenosis after coronary stent implantation," *Journal of the American College of Cardiology*, vol. 42, no. 8, pp. 1415 – 1420, 2003.

[82] D. Gavaghan, A. Garny, P. K. Maini, and P. Kohl, "Mathematical models in physiology," *Philosophical Transactions of the Royal Society A: Mathematical, Physical and Engineering Sciences*, vol. 364, no. 1842, pp. 1099–1106, 2006.

[83] A. Jarrett, A. Shah, M. Bloom, M. McKenna, D. Hormuth, T. Yankeelov, and A. Sorace, "Experimentally-driven mathematical modeling to improve combination targeted and cytotoxic therapy for her2+ breast cancer," *Scientific Reports*, vol. 9, no. 1, 2019.

[84] J. A. Sherratt and J. D. Murray, "Models of epidermal wound healing," *Proceedings. Biological Sciences*, vol. 241, no. 1300, pp. 29–36, 1990.

[85] C. Chiastra, S. Morlacchi, S. Pereira, G. Dubini, and F. Migliavacca, "Computational fluid dynamics of stented coronary bifurcations studied with a hybrid discretization method," *European Journal of Mechanics*, vol. 35, pp. 76–84, 2012.

[86] C. Dumoulin and B. Cochelin, "Mechanical behaviour modelling of balloon-expandable stents," *Journal of Biomechanics*, vol. 33, no. 11, pp. 1461–1470, 2000.

[87] F. Etave, G. Finet, M. Boivin, J.-C. Boyer, G. Rioufol, and G. Thollet, "Mechanical properties of coronary stents determined by using finite element analysis," *Journal of Biomechanics*, vol. 34, no. 8, pp. 1065–1075, 2001.

[88] F. Migliavacca, L. Petrini, M. Colombo, F. Auricchio, and R. Pietrabissa, "Mechanical behavior of coronary stents investigated through the finite element method," *Journal of Biomechanics*, vol. 35, no. 6, pp. 803–811, 2002.

[89] S. David Chua, B. MacDonald, and M. Hashmi, "Effects of varying slotted tube (stent) geometry on its expansion behaviour using finite element method," *Journal of Materials Processing Technology*, vol. 155-156, pp. 1764–1771, 2004.

[90] F. Migliavacca, L. Petrini, V. Montanari, I. Quagliana, F. Auricchio, and G. Dubini, "A predictive study of the mechanical behaviour of coronary stents by computer modelling," *Medical Engineering & Physics*, vol. 27, no. 1, pp. 13–18, 2005.

[91] M. De Beule, P. Mortier, S. G. Carlier, B. Verhegghe, R. Van Impe, and P. Verdonck, "Realistic finite element-based stent design: The impact of balloon folding," *Journal of Biomechanics*, vol. 41, no. 2, pp. 383–389, 2008.

[92] W.-Q. Wang, D.-K. Liang, D.-Z. Yang, and M. Qi, "Analysis of the transient expansion behavior and design optimization of coronary stents by finite element method," *Journal of Biomechanics*, vol. 39, no. 1, pp. 21–32, 2006.

[93] D. Lim, S.-K. Cho, W.-P. Park, A. Kristensson, J.-Y. Ko, S. Al-Hassani, and H.-S. Kim, "Suggestion of potential stent design parameters to reduce restenosis risk driven by foreshortening or dogboning due to non-uniform balloon-stent expansion," *Annals of biomedical engineering*, vol. 36, no. 7, pp. 1118–29, 2008.

[94] D. Martin and F. Boyle, "Finite element analysis of balloon-expandable coronary stent deployment: Influence of angioplasty balloon configuration," *International Journal for Numerical Methods in Biomedical Engineering*, vol. 29, no. 11, pp. 1161–1175, 2013.

[95] W. Yu and J. Wang, "Finite element analysis of free expansion of coronary stent based on ansys workbench," *Advanced Materials Research*, vol. 662, pp. 626–631, 2013.

[96] F. Auricchio, M. Loreto, and E. Sacco, "Finite-element analysis of a stenotic artery revascularization through a stent insertion," *Computer Methods in Biomechanics and Biomedical Engineering*, vol. 4, 2001.

[97] S. David Chua, B. MacDonald, and M. Hashmi, "Finite element simulation of slotted tube (stent) with the presence of plaque and artery by balloon expansion," *Journal of Materials Processing Technology*, vol. 155-156, pp. 1772–1779, 2004.

[98] C. Lally, F. Dolan, and P. Prendergast, "Cardiovascular stent design and vessel stresses: a finite element analysis," *Journal of Biomechanics*, vol. 38, no. 8, pp. 1574–1581, 2005.

[99] D. Liang, D. Yang, M. Qi, and W. Wang, "Finite element analysis of a stent implantation in a stenosed artery," *Key Engineering Materials*, vol. 288-289, pp. 571–574, 2005.

[100] A. Schiavone, L. Zhao, and A. Abdel-Wahab, "Effects of material, coating, design and plaque composition on stent deployment inside a stenotic artery-finite element simulation," *Materials science & engineering. C, Materials for biological applications*, vol. 42, pp. 479–488, 2014.

[101] L. Timmins, M. Miller, F. Clubb, and J. Moore, "Increased artery wall stress post-stenting leads to greater intimal thickening," *Laboratory investigation; a journal of technical methods and pathology*, vol. 91, pp. 955–67, 2011.

[102] J. Bedoya, C. A. Meyer, L. H. Timmins, M. R. Moreno, and J. Moore, James E., "Effects of Stent Design Parameters on Normal Artery Wall Mechanics," *Journal of Biomechanical Engineering*, vol. 128, no. 5, pp. 757–765, 2006.

[103] L. Timmins, J. Moore, J. Bedoya, , C. Meyer, and M. Moreno, "Stented artery biomechanics and device design optimization," *Medical & biological engineering & computing*, vol. 45, no. 5, pp. 505–13, 2007.

[104] L. Timmins, C. Meyer, M. Moreno, and J. Moore, "Effects of stent design and atherosclerotic plaque composition an arterial wall biomechanics," *Journal of endovascular therapy : an official journal of the International Society of Endovascular Specialists*, vol. 15, no. 6, pp. 643–54, 2009.

[105] C. Capelli, F. Gervaso, L. Petrini, G. Dubini, and F. Migliavacca, "Assessment of tissue prolapse after balloon-expandable stenting: Influence of stent cell geometry," *Medical engineering & physics*, vol. 31, no. 4, pp. 441–447, 2009.

[106] H. Li, T. Qiu, B. Zhu, J. Wu, and X. Wang, "Design optimization of coronary stent based on finite element models," *TheScientificWorldJournal*, vol. 2013, p. 630243, 2013.

[107] M. Imani, A. Goudarzi, S. Ghasemi, A. Kalani, and J. Mahdinejad, "Analysis of the stent expansion in a stenosed artery using finite element method: Application to stent versus stent study," *Proceedings of the Institution of Mechanical Engineers. Part H, Journal of engineering in medicine*, vol. 228, no. 10, pp. 996–1004, 2014.

[108] G. A. Holzapfel, M. Stadler, and T. C. Gasser, "Changes in the Mechanical Environment of Stenotic Arteries During Interaction With Stents: Computational Assessment of Parametric Stent Designs ," *Journal of Biomechanical Engineering*, vol. 127, no. 1, pp. 166–180, 2005.

[109] F. Gijsen, F. Migliavacca, S. Schievano, L. Socci, L. Petrini, A. Thury, J. Wentzel, A. van der Steen, P. Serruys, and G. Dubini, "Simulation of stent deployment in a realistic human coronary artery," *Biomedical engineering online*, vol. 7, p. 23, 02 2008.

[110] I. Pericevic, C. Lally, D. Toner, and D. J. Kelly, "The influence of plaque composition on underlying arterial wall stress during stent expansion: The case for lesion-specific stents," *Medical Engineering & Physics*, vol. 31, no. 4, pp. 428–433, 2009.

[111] A. Schiavone and L. Zhao, "A study of balloon type, system constraint and artery constitutive model used in finite element simulation of stent deployment," *Mechanics of Advanced Materials and Modern Processes*, vol. 1, no. 1, 2015.

[112] P. Mortier, Y. Hikichi, N. Foin, G. De Santis, P. Segers, B. Verhegghe, and M. De Beule, "Provisional stenting of coronary bifurcations: Insights into final kissing balloon post-dilation and stent design by computational modeling," *JACC: Cardiovascular Interventions*, vol. 7, no. 3, pp. 325–333, 2014.

[113] M. C. Arokiaraj, G. De Santis, M. De Beule, and I. F. Palacios, "A novel tram stent method in the treatment of coronary bifurcation lesions – finite element study," *PLOS ONE*, vol. 11, no. 3, pp. 1–15, 2016.

[114] X. Jiang, Y. Jie, S. Sohrabi, Y. Zhou, and Y. Liu, "Finite element analysis of the implantation process of overlapping stents," *Journal of Medical Devices*, vol. 11, no. 2, p. 0210101–0210109, 2017.

[115] R. He, L. Zhao, V. Silberschmidt, Y. Liu, and F. Vogt, "Patient-specific modelling of stent overlap: Lumen gain, tissue damage and in-stent restenosis," *Journal of the Mechanical Behavior of Biomedical Materials*, vol. 109, p. 103836, 2020.

[116] N. Debusschere, P. Segers, P. Dubruel, B. Verhegghe, and M. De Beule, "A finite element strategy to investigate the free expansion behaviour of a biodegradable polymeric stent," *Journal of Biomechanics*, vol. 48, no. 10, pp. 2012–2018, 2015.

[117] T. Welch, R. Eberhart, S. Banerjee, and C.-J. Chuong, "Mechanical interaction of an expanding coiled stent with a plaque-containing arterial wall: A finite element analysis," *Cardiovascular Engineering and Technology*, vol. 7, no. 1, pp. 58–68, 2016.

[118] A. Schiavone, T.-Y. Qiu, and L. Zhao, "Crimping and deployment of metallic and polymeric stents – finite element modelling," *Vessel Plus*, vol. 1, pp. 12–21, 2017.

[119] T. Qiu, R. He, C. Abunassar, S. Hossainy, and L. Zhao, "Effect of two-year degradation on mechanical interaction between a bioresorbable scaffold and blood vessel," *Journal of the Mechanical Behavior of Biomedical Materials*, vol. 78, pp. 254–265, 2018.

[120] T. Qiu, M. Song, and L. Zhao, "A computational study of crimping and expansion of bioresorbable polymeric stents," *Mechanics of Time-Dependent Materials*, vol. 22, no. 2, pp. 273–90, 2018.

[121] K. Peng, X. Cui, A. Qiao, and Y. Mu, "Mechanical analysis of a novel biodegradable zinc alloy stent based on a degradation model," *BioMedical Engineering OnLine*, vol. 18, no. 1, p. 39, 2019.

[122] R. He, L. Zhao, V. Silberschmidt, Y. Liu, and F. Vogt, "Finite element evaluation of artery damage in deployment of polymeric stent with pre- and post-dilation," *Biomechanics and Modeling in Mechanobiology*, vol. 19, no. 1, pp. 47–60, 2020.

[123] L. Antonini, F. Berti, B. Isella, D. Hossain, L. Mandelli, G. Pennati, and L. Petrini, "From the real device to the digital twin: A coupled experimental-numerical strategy to investigate a novel bioresorbable vascular scaffold," *PLOS ONE*, vol. 16, no. 6, pp. 1–20, 2021.

[124] P. Dong, H. Mozafari, J. Lee, Y. Gharaibeh, V. N. Zimin, L. A. Dallan, H. G. Bezerra, D. L. Wilson, and L. Gu, "Mechanical performances of balloon post-dilation for improving stent expansion in calcified coronary artery: Computational and experimental investigations," *Journal of the Mechanical Behavior of Biomedical Materials*, vol. 121, p. 104609, 2021.

[125] J. J. Wentzel, R. Krams, J. C. H. Schuurbiers, J. A. Oomen, J. Kloet, W. J. van der Giessen, P. W. Serruys, and C. J. Slager, "Relationship between neointimal thickness and shear stress after wallstent implantation in human coronary arteries," *Circulation*, vol. 103, no. 13, pp. 1740–1745, 2001.

[126] J. F. LaDisa, L. E. Olson, R. C. Molthen, D. A. Hettrick, P. F. Pratt, M. D. Hardel, J. R. Kersten, D. C. Warltier, and P. S. Pagel, "Alterations in wall shear stress predict sites of neointimal hyperplasia after stent implantation in rabbit iliac arteries," *American Journal of Physiology-Heart and Circulatory Physiology*, vol. 288, no. 5, pp. H2465–H2475, 2005.

[127] J. LaDisa, I. Guler, L. Olson, D. Hettrick, J. Kersten, D. Warltier, and P. Pagel, "Three-dimensional computational fluid dynamics modeling of alterations in coronary wall shear stress produced by stent implantation," *Annals of biomedical engineering*, vol. 31, no. 8, pp. 972–80, 2003.

[128] J. F. LaDisa, L. E. Olson, I. Guler, D. A. Hettrick, S. H. Audi, J. R. Kersten, D. C. Warltier, and P. S. Pagel, "Stent design properties and deployment ratio influence indexes of wall shear stress: a three-dimensional computational fluid dynamics investigation within a normal artery," *Journal of Applied Physiology*, vol. 97, no. 1, pp. 424–430, 2004.

[129] Y. He, N. Duraiswamy, A. O. Frank, and J. Moore, James E., "Blood Flow in Stented Arteries: A Parametric Comparison of Strut Design Patterns in Three Dimensions," *Journal of Biomechanical Engineering*, vol. 127, no. 4, pp. 637–647, 2005.

[130] J. LaDisa, L. Olson, D. Hettrick, D. Warltier, J. Kersten, and P. Pagel, "Axial stent strut angle influences wall shear stress after stent implantation: Analysis using 3d computational fluid dynamics models of stent foreshortening," *Biomedical engineering online*, vol. 4, p. 59, 2005.

[131] J. LaDisa, L. Olson, D. Hettrick, D. Warltier, J. Kersten, and P. Pagel, "Alterations in regional vascular geometry produced by theoretical stent implantation influence distributions of wall shear stress: Analysis of a curved coronary artery using 3d computational fluid dynamics modeling," *Biomedical engineering online*, vol. 5, p. 40, 2006.

[132] R. Balossino, F. Gervaso, F. Migliavacca, and G. Dubini, "Effects of different stent designs on local hemodynamics in stented arteries," *Journal of Biomechanics*, vol. 41, no. 5, pp. 1053–1061, 2008.

[133] V. Dehlaghi, M. T. Shadpoor, and S. Najarian, "Analysis of wall shear stress in stented coronary artery using 3d computational fluid dynamics modeling," *Journal of Materials Processing Technology*, vol. 197, no. 1, pp. 174–181, 2008.

[134] N. Duraiswamy, R. T. Schoephoerster, and J. Moore, James E., "Comparison of Near-Wall Hemodynamic Parameters in Stented Artery Models," *Journal of Biomechanical Engineering*, vol. 131, no. 6, 2009.

[135] S. Pant, N. Bressloff, A. Forrester, and N. Curzen, "The influence of strut-connectors in stented vessels: A comparison of pulsatile flow through five coronary stents," *Annals of biomedical engineering*, vol. 38, no. 5, pp. 1893–907, 2010.

[136] T. J. Gundert, A. L. Marsden, W. Yang, and J. LaDisa, John F., "Optimization of Cardiovascular Stent Design Using Computational Fluid Dynamics," *Journal of Biomechanical Engineering*, vol. 134, no. 1, 2012.

[137] S. Beier, J. Ormiston, M. Webster, J. Cater, S. Norris, P. Medrano-Gracia, A. Young, and B. Cowan, "Hemodynamics in idealized stented coronary arteries: Important stent design considerations," *Annals of Biomedical Engineering*, vol. 44, no. 2, pp. 315 – 329, 2016.

[138] V. B. Kolachalama, E. G. Levine, and E. R. Edelman, "Luminal flow amplifies stent-based drug deposition in arterial bifurcations," *PLOS ONE*, vol. 4, no. 12, pp. 1–9, 2009.

[139] A. R. Williams, B.-K. Koo, T. J. Gundert, P. J. Fitzgerald, and J. F. LaDisa, "Local hemodynamic changes caused by main branch stent implantation and subsequent virtual side branch balloon angioplasty in a representative coronary bifurcation," *Journal of Applied Physiology*, vol. 109, no. 2, pp. 532–540, 2010.

[140] D. G. Katritsis, A. Theodorakakos, I. Pantos, M. Gavaises, N. Karcanias, and E. P. Efstathopoulos, "Flow patterns at stented coronary bifurcations," *Circulation: Cardiovascular Interventions*, vol. 5, no. 4, pp. 530–539, 2012.

[141] V. Deplano, C. Bertolotti, and P. Barragan, "Three-dimensional numerical simulations of physiological flows in a stented coronary bifurcation," *Medical & Biological Engineering & Computing*, vol. 42, no. 5, pp. 650–59, 2004.

[142] J. Raben, S. Morlacchi, F. Burzotta, F. Migliavacca, and P. Vlachos, "Local blood flow patterns in stented coronary bifurcations: An experimental and numerical study," *Journal of applied biomaterials & functional materials*, vol. 13, no. 2, pp. e116–126, 2015.

[143] L. Genuardi, Y. Chatzizisis, C. Chiastra, G. Sgueglia, H. Samady, G. Kassab, F. Migliavacca, C. Trani, and F. Burzotta, "Local fluid dynamics in patients with bifurcated coronary lesions undergoing percutaneous coronary interventions," *Cardiology Journal*, vol. 28, no. 2, pp. 321–329, 2020.

[144] L. Ellwein-Fix, H. Otake, T. Gundert, B.-K. Koo, T. Shinke, Y. Honda, J. Shite, and J. LaDisa, "Optical coherence tomography for patient-specific 3d artery reconstruction and evaluation of wall shear stress in a left circumflex coronary artery," *Cardiovascular Engineering and Technology*, vol. 2, pp. 212–227, 2011.

[145] G. De Santis, P. Mortier, M. Beule, P. Segers, P. Verdonck, and B. Verhegghe, "Patient-specific computational fluid dynamics: Structured mesh generation from coronary angiography," *Medical & biological engineering & computing*, vol. 48, no. 4, pp. 371–80, 2010.

[146] T. Gundert, S. Shadden, A. Williams, B.-K. Koo, J. Feinstein, and J. LaDisa, "A rapid and computationally inexpensive method to virtually implant current and next-generation stents into subject-specific computational fluid dynamics models," *Annals of biomedical engineering*, vol. 39, no. 5, pp. 1423–37, 2011.

[147] C. Chiastra, S. Morlacchi, D. Gallo, U. Morbiducci, R. Cárdenes, I. Larrabide, and F. Migliavacca, "Computational fluid dynamic simulations of image-based stented coronary bifurcation models," *Journal of The Royal Society Interface*, vol. 10, no. 84, p. 20130193, 2013.

[148] S. Morlacchi, S. G. Colleoni, R. Cárdenes, C. Chiastra, J. L. Diez, I. Larrabide, and F. Migliavacca, "Patient-specific simulations of stenting procedures in coronary bifurcations: Two clinical cases," *Medical Engineering & Physics*, vol. 35, no. 9, pp. 1272–1281, 2013.

[149] P. Mortier, J. Wentzel, G. De Santis, C. Chiastra, F. Migliavacca, M. Beule, Y. Louvard, and G. Dubini, "Patient-specific computer modelling of coronary bifurcation stenting: The john doe programme," *EuroIntervention: journal of EuroPCR in collaboration with the Working Group on Interventional Cardiology of the European Society of Cardiology*, vol. 11, pp. V35–V39, 2015.

[150] J. Ng, C. V. Bourantas, R. Torii, H. Y. Ang, E. Tenekecioglu, P. W. Serruys, and N. Foin, "Local hemodynamic forces after stenting," *Arteriosclerosis, Thrombosis, and Vascular Biology*, vol. 37, no. 12, pp. 2231–2242, 2017.

[151] T. Gori, A. Polimeni, C. Indolfi, L. Räber, T. Adriaenssens, and T. Munzel, "Predictors of stent thrombosis and their implications for clinical practice," *Nature Reviews Cardiology*, vol. 16, no. 4, pp. 243–256, 2018.

[152] P. F. Davies, "Flow-mediated endothelial mechanotransduction," *Physiological Reviews*, vol. 75, no. 3, pp. 519–560, 1995.

[153] A. Barakat, "Responsiveness of vascular endothelium to shear stress: potential role of ion channels and cellular cytoskeleton (review)," *International journal of molecular medicine*, vol. 4, no. 4, pp. 323–32, 1999.

[154] A. Barakat and D. Lieu, "Differential responsiveness of vascular endothelial cells to different types of fluid mechanical shear stress," *Cell biochemistry and biophysics*, vol. 38, no. 3, pp. 323–43, 2003.

[155] A. Kumar *et al.*, "Low coronary wall shear stress is associated with severe endothelial dysfunction in patients with non-obstructive coronary artery disease," *JACC Cardiovasc. Interv.*, vol. 11, no. 20, pp. 2072–80, 2018.

[156] H. Samady, P. Eshtehardi, M. C. McDaniel, J. Suo, S. S. Dhawan, C. Maynard, L. H. Timmins, A. A. Quyyumi, and D. P. Giddens, "Coronary artery wall shear stress is associated with progression and transformation of atherosclerotic plaque and arterial remodeling in patients with coronary artery disease," *Circulation*, vol. 124, no. 7, pp. 779–788, 2011.

[157] N. Foin, J. L. Gutiérrez-Chico, S. Nakatani, R. Torii, C. Bourantas, S. Sen, S. Nijjer, R. Petraco, C. Kousera, M. Ghione, Y. Onuma, H. Garcia-Garcia, D. Francis, P. Wong, C. Di Mario, J. Davies, and P. Serruys, "Incomplete stent apposition causes high shear flow disturbances and delay in neointimal coverage as a function of strut to wall detachment distance: Implications for stent optimization," *Circulation. Cardiovascular interventions*, vol. 7, no. 2, pp. 180–9, 2014.

[158] T. Gori, "Endothelial function: A short guide for the interventional cardiologist," *International Journal of Molecular Sciences*, vol. 19, no. 12, 2018.

[159] K. C. Koskinas, Y. S. Chatzizisis, A. P. Antoniadis, and G. D. Giannoglou, "Role of endothelial shear stress in stent restenosis and thrombosis: Pathophysiologic mechanisms and implications for clinical translation," *Journal of the American College of Cardiology*, vol. 59, no. 15, pp. 1337–1349, 2012.

[160] S. Morlacchi, C. Chiastra, D. Gastaldi, G. Pennati, G. Dubini, and F. Migliavacca, "Sequential Structural and Fluid Dynamic Numerical Simulations of a Stented Bifurcated Coronary Artery," *Journal of Biomechanical Engineering*, vol. 133, no. 12, p. 121010, 2011.

[161] D. M. Martin, E. A. Murphy, and F. J. Boyle, "Computational fluid dynamics analysis of balloon-expandable coronary stents: Influence of stent and vessel deformation," *Medical Engineering & Physics*, vol. 36, no. 8, pp. 1047–1056, 2014.

[162] D. Martin and F. Boyle, "Sequential structural and fluid dynamics analysis of balloon-expandable coronary stents: A multivariable statistical analysis," *Cardiovascular Engineering and Technology*, vol. 6, no. 3, pp. 314–328, 2015.

[163] P. D. Morris, J. Iqbal, C. Chiastra, W. Wu, F. Migliavacca, and J. P. Gunn, "Simultaneous kissing stents to treat unprotected left main stem coronary artery bifurcation disease; stent expansion, vessel injury, hemodynamics, tissue healing, restenosis, and repeat revascularization," *Catheterization and Cardiovascular Interventions*, vol. 92, no. 6, pp. E381–E392, 2018.

[164] Łukasz A. Mazurkiewicz, J. Bukała, J. Małachowski, M. Tomaszewski, and P. P. Buszman, "Bvs stent optimisation based on a parametric model with a multistage validation process," *Materials & Design*, vol. 198, p. 109363, 2021.

[165] S. Mcginty, S. Mckee, R. Wadsworth, and C. Mccormick, "Modelling drug-eluting stents," *Mathematical medicine and biology*, vol. 28, no. 1, pp. 1–29, 2010.

[166] P. Zunino, "Multidimensional pharmacokinetic models applied to the design of drug-eluting stents," *Cardiovascular Engineering*, vol. 4, no. 2, pp. 181–191, 2004.

[167] H. Zhao, D. Jayasinghe, S. Hossainy, and L. Schwartz, "A theoretical model to characterize the drug release behavior of drug-eluting stents with durable polymer matrix coating," *Journal of biomedical materials research. Part A*, vol. 100, no. 1, pp. 120–4, 2012.

[168] F. Migliavacca, F. Gervaso, M. Prosi, P. Zunino, S. Minisini, L. Formaggia, and G. Dubini, "Expansion and drug elution model of a coronary stent," *Computer methods in biomechanics and biomedical engineering*, vol. 10, no. 1, pp. 63–73, 2007.

[169] J. Escuer, M. Cebollero, E. Peña, S. McGinty, and M. A. Martínez, "How does stent expansion alter drug transport properties of the arterial wall?," *Journal of the Mechanical Behavior of Biomedical Materials*, vol. 104, p. 103610, 2020.

[170] J. Escuer, A. Schmidt, E. Peña, M. Martínez, and S. Mcginty, "Mathematical modelling of endovascular drug delivery: balloons versus stents," *International Journal of Pharmaceutics*, vol. 620, p. 121742, 2022.

[171] S. Hossainy and S. Prabhu, "A mathematical model for predicting drug release from a biodurable drug-eluting stent coating," *Journal of Biomedical Materials Research Part A*, vol. 87A, no. 2, pp. 487–493, 2008.

[172] C. M. McKittrick, S. McKee, S. Kennedy, K. Oldroyd, M. Wheel, G. Pontrelli, S. Dixon, S. McGinty, and C. McCormick, "Combining mathematical modelling with in vitro experiments to predict in vivo drug-eluting stent performance," *Journal of Controlled Release*, vol. 303, pp. 151–161, 2019.

[173] S. Mcginty, S. Mckee, C. Mccormick, and M. Wheel, "Release mechanism and parameter estimation in drug-eluting stent systems: Analytical solutions of drug release and tissue transport," *Mathematical medicine and biology*, vol. 32, no. 2, pp. 163–186, 2014.

[174] G. Pontrelli, A. D. Mascio, and F. de Monte, "Local mass non-equilibrium dynamics in multi-layered porous media: application to the drug-eluting stent," *International Journal of Heat and Mass Transfer*, vol. 66, pp. 844–854, 2013.

[175] A. Tzafriri and E. Edelman, "Endovascular drug delivery and drug elution systems," *Interventional Cardiology Clinics*, vol. 5, no. 3, pp. 307–320, 2016.

[176] T. T. Vo, S. Morgan, C. McCormick, S. McGinty, S. McKee, and M. Meere, "Modelling drug release from polymer-free coronary stents with microporous surfaces," *International Journal of Pharmaceutics*, vol. 544, no. 2, pp. 392–401, 2018.

[177] S. McGinty, T. T. Vo, M. Meere, S. McKee, and C. McCormick, "Some design considerations for polymer-free drug-eluting stents: A mathematical approach," *Acta Biomaterialia*, vol. 18, pp. 213–225, 2015.

[178] S. Mcginty and G. Pontrelli, "On the role of specific drug binding in modelling arterial eluting stents," *Journal of Mathematical Chemistry*, vol. 54, pp. 967–976, 2016.

[179] N. Artzi, A. Tzafriri, K. Faucher, G. Moodie, T. Albergo, S. Conroy, S. Corbeil, P. Martakos, R. Virmani, and E. Edelman, "Sustained efficacy and arterial drug retention by a fast drug eluting cross-linked fatty acid coronary stent coating," *Annals of biomedical engineering*, vol. 44, no. 2, pp. 276–286, 2016.

[180] S. Prabhu and S. Hossainy, "Modeling of degradation and drug release from a biodegradable stent coating," *Journal of Biomedical Materials Research Part A*, vol. 80A, no. 3, pp. 732–741, 2007.

[181] X. Zhu and R. Braatz, "Modeling and analysis of drug-eluting stents with biodegradable plga coating: Consequences on intravascular drug delivery," *Journal of biomechanical engineering*, vol. 136, no. 11, pp. 1110041–11100410, 2014.

[182] X. Zhu and R. D. Braatz, "A mechanistic model for drug release in plga biodegradable stent coatings coupled with polymer degradation and erosion," *Journal of Biomedical Materials Research Part A*, vol. 103, no. 7, pp. 2269–2279, 2015.

[183] F. Rossi, T. Casalini, E. Raffa, M. Masi, and G. Perale, "Bioresorbable polymer coated drug eluting stent: a model study.," *Molecular pharmaceutics*, vol. 9, no. 7, pp. 1898–910, 2012.

[184] G. Pontrelli and F. de Monte, "A multi-layer porous wall model for coronary drug-eluting stents," *International Journal of Heat and Mass Transfer*, vol. 53, no. 19, pp. 3629–3637, 2010.

[185] J. E. Sousa, M. A. Costa, A. Abizaid, F. Feres, A. C. Seixas, L. F. Tanajura, L. A. Mattos, R. Falotico, J. Jaeger, J. J. Popma, P. W. Serruys, and A. G. Sousa, "Four-year angiographic and intravascular ultrasound follow-up of patients treated with sirolimus-eluting stents," *Circulation*, vol. 111, no. 18, pp. 2326–2329, 2005.

[186] A. Colombo, J. Drzewiecki, A. Banning, E. Grube, K. Hauptmann, S. Silber, D. Dudek, S. Fort, F. Schiele, K. Zmudka, G. Guagliumi, and M. E. Russell, "Randomized study to assess the effectiveness of slow- and moderate-release polymer-based paclitaxel-eluting stents for coronary artery lesions," *Circulation*, vol. 108, no. 7, pp. 788–794, 2003.

[187] P. W. Serruys, G. Sianos, A. Abizaid, J. Aoki, P. den Heijer, H. Bonnier, P. Smits, D. McClean, S. Verheye, J. Belardi, J. Condado, M. Pieper, L. Gambone, M. Bressers, J. Symons, E. Sousa, and F. Litvack, "The effect of variable dose and release kinetics on neointimal hyperplasia using a novel paclitaxel-eluting stent platform," *Journal of the American College of Cardiology*, vol. 46, no. 2, pp. 253–260, 2005.

[188] F. Bozsak, J.-M. Chomaz, and A. Barakat, "Modeling the transport of drugs eluted from stents: Physical phenomena driving drug distribution in the arterial wall," *Biomechanics and modeling in mechanobiology*, vol. 13, no. 2, pp. 327–347, 2014.

[189] F. Bozsak, D. Gonzalez-Rodriguez, Z. Sternberger, P. Belitz, T. Bewley, J.-M. Chomaz, and A. I. Barakat, "Optimization of drug delivery by drug-eluting stents," *PLOS ONE*, vol. 10, no. 6, pp. 1–29, 2015.

[190] G. Pontrelli and F. De Monte, "Modeling of mass dynamics in arterial drug-eluting stents," *Journal of Porous Media*, vol. 12, no. 1, pp. 19–28, 2009.

[191] M. Horner, S. Joshi, V. Dhruva, S. Sett, and S. Stewart, "A two-species drug delivery model is required to predict deposition from drug-eluting stents," *Cardiovascular Engineering and Technology*, vol. 1, no. 3, pp. 225–234, 2010.

[192] J. Abraham, J. Gorman, E. Sparrow, J. Stark, and R. Kohler, "A mass transfer model of temporal drug deposition in artery walls," *International Journal of Heat and Mass Transfer*, vol. 58, no. 1-2, p. 632–638, 2013.

[193] D. Sakharov, L. Kalachev, and D. Rijken, "Numerical simulation of local pharmacokinetics of a drug after intravascular delivery with an eluting stent," *Journal of drug targeting*, vol. 10, no. 6, pp. 507–13, 2002.

[194] A. Tzafriri, A. Levin, and E. Edelman, "Diffusion-limited binding explains binary dose response for local arterial and tumor drug delivery," *Cell proliferation*, vol. 42, no. 3, pp. 348–63, 2009.

[195] T. Vo, W. Lee, A. Peddle, and M. Meere, "Modelling chemistry and biology after implantation of a drug-eluting stent. part i: Drug transport," *Mathematical Biosciences and Engineering*, vol. 14, no. 2, pp. 491–509, 2017.

[196] J. Escuer, I. Aznar, C. McCormick, E. Peña, S. Mcginty, and M. Martínez, "Influence of vessel curvature and plaque composition on drug transport in the arterial wall following drug-eluting stent implantation," *Biomechanics and Modeling in Mechanobiology*, vol. 20, no. 2, pp. 767–786, 2021.

[197] A. D. Levin, N. Vukmirovic, C.-W. Hwang, and E. R. Edelman, "Specific binding to intracellular proteins determines arterial transport properties for rapamycin and paclitaxel," *Proceedings of the National Academy of Sciences*, vol. 101, no. 25, pp. 9463–9467, 2004.

[198] C.-W. Hwang, D. Wu, and E. R. Edelman, "Physiological transport forces govern drug distribution for stent-based delivery," *Circulation*, vol. 104, no. 5, pp. 600–605, 2001.

[199] B. Balakrishnan, J. Dooley, G. Kopia, and E. R. Edelman, "Thrombus causes fluctuations in arterial drug delivery from intravascular stents," *Journal of Controlled Release*, vol. 131, no. 3, pp. 173–180, 2008.

[200] B. Balakrishnan, A. R. Tzafriri, P. Seifert, A. Groothuis, C. Rogers, and E. R. Edelman, "Strut position, blood flow, and drug deposition," *Circulation*, vol. 111, no. 22, pp. 2958–2965, 2005.

[201] T. Seo and A. Barakat, "The assessment of the performance of drug-eluting stent using computational fluid dynamics," *Korea-Australia rheology journal*, vol. 21, no. 4, pp. 281–288, 2009.

[202] G. Vairo, M. Cioffi, R. Cottone, G. Dubini, and F. Migliavacca, "Drug release from coronary eluting stents: A multidomain approach," *Journal of Biomechanics*, vol. 43, no. 8, pp. 1580–1589, 2010.

[203] P. Zunino, C. D'Angelo, L. Petrini, C. Vergara, C. Capelli, and F. Migliavacca, "Numerical simulation of drug eluting coronary stents: Mechanics, fluid dynamics and drug release," *Computer Methods in Applied Mechanics and Engineering*, vol. 198, no. 45, pp. 3633–3644, 2009.

[204] M. Colombo, A. Corti, S. Berceli, F. Migliavacca, S. McGinty, and C. Chiastra, "3d modelling of drug-coated balloons for the treatment of calcified superficial femoral arteries," *PLOS ONE*, vol. 16, no. 10, pp. 1–17, 2021.

[205] A. Caiazzo, D. Evans, J.-L. Falcone, J. Hegewald, E. Lorenz, B. Stahl, D. Wang, J. Bernsdorf, B. Chopard, J. Gunn, D. Hose, M. Krafczyk, P. Lawford, R. Smallwood, D. Walker, and A. Hoekstra, "A complex automata approach for in-stent restenosis: Two-dimensional multiscale modelling and simulations," *J. Comput. Science*, vol. 2, no. 1, pp. 9–17, 2011.

[206] H. Tahir *et al.*, "Multi-scale simulations of the dynamics of in-stent restenosis: impact of stent deployment and design," *Interface Focus*, vol. 1, no. 3, pp. 365–73, 2011.

[207] A. Peddle, T. Vo, and W. Lee, "Modelling chemistry and biology after implantation of a drug-eluting stent. part ii: Cell proliferation," *Mathematical Biosciences and Engineering*, vol. 15, no. 5, pp. 1117–35, 2018.

[208] L. Maes, A.-S. Cloet, I. Fourneau, and N. Famaey, "A homogenized constrained mixture model of restenosis and vascular remodelling after balloon angioplasty," *Journal of The Royal Society Interface*, vol. 18, no. 178, p. 20210068, 2021.

[209] R. S. Schwartz, A. Chu, W. D. Edwards, S. S. Srivatsa, R. D. Simari, J. M. Isner, and D. R. Holmes, "A proliferation analysis of arterial neointimal hyperplasia: lessons for antiproliferative restenosis therapies," *International Journal of Cardiology*, vol. 53, no. 1, pp. 71–80, 1996.

[210] D. J. W. Evans *et al.*, "The application of multiscale modelling to the process of development and prevention of stenosis in a stented coronary artery," *Journal of Royal Society Interface*, vol. 366, no. 1879, pp. 3343–60, 2008.

[211] C. J. Boyle *et al.*, "Computational simulation methodologies for mechanobiological modelling: a cell-centred approach to neointima development in stents," *Philosophical transactions. Series A, A mathematical, physical and engineering sciences*, vol. 368, no. 1921, pp. 2919–935, 2010.

[212] C. J. Boyle, A. B. Lennon, and P. J. Prendergast, "Application of a mechanobiological simulation technique to stents used clinically," *Journal of Biomechanics*, vol. 46, no. 5, pp. 918–24, 2013.

[213] A. Caiazzo *et al.*, "Towards a complex automata multiscale model of in-stent restenosis," in *Computational Science – ICCS 2009*, (Berlin, Heidelberg), pp. 705–714, Springer Berlin Heidelberg, 2009.

[214] H. Zahedmanesh and C. Lally, "Determination of the influence of stent strut thickness using the finite element method: implications for vascular injury and in-stent restenosis," *Medical & biological engineering & computing*, vol. 47, no. 4, pp. 385–93, 2009.

[215] H. Zahedmanesh and C. Lally, "A multiscale mechanobiological modelling framework using agent-based models and finite element analysis: application to vascular tissue engineering," *Biomechanics and Modelig in Mechanobiology*, vol. 11, no. 3-4, pp. 363–77, 2012.

[216] M. Keshavarzian, C. Meyer, and H. Heather, "Mechanobiological model of arterial growth and remodeling," *Biomechanics and Modeling in Mechanobiology*, vol. 17, no. 1, pp. 87–101, 2018.

[217] P. Zun, A. Svitenkov, and A. Hoekstra, "Effects of local coronary blood flow dynamics on the predictions of a model of in-stent restenosis," *Journal of Biomechanics*, vol. 120, p. 110361, 2021.

[218] A. Corti, C. Chiastra, M. Colombo, M. Garbey, F. Migliavacca, and S. Casarin, "A fully coupled computational fluid dynamics - agent-based model of atherosclerotic plaque development: Multiscale modeling framework and parameter sensitivity analysis," *Computers in biology and medicine*, vol. 118, no. 31, p. 103623, 2020.

[219] M. Colombo, Y. He, A. Corti, D. Gallo, F. Ninno, S. Casarin, J. Rozowsky, F. Migliavacca, S. Berceli, and C. Chiastra, "In-stent restenosis progression in human superficial femoral arteries: Dynamics of lumen remodeling and impact of local hemodynamics," *Annals of Biomedical Engineering*, vol. 49, no. 9, pp. 2349–2364, 2021.

[220] S. Chen, H. Zhang, Q. Hou, Y. Zhang, and A. Qiao, "Multiscale modeling of vascular remodeling induced by wall shear stress," *Frontiers in Physiology*, vol. 12, p. 808999, 2022.

[221] J. Jansen, X. Escriva, F. Godeferd, and P. Feugier, "Multiscale bio-chemo-mechanical model of intimal hyperplasia," *Biomechanics and Modeling in Mechanobiology*, vol. 21, no. 4, pp. 1–26, 2022.

[222] E. L. Boland, J. A. Grogan, and P. E. McHugh, "Computational modelling of magnesium stent mechanical performance in a remodelling artery: Effects of multiple remodelling stimuli," *International Journal for Numerical Methods in Biomedical Engineering*, vol. 35, no. 10, p. e3247, 2019.

[223] R. He, L. Zhao, V. Silberschmidt, and Y. Liu, "Mechanistic evaluation of long-term in-stent restenosis based on models of tissue damage and growth," *Biomechanics and Modeling in Mechanobiology*, vol. 19, no. 6, pp. 1425–1446, 2020.

[224] B. Fereidoonnezhad, R. Naghdabadi, S. Sohrabpour, and G. Holzapfel, "A mechanobiological model for damage-induced growth in arterial tissue with application to in-stent restenosis," *Journal of the Mechanics and Physics of Solids*, vol. 101, pp. 311 – 327, 2017.

[225] A. Corti, M. Colombo, F. Migliavacca, J. F. Rodriguez Matas, S. Casarin, and C. Chiastra, "Multiscale computational modeling of vascular adaptation: A systems biology approach using agent-based models," *Frontiers in Bioengineering and Biotechnology*, vol. 9, p. 978, 2021.

[226] A. Corti, M. Colombo, J. M. Rozowsky, S. Casarin, Y. He, D. Carbonaro, F. Migliavacca, J. F. Rodriguez Matas, S. A. Berceli, and C. Chiastra, "A predictive multiscale model of in-stent restenosis in femoral arteries: linking haemodynamics and gene expression with an agent-based model of cellular dynamics," *Journal of The Royal Society Interface*, vol. 19, no. 188, p. 20210871, 2022.

[227] M. Colombo, Y. He, A. Corti, D. Gallo, S. Casarin, J. Rozowsky, F. Migliavacca, S. Berceli, and C. Chiastra, "Baseline local hemodynamics as predictor of lumen remodeling at 1-year follow-up in stented superficial femoral arteries," *Scientific Reports*, vol. 11, no. 1, pp. 1–13, 2021.

[228] M. Cilla, E. Peña, and M. A. Martínez, "Mathematical modelling of atheroma plaque formation and development in coronary arteries," *Journal of The Royal Society Interface*, vol. 11, no. 90, p. 20130866, 2014.

[229] P. Zun *et al.*, "Location-specific comparison between a 3d in-stent restenosis model and micro-ct and histology data from porcine in vivo experiments," *Cardiovascular Engineering and Technology*, vol. 10, no. 4, pp. 568–82, 2019.

[230] M. Gierig, P. Wriggers, and M. Marino, "Computational model of damage-induced growth in soft biological tissues considering the mechanobiology of healing," *Biomechanics and Modeling in Mechanobiology*, vol. 20, no. 4, pp. 297–1315, 2021.

[231] R. A. Byrne, F. Alfonso, S. Schneider, M. Maeng, J. Wiebe, E. Kretov, C. Bradaric, H. Rai, J. Cuesta, F. Rivero, P. Hoppmann, J. Schlichtenmaier, E. H. Christiansen, S. Cassese, M. Joner, H. Schunkert, K.-L. Laugwitz, and A. Kastrati, "Prospective, randomized trial of bioresorbable scaffolds vs. everolimus-eluting stents in patients undergoing coronary stenting for myocardial infarction: the Intracoronary Scaffold Assessment a Randomized evaluation of Absorb in Myocardial Infarction (ISAR-Absorb MI) trial," *European Heart Journal*, vol. 40, no. 2, pp. 167–176, 2018.

[232] P. W. Serruys, M.-C. Morice, A. P. Kappetein, A. Colombo, D. R. Holmes, M. J. Mack, E. Ståhle, T. E. Feldman, M. van den Brand, E. J. Bass, N. Van Dyck, K. Leadley, K. D. Dawkins, and F. W. Mohr, "Percutaneous coronary intervention versus coronary-artery bypass grafting for severe coronary artery disease," *New England Journal of Medicine*, vol. 360, no. 10, pp. 961–972, 2009.

[233] A. R. Tzafriri, N. Vukmirovic, V. B. Kolachalama, I. Astafieva, and E. R. Edelman, "Lesion complexity determines arterial drug distribution after local drug delivery," *Journal of Controlled Release*, vol. 142, no. 3, pp. 332–338, 2010.

[234] C. Chiastra, W. Wu, B. Dickerhoff, A. Aleiou, G. Dubini, H. Otake, F. Migliavacca, and J. F. LaDisa, "Computational replication of the patient-specific stenting procedure for coronary artery bifurcations: From oct and ct imaging to structural and hemodynamics analyses," *Journal of Biomechanics*, vol. 49, no. 11, pp. 2102–2111, 2016.

[235] C. Chiastra, S. Migliori, F. Burzotta, G. Dubini, and F. Migliavacca, "Patient-specific modeling of stented coronary arteries reconstructed from optical coherence tomography: Towards a widespread clinical use of fluid dynamics analyses," *Journal of Cardiovascular Translational Research*, vol. 11, no. 2, pp. 156–72, 2018.

[236] E. H and C. M. A. J., "Mathematical modeling of tumor growth and treatment," *Current Pharmaceutical Design*, vol. 20, no. 30, pp. 4934–4940, 2014.

[237] R. B, H. NH, M. P, and others., "A review of mixed-effects models of tumour growth and effects of anticancer drug treatment used in population analysis," *CPT Pharmacometrics Syst Pharmacol*, vol. 3, no. 5, p. e113, 2014.

[238] A. M. Jarrett, E. A. Lima, D. A. H. II, M. T. McKenna, X. Feng, D. A. Ekrut, A. C. M. Resende, A. Brock, and T. E. Yankeelov, "Mathematical models of tumor cell proliferation: A review of the literature," *Expert Review of Anticancer Therapy*, vol. 18, no. 12, pp. 1271–1286, 2018.

[239] E. Pasquier, M. Carré, B. Pourroy, L. Camoin, O. Rebaï, C. Briand, and D. Braguer, "Antiangiogenic activity of paclitaxel is associated with its cytostatic effect, mediated by the initiation but not completion of a mitochondrial apoptotic signaling pathway," *Molecular Cancer Therapeutics*, vol. 3, no. 10, pp. 1301–1310, 2004.

[240] M. V. Blagosklonny, Z. N. Demidenko, M. Giovino, C. Szynal, E. Donskoy, R. A. Herrmann, J. J. Barry, and A. M. Whalen, "Cytostatic activity of paclitaxel in coronary artery smooth muscle cells is mediated through transient mitotic arrest followed by permanent post-mitotic arrest: Comparison with cancer cells," *Cell Cycle*, vol. 5, no. 14, pp. 1574–1579, 2006.

[241] J. Li, S.-G. Kim, and J. Blenis, "Rapamycin: One drug, many effects," *Cell metabolism*, vol. 19, no. 3, pp. 373–379, 2014.

[242] R. Roe-Dale, D. Isaacson, and M. Kupferschmid, "A mathematical model of breast cancer treatment with cmf and doxorubicin," *Bulletin of Mathematical Biology*, vol. 73, no. 3, pp. 585–608, 2011.

[243] N. Frances, L. Claret, R. Bruno, *et al.*, "Tumor growth modeling from clinical trials reveals synergistic anticancer effect of the capecitabine and docetaxel combination in metastatic breast cancer," *Cancer Chemother Pharmacol*, vol. 68, no. 6, p. 1413–1419, 2011.

[244] A. Stein, W. Wang, A. Carter, O. Chiparus, N. Hollaender, H. Kim, R. Motzer, and C. Sarr, "Dynamic tumor modeling of the dose–response relationship for everolimus in metastatic renal cell carcinoma using data from the phase 3 record-1 trial," *BMC cancer*, vol. 12, p. 311, 2012.

[245] J. C. Panetta, "A mathematical model of breast and ovarian cancer treated with paclitaxel," *Mathematical Biosciences*, vol. 146, no. 2, pp. 89 – 113, 1997.

[246] F. Del Bene, M. Germani, G. De Nicolao, P. Magni, C. E. Re, D. Ballinari, and M. Rocchetti, "A model-based approach to the in vitro evaluation of anticancer activity," *Cancer Chemotherapy and Pharmacology*, vol. 63, no. 5, pp. 827–836, 2009.

[247] S. Stein, R. Zhao, H. Haeno, I. Vivanco, and F. Michor, "Mathematical modeling identifies optimum lapatinib dosing schedules for the treatment of glioblastoma patients," *PLOS Computational Biology*, vol. 14, no. 1, pp. 1–24, 2018.

[248] S. Benzekry, G. Chapuisat, J. Ciccolini, A. Erlinger, and F. Hubert, "A new mathematical model for optimizing the combination between antiangiogenic and cytotoxic drugs in oncology," *Comptes Rendus Mathematique*, vol. 350, no. 1, pp. 23 – 28, 2012.

[249] A. McQueen, J. Escuer, A. Aggarwal, S. Kennedy, C. Mccormick, K. Oldroyd, and S. Mcginty, "Do we really understand how drug eluted from stents modulates arterial healing?," *International Journal of Pharmaceutics*, vol. 601, p. 120575, 04 2021.

[250] V. Busini, P. Arosio, and M. Masi, "Mechanistic modelling of avascular tumor growth and pharmacokinetics influence—part i," *Chemical Engineering Science*, vol. 62, no. 7, pp. 1877–1886, 2007.

[251] M. V. Blagosklonny *et al.*, "Paclitaxel induces primary and postmitotic g1 arrest in human arterial smooth muscle cells," *Cell Cycle*, vol. 3, no. 8, pp. 1050–56, 2004.

[252] K. L. Rock and H. Kono, "The inflammatory response to cell death," *Annual Review of Pathology: Mechanisms of Disease*, vol. 3, no. 1, pp. 99–126, 2008.

[253] E. M. Rzucidlo, K. A. Martin, and R. J. Powell, "Regulation of vascular smooth muscle cell differentiation," *Journal of Vascular Surgery*, vol. 45, no. 6, Supplement, pp. A25–A32, 2007.

[254] K. A. Martin, E. M. Rzucidlo, B. L. Merenick, D. C. Fingar, D. J. Brown, R. J. Wagner, and R. J. Powell, "The mtor/p70 s6k1 pathway regulates vascular smooth muscle cell differentiation," *American Journal of Physiology-Cell Physiology*, vol. 286, no. 3, pp. C507–C517, 2004.

[255] K. A. Martin, B. L. Merenick, M. Ding, K. M. Fetalvero, E. M. Rzucidlo, C. D. Kozul, D. J. Brown, H. Y. Chiu, M. Shyu, B. L. Drapeau, R. J. Wagner, and R. J. Powell, "Rapamycin promotes vascular smooth muscle cell differentiation through insulin receptor substrate-1/phosphatidylinositol 3-kinase/akt2 feedback signaling*," *Journal of Biological Chemistry*, vol. 282, no. 49, pp. 36112–36120, 2007.

[256] S. O. Marx, T. Jayaraman, L. O. Go, and A. R. Marks, "Rapamycin-fkbp inhibits cell cycle regulators of proliferation in vascular smooth muscle cells," *Circulation Research*, vol. 76, no. 3, pp. 412–417, 1995.

[257] D. I. Axel, W. Kunert, C. Göggelmann, M. Oberhoff, C. Herdeg, A. Küttner, D. H. Wild, B. R. Brehm, R. Riessen, G. Köveker, and K. R. Karsch, "Paclitaxel inhibits arterial smooth muscle cell proliferation and migration in vitro and in vivo using local drug delivery," *Circulation*, vol. 96, no. 2, pp. 636–645, 1997.

[258] R. Wessely, A. Schomig, and A. Kastrati, "Sirolimus and paclitaxel on polymer-based drug-eluting stents," *Journal of the American College of Cardiology*, vol. 47, no. 4, pp. 708–714, 2006.

[259] J. Wiskirchen, W. Schöber, N. Schart, R. Kehlbach, A. Wersebe, G. Tepe, C. Claussen, and S. Duda, "The effects of paclitaxel on the three phases of restenosis: smooth muscle cell proliferation, migration, and matrix formation: an in vitro study," *Investigative radiology*, vol. 39, no. 9, pp. 565–71, 2004.

[260] R. Gallo, A. Padurean, T. Jayaraman, S. Marx, M. Roque, S. Adelman, J. Chesebro, J. Fallon, V. Fuster, A. Marks, and J. J. Badimon, "Inhibition of intimal thickening after balloon angioplasty in porcine coronary arteries by targeting regulators of the cell cycle," *Circulation*, vol. 99, no. 16, pp. 2164–2170, 1999.

[261] M. A. Shah and G. K. Schwartz, "Cell cycle-mediated drug resistance," *Clinical Cancer Research*, vol. 7, no. 8, pp. 2168–2181, 2001.

[262] W. Li, Q. Li, L. Qin, R. Ali, Y. Qyang, M. Tassabehji, B. R. Pober, W. C. Sessa, F. J. Giordano, and G. Tellides, "Rapamycin inhibits smooth muscle cell proliferation and obstructive arteriopathy attributable to elastin deficiency," *Arteriosclerosis, Thrombosis, and Vascular Biology*, vol. 33, no. 5, pp. 1028–1035, 2013.

[263] D. Rosner, N. McCarthy, and M. Bennett, "Rapamycin inhibits human in stent restenosis vascular smooth muscle cells independently of pRB phosphorylation and p53," *Cardiovascular Research*, vol. 66, no. 3, pp. 601–610, 2005.

[264] G. Fedele, S. Castiglioni, J. A. Maier, and L. Locatelli, "High magnesium and sirolimus on rabbit vascular cells—an in vitro proof of concept," *Materials*, vol. 14, no. 8, 2021.

[265] R. Voisard, S. Zellmann, F. Müller, F. Fahlisch, L. von Müller, R. Baur, J. Braun, J. Gschwendt, M. Kountides, V. Hombach, and J. Kamenz, "Sirolimus inhibits key events of restenosis in vitro/ex vivo: Evaluation of the clinical relevance of the data by si/mpl- and si/des-ratio's," *BMC cardiovascular disorders*, vol. 7, p. 15, 2007.

[266] M. Lavigne, J. Grimsby, and M. Eppihimer, "Antirestenotic mechanisms of everolimus on human coronary artery smooth muscle cells," *Journal of cardiovascular pharmacology*, vol. 59, no. 2, pp. 165–74, 2012.

[267] Y.-W. Chen, M. Smith, M. Sheets, S. Ballaron, J. Trevillyan, S. Burke, T. Rosenberg, C. Henry, R. Wagner, J. Bauch, K. Marsh, T. Fey, G. Hsieh, D. Gauvin, K. Mollison, G. Carter, and S. Djuric, "Zotarolimus, a novel sirolimus analogue with potent anti-proliferative activity on coronary smooth muscle cells and reduced potential for systemic immunosuppression," *Journal of cardiovascular pharmacology*, vol. 49, no. 4, pp. 228–35, 2007.

[268] Y. Kim, J. Park, J.-H. Seo, H.-S. Ryu, K. Lim, M. Jeong, D. Kang, and S. Kang, "A rapamycin derivative, biolimus, preferentially activates autophagy in vascular smooth muscle cells," *Scientific Reports*, vol. 8, no. 1, p. 16551, 2018.

[269] D. E. Marra, T. Simoncini, and J. K. Liao, "Inhibition of vascular smooth muscle cell proliferation by sodium salicylate mediated by upregulation of $p21_{Waf1}$ and $p27_{Kip1}$," *Circulation*, vol. 102, no. 17, pp. 2124–2130, 2000.

[270] W. Sun, Y. Huang, T. Yin, J. Wang, R. Du, J. Qiu, Y. Zhang, Y. Wang, J. Chen, and G. Wang, "Effects of elemene on inhibiting proliferation of vascular smooth muscle cells and promoting reendothelialization at the stent implantation site," *Biomater. Sci.*, vol. 5, no. 6, pp. 1144–1155, 2017.

[271] W. Zhu, T. Masaki, A. Cheung, and S. Kern, "In-vitro release of rapamycin from a thermosensitive polymer for the inhibition of vascular smooth muscle cell proliferation," *Journal of bioequivalence & bioavailability*, vol. 1, pp. 3–12, 2009.

[272] R. Jabara, N. Chronos, and K. Robinson, "Novel bioabsorbable salicylate-based polymer as a drug-eluting stent coating," *Catheterization and cardiovascular interventions : official journal of the Society for Cardiac Angiography & Interventions*, vol. 72, no. 2, pp. 186–94, 2008.

[273] C. Lee, Y. Lin, Y. Tung, *et al.*, "Local sustained delivery of acetylsalicylic acid via hybrid stent with biodegradable nanofibers reduces adhesion of blood cells and promotes reendothelialization of the denuded artery," *International journal of nanomedicine*, vol. 9, pp. 311–26, 2014.

[274] K. Cysewska, J. Karczewski, and P. Jasiński, "Influence of the electrosynthesis conditions on the spontaneous release of anti-inflammatory salicylate during degradation of polypyrrole coated iron for biodegradable cardiovascular stent," *Electrochimica Acta*, vol. 320, p. 134612, 2019.

[275] R. S. Schwartz, A. Chu, W. D. Edwards, S. S. Srivatsa, R. D. Simari, J. M. Isner, and D. R. Holmes, "A proliferation analysis of arterial neointimal hyperplasia: lessons for antiproliferative restenosis therapies," *International Journal of Cardiology*, vol. 53, no. 1, pp. 71 – 80, 1996.

[276] W. Jin, E. Shah, C. Penington, S. McCue, P. Maini, and M. Simpson, "Logistic proliferation of cells in scratch assays is delayed," *Bulletin of Mathematical Biology*, vol. 79, no. 5, pp. 028–1050, 2017.

[277] S. N. Gardner, "A mechanistic, predictive model of dose-response curves for cell cycle phase-specific and -nonspecific drugs," *Cancer Research*, vol. 60, no. 5, pp. 1417–1425, 2000.

[278] L.-S. Tham, L. Wang, R. A. Soo, S.-C. Lee, H.-S. Lee, W.-P. Yong, B.-C. Goh, and N. H. Holford, "A pharmacodynamic model for the time course of tumor shrinkage by gemcitabine + carboplatin in non–small cell lung cancer patients," *Clinical Cancer Research*, vol. 14, no. 13, pp. 4213–4218, 2008.

[279] S. Goutelle, M. Maurin, F. Rougier, X. Barbaut, L. Bourguignon, M. Ducher, and P. Maire, "The hill equation: A review of its capabilities in pharmacological modelling," *Fundamental & clinical pharmacology*, vol. 22, no. 6, pp. 633–48, 2009.

[280] Clairambault, J., "Modelling physiological and pharmacological control on cell proliferation to optimise cancer treatments," *Mathematical Modelling of Natural Phenomena*, vol. 4, no. 3, pp. 12–67, 2009.

[281] F. Clarelli, J. Liang, A. Martinecz, I. Heiland, and P. Abel zur Wiesch, "Multi-scale modeling of drug binding kinetics to predict drug efficacy," *Cellular and Molecular Life Sciences CMLS*, vol. 77, no. 3, pp. 381–94, 2020.

[282] "Live Cell Imaging of Cell Cycle and Division thermo fisher." `https://www.thermofisher.com/uk/en/home/life-science/cell-analysis/cell-viability-and-regulation/cell-cycle/live-cell-imaging-of-cell-cycle-and-division.html`. Accessed: 2022-02-04.

[283] D. Charlebois and G. Balázsi, "Modeling cell population dynamics," *In Silico Biology*, vol. 13, no. 1-2, pp. 21–39, 2019.

[284] S. T. Vittadello, S. W. McCue, G. Gunasingh, N. K. Haass, and M. J. Simpson, "Mathematical models incorporating a multi-stage cell cycle replicate normally-hidden inherent synchronization in cell proliferation," *Journal of The Royal Society Interface*, vol. 16, no. 157, p. 20190382, 2019.

[285] S. Vittadello, S. McCue, G. Gunasingh, N. Haass, and M. Simpson, "Mathematical models for cell migration with real-time cell cycle dynamics," *Biophysical Journal*, vol. 114, no. 5, p. 1241–1253, 2018.

[286] S. T. Vittadello, S. W. McCue, G. Gunasingh, N. K. Haass, and M. J. Simpson, "Examining go-or-grow using fluorescent cell-cycle indicators and cell-cycle-inhibiting drugs," *Biophysical Journal*, vol. 118, no. 6, pp. 1243–1247, 2020.

[287] K. A. Beaumont, D. S. Hill, S. M. Daignault, G. Y. Lui, D. M. Sharp, B. Gabrielli, W. Weninger, and N. K. Haass, "Cell cycle phase-specific drug resistance as an escape mechanism of melanoma cells," *Journal of Investigative Dermatology*, vol. 136, no. 7, pp. 1479–1489, 2016.

[288] N. K. Haass and B. Gabrielli, "Cell cycle-tailored targeting of metastatic melanoma: Challenges and opportunities," *Experimental Dermatology*, vol. 26, no. 7, pp. 649–655, 2017.

[289] N. T. Ingolia and A. W. Murray, "The ups and downs of modeling the cell cycle," *Current Biology*, vol. 14, no. 18, pp. R771–R777, 2004.

[290] H. Fuss, W. Dubitzky, C. Downes, and M. J. Kurth, "Mathematical models of cell cycle regulation," *Briefings in bioinformatics*, vol. 6, no. 2, pp. 163–77, 2005.

[291] J. Ferrell, T. Tsai, and Q. Yang, "Modeling the cell cycle: Why do certain circuits oscillate?," *Cell*, vol. 144, no. 6, pp. 874–85, 2011.

[292] M. Barberis, R. Todd, and L. van der Zee, "Advances and challenges in logical modeling of cell cycle regulation: perspective for multi-scale, integrative yeast cell models," *FEMS yeast research*, vol. 17, no. 1, 2016.

[293] "Useful Numbers for Cell Culture thermo fisher." `https://www.thermofisher.com/uk/en/home/references/gibco-cell-culture-basics/cell-culture-protocols/cell-culture-useful-numbers.html`. Accessed: 2020-12-12.

[294] R. Venkatasubramanian, M. A. Henson, and N. S. Forbes, "Integrating cell-cycle progression, drug penetration and energy metabolism to identify improved cancer therapeutic strategies.," *Journal of theoretical biology*, vol. 253, no. 1, pp. 98–117, 2008.

[295] S. Baez, "Vascular smooth muscle: Quantitation of cell thickness in the wall of arterioles in the living animal in situ," *Science*, vol. 159, no. 3814, pp. 536–538, 1968.

[296] M. Poon, S. O. Marx, R. Gallo, J. J. Badimon, M. B. Taubman, and A. R. Marks, "Rapamycin inhibits vascular smooth muscle cell migration.," *The Journal of Clinical Investigation*, vol. 98, no. 10, pp. 2277–2283, 1996.

[297] O. V. Leontieva, Z. N. Demidenko, and M. V. Blagosklonny, "Contact inhibition and high cell density deactivate the mammalian target of rapamycin pathway, thus suppressing the senescence program," *Proceedings of the National Academy of Sciences*, vol. 111, no. 24, pp. 8832–8837, 2014.

[298] M. Blagosklonny, "Geroconversion: Irreversible step to cellular senescence," *Cell cycle*, vol. 13, no. 23, pp. 3628–35, 2014.

[299] A. Ducrot, F. Le Foll, P. Magal, H. Murakawa, J. Pasquier, and G. Webb, "An in vitro cell population dynamics model incorporating cell size, quiescence, and contact inhibition," *Mathematical Models and Methods in Applied Sciences*, vol. 21, pp. 871–892, 2011.

[300] N. J. Armstrong, K. J. Painter, and J. A. Sherratt, "A continuum approach to modelling cell–cell adhesion," *Journal of Theoretical Biology*, vol. 243, no. 1, pp. 98–113, 2006.

[301] N. J. Armstrong, K. J. Painter, and J. A. Sherratt, "Adding adhesion to a chemical signaling model for somite formation," *Bulletin of Mathematical Biology*, vol. 71, no. 1, pp. 1–24, 2009.

[302] J. Dyson, S. A. Gourley, R. Villella-Bressan, and G. F. Webb, "Existence and asymptotic properties of solutions of a nonlocal evolution equation modeling cell-cell adhesion," *SIAM Journal on Mathematical Analysis*, vol. 42, no. 4, pp. 1784–1804, 2010.

[303] X. Miao, G. Koch, S. Ait-Oudhia, R. M. Straubinger, and W. J. Jusko, "Pharmacodynamic modeling of cell cycle effects for gemcitabine and trabectedin combinations in pancreatic cancer cells," *Frontiers in Pharmacology*, vol. 7, 2016.

[304] C. Lally and P. J. Prendergast, *Simulation of In-stent Restenosis for the Design of Cardiovascular Stents*, pp. 255–267. Berlin, Heidelberg: Springer Berlin Heidelberg, 2006.

[305] A. Corti, S. Casarin, C. Chiastra, M. Colombo, F. Migliavacca, and M. Garbey, "A multiscale model of atherosclerotic plaque development: Toward a coupling between an agent-based model and cfd simulations," in *Computational Science – ICCS 2019* (J. M. F. Rodrigues, P. J. S. Cardoso, J. Monteiro, R. Lam, V. V. Krzhizhanovskaya, M. H. Lees, J. J. Dongarra, and P. M. Sloot, eds.), pp. 410–423, 2019.

[306] A. Corti, M. Colombo, F. Migliavacca, S. A. Berceli, S. Casarin, J. F. Rodriguez Matas, and C. Chiastra, "Multiscale agent-based modeling of restenosis after percutaneous transluminal angioplasty: Effects of tissue damage and hemodynamics on cellular activity," *Computers in Biology and Medicine*, vol. 147, p. 105753, 2022.

[307] R. Mongrain, R. Leask, J. Brunette, I. Faik, N. Bulman-Feleming, and T. Nguyen, "Numerical modeling of coronary drug eluting stents," *Studies in health technology and informatics*, vol. 113, pp. 443–58, 2005.

[308] G. G. Stefanini, M. Taniwaki, and S. Windecker, "Coronary stents: novel developments," *Heart*, vol. 100, no. 13, pp. 1051–1061, 2014.

[309] R. Byrne, G. Stone, J. Ormiston, and A. Kastrati, "Coronary balloon angioplasty, stents, and scaffolds," *The Lancet*, vol. 390, no. 10096, pp. 781–792, 2017.

[310] S. Cassese, A. Lahmann, and M. Joner, "Ultrathin strut biodegradable-polymer sirolimus-eluting stents: Being wary or going with the flow?," *Journal of Thoracic Disease*, vol. 10, no. 2, pp. 688–692, 2018.

[311] T. E. Carew, R. N. Vaishnav, and D. J. Patel, "Compressibility of the arterial wall," *Circulation Research*, vol. 23, no. 1, pp. 61–68, 1968.

[312] X. Girerd, C. Acar, J.-J. Mourad, P. Boutouyrie, M. E. Safar, and S. Laurentt, "Incompressibility of the human arterial wall: an in vitro ultrasound study," *Journal of Hypertension*, vol. 10, no. 6, p. S111–S114, 1992.

[313] P. Skacel and J. Bursa, "Compressibility of arterial wall – direct measurement and predictions of compressible constitutive models," *Journal of the Mechanical Behavior of Biomedical Materials*, vol. 90, pp. 538–546, 2019.

[314] G. A. Holzapfel, G. Sommer, C. T. Gasser, and P. Regitnig, "Determination of layer-specific mechanical properties of human coronary arteries with nonatherosclerotic intimal thickening and related constitutive modeling," *American Journal of Physiology-Heart and Circulatory Physiology*, vol. 289, no. 5, pp. H2048–H2058, 2005.

[315] T. C. Gasser, R. W. Ogden, and G. A. Holzapfel, "Hyperelastic modelling of arterial layers with distributed collagen fibre orientations," *Journal of The Royal Society Interface*, vol. 3, no. 6, pp. 15–35, 2006.

[316] G. Holzapfel, T. Gasser, and R. Ogden, "A new constitutive framework for arterial wall mechanics and a comparative study of material models," *Journal of Elasticity*, vol. 61, no. 1, pp. 1–48, 2000.

[317] L. Wang, S. Roper, N. Hill, and X. Luo, "Propagation of dissection in a residually-stressed artery model," *Biomechanics and Modeling in Mechanobiology*, vol. 16, no. 1, pp. 139–19, 2016.

[318] G. A. Holzapfel, R. W. Ogden, and S. Sherifova, "On fibre dispersion modelling of soft biological tissues: a review," *Proceedings of the Royal Society A: Mathematical, Physical and Engineering Sciences*, vol. 475, no. 2224, p. 20180736, 2019.

[319] M. Tittelbach and T. Diener, "Orsiro – the first hybrid drug-eluting stent, opening up a new class of drug-eluting stents for superior patient outcomes," *Interventional Cardiology Review*, vol. 6, no. 2, p. 142, 2011.

[320] A. Schiavone, L. G. Zhao, and A. A. Abdel-Wahab, "Dynamic simulation of stent deployment – effects of design, material and coating," *Journal of Physics: Conference Series*, vol. 451, p. 012032, 2013.

[321] C. Hopkins, P. Mchugh, and P. Mcgarry, "Computational investigation of the delamination of polymer coatings during stent deployment," *Annals of biomedical engineering*, vol. 38, no. 7, pp. 2263–73, 2010.

[322] C. Conway, F. R. Nezami, C. Rogers, A. Groothuis, J. C. Squire, and E. R. Edelman, "Acute stent-induced endothelial denudation: Biomechanical predictors of vascular injury," *Frontiers in Cardiovascular Medicine*, vol. 8, p. 733605, 2021.

[323] J. Jukema, J. Verschuren, T. Ahmed, and P. Quax, "Restenosis after pci. part 1: Pathophysiology and risk factors," *Nature reviews. Cardiology*, vol. 9, no. 1, pp. 53–62, 2011.

[324] A. I. Barakat, "Blood flow and arterial endothelial dysfunction: Mechanisms and implications," *Comptes Rendus Physique*, vol. 14, no. 6, pp. 479–496, 2013.

[325] P. Petsophonsakul, M. Furmanik, R. Forsythe, M. Dweck, G. W. Schurink, E. Natour, C. Reutelingsperger, M. Jacobs, B. Mees, and L. Schurgers, "Role of vascular smooth muscle cell phenotypic switching and calcification in aortic aneurysm formation," *Arteriosclerosis, Thrombosis, and Vascular Biology*, vol. 39, no. 7, pp. 1351–1368, 2019.

[326] J. Thyberg, K. Blomgren, J. Roy, P. K. Tran, and U. Hedin, "Phenotypic modulation of smooth muscle cells after arterial injury is associated with changes in the distribution of laminin and fibronectin," *Journal of Histochemistry & Cytochemistry*, vol. 45, no. 6, pp. 837–846, 1997.

[327] W. Casscells, "Migration of smooth muscle and endothelial cells. critical events in restenosis.," *Circulation*, vol. 86, no. 3, pp. 723–729, 1992.

[328] J. S. Forrester, M. Fishbein, R. Helfant, and J. Fagin, "A paradigm for restenosis based on cell biology: Clues for the development of new preventive therapies," *Journal of the American College of Cardiology*, vol. 17, no. 3, pp. 758–769, 1991.

[329] C. Schulz, R. A. Herrmann, C. Beilharz, J. Pasquantonio, and E. Alt, "Coronary stent symmetry and vascular injury determine experimental restenosis," *Heart*, vol. 83, no. 4, pp. 462–467, 2000.

[330] K. M. Katsaros, S. P. Kastl, G. Zorn, G. Maurer, J. Wojta, K. Huber, G. Christ, and W. S. Speidl, "Increased restenosis rate after implantation of drug-eluting stents in patients with elevated serum activity of matrix metalloproteinase-2 and -9," *JACC: Cardiovascular Interventions*, vol. 3, no. 1, pp. 90–97, 2010.

[331] B. S. Zuckerbraun *et al.*, "Nitric oxide-induced inhibition of smooth muscle cell proliferation involves s-nitrosation and inactivation of rhoa," *American Journal of Physiology. Cell physiology*, vol. 292, no. 2, pp. 824–31, 2007.

[332] R. S. Paula Budu-Grajdeanu *et al.*, "A mathematical model of venous neointimal hyperplasia formation," *Theoretical Biology and Medical Modelling*, vol. 5, no. 2, 2008.

[333] J. McLaren, A. Prentice, D. Charnock-Jones, and S. Smith, "Vascular endothelial growth factor (vegf) concentrations are elevated in peritoneal fluid of women with endometriosis," *Human reproduction (Oxford, England)*, vol. 11, no. 1, pp. 220–3, 1996.

[334] P. Saez, E. Peña, M. Martínez, and E. Kuhl, "Mathematical modeling of collagen turnover in biological tissue," *Journal of mathematical biology*, vol. 67, pp. 1765–93, 11 2012.

[335] R. Tracy, "Declining density of intimal smooth muscle cells as a precondition for atheronecrosis in the coronary artery," *Virchows Archiv : an international journal of pathology*, vol. 430, no. 2, pp. 155–62, 1997.

[336] M. Nicolás, E. Peña, M. Malvè, and M. Martínez, "Mathematical modeling of the fibrosis process in the implantation of inferior vena cava filters," *Journal of Theoretical Biology*, vol. 387, pp. 228–240, 2015.

[337] M. Farcas, L. Rouleau, R. Fraser, and R. Leask, "The development of 3-d, in vitro, endothelial culture models for the study of coronary artery disease," *Biomedical engineering online*, vol. 8, p. 30, 2009.

[338] K. Garikipati, "A continuum treatment of growth in biological tissue: the coupling of mass transport and mechanics," *Journal of the Mechanics and Physics of Solids*, vol. 52, no. 7, pp. 1595–1625, 2004.

[339] A. Kastrati, J. Mehilli, J. Dirschinger, F. Dotzer, H. Schühlen, F.-J. Neumann, M. Fleckenstein, C. Pfafferott, M. Seyfarth, and A. Schömig, "Intracoronary stenting and angiographic results," *Circulation*, vol. 103, no. 23, pp. 2816–2821, 2001.

[340] A. Saito, Z. Dai, M. Ono, T. Kanie, Y. Takaoka, A. Mizuno, N. Komiyama, and T. Asano, "The relationship between coronary stent strut thickness and the incidences of clinical outcomes after drug-eluting stent implantation: A systematic review and meta-regression analysis," *Catheterization and Cardiovascular Interventions*, vol. 99, no. 3, pp. 575–582, 2022.

[341] M. Iantorno, M. J. Lipinski, H. M. Garcia-Garcia, B. J. Forrestal, T. Rogers, D. Gajanana, K. D. Buchanan, R. Torguson, W. S. Weintraub, and R. Waksman, "Meta-analysis of the impact of strut thickness on outcomes in patients with drug-eluting stents in a coronary artery," *The American Journal of Cardiology*, vol. 122, no. 10, pp. 1652–1660, 2018.

[342] A. Sakamoto, H. Jinnouchi, S. Torii, R. Virmani, and A. Finn, "Understanding the impact of stent and scaffold material and strut design on coronary artery thrombosis from the basic and clinical points of view," *Bioengineering*, vol. 5, no. 3, p. 71, 2018.

[343] Y. He, N. Duraiswamy, A. O. Frank, and J. Moore, James E., "Blood Flow in Stented Arteries: A Parametric Comparison of Strut Design Patterns in Three Dimensions," *Journal of Biomechanical Engineering*, vol. 127, no. 4, pp. 637–647, 2005.

[344] A. K. Hassan, S. C. Bergheanu, T. Stijnen, B. L. van der Hoeven, J. D. Snoep, J. W. Plevier, M. J. Schalij, and J. Wouter Jukema, "Late stent malapposition risk is higher after drug-eluting stent compared with bare-metal stent implantation and associates with late stent thrombosis," *European Heart Journal*, vol. 31, no. 10, pp. 1172–1180, 2010.

[345] P. H. Groves, A. P. Banning, W. J. Penny, M. J. Lewis, H. A. Cheadle, and A. C. Newby, "Kinetics of smooth muscle cell proliferation and intimal thickening in a pig carotid model of balloon injury," *Atherosclerosis*, vol. 117, no. 1, pp. 83–96, 1995.

[346] Y. Shi *et al.*, "Adventitial myofibroblasts contribute to neointimal formation in injured porcine coronary arteries," *Circulation*, vol. 94, no. 7, pp. 1655–664, 1996.

[347] A. Giudici and B. Spronck, "The role of layer-specific residual stresses in arterial mechanics: Analysis via a novel modelling framework," *Artery Research*, vol. 28, no. 1, pp. 41–54, 2022.

[348] H. D. Leon, J. D. Ollerenshaw, K. K. Griendling, and J. N. Wilcox, "Adventitial cells do not contribute to neointimal mass after balloon angioplasty of the rat common carotid artery," *Circulation*, vol. 104, no. 14, pp. 1591–1593, 2001.

[349] A. C. Doran, N. Meller, and C. A. McNamara, "Role of smooth muscle cells in the initiation and early progression of atherosclerosis," *Arteriosclerosis, Thrombosis, and Vascular Biology*, vol. 28, no. 5, pp. 812–819, 2008.

[350] M. R. Bennett, S. Sinha, and G. K. Owens, "Vascular smooth muscle cells in atherosclerosis," *Circulation Research*, vol. 118, no. 4, pp. 692–702, 2016.

[351] F. Gijsen, Y. Katagiri, P. Barlis, C. Bourantas, C. Collet, U. Coskun, J. Daemen, J. Dijkstra, E. Edelman, P. Evans, K. Van der Heiden, R. Hose, B.-K. Koo, R. Krams, A. Marsden, F. Migliavacca, Y. Onuma, A. Ooi, E. Poon, and P. Serruys, "Expert recommendations on the assessment of wall shear stress in human coronary arteries: Existing methodologies, technical considerations, and clinical applications," *European heart journal*, vol. 40, no. 41, pp. 3421–33, 2019.

[352] P. Davies, "Hemodynamic shear stress and the endothelium in cardiovascular pathophysiology," *Nature clinical practice. Cardiovascular medicine*, vol. 6, no. 1, pp. 16–26, 2009.

[353] R. Byrne, M. Joner, and A. Kastrati, "Stent thrombosis and restenosis: What have we learned and where are we going? the andreas grüntzig lecture esc 2014," *European Heart Journal*, vol. 36, no. 47, pp. 3320–31, 2015.

[354] D. Zohlnhöfer, C. A. Klein, T. Richter, R. Brandl, A. Murr, T. Nührenberg, A. Schömig, P. A. Baeuerle, and F.-J. Neumann, "Gene expression profiling of human stent-induced neointima by cdna array analysis of microscopic specimens retrieved by helix cutter atherectomy," *Circulation*, vol. 103, no. 10, pp. 1396–1402, 2001.

[355] G. Bauriedel, A. Jabs, D. Skowasch, R. Hutter, J. J. Badimón, V. Fuster, U. Welsch, and B. Lüderitz, "Dendritic cells in neointima formation after rat carotid balloon injury: coordinated expression withanti-apoptotic bcl-2 and hsp47 in arterial repair.," *Journal of the American College of Cardiology*, vol. 42, no. 5, pp. 930–8, 2003.

[356] A. Lansky, W. Wijns, *et al.*, "Targeted therapy with a localised abluminal groove, low-dose sirolimus-eluting, biodegradable polymer coronary stent (target all comers): a multicentre, open-label, randomised non-inferiority trial," *The Lancet*, vol. 392, no. 10153, pp. 1117–26, 2018.

[357] W. J. van der Giessen, O. Sorop, P. W. Serruys, I. Peters-Krabbendam, and H. M. van Beusekom, "Lowering the dose of sirolimus, released from a nonpolymeric hydroxyapatite coated coronary stent, reduces signs of delayed healing," *JACC: Cardiovascular Interventions*, vol. 2, no. 4, pp. 284–290, 2009.

[358] C. Calderas, J. F. Condado, J. A. Condado, A. Flores, A. Mueller, J. Thomas, D. Nakatani, Y. Honda, K. Waseda, and P. Fitzgerald, "Safety and efficacy of low-dose paclitaxel utilizing the cobra-p drug-eluting stent system with a novel biodegradable coating in de novo coronary lesions: The plus-one first-in-man study," *Cardiovascular Revascularization Medicine*, vol. 15, no. 1, pp. 18–22, 2014.

[359] H. Kitahara, K. Waseda, R. Yamada, K. Sakamoto, P. G. Yock, P. J. Fitzgerald, and Y. Honda, "Relative dose and vascular response after drug-eluting stent implantation: A dosimetric 3d-intravascular ultrasound study," *International Journal of Cardiology*, vol. 204, pp. 211–217, 2016.

[360] A. Tzafriri, S. Parikh, and E. Edelman, "Taking paclitaxel coated balloons to a higher level: Predicting coating dissolution kinetics, tissue retention and dosing dynamics," *Journal of Controlled Release*, vol. 310, pp. 94–102, 2019.

[361] T. Seo, A. Lafont, S. Y. Choi, and A. Barakat, "Drug-eluting stent design is a determinant of drug concentration at the endothelial cell surface," *Annals of biomedical engineering*, vol. 44, no. 2, pp. 302–14, 2016.

[362] R. A. Byrne, A. Kastrati, S. Massberg, A. Wieczorek, K.-L. Laugwitz, M. Hadamitzky, S. Schulz, J. Pache, M. Fusaro, J. Hausleiter, A. Schömig, and J. Mehilli, "Biodegradable polymer versus permanent polymer drug-eluting stents and everolimus- versus sirolimus-eluting stents in patients with coronary artery disease: 3-year outcomes from a randomized clinical trial," *Journal of the American College of Cardiology*, vol. 58, no. 13, pp. 1325 – 1331, 2011.

[363] T. S. Al-Shehabi, R. Iratni, and A. H. Eid, "Anti-atherosclerotic plants which modulate the phenotype of vascular smooth muscle cells," *Phytomedicine*, vol. 23, no. 11, pp. 1068–81, 2016.

[364] A. Habib and A. V. Finn, "Endothelialization of drug eluting stents and its impact on dual anti-platelet therapy duration," *Pharmacological Research*, vol. 93, pp. 22–27, 2015.

[365] A. Habib, V. Karmali, R. Polavarapu, H. Akahori, Q. Cheng, K. Pachura, F. D. Kolodgie, and A. V. Finn, "Sirolimus–fkbp12.6 impairs endothelial barrier function through protein kinase c-$\alpha$ activation and disruption of the p120–vascular endothelial cadherin interaction," *Arteriosclerosis, Thrombosis, and Vascular Biology*, vol. 33, no. 10, pp. 2425–2431, 2013.

[366] K. Kolandaivelu, R. Swaminathan, W. J. Gibson, V. B. Kolachalama, K.-L. Nguyen-Ehrenreich, V. L. Giddings, L. Coleman, G. K. Wong, and E. R. Edelman, "Stent thrombogenicity early in high-risk interventional settings is driven by stent design and deployment and protected by polymer-drug coatings," *Circulation*, vol. 123, no. 13, pp. 1400–1409, 2011.